Politecnico di Torino

ScuDo
Scuola di Dottorato ~ Doctoral School
WHAT YOU ARE, TAKES YOU FAR

Doctoral Dissertation
Doctoral Program in Electrical Engineering (38^{th}cycle)

Experimental assessment of photovoltaic generators and enhanced model characterization

By

Stefano Schubert

******

Supervisors:
Prof. Filippo Spertino
Prof. Gianfranco Chicco

Doctoral Examination Committee:
Prof. Díaz-González Francisco , Referee, Universitat Politècnica de Catalunya
Prof. Sumaili Jean Akilimali, Referee, Université Officielle de Ruwenzori
Dr. Piliougine Rocha Michel, Referee, Consiglio Nazionale delle Ricerche
Prof. Pons Enrico, Politecnico di Torino
Prof. Spertino Filippo, Politecnico di Torino
Prof. Chicco Gianfranco, Politecnico di Torino

Politecnico di Torino
2026

Declaration

I hereby declare that, the contents and organization of this dissertation constitute my own original work and does not compromise in any way the rights of third parties, including those relating to the security of personal data.

Stefano Schubert
2026

* This dissertation is presented in partial fulfillment of the requirements for **Ph.D. degree** in the Graduate School of Politecnico di Torino (ScuDo).

Acknowledgements

I would like to express my sincere gratitude to all the people who have made this journey possible.

I thank **Prof. Filippo Spertino**, my supervisor, who guided me through this complex and deeply rewarding doctoral path with genuine passion and constant dedication. His presence has been an essential point of reference throughout.

I thank **Prof. Gianfranco Chicco**, my co-supervisor, who taught me with great patience that determination and attention to detail are what separate good work from excellent work. His precise and thoughtful feedback has shaped the way I think and carry out research.

I thank **Prof. Mario Paolone**, who welcomed me into his laboratory at EPFL and taught me with care how to organise a research project from its conception through to publication. The months I spent in his group were among the most formative of this doctorate.

A heartfelt thank you goes to my **parents and my grandmother**, who have been, and continue to be without reservation, the pillars of my growth. They taught me that passion is always the first thing in everything one does, and that lesson has guided every choice I have made.

I thank my brother **Emanuele**, with whom I continue to share moments of complicity and lightheartedness that make everything easier.

I thank **Marta**, who has always been a point of reference for me. She pushes me every day to become a better person, lifts me up when I need it, and drives me to give my best in everything I undertake. Her presence throughout these years has been as precious as it is unique.

Finally, I thank my friends *Federico, Nick, Bob, Gio', Lucio, Francesca, Song, Kun, Maedeh, Fabiana, Sarah, Erica, Aurora, Chiara, Matteo, Marco, Lucia, Elisa,*

Irene, Elena, Samu, Ale, Giulia, Enrico, Mauro, Myriam, Alberto, Alejandrina, Cora, Gelato, Paolo, Pilar, Luca, Cristian and Anne Marie who, whether we grew up together or met only recently, have turned this journey into a life experience I will never forget.

Desidero esprimere la mia sincera gratitudine a tutte le persone che hanno reso possibile questo percorso.

Ringrazio il **Prof. Filippo Spertino**, mio supervisore, che con autentica passione e dedizione costante mi ha guidato lungo questo complesso e profondamente appagante cammino di dottorato. La sua presenza è stata un punto di riferimento essenziale.

Ringrazio il **Prof. Gianfranco Chicco**, mio co-supervisore, che con grande pazienza mi ha insegnato che la determinazione e la cura nei dettagli sono ciò che distingue un buon lavoro da un lavoro eccellente. I suoi consigli precisi e attenti hanno plasmato il mio modo di pensare e di fare ricerca.

Ringrazio il **Prof. Mario Paolone**, che mi ha accolto nel suo laboratorio all'EPFL e mi ha insegnato con cura come organizzare un lavoro di ricerca dal suo concepimento fino alla pubblicazione. I mesi trascorsi nel suo gruppo sono stati tra i più formativi di questo dottorato.

Un ringraziamento sentito va ai miei **genitori e a mia nonna**, che sono stati, e continuano a essere senza riserbo, le colonne portanti della mia crescita. Mi hanno insegnato che la passione è sempre la prima cosa in tutto ciò che si fa, e questo insegnamento ha guidato ogni mia scelta.

Ringrazio mio fratello **Emanuele**, con il quale continuo a condividere momenti di complicità e spensieratezza che rendono tutto più leggero.

Ringrazio **Marta**, che è sempre stata un punto di riferimento per me. Mi sprona ogni giorno a diventare una persona migliore, mi tira su quando ne ho bisogno e mi spinge a dare il massimo in tutto ciò che intraprendo. La sua presenza in questi anni è stata preziosa quanto unica.

Infine, ringrazio i miei amici *Federico, Nick, Bob, Gio', Lucio, Francesca, Song, Kun, Maedeh, Fabiana, Sarah, Erica, Aurora, Chiara, Matteo, Marco, Lucia, Elisa, Irene, Elena, Samu, Ale, Giulia, Enrico, Mauro, Myriam, Alberto, Alejandrina, Cora, Gelato, Paolo, Pilar, Luca, Cristian e Anne Marie* che, non importa se siamo cresciuti insieme o ci siamo incontrati solo di recente, hanno reso questo percorso un'esperienza di vita che non dimenticherò mai.

Abstract

Photovoltaic generation represents a key technology for the large-scale integration of renewable energy sources into modern power systems. Accurate modelling and characterisation of photovoltaic devices are essential to assess their performance, predict energy production, and support the design and optimisation of photovoltaic installations. Equivalent-circuit models are widely adopted for this purpose, as they provide a compact and physically meaningful description of the electrical behaviour of photovoltaic cells and modules through a limited set of parameters.

This Ph.D. thesis develops an integrated methodology including theoretical aspects and experimental characterization for the identification and application of equivalent-circuit parameters of photovoltaic modules under varying operating conditions. The proposed methodology proceeds from theoretical formulations that require experimental verification, whose results are subsequently used to perform an a posteriori correction and recalibration of the model parameters, thereby improving the accuracy and physical consistency of the equivalent-circuit representation.

The work addresses the limitations of conventional parameter-estimation approaches, which are often restricted to specific irradiance and temperature levels and therefore unsuitable for long-term energy-yield prediction. The proposed procedure explicitly accounts for the dependence of the model parameters on environmental variables, enabling the use of equivalent-circuit representations as a basis for photovoltaic energy estimation.

Two complementary measurement systems are developed and employed for the experimental characterisation of photovoltaic modules. The first system is based on a capacitor-charging circuit and reconstructs the current–voltage (I–V) characteristic curve from the transient electrical response. The second system employs a programmable electronic load to impose controlled operating points and acquire steady-state current–voltage data. Both platforms are integrated within

a unified post-processing pipeline, allowing consistent data handling, parameter estimation, and comparative analysis.

Parameter identification is formulated as a nonlinear estimation problem and addressed using least-squares techniques combined with uncertainty analysis. The Fisher Information Matrix and the associated Cramér–Rao Lower Bound are employed to quantify parameter uncertainty and to guide the optimisation of current–voltage sampling strategies. A D-optimal design criterion is adopted to improve the information content of experimental measurements and enhance estimation robustness, particularly under partial shading and mismatch conditions. This approach is particularly advantageous in practical scenarios where only a limited number of operating points can be acquired for the characterisation of photovoltaic modules, as is typically the case in maximum power point tracking algorithms, where measurement opportunities are constrained by real-time operation and energy-harvesting requirements.

The proposed framework is validated through numerical simulations and experimental campaigns conducted on photovoltaic modules of different technologies and power ratings. The results demonstrate that the identified parameter sets accurately reproduce measured electrical behaviour and enable reliable energy-production estimates when compared against reference models and experimental data. The methodologies developed in this thesis provide a systematic approach to photovoltaic modelling, parameter estimation, and uncertainty-aware energy assessment, with direct applicability to both research and practical photovoltaic system analysis.

Contents

List of Figures

List of Tables

Chapter 1

Introduction

The global demand for electrical energy has increased steadily over recent decades, driven by population growth, industrial expansion, and the progressive electrification of services and infrastructures. This trend poses significant challenges in terms of sustainability, environmental impact, and security of supply, particularly in systems still dominated by fossil-fuel-based generation. In this context, the large-scale deployment of renewable energy sources represents a central strategy for reducing greenhouse gas emissions and mitigating climate change.

Among renewable technologies, solar photovoltaic generation occupies a prominent role due to its modularity, scalability, and declining costs. Photovoltaic systems can be deployed across a wide range of power levels, from small residential installations to utility-scale plants, and can be integrated into both centralized and distributed energy systems. Despite these advantages, the intrinsic variability of solar irradiance and the complex electrical behaviour of photovoltaic devices introduce non-negligible challenges in system design, performance assessment, and energy-yield prediction.

Accurate electrical modelling of photovoltaic cells and modules is therefore essential for the analysis, simulation, and optimisation of photovoltaic systems. Equivalent-circuit models, based on diode representations combined with lumped resistive elements, are widely adopted to reproduce the current-voltage characteristic of photovoltaic devices under different operating conditions. The parameters of these models describe the physical and technological properties of the devices and provide a compact description of their electrical behaviour.

A critical aspect in the practical use of equivalent-circuit models lies in the identification of their parameters from experimental data. Over the past two decades, a wide variety of methods have been proposed to address this problem, and they can be broadly classified into three families: analytical methods, numerical iterative methods, and metaheuristic optimisation algorithms [1, 2].

- Analytical approaches exploit closed-form or semi-analytical relationships derived from the I–V characteristic at selected operating points, typically short-circuit, open-circuit, and maximum power, to express the model parameters explicitly. Notable contributions in this direction include the Lambert W-function-based solutions developed by Nassar-Eddine et al. [3] and Batzelis et al. [4], as well as the characteristic-point extraction procedures proposed by Rhouma and Gastli [5] and Majdoul et al. [6]. Although analytically elegant, these methods often involve simplifying assumptions (e.g. neglecting the shunt resistance or assuming a fixed ideality factor) that can reduce accuracy when applied outside the conditions for which they were calibrated [7, 8].

- Numerical iterative methods solve the implicit single-diode or double-diode equation by means of Newton–Raphson, Levenberg–Marquardt, or trust-region algorithms applied to the full measured I–V curve. The comprehensive modelling framework proposed by Villalva et al. [9] represents a widely cited example of this approach, combining analytical initialisation with an iterative adjustment of the series and shunt resistances. While generally more accurate than pure analytical methods, numerical approaches are sensitive to the initial parameter estimates and may converge to local minima in the strongly nonlinear, five-dimensional parameter space [10].

- Metaheuristic and evolutionary algorithms have therefore attracted growing interest, as they can explore the solution space globally without requiring gradient information. Differential evolution [11], simulated annealing, particle swarm optimisation, and hybrid strategies combining several heuristics [12] have been applied to both single-diode and double-diode models. Comprehensive surveys of these techniques are provided by Jordehi [1], Fahim et al. [10], and Li et al. [13], which together review more than a hundred algorithms and benchmark them on standard cell datasets.

Despite this substantial body of work, the vast majority of the proposed methods are designed to operate at a single irradiance–temperature operating point, typically under Standard Test Conditions (STC). The dependence of the equivalent-circuit parameters on environmental variables is either neglected or treated through simplified datasheet-based corrections. A seminal contribution towards overcoming this limitation was the five-parameter model proposed by De Soto et al. [14], which introduced semi-empirical equations to express each parameter as a function of absorbed irradiance and cell temperature. This model was subsequently adopted in the PVsyst simulation environment, and Sauer et al. [15] demonstrated that a more accurate fitting of the irradiance and temperature dependences can yield improvements in annual energy yield predictions on the order of 0.8–1.0%. The experimental study by Ruschel et al. [16] confirmed that the single-diode model parameters exhibit a non-trivial dependence on both irradiance and temperature, and that accounting for this dependence is essential for accurate long-term predictions. Nonetheless, a unified procedure that integrates rigorous parameter identification across a wide range of operating conditions with uncertainty quantification and energy-yield estimation is still lacking.

An additional challenge arises when photovoltaic modules operate under non-uniform irradiance conditions. Partial shading induces mismatch among series-connected cells and activates bypass diodes, resulting in piecewise and multi-modal I–V characteristics that cannot be described by a single set of equivalent-circuit parameters. Previous studies have addressed the adjustment of model parameters under shading [17], but these procedures were limited to conventional full-cell module architectures. The extension of parameter identification techniques to contemporary half-cell module designs, which exhibit a more complex internal parallelisation, remains an open research problem.

Furthermore, the question of how to optimally sample the I–V curve to maximise the information content of the measurements has received limited attention in the photovoltaic literature. In other fields of circuit-parameter identification, for instance, lithium-ion cell modelling, the Cramér–Rao Lower Bound (CRLB) and the Fisher Information Matrix (FIM) have been successfully employed to quantify parameter uncertainty and to guide experimental design [18, 19]. However, the application of these estimation-theoretic tools to photovoltaic equivalent-circuit models, and in particular the development of D-optimal sampling strategies for I–V curve acquisition, has not been explored prior to the present work.

Finally, the estimation of photovoltaic energy production is typically performed using simplified models that do not fully exploit the information contained in the equivalent-circuit parameters. Simple irradiance-proportional formulations [20] relate the output power linearly to the incident irradiance, while temperature-corrected models incorporate the power temperature coefficient [21, 22]. More elaborate semi-empirical models introduce additional meteorological variables such as wind speed and air mass [23–25], but their coefficients are often site-specific and require recalibration for each installation. Integrated single-diode approaches that model the parameter dependence on environmental conditions have been proposed by Tossa et al. [26] and Malik and Chandel [27], yet a systematic comparison of these models against a unified, experimentally validated, equivalent-circuit framework across multiple climates and PV technologies is still lacking.

This thesis addresses these limitations by developing a comprehensive experimental and methodological framework for the identification and use of photovoltaic equivalent-circuit parameters. The proposed approach combines controlled experimental characterisation, rigorous parameter estimation, and uncertainty analysis to derive parameter sets that remain valid over a range of irradiance and temperature conditions. By explicitly modelling the dependence of the equivalent-circuit parameters on environmental variables, the framework enables the prediction of photovoltaic energy production using physically meaningful quantities.

Objectives of the thesis

Based on the limitations identified in the existing literature, the present thesis pursues the following specific objectives:

1. **Design and implementation of dedicated measurement platforms.** Develop two complementary experimental systems for the acquisition of I–V characteristics of photovoltaic modules under outdoor conditions: a capacitor-based transient tracer and a programmable electronic-load system. Both platforms shall provide synchronised acquisition of electrical and environmental quantities and shall be integrated within a unified post-processing pipeline, enabling consistent data handling and comparative analysis.

2. **Parameter identification of equivalent-circuit models under partial shading.** Propose and validate a two-test procedure capable of recovering the single-diode model parameters of individual photovoltaic cells operating under non-uniform irradiance. The method shall be applicable to both conventional full-cell and contemporary half-cell module architectures, explicitly accounting for the piecewise behaviour of the I–V curve induced by bypass diode activation.

3. **Optimal experimental design for I–V curve sampling.** Develop a D-optimal sampling strategy grounded in the Fisher Information Matrix and the Cramér–Rao Lower Bound to identify the current–voltage operating regions that are most informative for parameter estimation. The objective is to minimise the variance of the estimated parameters for a given number of measurement points, which is particularly relevant in scenarios where sampling opportunities are limited, such as in maximum power point tracking algorithms.

4. **Uncertainty-aware energy-yield estimation across multiple climates and technologies.** Formulate a complete workflow that propagates the experimentally identified equivalent-circuit parameters through nonlinear regression models describing their dependence on irradiance and temperature, and employ these models to predict photovoltaic energy production over extended periods. The procedure shall be validated against experimental data acquired in different climatic conditions (Italy and Spain) and benchmarked against representative energy-prediction models available in the literature.

Publications arising from this thesis

The research presented in this thesis has resulted in three peer-reviewed journal articles published in IEEE journals.

- The two-test parameter identification procedure for shaded half-cell modules described in Chapter 6 is reported in [28]: G. Malgaroli, S. Schubert, A. Ciocia, F. Spertino, and A. F. Murtaza, "Two-Tests Procedure to Determine the Equivalent Circuit's Parameters of Half-Cells in Commercial PV Modules under

Sunlight and Partial Shading", *IEEE Transactions on Industry Applications*, 2025.

- The D-optimal FIM-based sampling framework presented in Chapter 7 is reported in [29]: S. Schubert, V. Sovljanski, F. Spertino, G. Chicco, and M. Paolone, "Accurate Parameter Estimation on Photovoltaic Modules Using Fisher Information Matrix and D-Optimal Design", *IEEE Access*, vol. 13, pp. 212378–212406, 2025.

- The energy yield assessment methodology across multiple climates and technologies presented in Chapter 8 is reported in [30]: G. Malgaroli, A. Ciocia, S. Gulkowski, J. V. Muñoz Díez, S. Schubert, and F. Spertino, "Innovative Model for Energy Assessment of New Crystalline Silicon Technologies Tested Under Different Climates", *IEEE Transactions on Industry Applications*, 2026.

Outline of the thesis

The thesis is organised as follows.

Chapter 2 provides the theoretical background on solar energy conversion and photovoltaic device physics. The chapter introduces the single-diode and double-diode equivalent-circuit models, discusses the dependence of the model parameters on irradiance and temperature, and describes the series and parallel connection of photovoltaic cells into modules and generators. This material establishes the modelling framework used throughout the remainder of the thesis.

Chapter 3 analyses the electrical architectures of contemporary photovoltaic modules, with emphasis on the comparison between full-cell and half-cell layouts. The behaviour of these architectures under uniform and partial-shading conditions is discussed, together with the implications for I–V curve sampling and parameter identifiability.

Chapter 4 presents the experimental characterisation of a first-order RC filtering stage. This chapter serves as a controlled validation of the modelling, measurement, and parameter-identification methodology on a simple and analytically tractable system, before its application to the more complex photovoltaic case.

Chapter 5 describes the two dedicated measurement systems developed for the experimental characterisation of photovoltaic modules: a capacitor-based I–V tracer and a programmable electronic-load system. The design, implementation, automation, and post-processing pipeline of both platforms are presented.

Chapter 6 proposes a two-test parameter-identification procedure for photovoltaic modules operating under partial shading. The method recovers the equivalent-circuit parameters of individual shaded cells from two I–V curve measurements, one under uniform irradiance and one under controlled shading, and is validated on both mini-modules and commercial half-cell modules.

Chapter 7 introduces a D-optimal experimental design framework for I–V curve sampling based on the Fisher Information Matrix and the Cramér–Rao Lower Bound. The method identifies the current–voltage operating regions that are most informative for parameter estimation and optimises the sampling strategy to minimise parameter variance. The approach is validated through numerical simulations and experimental campaigns on modules of different technologies.

Chapter 8 addresses the energy-yield assessment of photovoltaic modules across multiple climates and technologies. The identified equivalent-circuit parameters are propagated through empirical regression models to predict power output over extended periods. The proposed procedure is benchmarked against several reference models from the literature, using experimental data acquired in Italy and Spain on ten modules of different technologies.

Chapter 9 summarises the main conclusions and outlines directions for future work.

The proposed methods are demonstrated through numerical simulations and experimental campaigns conducted on photovoltaic modules of different technologies and power ratings. The results show that the adopted framework supports accurate parameter estimation, improved understanding of measurement uncertainty, and enhanced reliability in photovoltaic energy assessment. Overall, the thesis aims to contribute to the quantitative modelling and experimental characterisation of photovoltaic devices, with direct relevance to system design, performance evaluation, and energy prediction.

Chapter 2

Energy conversion by solar photovoltaic generators

2.1 Solar irradiance

Solar irradiance, G (in $\mathrm{W{\cdot}m^{-2}}$), is the total radiant power from a source incident on a unit area. The Sun can be modelled as an ideal black-body emitter with temperature $T \approx 5800$ K. Outside Earth's atmosphere, its spectral power distribution g_0 ($\mathrm{W{\cdot}m^{-2}}$ $\mu\mathrm{m^{-1}}$) spans from the ultraviolet to the infrared, peaking in the visible around $\lambda \approx 0.5$ μm. Passing through the atmosphere, part of this radiation is lost due to absorption, scattering and reflection by clouds, carbon dioxide, ozone and other air constituents. For a unit surface oriented normal to the solar rays, the "solar irradiance" is the integral of the spectral irradiance $g(\lambda)$ ($\mathrm{W{\cdot}m^{-2}}$ $\mathrm{nm^{-1}}$) over all wavelengths:

$$G = \int g(\lambda) d\lambda \approx 1367\,\mathrm{W \cdot m^{-2}}. \tag{2.1}$$

Figure 2.1 illustrates the spectral distribution of solar irradiance above the atmosphere and at ground level, alongside the ideal black-body curve.

The component that reaches Earth's surface without scattering, and therefore without energy loss, is the beam irradiance, G_b ($\mathrm{W{\cdot}m^{-2}}$). The diffuse component, G_d ($\mathrm{W{\cdot}m^{-2}}$), is the portion that arrives after scattering and appears to originate from across the sky dome. Their relative magnitudes depend on weather: on clear

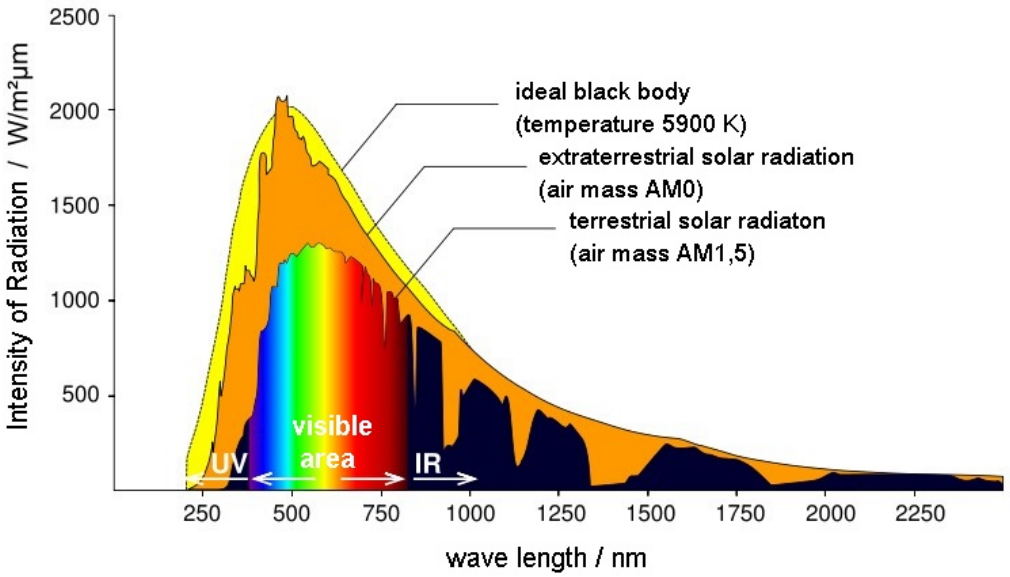

Fig. 2.1 Spectral profile of the solar irradiance g(λ) under varying conditions.

days, radiation is primarily beam (diffuse/global < 20%), whereas on cloudy days the diffuse share is dominant. A third contribution, the albedo G_r ($W \cdot m^{-2}$), is the radiation reflected from the ground. It is characterised by the reflectance ρ, defined as the ratio of reflected to incident global radiation, and depends on surface type and colour (for example, snow yields high reflectance).

The global irradiance incident on a receiver is the sum of these three terms:

$$G_g = G_b + G_d + G_r. \tag{2.2}$$

Solar radiation at the surface varies daily and seasonally due to the Sun's apparent motion, as well as with weather and atmospheric composition. Consequently, PV system design should be based on local meteorological measurements. At ground level, irradiance also depends on site altitude and on the tilt of the receiving surface relative to horizontal.

The Air Mass (AM) quantifies the path length of solar radiation through a clear atmosphere. Its minimum value is 1, corresponding to the Sun at the zenith. For other solar elevations, AM > 1 and, neglecting Earth's curvature, can be approximated by $(\cos\theta_z)^{-1}$, where θ_z is the zenith angle (see Figure 2.2). Solar-cell efficiency depends on the incident spectrum, so standard spectra are used for comparison:

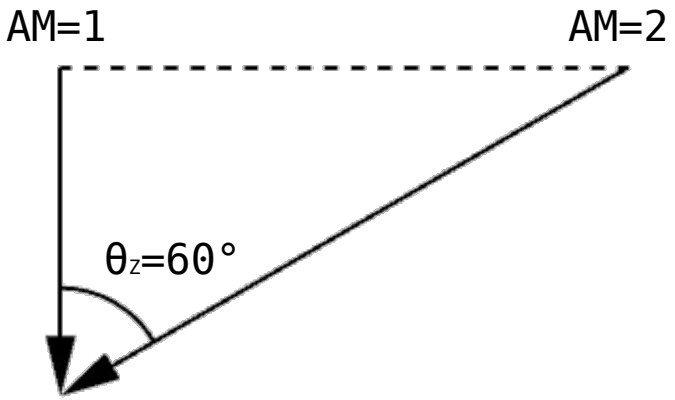

Fig. 2.2 Geometrical scheme of air mass.

AM1.5G (global—beam plus diffuse) and AM1.5D (diffuse only) at Earth's surface, and AM0 above the atmosphere. The AM1.5G spectrum is normalised to represent a clear-sky irradiance of G = 1000 W·m^{-2}; AM0 is relevant for aerospace applications.

Figure 2.1 indicates the visible band b_1 (380–780 nm). The usable spectral band depends on cell technology; for c-Si, b_2 spans roughly 400–1100 nm. Figure 2.3 details the spectral responses of three widely used technologies. Notably, the photo-generated current density J_{ph} (A·m^{-2}) is given by the integral $\int g(\lambda) \cdot S(\lambda) d\lambda$, where S($\lambda$) is the device spectral response.

Irradiance integrated over time is termed radiation, H (kWh·m^{-2}). Daily (H_d), monthly (H_m) and yearly (H_y) radiation values are key inputs for PV system design.

2.2 Solar cell: structure and operation

The solar cells represent the fundamental components of PV generators. For terrestrial applications, these devices are primarily fabricated using crystalline silicon (c-Si), which can be further classified into monocrystalline (m-Si) and polycrystalline (p-Si) forms, or using thin-film technologies such as amorphous silicon (a-Si), copper indium-gallium selenide (CIGS), or cadmium telluride (CdTe).

Solar cells are large-area diodes, whose geometrical configuration depends on their technology: p-Si cells are usually square, m-Si cells can be pseudo-square or

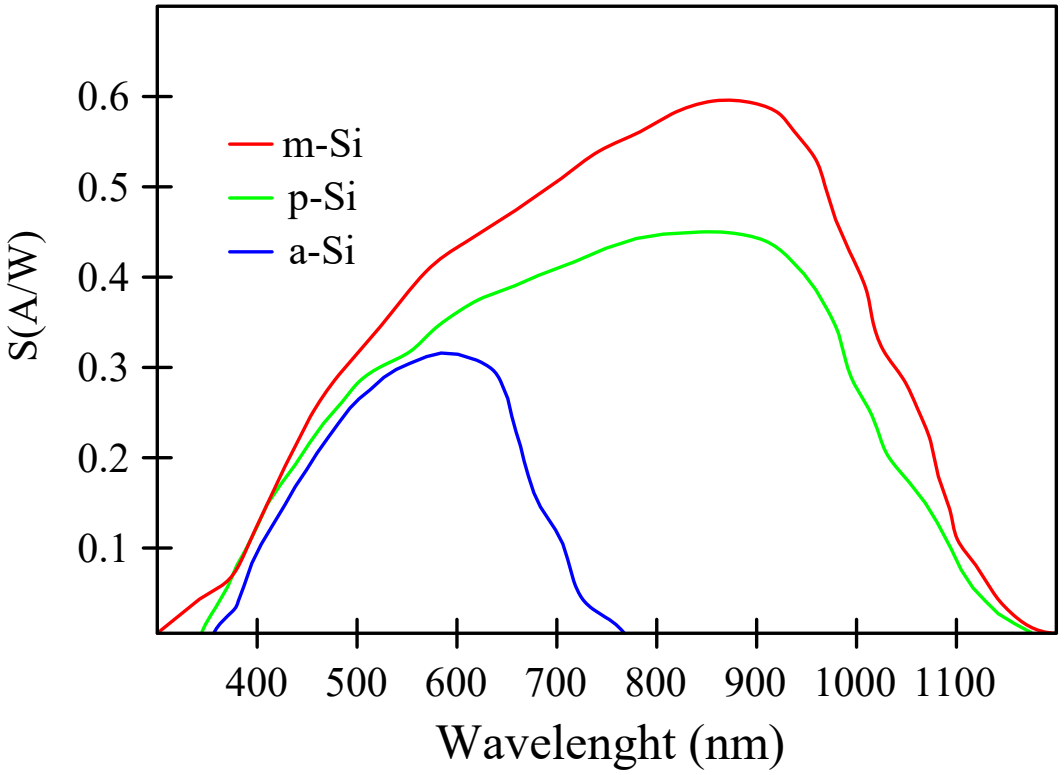

Fig. 2.3 Geometrical scheme of air mass.

circular, whereas a-Si, CIGS, and CdTe cells are commonly rectangular. The diode is positioned between two electrodes: the front contact, which is either transparent and relatively thick in thin-film devices or grid-shaped in c-Si cells, and the rear contact, which is typically a continuous metallic layer. A schematic representation of a typical c-Si cell is shown in Figure 2.4. The physical thickness of PV cells generally ranges from approximately 1 μm in thin-film devices to several hundred micrometres (150–100 μm for c-Si).

The performance of a PV cell under dark conditions can be described by the classical theory of the p–n junction. A typical c-Si diode consists of two semiconductor layers: an n-type layer, heavily doped with pentavalent impurities such as phosphorus, deposited over a p-type layer doped with trivalent elements such as boron. The n-type region is sufficiently shallow to allow incident solar radiation to reach the junction-region, which is subject to an internal electric field. This field arises from the diffusion of mobile charge carriers across the p–n interface. As illustrated in Figure 2.4, electrons diffuse from the n-type to the p-type side, producing a positive

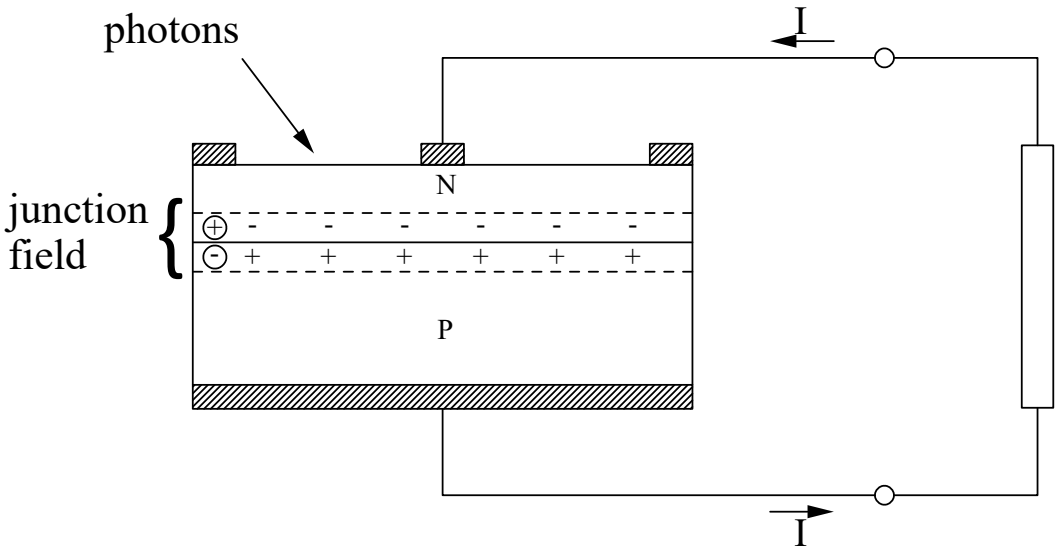

Fig. 2.4 Structural configuration of a polycrystalline p-type silicon (p-Si) solar cell.

charge distribution in the n-region. Conversely, holes diffuse from the p-type to the n-type region, creating a negative charge distribution within the p-region. This diffusion occurs from regions of higher to lower carrier concentration.

The interface formed between the two regions is termed the depletion or space-charge region, which is depleted of free charge carriers: positive ions remain in the n-region, while negative ions persist in the p-region. Such a charge separation establishes a potential barrier, also called the junction field, which opposes any further diffusion of electrons and holes. Under open-circuit conditions, the drift current generated by this field balances the diffusion current. When an external voltage is applied, this equilibrium is disturbed. A positive bias applied to the p-region (forward bias) reduces the potential barrier, allowing the diffusion current to dominate over the drift current. Under reverse bias (negative voltage applied to the p-region), the potential barrier increases, and only a small current, known as the reverse saturation current, flows due to minority carrier drift.

The junction thus behaves as a rectifying element, whose I–V characteristic is described by the Shockley diode equation [31]. The diffusion and drift currents are

the two main contributions to this equation, which are balanced in the absence of external voltage, resulting in zero net current flow.

$$I = I_0 \left[\exp\left(\frac{qV}{nk_B T_c} \right) - 1 \right]. \tag{2.3}$$

Here, I_0 (A) denotes the saturation current, T_c the junction temperature (K), q the electron charge (1.6×10^{-19} C), n the diode quality factor (typically between 1 and 2), and k_B the Boltzmann constant (1.38×10^{-23} J·K^{-1}). This model neglects breakdown effects occurring under high reverse-bias conditions.

According to the principle of wave–particle duality, light exhibits both wave-like and particle-like behaviour. Photovoltaic energy conversion is explained by considering light as a flux of photons, each carrying a discrete amount of energy given by:

$$E = \frac{hc}{\lambda}. \tag{2.4}$$

where h is Planck's constant ($6.63 \times 10^{-34} \mathrm{m}^2 \cdot \mathrm{kg} \cdot \mathrm{s}^{-1}$), c is the speed of light ($3 \times 10^8 \mathrm{m} \cdot \mathrm{s}^{-1}$), and λ is the radiation wavelength. Under clear-sky conditions, approximately 4.4×10^{17} photons per second strike every square centimetre of the Earth's surface. Only a fraction of these photons, specifically those whose energy exceeds the bandgap energy E_g (eV) of the semiconductor material, can contribute to the photovoltaic effect. When such photons are absorbed, they promote electrons from the valence band to the conduction band, thus creating electron–hole pairs. Since many absorbed photons have energy greater than E_g, the excess energy is dissipated as heat following thermal relaxation of the carriers to the band edges.

The photogenerated current (I_{ph}) represents the flow of electrons induced by light absorption and can be expressed, neglecting losses, as:

$$I_{ph} = qNA, \tag{2.5}$$

where N is the photon flux ($\mathrm{cm}^{-2} \cdot \mathrm{s}^{-1}$) and A is the illuminated semiconductor area. The current density J is therefore:

$$J = qN \tag{2.6}$$

For the terrestrial solar spectrum, J is approximately $70\,\mathrm{mA}\cdot\mathrm{cm}^2$ [32]. c-Si cells can effectively convert about $44\,\mathrm{mA}\cdot\mathrm{cm}^2$ of this value (roughly 63%), corresponding to a bandgap of approximately 1.1 eV. The maximum theoretical voltage produced by a solar cell is limited by the bandgap energy and can be expressed as $\mathrm{E_g}\cdot\mathrm{q}^{-1}$. In practice, the actual voltage is always lower than this theoretical value. Semiconductors with larger bandgaps produce higher voltages but have a narrower spectral response. For example, amorphous silicon (a-Si) with $E_g \approx 1.7$ eV produces around 0.8 V, while monocrystalline silicon (m-Si) with $E_g \approx 1.1$ eV yields approximately 0.6 V. However, wider bandgaps correspond to shorter spectral cut-off wavelengths (750 nm for a-Si and 1100 nm for m-Si) and lower current densities (about 13 $\mathrm{mA}\cdot\mathrm{cm}^{-2}$ for a-Si and 35 $\mathrm{mA}\cdot\mathrm{cm}^{-2}$ for m-Si under an irradiance of $1000\,\mathrm{W}\cdot\mathrm{m}^{-2}$). Therefore, the optimal photovoltaic material represents a trade-off between voltage and current generation, maximising the overall output power.

2.2.1 Equivalent circuit of a solar cell

As a first approximation, the electrical behaviour of a photovoltaic (PV) cell can be represented by means of an equivalent electrical circuit. In the scientific literature, a wide variety of circuital models has been proposed, differing in the number of parameters, physical assumptions, and computational complexity [3]. Despite these differences, most formulations belong to the family of diode-based models, in which the PV device is described as a photogenerated current source connected to one or more diodes, complemented by lumped resistive elements that account for non-ideal ohmic and leakage effects.

The simplest representation consists of an ideal current source, whose magnitude is proportional to the incident irradiance, connected in anti-parallel with a single diode. While this model allows a basic qualitative description of the photovoltaic effect, it is insufficient to reproduce the actual shape of the current–voltage (I–V) characteristic observed in real devices. For this reason, more elaborate configurations are commonly adopted.

One of the most widely used equivalent circuits is illustrated in Figure 2.5. In this representation, two additional elements are introduced with respect to the ideal model: a shunt resistance R_{sh} and a series resistance R_{s}. The shunt resistance accounts for leakage currents flowing through alternative paths parallel to the p–n

junction, primarily associated with crystal defects and imperfect edge insulation during the manufacturing process. The series resistance, on the other hand, is a composite parameter that includes the bulk resistance of the semiconductor material, the resistance of the metallic contacts, and the contact resistances between metal and semiconductor.

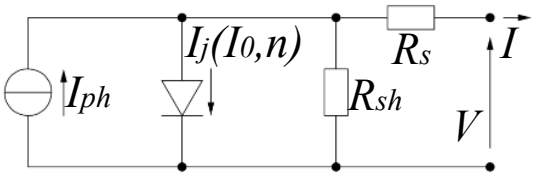

Fig. 2.5 Equivalent circuit of a solar cell (five-parameter single-diode model).

In crystalline-silicon technologies, the dominant contribution to the series resistance typically arises from the front metallisation. This consists of a grid-like structure formed by busbars and fingers. Busbars, usually two or three in older cell generations and up to ten in more recent designs, provide the electrical interconnection between adjacent cells. Fingers are thin metallic lines oriented perpendicularly to the busbars and are responsible for collecting and transporting the photogenerated current from the illuminated surface of the cell to the external terminals.

From a modelling perspective, the circuit in Figure 2.5 corresponds to the so-called five-parameter (5P) or single-diode model, which represents a compromise between analytical simplicity and descriptive accuracy. This model can be regarded as an extension of simpler formulations, such as the three-parameter (3P), the four-parameter (4P) and the seven-parameter (7P) models, which are reviewed in the following for completeness and contextualisation.

The three-parameter model comprises only the photogenerated current I_{ph}, the diode reverse saturation current I_0, and the diode ideality factor n. Its equivalent circuit is shown in Figure 2.6. The resulting I–V relationship is explicit in the output current and therefore allows direct analytical evaluation without the need for numerical solvers. However, the absence of both series and shunt resistances prevents an accurate representation of the slope of the I–V curve near short-circuit and open-circuit conditions.

The four-parameter model improves upon this description by introducing a series resistance R_{s}, as illustrated in Figure 2.7. Although R_{s} typically assumes small

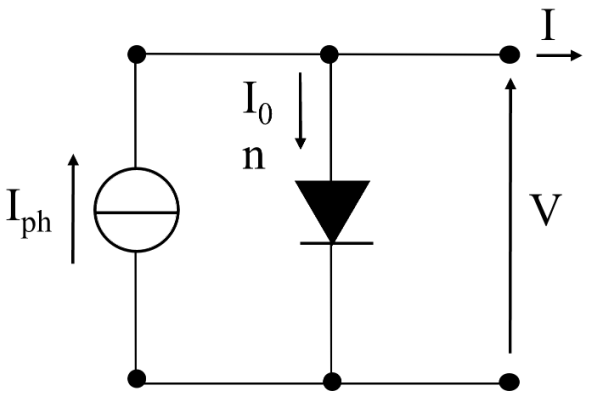

Fig. 2.6 Equivalent circuit with three parameters (3P).

numerical values, it significantly affects the curvature of the *I*–*V* characteristic in the high-voltage region, particularly around the maximum power point. The resulting governing equation becomes implicit, thereby requiring numerical methods for its solution.

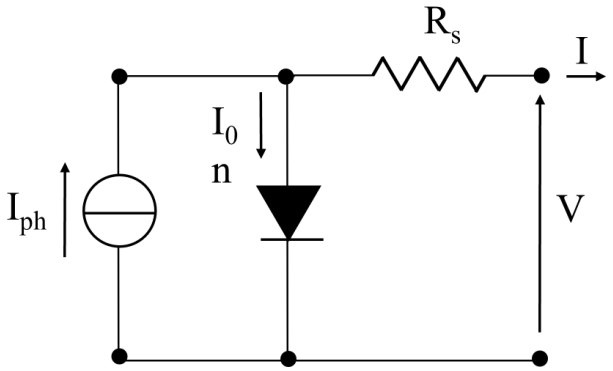

Fig. 2.7 Equivalent circuit with four parameters (4P).

The five-parameter single-diode model further augments the circuit by including a shunt resistance R_{sh}, as shown in Figure 2.8. This element models parasitic leakage paths across the junction and along the cell edges, which become particularly relevant under low-voltage or low-irradiance operating conditions. For most commercial crystalline-silicon cells, R_{sh} assumes relatively large values, yet its inclusion is essential for accurately reproducing the short-circuit region of the *I*–*V* curve.

More sophisticated formulations are also available, such as the seven-parameter (7P) or double-diode model, depicted in Figure 2.9. In this case, two diodes are employed to separately describe diffusion and recombination mechanisms within

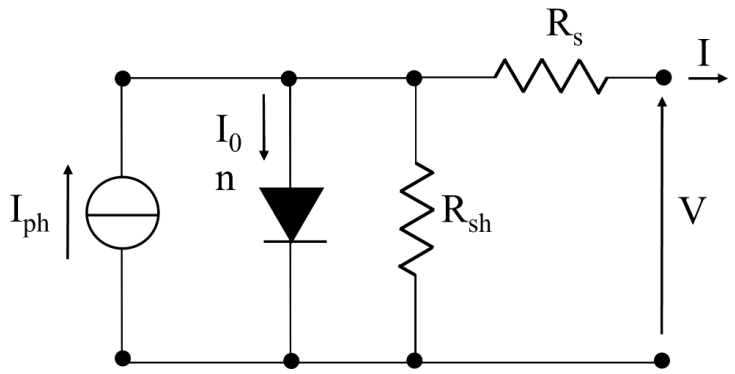

Fig. 2.8 Equivalent circuit with five parameters (5P, single-diode model).

the p–n junction. While this approach can improve modelling accuracy under low-irradiance or mismatch conditions, it comes at the cost of increased computational burden and a more challenging parameter-identification process.

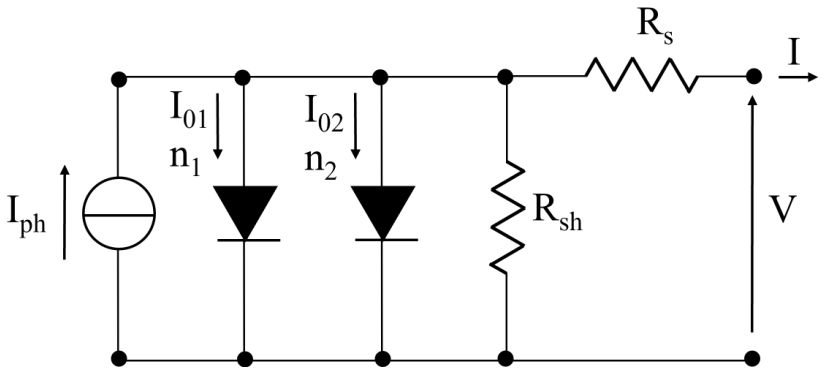

Fig. 2.9 Equivalent circuit with seven parameters (7P, double-diode model).

In this thesis, the five-parameter single-diode model is adopted as the reference representation [9], as it provides a satisfactory balance between physical fidelity and numerical tractability. By applying Kirchhoff's voltage and current laws to the circuit in Figure 2.5, the following relations are obtained:

$$I = I_{\mathrm{ph}} - I_{\mathrm{d}} - I_{\mathrm{sh}}, \tag{2.7}$$

$$V = V_{\mathrm{d}} - IR_{\mathrm{s}}, \tag{2.8}$$

where V and I denote the voltage across the external load and the output current of the PV cell, respectively.

Combining these expressions with the Shockley diode equation yields the implicit I–V characteristic:

$$I = I_{\mathrm{ph}} - I_0 \left[\exp\!\left(\frac{\mathrm{q}(V + IR_{\mathrm{s}})}{n \mathrm{k_b} T} \right) - 1 \right] - \frac{V + IR_{\mathrm{s}}}{R_{\mathrm{sh}}}. \tag{2.9}$$

This transcendental equation cannot be solved in closed form and therefore requires numerical techniques for its evaluation. The equivalent circuit is fully characterised by the parameter vector

$$\theta = \begin{bmatrix} I_{\mathrm{ph}} & I_0 & n & R_{\mathrm{s}} & R_{\mathrm{sh}} \end{bmatrix}^{\top}, \tag{2.10}$$

from which the complete I–V curve can be reconstructed under given irradiance and temperature conditions.

From the I–V characteristic, the corresponding power–voltage (P–V) curve can be derived. Its most significant feature is the maximum power point $P_M(\mathrm{V_{mpp}}, \mathrm{I_{mpp}})$, which lies between the short-circuit condition $(0, \mathrm{I_{sc}})$ and the open-circuit condition $(\mathrm{V_{oc}}, 0)$. A commonly used figure of merit is the fill factor K_{f}, defined as

$$K_{\mathrm{f}} = \frac{P_M}{\mathrm{I_{sc}} \mathrm{V_{oc}}}. \tag{2.11}$$

The fill factor quantifies the deviation of the real device from ideal behaviour and is strongly influenced by the internal resistances R_{s} and R_{sh}. For crystalline-silicon cells, typical values range between 0.72 and 0.76 [32], corresponding to ratios $\mathrm{I_{mpp}}/\mathrm{I_{sc}} \approx 0.90$–$0.95$ and $\mathrm{V_{mpp}}/\mathrm{V_{oc}} \approx 0.8$.

The effect of the resistive parameters on the I–V curve can be summarised as follows. A reduction in R_{sh} leads to a decrease in the open-circuit voltage $\mathrm{V_{oc}}$ and an increase in the absolute slope $\mathrm{d}I/\mathrm{d}V$ near the short-circuit region. Conversely, an increase in R_{s} reduces the short-circuit current $\mathrm{I_{sc}}$ and flattens the I–V curve in the vicinity of the open-circuit point.

Finally, it is worth noting that the complete I–V characteristic of a PV cell spans both the second and fourth quadrants of the current–voltage plane, as illustrated in Figure 2.10. In the second quadrant ($V < 0$, $I > 0$), the device operates under reverse bias and behaves as a load, whereas in the fourth quadrant ($V > 0$, $I < 0$) it acts as a current source delivering power to the external circuit. Operation beyond

the hyperbola corresponding to the maximum dissipated power P_{dM} may lead to hazardous conditions. In particular, if the reverse voltage exceeds the breakdown voltage V_{b}, typically of the order of a few tens of volts for crystalline-silicon cells, irreversible damage and permanent short-circuit failure may occur.

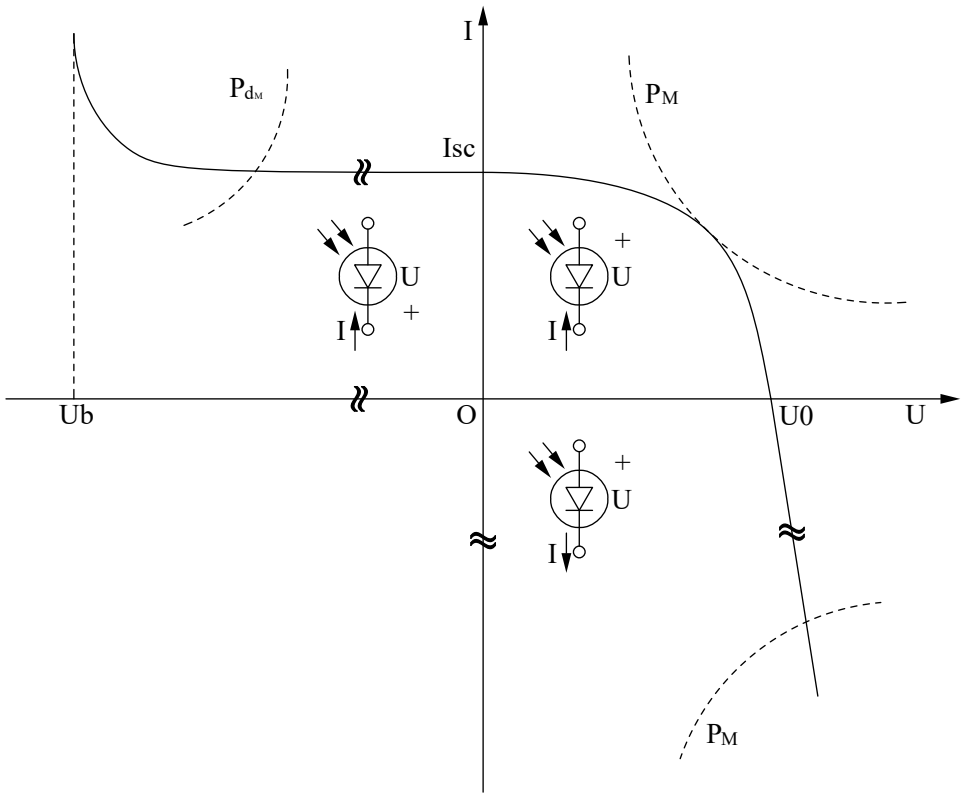

Fig. 2.10 Modes of operation of a solar cell in the current–voltage plane.

2.2.2 Dependence on irradiance and temperature

The *I–V* characteristic of photovoltaic (PV) cells is strongly influenced by both the cell temperature (T_{c}) and the incident irradiance (G). For a given temperature, when the irradiance decreases, two principal effects are observed. Firstly, the short-circuit current ($\mathrm{I_{sc}}$) decreases approximately in direct proportion to the reduction in irradiance. Secondly, the open-circuit voltage ($\mathrm{V_{oc}}$) exhibits a logarithmic decrease with diminishing irradiance, as described in [33].

Figure 2.11 illustrates the influence of varying irradiance on the *I–V* characteristic, together with the locus of the corresponding maximum power points (indicated

by the dotted line). The most apparent effect of variable irradiance is the significant change in V_{oc}. In contrast, the variation of V_{oc} remains relatively small over a broad range of irradiance levels and becomes appreciable only under low-irradiance conditions ($G \ll 200\ \mathrm{W/m^2}$). In c-Si cells, the dynamic response of the *I–V* curve to irradiance variations typically occurs within a time constant between 10 and 20 μs.

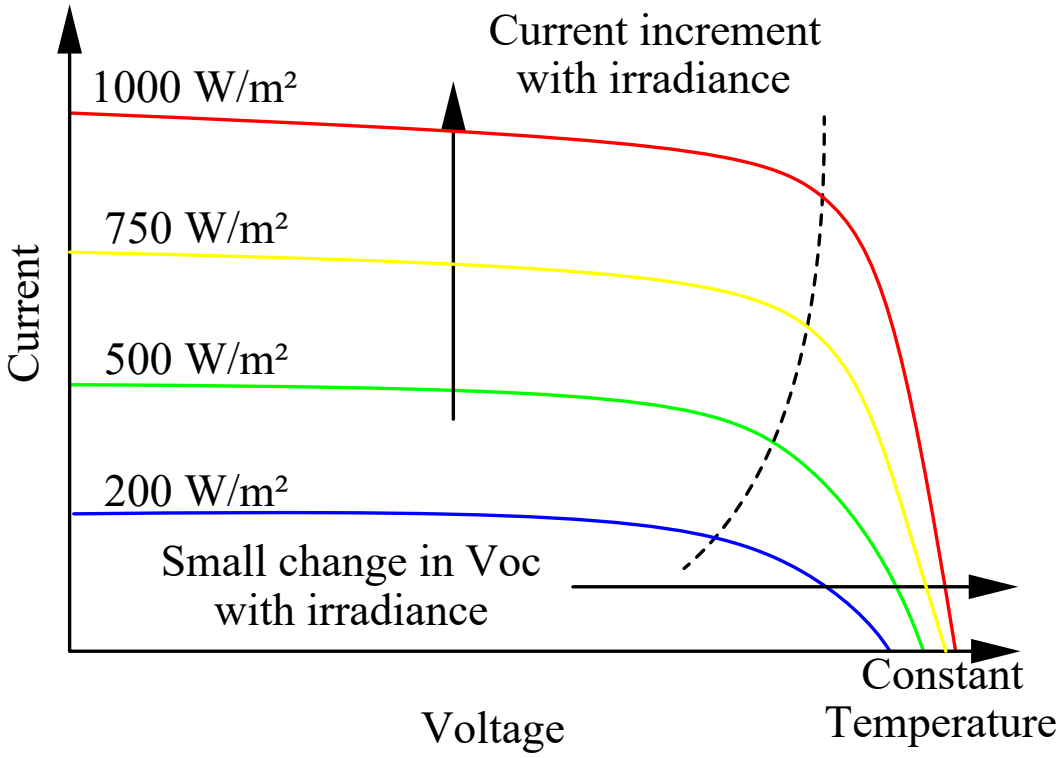

Fig. 2.11 *I–V* characteristic curve variation as a function of irradiance

Conversely, for a fixed irradiance, variations in the *I–V* curve with increasing cell temperature are characterised by two predominant phenomena. Firstly, the photo-generated current (I_{ph}), and consequently the short-circuit current (I_{sc}), slightly increase owing to the reduction in the semiconductor bandgap. For c-Si, the typical temperature coefficient is $\mathrm{d}J_{sc}/\mathrm{d}T_c \approx 0.01\ \mathrm{mA\ cm^{-2}\ ^\circ C^{-1}}$ [34], whereas amorphous silicon (a-Si) materials exhibit a higher sensitivity. Secondly, the diode (or junction) current (I_j) increases with temperature, resulting in a reduction of the open-circuit voltage. A typical temperature coefficient for c-Si is $\mathrm{d}V_{oc}/\mathrm{d}T_c \approx -2.2\ \mathrm{mV/^\circ C}$ [34].

Figure 2.11 presents the *I–V* characteristics of a PV generator under different irradiance levels. As a result of the combined effects of irradiance and temperature,

the thermal coefficient of the maximum power relative to the rated power under standard test conditions (P_{STC}) can be considered approximately constant. For c-Si, typical values of $\frac{1}{P_{\mathrm{STC}}}\frac{\mathrm{d}P_M}{\mathrm{d}T_c}$ lie between -0.38 and -0.35 $\%/^{\circ}\mathrm{C}$ [35], whereas amorphous silicon cells generally exhibit lower absolute values of this coefficient. In practical modelling approaches, it is commonly assumed that the short-circuit current V_{oc} is affected solely by irradiance, while the open-circuit voltage I_{sc} is primarily influenced by temperature.

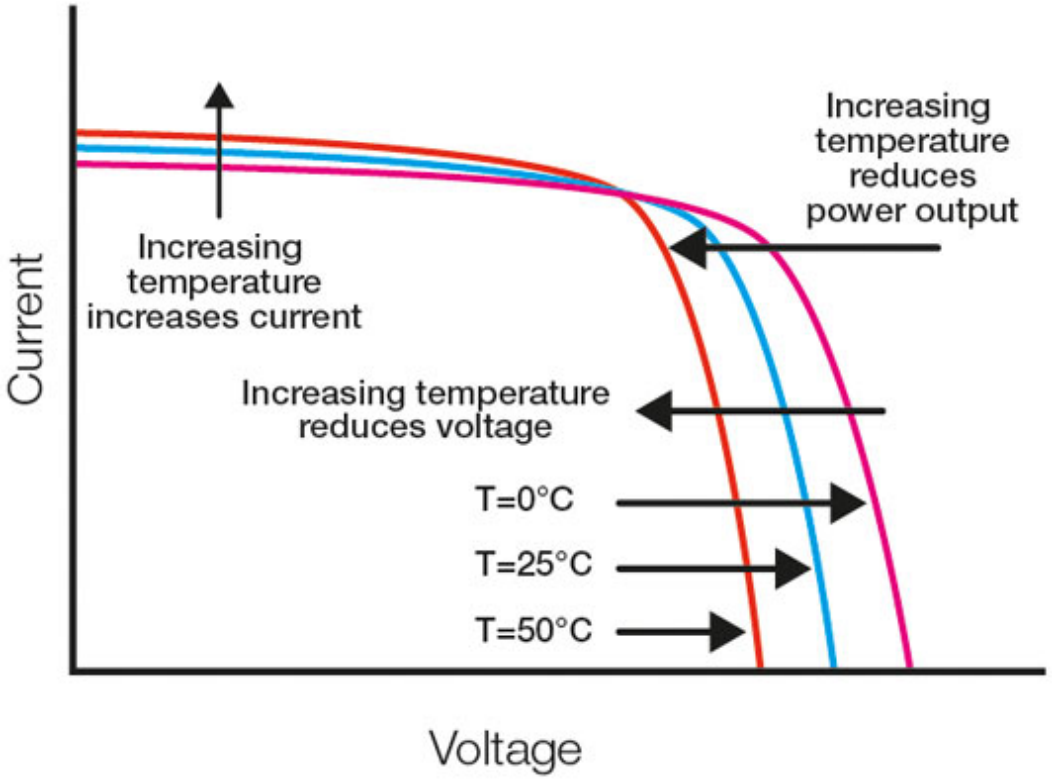

Fig. 2.12 *I–V* characteristic curve variation as a function of temperature

2.2.3 Sources of losses in a photovoltaic cell

The conversion of incident solar irradiance into electrical power within a photovoltaic (PV) cell is inevitably subject to several loss mechanisms that cannot be entirely eliminated. The principal sources of such losses are summarised as follows.

- **Reflection and surface coverage losses (up to $\approx 10\%$).** A small portion of the incoming radiation striking the front surface of the cell is reflected,

particularly by the metallic grid lines of the front contact. To mitigate this effect, anti-reflective coatings are commonly applied to the cell surface. More recently, technological advances have enabled the fabrication of PV cells with rear-contact architectures, in which the electrical contacts are located entirely on the back surface. This configuration reduces the area occupied by the front grid, thereby minimising reflection losses.

- **Excess photon energy losses (up to $\approx 25\%$).** Only a fraction of the absorbed radiant energy is converted into electrical energy. When the photon energy exceeds the energy threshold required to generate electron–hole pairs, the surplus energy is not utilised for charge carrier generation but is instead dissipated as heat.

- **Insufficient photon energy losses (up to $\approx 20\%$).** Photons whose energy is below the semiconductor bandgap energy cannot induce the generation of electron–hole pairs. Consequently, this portion of the incident energy is absorbed as thermal energy, contributing to the overall heating of the cell without producing electrical output.

- **Recombination losses (up to $\approx 2\%$).** Although the electric field within the p–n junction acts to separate electron–hole pairs, a fraction of these carriers recombines before contributing to the electrical current. The associated energy is released as heat. This type of loss is influenced by material defects, impurities, and imperfections within the semiconductor structure.

- **Fill factor and resistive losses (up to $\approx 20\%$).** The combined effects of the diode behaviour and the resistive components (R_s and R_sh) distort the I–V characteristic curve of the PV cell. As a result, the real curve deviates from the ideal rectangular shape, thereby reducing the maximum extractable electrical power.

The input power available to a PV generator, determined by the solar irradiance incident on its surface, remains independent of the electrical power delivered to or absorbed by the external load. For a specific installation site and under defined environmental conditions, this incident power is considered constant. The conversion efficiency of a PV cell, defined as the ratio between the maximum output power (P_M) and the irradiance incident on the cell surface under Standard Test Conditions (STC),

has improved substantially over the past decade. State-of-the-art commercial PV modules can now achieve electrical efficiencies of up to approximately 23% [11, 36]. As the electrical load increases, the operating temperature of the PV cell tends to decrease; however, this effect is generally negligible for devices with relatively low conversion efficiency. The maximum cell temperature typically occurs under open-circuit conditions, when electrical power extraction is absent.

2.3 Connection of photovoltaic cells

2.3.1 Series connection of photovoltaic cells

In order to supply conventional electrical loads, the voltage and current produced by a single photovoltaic (PV) cell are insufficient. Consequently, multiple PV cells must be interconnected in series or in parallel to achieve the desired electrical output. However, in PV generators comprising several interconnected cells, one of the main sources of performance degradation is the phenomenon known as mismatch (or mismatching). This term refers to the deviation among the *I*–*V* characteristics of individual cells within the same array, which may arise from manufacturing tolerances, material defects, or non-uniform shading conditions.

Figure 2.13 illustrates a typical case of mismatch affecting N_s PV cells connected in series, forming a single string, in which the characteristic curve of one cell differs from that of the others. This deviation may be caused either by a manufacturing defect (curve a in Figure 2.13) or by partial shading (curve a'). As a result, the equivalent *I*–*V* characteristic of the string (curve c or curve c', respectively) is obtained by summing, for a given current, the voltage of the $(N_s - 1)$ identical cells and that of the defective or shaded cell. The dashed curve b in Figure 2.13 represents the *I*–*V* characteristic of the identical cells, while point P denotes their maximum power point.

In both cases, whether caused by a manufacturing defect or by shading, the total power output of the string is lower than the sum of the maximum powers of the individual identical cells. In situations of severe shading (curve c'), this reduction becomes particularly significant, resulting in a drastic decrease in the string's output power.

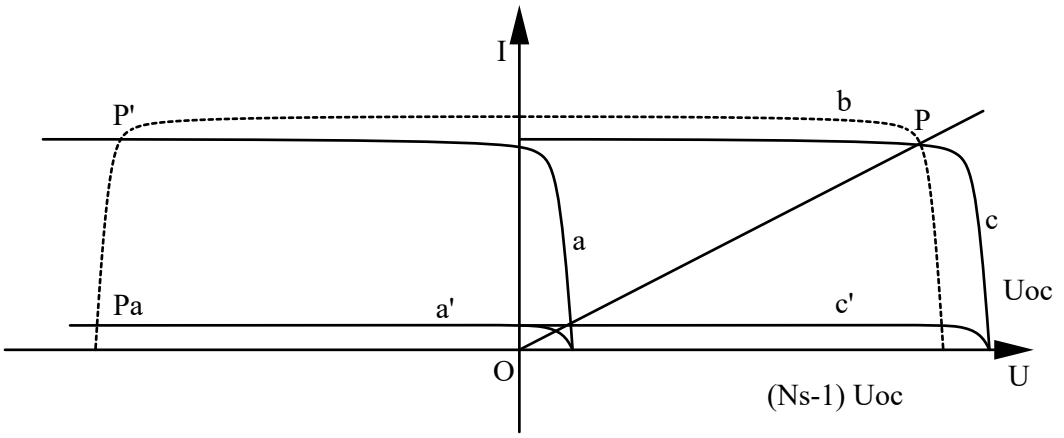

Fig. 2.13 *I–V* characteristic of series-connected cells in case of mismatch.

For a series-connected configuration, the open-circuit voltage V_{oc} of the equivalent string is equal to the sum of the open-circuit voltages of the individual cells:

$$V_{oc} = \sum_{i=1}^{N_s} V_{oc,i} \tag{2.12}$$

Conversely, the equivalent short-circuit current I_{sc} of the string is approximately equal to that of the cell delivering the lowest current:

$$I_{sc} \approx \min(I_{sc,i}) \tag{2.13}$$

In the case of a completely shaded cell (where $I_{sc} \approx 0$), the element ideally behaves as an open circuit. In practice, however, a PV cell under such conditions behaves as a resistive element with a high equivalent resistance, typically ranging from tens to hundreds of ohms. Under these circumstances, the cell dissipates thermal power, which depends on the reverse voltage and, consequently, on the

operating point imposed on the string.[1] The higher the reverse voltage imposed on the shaded cell, the greater the corresponding power dissipation.

The most critical situation occurs when one cell in the string is shaded while the remaining $(N_s - 1)$ cells are fully illuminated and the string operates under short-circuit conditions. In this case, the voltage generated by the illuminated cells is entirely applied across the shaded cell. This scenario can be represented in Figure 2.13 by mirroring curve b with respect to the current axis (vertical axis). The intersections of this mirrored curve with curves a and a' in the second quadrant identify the operating points of the string. If the shaded cell is required to dissipate excessive thermal power, localised overheating, known as hot-spot formation, may occur. After a certain exposure time, which depends on both the duration of the overload and the thermal dissipation conditions, the cell may suffer irreversible damage. Specifically, if the reverse voltage generated by the $(N_s - 1)$ irradiated cells exceeds the breakdown voltage, the shaded cell fails permanently. The breakdown voltage V_b typically ranges from 25 to 50 V for c-Si cells [37, 38]. Considering that each c-Si cell generates a voltage of approximately 0.5–0.6 V, a series string comprising 50–100 cells may cause cell failure when a single element becomes shaded.

To mitigate this issue, a protection diode can be connected in anti-parallel with each cell. In this configuration, the shaded cell no longer behaves as a load under reverse bias, and the string's short-circuit current is not limited to the lowest current value but remains determined by the illuminated cells. Consequently, only the shaded cell ceases to contribute to power generation, while the remaining cells continue operating close to their maximum power point. Although an anti-parallel diode can be connected to every cell, this approach is implemented only in high-cost applications, such as satellite systems, because of its high expense. In terrestrial installations, a single diode is typically connected in anti-parallel to each group or sub-string of cells connected in series, usually composed of 18, 24, or 36 elements.

[1] In grid-connected photovoltaic systems, the operating point of the string is typically controlled by a power electronics interface, most commonly a DC/DC converter or an inverter, which decouples the PV generator from the external load and imposes the string voltage independently of the load impedance. Consequently, the thermal power dissipated by the shaded cell is determined by the voltage set by the power electronics module rather than by the external load directly. The worst-case dissipation scenario described in this section therefore corresponds to a string operated near short-circuit conditions by the converter, for instance during fault detection or maximum power point tracking transients.

If a cell becomes electrically open within a string, the entire string ceases to deliver current and, therefore, power. Similarly, if a short-circuit occurs in one of the cells, the string output is reduced by the contribution of that specific element, though current may still flow through the remaining cells.

2.3.2 Parallel connection of photovoltaic cells

When photovoltaic (PV) cells are connected in parallel, the overall I–V characteristic of the system depends on the behaviour of each individual cell. If one of the N_P cells exhibits an I–V curve different from the others, for instance due to partial shading, the equivalent characteristic is obtained by summing, for a given voltage, the current of the shaded cell and the currents of the remaining $(N_\mathrm{P}-1)$ irradiated cells. In particular, the equivalent short-circuit current is given by the sum of the short-circuit currents of all the N_P cells, while the equivalent open-circuit voltage corresponds to the lowest open-circuit voltage among the connected cells:

$$I_{\mathrm{sc,eq}} = \sum_{i=1}^{N_\mathrm{P}} I_{\mathrm{sc},i} \tag{2.14}$$

$$V_{\mathrm{oc,eq}} = \min(V_{\mathrm{oc},i}) \tag{2.15}$$

If one of the cells is shaded, the behaviour of the system resembles that of a parallel connection composed of $(N_\mathrm{P}-1)$ active cells. The most critical operating condition occurs under open-circuit conditions, when the shaded cell is forced to absorb current from the irradiated ones. This process causes significant power dissipation in the shaded cell, which results in local heating and can eventually lead to thermal degradation or permanent damage.

The electrical behaviour of the irradiated cells depends on the characteristics of the shaded cell. If the shaded cell acts as an open circuit, the remaining cells continue to operate in parallel without substantial disturbance. Conversely, if the shaded cell conducts current, the operating points of the other cells may shift toward the short-circuit condition. Nevertheless, this configuration is uncommon because PV systems are generally not composed of individual cells connected directly in parallel.

From the standpoint of the external load, the shading of a single cell in a parallel arrangement is less critical than in the series configuration. To prevent a shaded cell from behaving as a load and absorbing current from the others, a protection diode can be connected in series with each cell. However, the voltage drop across the terminals of each diode is approximately equal to the voltage produced by one PV cell, making this solution impractical for individual cells in terrestrial systems. Therefore, in common practice, such protective diodes are connected in series with entire strings consisting of several tens of series-connected cells.

In conclusion, whether PV cells are connected in series or in parallel, it is highly desirable to ensure that all elements exhibit *I*–*V* characteristics as similar as possible to minimise mismatch effects. To achieve this objective, PV cells undergo a rigorous selection process, known as sorting, during module fabrication. This procedure aims to group cells with nearly identical electrical characteristics, particularly regarding short-circuit current (I_{sc}), open-circuit voltage (V_{oc}), and maximum power (P_M). Despite this selection, unavoidable power losses still occur due to interconnection effects within the module. Indeed, the maximum power of a complete PV module is typically 2–3% lower than the sum of the maximum powers of its individual cells, and this reduction cannot be fully eliminated. Furthermore, sorting cannot prevent mismatch phenomena originating from external causes, such as partial shading of one or more cells within the module.

2.3.3 Photovoltaic module

A photovoltaic (PV) module is an environmentally protected assembly of PV cells designed to generate electrical energy when exposed to solar irradiance. It can comprise a variable number of cells, typically ranging from 36 to 96. Different manufacturing techniques enable the assembly of the module in a manner that ensures protection from environmental agents such as humidity, hail, wind, and dust, while maintaining its temperature within a safe range, generally between 45 and 75 °C.

Concerning c-Si technology, monocrystalline cells are produced through the crystal growth process and exhibit a round geometry. However, the efficiency of PV modules employing round-shaped cells is limited due to inefficient use of the available surface area. Monocrystalline cells may undergo additional processing to

obtain a square shape by trimming their borders; in this case, part of the material is wasted but later recovered and recycled in a subsequent stage. Conversely, polycrystalline cells possess an inherently square geometry, which allows for a more efficient utilisation of the module surface.

The PV cells are electrically interconnected through welding and subsequently encapsulated between two flat layers. The front layer is composed of a high-transmittance glass, which must be transparent to incoming light. The rear cover may consist either of another glass sheet or of a thin polymeric film made of Mylar, Tedlar, or PET. A thermoplastic polymer encapsulant surrounds the cells, bonding the two layers together and rendering the overall structure compact and resistant to weathering.

This encapsulant, Ethylene Vinyl Acetate (EVA), is transparent to light and exhibits long-term durability. Furthermore, EVA provides electrical insulation between the cells, preventing the ingress of moisture and, consequently, corrosion. Nevertheless, this polymer shows limited resistance to elevated temperatures, specifically above 85 °C.

2.3.4 Main parameters of a photovoltaic module

The most significant parameter of a photovoltaic (PV) module is its global conversion efficiency. This parameter is evaluated under Standard Test Conditions (STC), which correspond to an irradiance of $G = 1000\ \mathrm{W/m^2}$, an air mass of $AM = 1.5$, and a module temperature of $T_{c,\mathrm{STC}} = 25\ ^\circ\mathrm{C}$. These conditions are representative of typical sunny days in spring or autumn.

The efficiency of a PV module is influenced by the specific photovoltaic technology employed and generally ranges between 7% and 24%. Environmental conditions during summer or winter are less favourable for solar energy conversion, leading to efficiency reductions of up to approximately 2% due to lower current density.

Another fundamental characteristic of PV modules is their peak power, expressed in Watt, which represents the maximum output power under STC. Typical values for commercial PV modules can reach up to approximately 400 W, depending on the cell technology. To obtain higher output powers, multiple modules can be interconnected, forming more complex configurations. The following terminology is commonly adopted to describe these configurations:

- **PV string.** A group of modules, or cells, that are mechanically pre-assembled and electrically connected in series.
- **PV array.** An assembly of PV modules mounted on a supporting structure.
- **PV field or PV system.** The overall group of PV arrays constituting the entire installation. Most PV systems are composed of PV strings connected in parallel, each string being formed by modules connected in series.

Furthermore, the following electrical quantities are specified under STC: the short-circuit current I_{sc}, the open-circuit voltage V_{oc}, and the current and voltage at the maximum power point, denoted as I_{mpp} and V_{mpp}, respectively. These test conditions are reproduced in specialised laboratories, and an additional parameter is defined to better characterise the performance of PV modules: the Nominal Operating Cell Temperature (NOCT).

The NOCT represents the temperature of the module operating under open-circuit conditions and in thermal equilibrium with the following environmental conditions: $G = 800\ W/m^2$, ambient temperature $T_a = 20\ °C$, and wind speed of $1\ m/s$. Typically, the NOCT ranges between 42 and 50 °C, and its value allows the estimation of the module temperature under various weather conditions. Indeed, the temperature difference between the module temperature T_c and the ambient temperature T_a can be assumed to depend linearly on the irradiance G. Under this assumption, the PV module temperature can be calculated using the following expression:

$$T_c = T_a + \frac{\mathrm{NOCT} - 20°C}{800\frac{W}{m^2}} \cdot G \tag{2.16}$$

The shape of the *I–V* curve of a PV module is analogous to that of an individual cell, although the voltage scale differs. Connecting multiple PV cells in series increases the generated voltage, whereas connecting several strings of PV modules in parallel enhances the total output current. In stand-alone applications, the number of series-connected cells within a PV module typically ranges between 34 and 40. In such configurations, PV modules are usually coupled with batteries, and therefore the PV voltage must be sufficient to allow battery charging (typically 12 V), even under elevated temperature conditions, up to approximately 60 °C.

2.3.5 Protection of photovoltaic systems

Similarly to individual photovoltaic (PV) cells, electrical mismatches among the I–V characteristics of different PV modules can result in power losses and other operational issues within the system. Therefore, appropriate protection devices are necessary to minimise power reduction caused by electrical mismatches.

In particular, when one or more modules are partially shaded, localised temperature peaks may occur, potentially leading to module failure. To mitigate this risk, a bypass diode (D_p) can be employed to protect the module against reverse voltage conditions induced by shading. With the inclusion of a bypass diode, the power output of the string is limited to the contribution of the illuminated modules, thereby excluding only the shaded module from power generation. In a PV string composed of series-connected modules, each module (or, in some cases, each group of cells—typically 18 or 24) is equipped with an individual bypass diode connected in parallel.

Additionally, another diode, referred to as the series diode (D_s), can be used in the parallel interconnection of PV strings to prevent voltage asymmetries. This diode is connected in series with each string, allowing the current to flow in the desired direction. However, the presence of this diode introduces a voltage drop, typically within the range of 0.6–0.8 V, resulting in a corresponding power loss. To minimise this loss, the voltage drop across the diode must remain negligible compared with the overall string voltage.

If certain cells within a PV string are defective, their open-circuit voltages may differ from those of the healthy strings connected in parallel, leading to electrical asymmetry. In such a situation, the series diode D_s isolates the defective string, preventing it from influencing the rest of the system and rendering it inactive in terms of power generation. Under normal operating conditions, however, the voltage at the working point of the PV system is substantially lower than the open-circuit voltage, thereby reducing the likelihood of this event. Indeed, in PV systems equipped with maximum power point tracking (MPPT) devices, the working point voltage typically corresponds to approximately 80% of the open-circuit voltage.

Furthermore, the series diode D_s provides protection against reverse current flow in the event of shading or other external influences. Such reverse currents may arise due to the electromotive forces generated by external sources, such as storage

systems or engines, and could otherwise damage the PV modules or strings if not properly mitigated.

2.3.6 Configurations of photovoltaic systems

The selection of an appropriate array configuration represents a fundamental step in the design of a photovoltaic (PV) system. Indeed, both the performance and the reliability of PV generators are strongly influenced by the type of electrical interconnection adopted among the PV modules in the installation. This aspect becomes particularly critical when the operating conditions deviate from the ideal case, as in the presence of non-uniformities in cell parameters, partial shading, material degradation, electrical breakdowns, or transient events such as lightning strikes.

In this framework, several PV array configurations can be implemented, and the optimal configuration is determined by a set of design constraints, such as the need to maintain a constant voltage at the load terminals or to minimise power losses. One of the most widespread configurations is the parallel of series arrangement (configuration b in Figure 2.14).

In this configuration, each PV string consists of modules connected in series, while multiple strings are connected in parallel. A shaded cell within a module produces only a minor reduction in the total voltage generated by the string; however, the power contribution of the affected string is effectively lost.

Another common configuration is the series of parallel connection (Figure 2.15). In this case, the number of bypass diodes D_p required is lower compared with the parallel of series configuration.

Specifically, one diode is connected in parallel to each string rather than to each individual module (or to groups of modules), although such diodes must be capable of handling a higher current. Nevertheless, in this configuration, no protection diodes are connected in series with the modules themselves, and consequently, shaded cells can endanger the corresponding module, particularly under open-circuit conditions.

When a PV generator supplies a load, its operating point is determined by the intersection between the I–V characteristic of the generator and that of the load. This operating point can lie anywhere along the PV I–V curve, between the short-

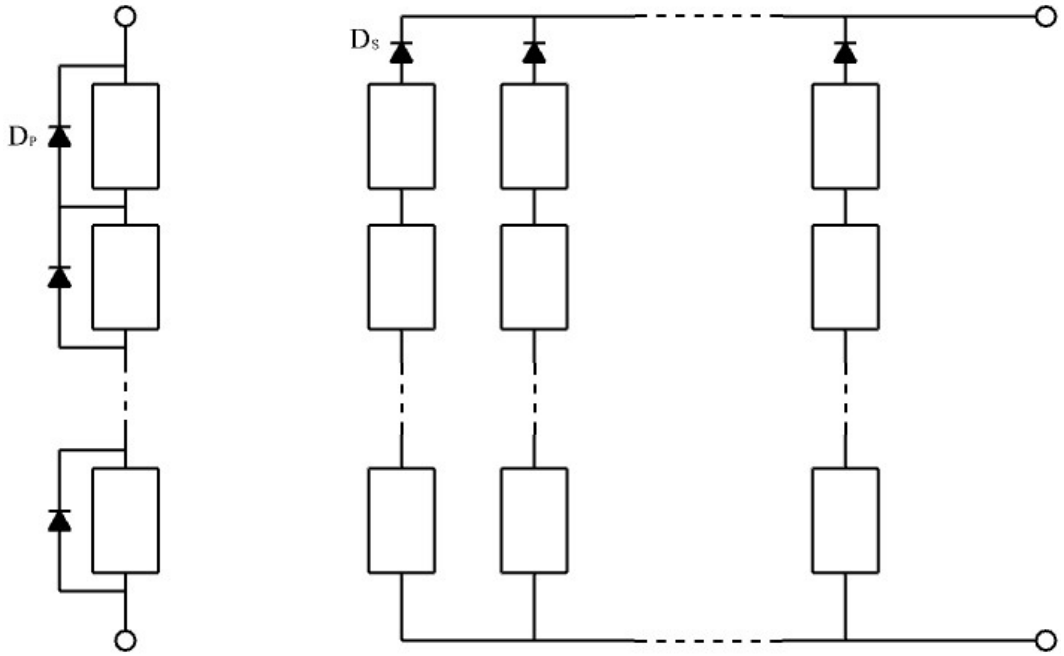

Fig. 2.14 Diodes in PV generators: single-string (a) parallel-series (b)

circuit and open-circuit conditions. The I–V characteristic of PV generators can be conceptually divided into two distinct regions. The first region extends from the short-circuit condition ($V = 0$ V, $I = \mathrm{I_{sc}}$) to the maximum power point (MPP) defined by coordinates (V_M, I_M), while the second region extends from the MPP to the open-circuit condition ($V = \mathrm{V_{oc}}$, $I = 0$ A).

These two portions of the I–V curve can be approximately modelled using linear segments with distinct angular coefficients. In particular, the first region—between the short-circuit point and the MPP—can be effectively represented by a Norton equivalent circuit, whereas the second region—between the MPP and the open-circuit point—can be represented by a Thévenin equivalent circuit. Such equivalent models are particularly useful for simplifying the analysis of PV systems under various load and environmental conditions.

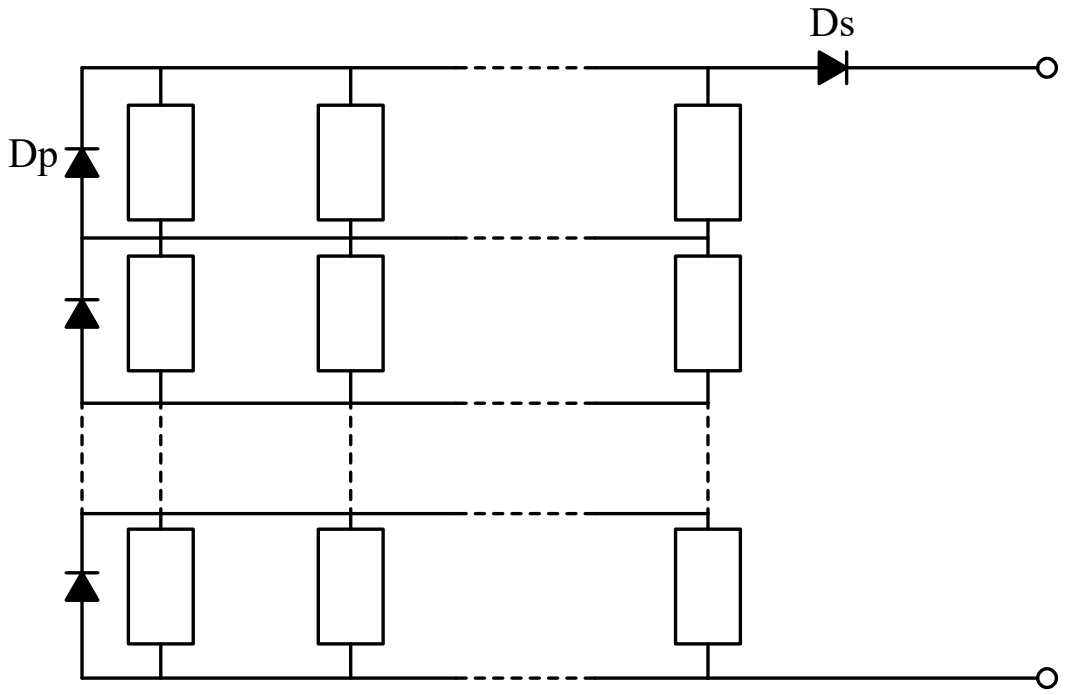

Fig. 2.15 Series of parallel configuration.

2.3.7 Connection of photovoltaic generators to loads

For each environmental condition defined by irradiance and ambient temperature, photovoltaic (PV) generators should operate in the vicinity of their maximum power point (MPP). When a PV system is connected to a purely resistive load, the identification of the MPP under specific weather conditions allows for the determination of an optimal load resistance, denoted as R_o. A straight line can be drawn on the I–V characteristic by connecting the origin of the graph to the MPP; the slope of this line, equal to $1/R_o$, provides the value of the optimal resistance.

In order to exploit the maximum available power from the PV generator, the slope of the generator's I–V curve must be known. To ensure maximum power transfer between the generator and an external load, the slope of the generator I–V characteristic must equal the slope of the resistive load characteristic, such that $|dI/dV| = 1/R_o$. Since the input power of PV generators is determined by the solar irradiance, it cannot be externally controlled or increased. Therefore, adapting the

load to the generator is essential to extract the maximum power from the PV system. This condition differs from that of conventional electrical generators, for which the input power can be adjusted upon demand.

As discussed previously, at constant temperature, an increase in irradiance results in a proportional increase in the short-circuit current I_{sc} of the PV generator, while the open-circuit voltage V_{oc} remains approximately unaffected by irradiance variations. Consequently, the locus of the MPPs, corresponding to different irradiance levels but constant temperature, can be approximated by a vertical line on the I–V plane. The coupling between a PV generator and its load is considered optimal when the load characteristic curve coincides with the locus of the generator's MPPs.

For these reasons, the direct connection of PV generators to purely resistive loads is generally not recommended. Nevertheless, such a condition may naturally occur in systems including electrochemical batteries, direct-current (DC) motors, or electrolytic devices (for instance, fuel cells performing water electrolysis for hydrogen production), where the presence of an internal or induced electromotive force enables partial self-adjustment of the operating point.

In the case of small-scale PV installations, with rated power up to a few kilowatts, PV generators can be directly connected to DC motors employed in applications such as water pumping, drying, or ventilation systems. This configuration is relatively simple and enhances the reliability of the overall PV system by eliminating the need for complex power conditioning electronics.

2.3.8 Components of photovoltaic systems

Photovoltaic (PV) systems comprise multiple components, in addition to PV modules, in order to effectively convert, control, and utilise the electrical energy produced. The principal elements of a PV system are summarised below:

- **Maximum Power Point Tracker (MPPT).** The input energy of PV generators originates from solar irradiance, which varies according to atmospheric and solar conditions. To ensure that the PV generator operates close to its Maximum Power Point (MPP), DC/DC converters are typically employed. These devices dynamically adjust the operating point of the generator to maximise the extracted power under varying environmental conditions.

- **DC/AC Converters.** PV generators produce electrical energy in the form of direct current (DC), whereas most electrical loads and utility grids operate using alternating current (AC). The conversion from DC to AC is performed by DC/AC converters, commonly referred to as inverters. Modern inverters integrate both hardware and software algorithms to track the maximum power point of PV generators, even in the presence of electrical mismatches among PV modules.

- **PV Connectors.** These components consist of a copper conductor enclosed by a weather-resistant plastic insulation capable of withstanding environmental stressors such as rain, heat, and ultraviolet (UV) radiation. Each PV module is equipped with two connectors, one positive and one negative, that allow safe and reliable interconnection between modules.

- **Fuses.** Fuses serve as overcurrent protection devices. They contain an internal metallic filament that melts when subjected to an excessive current, thereby interrupting the circuit and preventing damage. Typically, each PV string is equipped with two fuses to ensure adequate protection.

- **Blocking Diodes.** Blocking diodes prevent reverse current flow in shaded or underperforming strings. In PV arrays composed of multiple parallel strings, each string is generally equipped with its own blocking diode.

- **DC Breaker.** This circuit breaker provides a means of disconnecting the PV array from the inverter. The number of DC breakers installed depends on the size and configuration of the plant: small systems may use a single breaker for the entire array, whereas large-scale installations often employ one breaker per string for enhanced protection and maintainability.

- **Automatic AC Circuit Breaker.** This device safeguards the AC section of the system by interrupting both conductors of an AC line when necessary. Typically, one or more AC circuit breakers are installed within each plant for effective system protection.

- **Grid Interface.** The grid interface continuously monitors the grid voltage and frequency, ensuring that they remain within acceptable root mean square (RMS) voltage and frequency limits prior to connection.

- **General AC Breaker.** The general AC breaker serves to isolate the entire PV plant from the electrical grid. It is often motorised and coupled with a Residual Current Device (RCD), which is installed upstream of the grid connection to enhance electrical safety.
- **Electrochemical Energy Storage.** Due to the inherent daily and seasonal variability of solar irradiance, the power output of PV systems is intermittent. In stand-alone systems, continuous power supply must be ensured even under unfavourable weather conditions. To achieve this, electrochemical energy storage systems (e.g., batteries) are integrated into the plant. During periods of energy surplus, when the PV generation exceeds the consumption, the excess energy is stored by charging the batteries. The stored energy can then be used during periods of low irradiance or at night, thus enhancing the self-sufficiency and stability of the system.
- **Other Electrical Safety and Monitoring Devices.** These include Surge Protection Devices (SPD) for transient voltage suppression, and energy meters for continuous monitoring and performance evaluation of the system.

PV systems can be broadly classified into two categories: stand-alone systems and grid-connected systems. Stand-alone systems operate autonomously and are not connected to the public electricity grid, whereas grid-connected systems are interfaced with the grid either as centralised or distributed power generation units.

Throughout the operational lifetime of PV systems, most failures are not directly attributable to the PV modules themselves. Instead, the majority of faults arise from the auxiliary components collectively referred to as the Balance of System (BoS). Although the technology of these BoS components is sufficiently mature to ensure reliable operation over thousands of hours, the unconventional electrical characteristics of PV generators may occasionally impose non-standard or stressful operating conditions. Such conditions can degrade the performance of BoS components, potentially leading to higher frequency of malfunctions or failures.

Chapter 3

PV Module Architectures

3.1 Introduction

In PV systems, the interaction between device-level phenomena and system-level layout has a decisive impact on performance, reliability, and energy yield. At the module level, the interconnection of cells into substrings, the placement of bypass diodes, and the choice between full-cell and half-cell layouts shape the response of the generator under mismatch and partial shading.

This chapter provides an overview of this two aspects. It discusses contemporary module architectures, with emphasis on the comparison between full-cell and half-cell technologies and their behaviour under partial shading. The material presented here establishes the modelling framework used throughout the remainder of the thesis for parameter identification, uncertainty analysis, and optimisation of I–V sampling strategies.

3.2 Full-Cell and Half-Cell PV Module Architectures

3.2.1 Electrical Layouts of Full-Cell and Half-Cell Modules

Commercial PV modules commonly adopt either full-cell or half-cell layouts, which differ primarily in the way individual cells are interconnected at substring level.

In conventional full-cell modules, the generator is typically composed of three substrings connected in series. Each substring contains a series chain of full-size PV cells (typically, 20 cells per substring for modules with rated power up to approximately 400 W) and is antiparallel-connected to a bypass diode. A representative interconnection scheme for such a full-cell PV module is shown in Fig. 3.1a.

In half-cell modules, each full-size cell is physically divided into two equal halves. The two half cells are then reconnected so as to form, within each substring, two parallel branches, each branch consisting of a series chain of half cells, as illustrated in Fig. 3.1b. At the module level, the overall structure again consists of three (or more) substrings in series, each protected by its own bypass diode.

Under spatially uniform irradiance, this arrangement effectively halves the current flowing in each half cell relative to the corresponding full-cell design, while the total module voltage remains essentially unchanged. The reduced current in each branch leads to lower resistive losses, which scale with the square of the current ($P_{\text{loss}} \propto I^2R$), and to a more favourable temperature distribution across the module. Moreover, the presence of internal parallel branches within each substring introduces a current-sharing mechanism that becomes relevant under non-uniform operating conditions.

3.2.2 *I–V* Behaviour Under Uniform and Partial Shaded Conditions

Figure 3.2 compares the *I–V* curves of two representative modules—one full-cell and one half-cell—with comparable open-circuit voltage and short-circuit current. For each module, the curves are reported under uniform irradiance (blue trace) and under partial shading with one shaded cell (orange trace). The shading pattern is indicated in Fig. 3.1 for both layouts, highlighting the position of the shaded cell. The global maximum power point (red marker) and additional local maxima (green markers) are also identified.

Under uniform irradiance, both modules behave similarly, exhibiting a single, well-defined maximum power point. When a single cell is shaded, the overall performance of the two technologies remains broadly comparable, and the *I–V* curves display the characteristic stepped shape associated with the turn-on of bypass

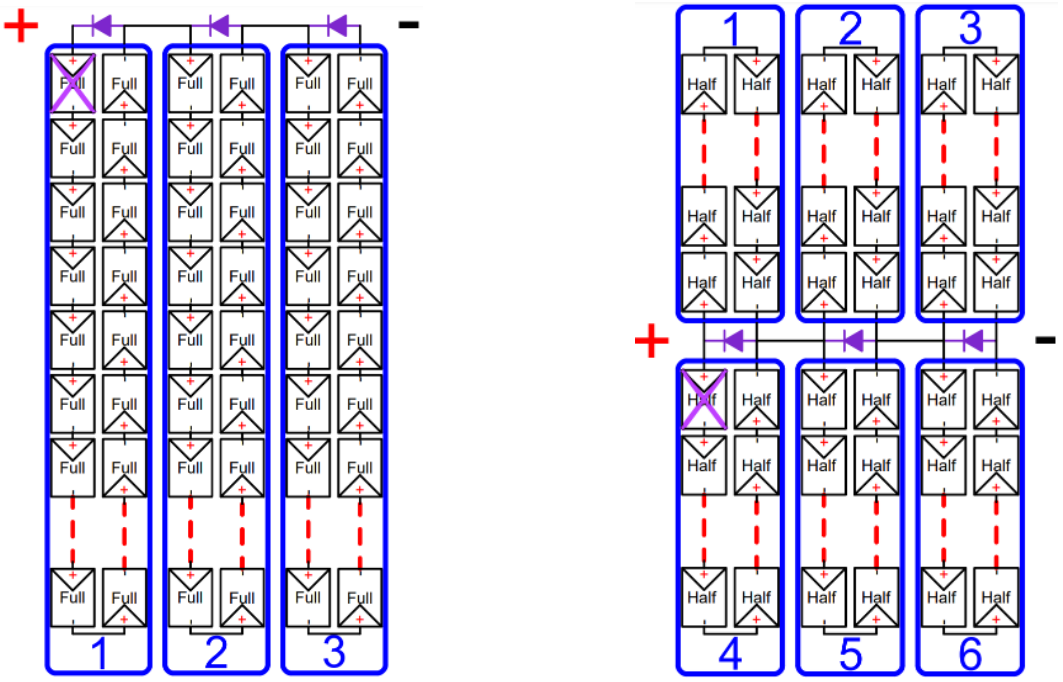

(a) (b)

Fig. 3.1 Electrical connection of PV modules with full cells (a) half cells (b)

diodes: the module voltage drops abruptly when the bypass diode of the affected substring starts conducting.

More pronounced differences arise when two or more cells belonging to different substrings are shaded or when the shaded regions are spatially distributed. In such scenarios, the internal parallelisation of half-cell modules allows currents to be redistributed between parallel branches within each substring. This capability can limit the effective impact of the shaded areas and leads, in many practical situations, to a higher energy yield compared with full-cell modules, in which each substring provides a single series path without internal current sharing.

3.2.3 Representative Topologies and Experimental Shading Patterns

A more detailed view of the half-cell architecture, together with its I–V response under non-uniform irradiance, is provided in Fig. 3.3. The module is composed of three series-connected strings, each associated with a dedicated bypass diode. Within

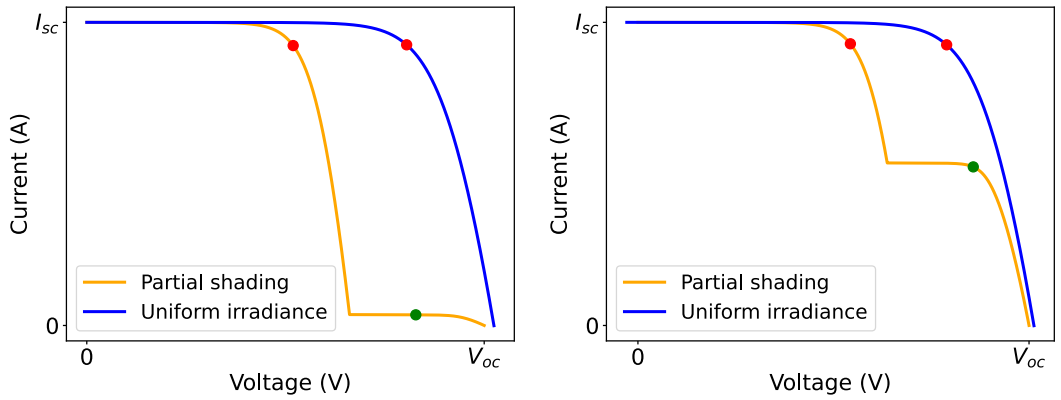

Fig. 3.2 I–V curves of full-cell (a) and half-cell (b) modules under uniform and shaded conditions.

each string, two series chains of half cells are connected in parallel, a configuration widely adopted in high-efficiency modules to limit internal ohmic losses.

The two I–V curves in Fig. 3.3 illustrate the effect of partial shading on the half-cell module. The orange trace corresponds to uniform irradiance, for which all strings are fully illuminated and none of the bypass diodes conducts. The blue trace, by contrast, exhibits a multi-step profile arising from the sequential turn-on of the bypass diodes as the operating current is increased under partial shading.

In the specific partial-shading case depicted (blue curve), all strings are uniformly illuminated except two regions: region `2A`, receiving about 50% of nominal irradiance, and region `0A`, fully shaded. The associated bypass diodes conduct, thereby limiting the contribution of the affected strings while preserving the overall module current. This gives rise to the three-step voltage evolution visible in the blue I–V trace.

Figure 3.4 shows the practical implementation of this shading pattern on a commercial half-cell module using physical masks. Partial coverage is applied to the area corresponding to region `2A`, whereas region `0A` is fully covered, as indicated by the “COVER” labels. The use of such controlled patterns enables reproducible experiments for the validation of shade-aware modelling approaches.

For completeness, Fig. 3.5 reports the topology and I–V response of a full-cell module with three substrings in series under an analogous non-uniform irradiance scenario. Substrings 0, 1, and 2 are connected in series and each is protected by a

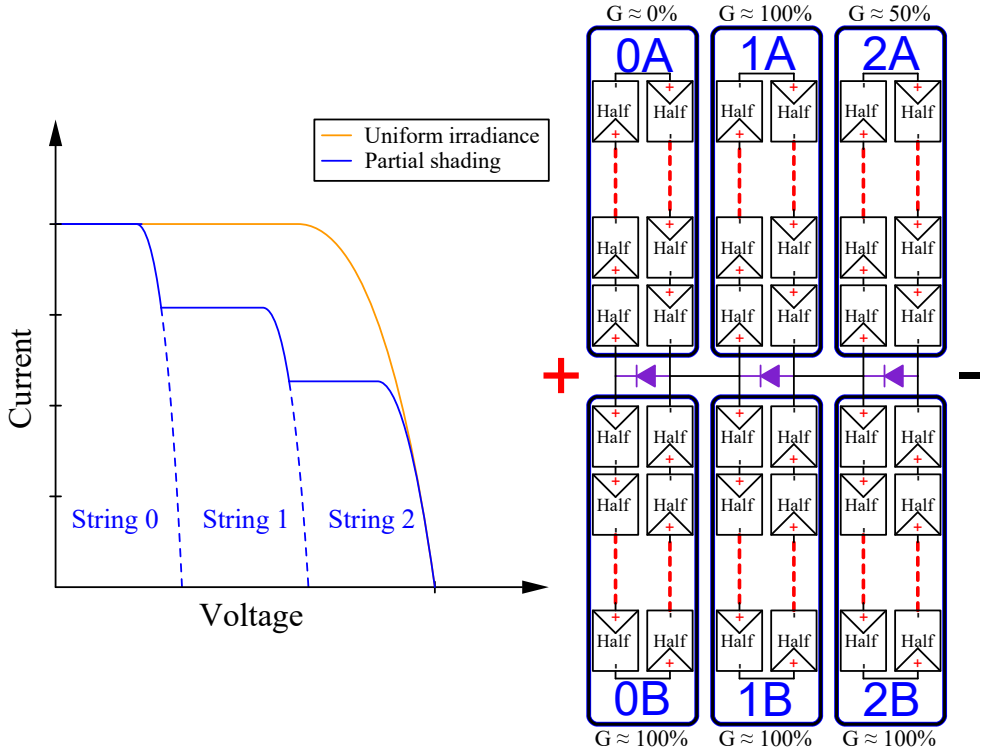

Fig. 3.3 Half-cell PV topology and *I*–*V* curves under uniform and shaded conditions

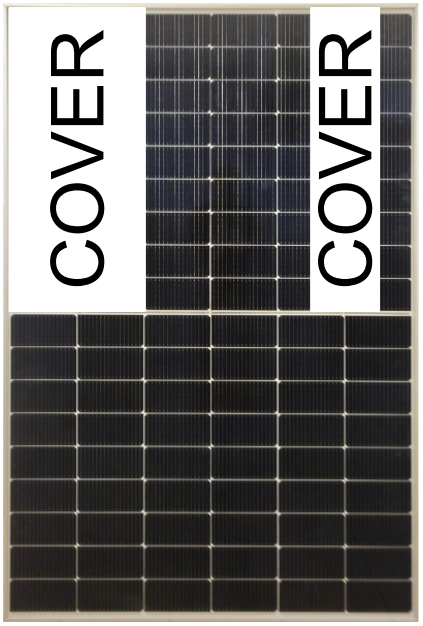

Fig. 3.4 Example of a partial-shading mask applied to the half cells of a PV module.

bypass diode. In the operating condition illustrated, substring 0 is fully illuminated ($G \approx 100\%$), substring 1 is partially shaded ($G \approx 50\%$), and substring 2 is almost completely shaded ($G \approx 0\%$), with a small current contribution due to diffuse light.

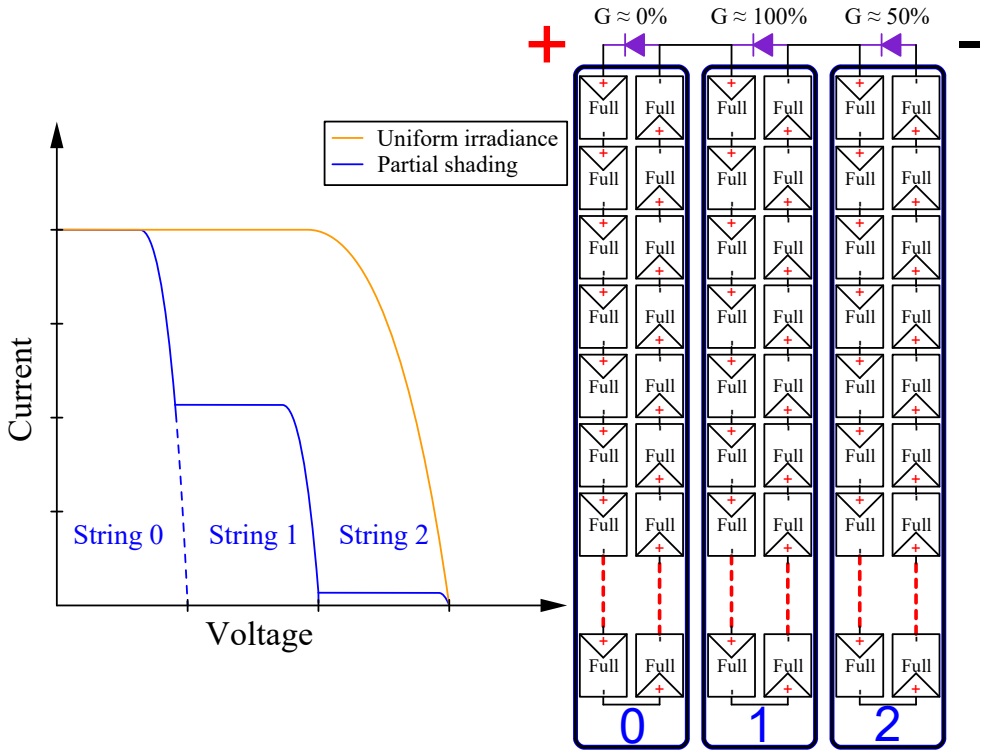

Fig. 3.5 Electrical configuration and I–V response of a full-cell PV module with three substrings under partial shading.

The resulting I–V curve again shows a stepped behaviour due to the turn-on of the bypass diodes, qualitatively similar to the half-cell case. However, the absence of internal parallel branches within the substrings leads to quantitative differences in the detailed shape of the curve and in the location and height of local maxima, because the current cannot be redistributed between parallel paths inside each substring.

3.2.4 Implications for I–V Curve Sampling

For modules comprising series-connected substrings with internal parallel branches, as in half-cell architectures, an I–V characterisation strategy particularly well suited to the internal layout consists of imposing the current and measuring the resulting voltage. This approach is consistent with the internal structure, where each substring

contains parallel branches formed by series chains of cells, and it captures accurately the progressive activation of bypass diodes as the test current is varied.

For conventional full-cell modules, which lack internal parallelisation within substrings but still feature bypass diodes across each substring, current-programmed sampling is also advantageous. By controlling the imposed module current, one can directly observe the turn-on of individual bypass diodes and separately analyse each substring's contribution to the overall response. These considerations are particularly relevant for the I–V sampling optimisation and parameter-estimation methods developed in later chapters, where the interplay between module architecture and measurement strategy plays a crucial role.

Chapter 4

Experimental Characterization of a First-Order RC Filtering Stage

4.1 Introduction and experimental motivation

Equivalent circuit modelling constitutes a central methodological tool in the analysis and parameter identification of photovoltaic devices [9]. In the present thesis, the theoretical foundations and the range of equivalent circuit representations adopted for PV cells are discussed in detail in Chapter 3. The present chapter introduces a preliminary experimental exercise that was conceived to consolidate the end-to-end workflow that is subsequently applied to the estimation of PV cell parameters under both illuminated and dark conditions, as reported in Chapter 6.

The activity described here consists of the design, fabrication, and characterisation of a simple first-order RC filtering stage comprising a low-pass and a high-pass circuit. Although the circuit is intentionally elementary, it provides a controlled environment in which each step of the experimental method can be executed, verified, and quantitatively assessed. Specifically, the exercise was structured to mirror the workflow adopted later for PV device identification. First, an analytical model is selected and used to define design targets and component values. Second, the circuit is physically realised on a printed circuit board, thereby introducing realistic aspects such as component tolerances, parasitic effects, and instrument loading. Third, the implemented device is experimentally characterised in the time and frequency domains, and the measured responses are compared against the model predictions.

Finally, the discrepancy between nominal design values and identified parameters is analysed and interpreted in terms of the combined influence of non-ideal components and measurement-chain interactions.

This preparatory project played a practical role in developing a robust understanding of experimental parameter estimation procedures. In particular, it enabled the validation of measurement techniques and curve-fitting algorithms that are later employed to identify resistive and reactive parameters in photovoltaic equivalent circuit models. The emphasis on closing the loop between modelling, implementation, and quantitative identification is integral to the subsequent experimental work on PV cells, where the same methodological steps are followed under more complex operating conditions and with additional sources of uncertainty.

Beyond its research-oriented function, the filtering-stage device was also employed in didactic laboratories as a demonstrator [39]. In that context, it served as an example of first-order dynamics, Bode analysis, and parameter estimation, thereby reinforcing fundamental concepts that underpin the more advanced modelling and identification tasks developed later in this thesis.

4.2 Filter design and circuit implementation

The starting point of the design is the standard expression for the cut-off frequency of a first-order RC filter [40],

$$f_c = \frac{1}{2\pi RC}. \tag{4.1}$$

The filters were deliberately designed such that their cut-off frequencies lie slightly above and slightly below the mains frequency of 50 Hz, respectively.

A nominal resistance value of 1 kΩ was selected for both filters. This choice represents a compromise between reducing the influence of the function generator output impedance (50 Ω), limiting current consumption, and avoiding excessive sensitivity to parasitic capacitances. Once the resistance value was fixed, the capacitances were selected to achieve the desired cut-off frequencies:

- LPF: $R = 1\,\mathrm{k\Omega}$, $C = 2.2\,\mu\mathrm{F}$, yielding $f_{c,\mathrm{LP}} \approx 72\,\mathrm{Hz}$;
- HPF: $R = 1\,\mathrm{k\Omega}$, $C = 4.7\,\mu\mathrm{F}$, yielding $f_{c,\mathrm{HP}} \approx 34\,\mathrm{Hz}$.

The corresponding circuit schematics are shown in Fig. 4.1. The low-pass filter output is taken across the capacitor, while the high-pass filter output is taken across the resistor. This difference in the observation point has direct consequences on the time-domain behaviour of the two circuits.

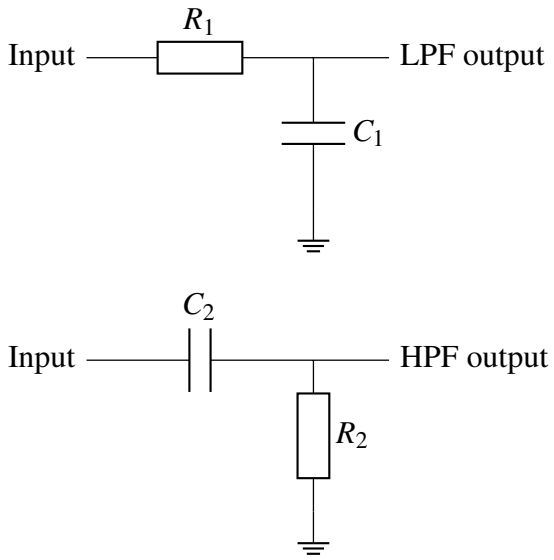

Fig. 4.1 First-order RC low-pass and high-pass filter topologies implemented on the experimental board.

The circuits were implemented on a dedicated printed circuit board designed using KiCad. Particular attention was paid to grounding and trace layout in order to ensure reproducible and low-noise measurement conditions.

4.3 Time-domain characterisation and estimation of the time constant

The time-domain behaviour of the filters was investigated by applying a voltage step at the input. The input excitation was generated using a Siglent SDG1022X Plus function generator, while input and output voltages were monitored with a Rigol DS1054 digital oscilloscope. The same instrumentation was employed for both the time-domain and frequency-domain experiments.

For a first-order system, the dynamics are governed by the time constant

$$\tau = R_{\text{eq}} C, \tag{4.2}$$

where R_{eq} includes both the nominal resistance and the output resistance of the function generator.

For the low-pass filter, the output voltage across the capacitor follows

$$v_{\text{out}}(t) = V_{\text{step}} \left(1 - e^{-t/\tau}\right), \tag{4.3}$$

whereas for the high-pass filter, when the output is taken across the resistor, the response is characterised by an exponential decay,

$$v_{\text{out}}(t) = V_{\text{step}} K e^{-t/\tau}, \tag{4.4}$$

with K accounting for the instantaneous voltage division at $t = 0^{+}$.

Figure 4.2 shows the measured step response of the low-pass filter, together with the fitted model. The close relation between experimental data and model demonstrates the validity of the first-order approximation.

A similar analysis was performed for the high-pass filter. Figure 4.3 reports the exponentially decaying output voltage following the input step, together with the fitted response.

In both cases, the time constant τ was estimated through a non-linear least-squares curve-fitting procedure implemented using `scipy.optimize.curve_fit` [41]. In practice, the numerical model used for parameter identification was obtained by minimising the sum of squared residuals between the measured output samples and the corresponding model predictions. Given a set of N measurement points $\{(t_i, y_i)\}_{i=1}^{N}$ (or, equivalently, $\{(f_i, y_i)\}_{i=1}^{N}$ in the frequency domain), and a parametric model $\hat{y}(x_i; \boldsymbol{\theta})$ with parameter vector $\boldsymbol{\theta}$, the least-squares objective function can be written as

$$S(\boldsymbol{\theta}) = \sum_{i=1}^{N} \left[y_i - \hat{y}(x_i; \boldsymbol{\theta})\right]^2, \tag{4.5}$$

where the residual $y_i - \hat{y}(x_i; \boldsymbol{\theta})$ represents the discrepancy between the measured response and the model at the i-th sample. The optimisation performed by `scipy.optimize.curve_-`

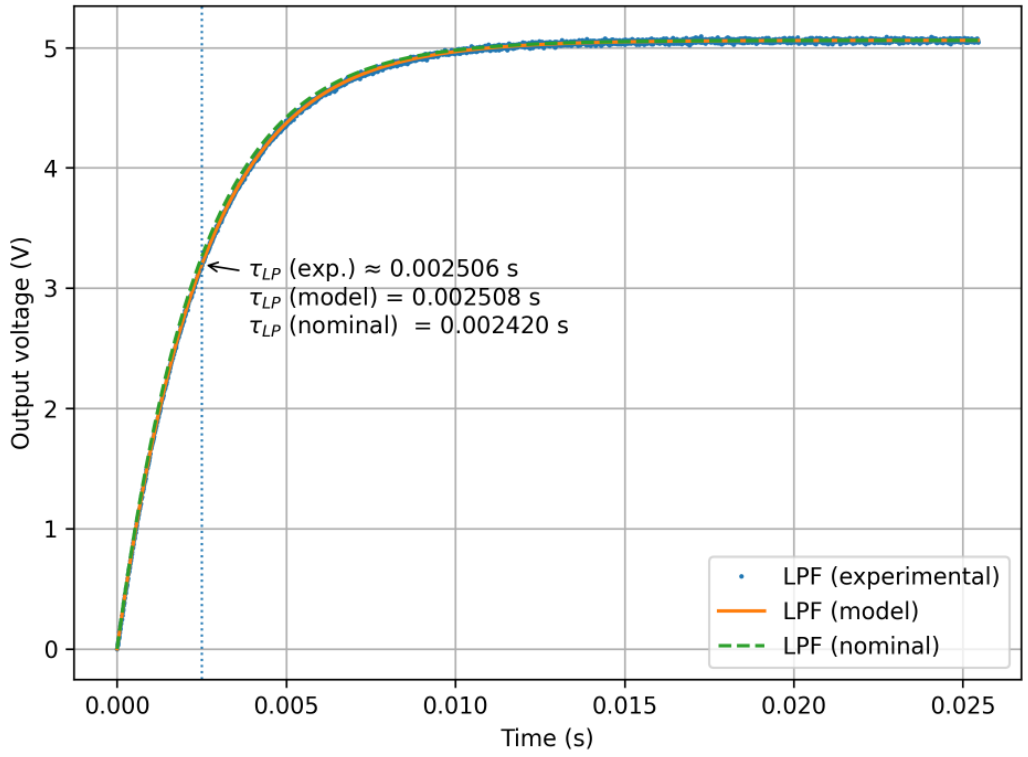

Fig. 4.2 Measured step response of the low-pass filter. Experimental data are compared with the fitted and the design first-order model.

`fit` consists in finding the parameter vector $\boldsymbol{\theta}$ that minimises $S(\boldsymbol{\theta})$, thereby yielding the best-fit model in the least-squares sense.

4.3.1 Time-domain results

The measured step response of the low-pass filter is shown in Fig. 4.2. The experimental waveform exhibits the expected monotonic rise towards the steady-state value, characteristic of a first-order system. The fitted exponential model closely follows the measured data over the entire transient, indicating that higher-order effects and parasitic elements are negligible within the investigated time window.

The time constant extracted from the non-linear curve fitting procedure is $\tau_{\mathrm{LP}} \approx 2.49\,\mathrm{ms}$, which differs by less than 1% from the theoretical value obtained by accounting for the generator output resistance. This level of agreement confirms both the validity of the modelling assumptions and the reliability of the fitting procedure.

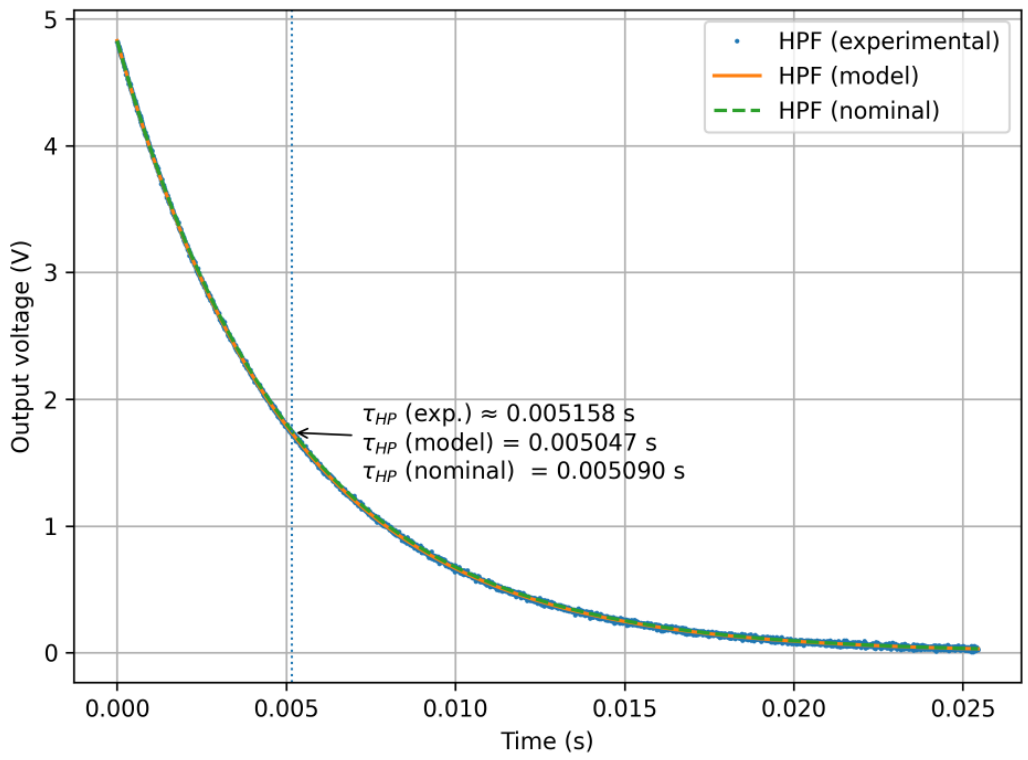

Fig. 4.3 Measured step response of the high-pass filter.

Figure 4.3 reports the step response of the high-pass filter. As expected from the circuit topology, the output voltage exhibits an exponentially decaying transient, starting from a finite initial value determined by the instantaneous resistive voltage division at $t = 0^+$. The fitted model accurately reproduces the decay profile, yielding a time constant of $\tau_{\mathrm{HP}} \approx 5.25\,\mathrm{ms}$.

The slightly larger deviation observed in the high-pass case is attributed to the combined effect of component tolerances and increased sensitivity to noise at low output voltages, particularly at long times.

4.4 Frequency-domain characterisation

The frequency-domain behaviour of the filters was investigated by performing a sinusoidal frequency sweep and measuring the magnitude and phase of the transfer function. For the frequency sweep, the function generator and oscilloscope

were programmed via a custom LabVIEW application, which coordinated instrument settings across the frequency range and stored the acquired waveforms and derived measurements directly to the host computer storage memory for subsequent processing.

The resulting Bode diagrams are shown in Figs. 4.4 and 4.5 [40].

Under the assumption of an ideal voltage source, the first-order transfer functions of the implemented networks are given by

$$H_{\mathrm{LP}}(s) = \frac{V_{\mathrm{out}}(s)}{V_{\mathrm{in}}(s)} = \frac{1}{1+sRC}, \qquad H_{\mathrm{HP}}(s) = \frac{V_{\mathrm{out}}(s)}{V_{\mathrm{in}}(s)} = \frac{sRC}{1+sRC}, \tag{4.6}$$

where $s = j\omega$ and $\omega = 2\pi f$. These expressions correspond to a single-pole low-pass response and a single-pole high-pass response, respectively, both characterised by the same cut-off angular frequency $\omega_c = (RC)^{-1}$ and cut-off frequency $f_c = \omega_c/(2\pi)$.

By evaluating (4.6) at $s = j\omega$, the frequency responses are

$$H_{\mathrm{LP}}(j\omega) = \frac{1}{1+j\omega RC}, \qquad H_{\mathrm{HP}}(j\omega) = \frac{j\omega RC}{1+j\omega RC}. \tag{4.7}$$

The corresponding phase responses (i.e., the phase shift between output and input) are obtained as $\phi(\omega) = \arg\{H(j\omega)\}$, yielding

$$\phi_{\mathrm{LP}}(\omega) = -\arctan(\omega RC), \qquad \phi_{\mathrm{HP}}(\omega) = \frac{\pi}{2} - \arctan(\omega RC) = \arctan\left(\frac{1}{\omega RC}\right), \tag{4.8}$$

where $\omega = 2\pi f$. At the cut-off frequency $\omega = \omega_c = (RC)^{-1}$, both filters exhibit a phase magnitude of 45°, i.e., $\phi_{\mathrm{LP}}(\omega_c) = -\pi/4$ and $\phi_{\mathrm{HP}}(\omega_c) = +\pi/4$, consistently with the single-pole behaviour observed in Fig. 4.5.

Figure 4.4 reports the magnitude response of both filters. The experimental data closely follow the expected first-order behaviour, with slopes of approximately $-20\,\mathrm{dB/decade}$ in the attenuation regions. The cut-off frequencies extracted using the $-3\,\mathrm{dB}$ criterion are $f_{c,\mathrm{LP}} \approx 64\,\mathrm{Hz}$ and $f_{c,\mathrm{HP}} \approx 28\,\mathrm{Hz}$, slightly shifted with respect to nominal values due to component tolerances and generator loading.

The corresponding phase responses are shown in Fig. 4.5. The phase transitions span approximately 90°, as expected for first-order systems, and the experimental points are in good relation with the analytical model over the entire frequency range.

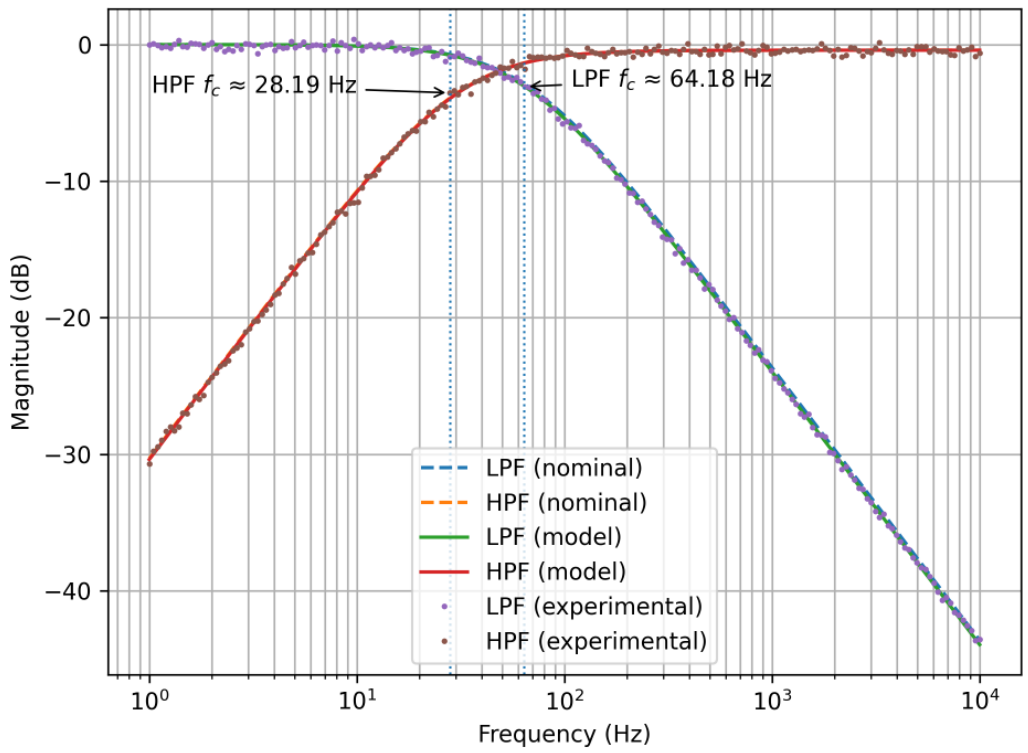

Fig. 4.4 Designed, measured and modelled magnitude response of the low-pass and high-pass filters. The dashed lines indicate the experimentally estimated cut-off frequencies.

4.4.1 Frequency-domain results: magnitude

The magnitude responses of the low-pass and high-pass filters are shown in Fig. 4.4. The experimental data points closely follow the analytical first-order models over more than three decades of frequency. The asymptotic slopes in the attenuation regions approach the theoretical value of $-20\,\mathrm{dB/decade}$, confirming the single-pole nature of the implemented circuits.

The cut-off frequencies extracted using the $-3\,\mathrm{dB}$ criterion are $f_{c,\mathrm{LP}} \approx 64.2\,\mathrm{Hz}$ and $f_{c,\mathrm{HP}} \approx 28.2\,\mathrm{Hz}$. These values are slightly shifted with respect to the nominal design targets, an effect that is quantitatively explained by the inclusion of the generator output resistance and by small deviations of the effective capacitance values from their nominal ratings.

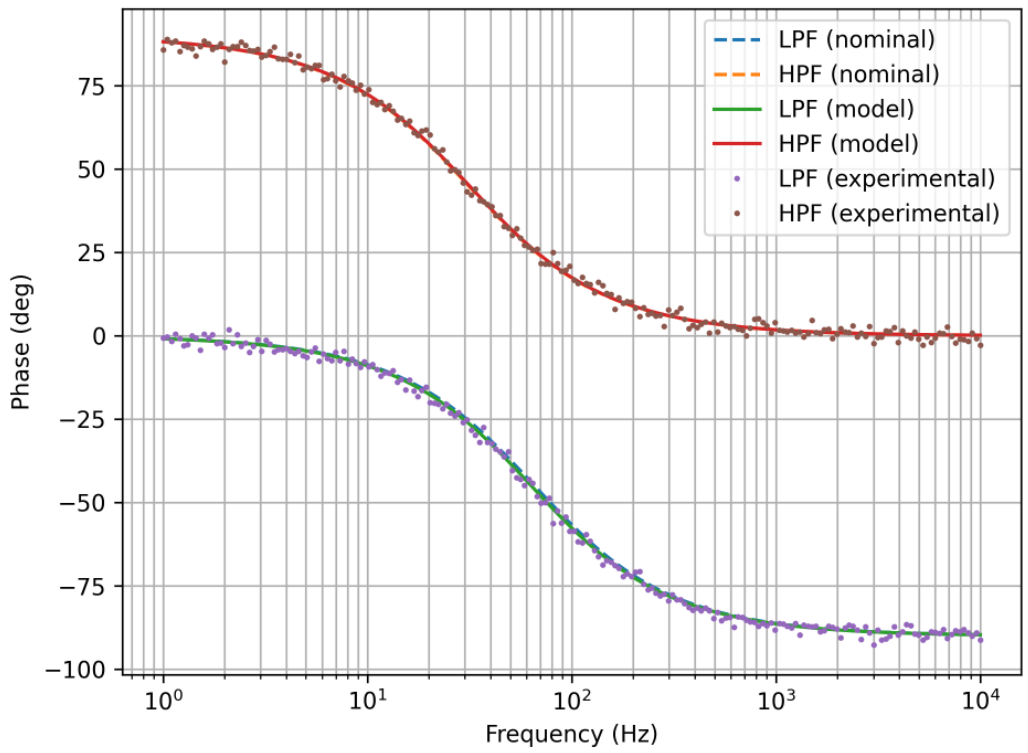

Fig. 4.5 Designed, measured and modelled phase response of the low-pass and high-pass filters.

The relation between model and experiment supports the consistency of the parameter identification process and validates the use of the fitted parameters for subsequent analysis.

4.4.2 Frequency-domain results: phase

Figure 4.5 shows the measured and modelled phase responses of both filters. The phase transitions extend over approximately 90°, as expected for first-order systems, with the transition regions centred around the experimentally identified cut-off frequencies.

The experimental phase data exhibit limited scatter and remain in good correlation with the analytical predictions over the entire frequency range. This confirms that the identified parameters consistently describe both the magnitude and phase behaviour of the system, reinforcing the validity of the first-order approximation.

4.5 Summary of identified parameters

Table 4.1 summarises the nominal component values, the corresponding theoretical parameters, and the values experimentally identified through frequency-domain analysis and time-domain curve fitting. The experimental resistance and capacitance values were inferred by fitting the measured transfer functions and step responses to first-order analytical models.

Table 4.1 Nominal, theoretical, and experimentally identified parameters of the RC filters.

Parameter	Nominal	Exprmental	Fitted model	Method
τ_{LP} [ms]	2.20	2.51	2.49	Step response fit
$f_{c,\mathrm{LP}}$ [Hz]	72.3	63.4	64.2	Bode magnitude
τ_{HP} [ms]	4.70	5.05	5.25	Step response fit
$f_{c,\mathrm{HP}}$ [Hz]	33.9	31.5	28.2	Bode magnitude

4.6 Conclusions

This chapter presented the design, fabrication, and experimental characterisation of a first-order RC filtering stage comprising a low-pass and a high-pass network, with cut-off frequencies selected to bracket the 50 Hz mains frequency. The activity was conceived as a preparatory exercise to validate an end-to-end experimental workflow that is subsequently applied to photovoltaic device parameter estimation.

Time-domain measurements under step excitation, combined with non-linear least-squares fitting implemented through `scipy.optimize.curve_fit`, provided robust estimates of the time constants τ_{LP} and τ_{HP}. Frequency-domain measurements via sinusoidal sweep yielded Bode magnitude and phase responses consistent with single-pole dynamics and enabled the extraction of cut-off frequencies using the -3 dB criterion. The identified parameters exhibit overall consistency with theoretical expectations once the contribution of the function generator output impedance and component tolerances are accounted for, as summarised in Table 4.1.

Chapter 5

Measurement System for the Experimental Characterization of PV Modules

This chapter presents the measurement framework developed for the controlled characterization of PV modules under outdoor operating and mismatch conditions. Two complementary systems are described in detail.

The first system is based on a capacitor-charging circuit actuated and monitored through a LabVIEW application. In this configuration, the I–V curve of the device under test (DUT) is reconstructed from the transient response generated when a previously pre-charged capacitor is connected to the PV module. The associated software architecture is built around an event-driven, producer–consumer paradigm, which ensures deterministic execution of the measurement sequence and provides synchronized acquisition of electrical and environmental quantities.

The second system employs a programmable electronic load to impose a prescribed sequence of operating points on the PV module. In this case, the I–V curve is reconstructed by driving the module along a discretized voltage or current sweep and recording the corresponding current or voltage response. The entire procedure is automated through a Python-based control script that manages communication with the electronic load, acquires environmental data via NI cDAQ hardware, and stores the resulting measurement dataset for subsequent analysis.

Flowcharts and commented code are used to clarify the internal logic of the acquisition procedures. The final section discusses data organization and integration into the unified post-processing pipeline adopted for model validation and performance assessment of PV modules under real operating conditions.

5.1 Description of a Capacitor-Based PV Characterization Circuit

The measurement platform is implemented in LabVIEW and is designed to perform controlled characterization of PV modules by actuating a dedicated electrical circuit and acquiring the associated electrical and environmental quantities. The adopted software architecture follows a producer–consumer, event-driven pattern, which is particularly suitable in this context because measurements are not performed at fixed time intervals. Instead, acquisitions are manually triggered by the operator only when irradiance conditions are sufficiently high and spatially uniform.

The electrical circuit used for the measurements is illustrated in Figure 5.1, where the main switch R_1, the pre-charge branch (controlled by R_2), the measurement capacitor, and the current and voltage sensing points are indicated.

5.1.1 Front Panel Elements

The LabVIEW front panel provides the graphical user interface through which the operator configures the system and initiates measurements. Elements are numbered for clarity and correspond to labels in the screenshot shown in Fig. 5.2.

Element 1: Control Sliders for Switching and Operating Modes

Element 1 consists of three binary sliders, each mapping directly to a specific function in the measurement system:

- **Main switch control (relay R_1).** This slider directly commands relay R_1 in the circuit of Fig. 5.1. When set to the “on” state, R_1 closes and the device under test (DUT) is connected so that it can charge the measurement capacitor.

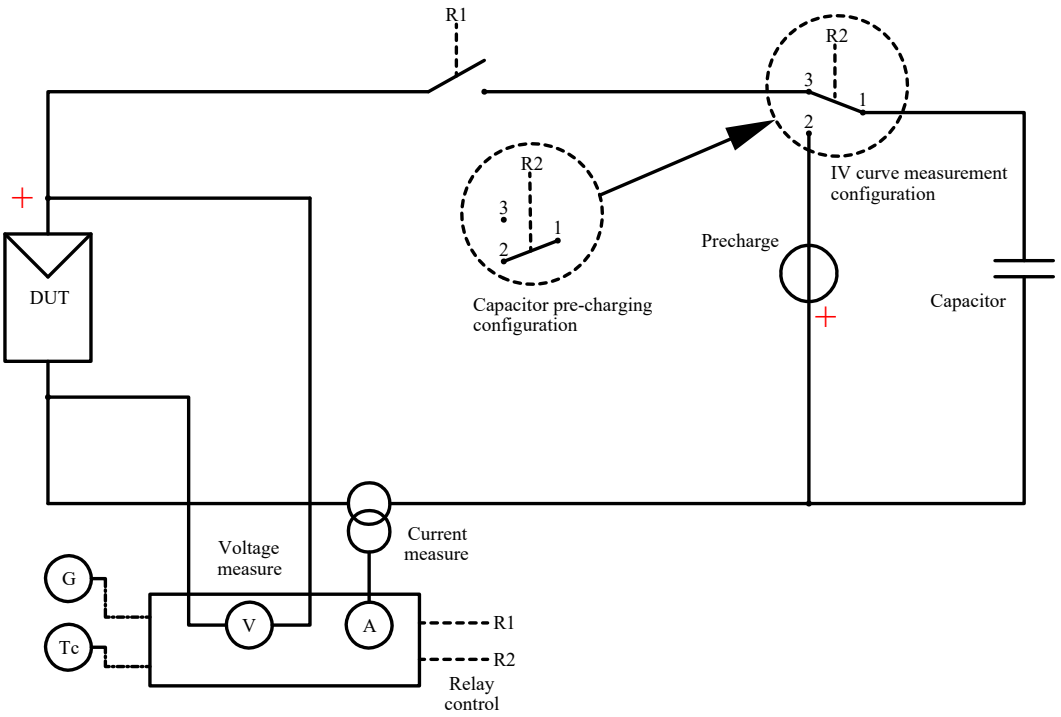

Fig. 5.1 Schematic of the measurement circuit adopted for PV module characterization in the capacitor-charging configuration.

This effectively enables the measurement procedure. When set to the "off" state, R_1 opens and the DUT is electrically isolated.

- **Pre-charge control (relay R_2).** The slider directly controls relay R_2, which is a single-pole, double-throw device with terminals labelled 1, 2, and 3. When terminals 1 and 2 are connected, the circuit is set in the capacitor pre-charge configuration, and the capacitor is driven to a negative initial voltage prior to the measurement. When terminals 1 and 3 are connected, the circuit is switched to the I–V curve measurement configuration, in which the capacitor is connected to the device under test. The negative pre-charge condition is required because the analogue trigger (Section 5.1.2) is defined on the capacitor voltage waveform and is configured to start the acquisition when the voltage crosses 0 V from negative values.

- **Data-saving control.** This slider enables or disables the logging of all acquired signals to a TDMS output file. TDMS (Technical Data Management

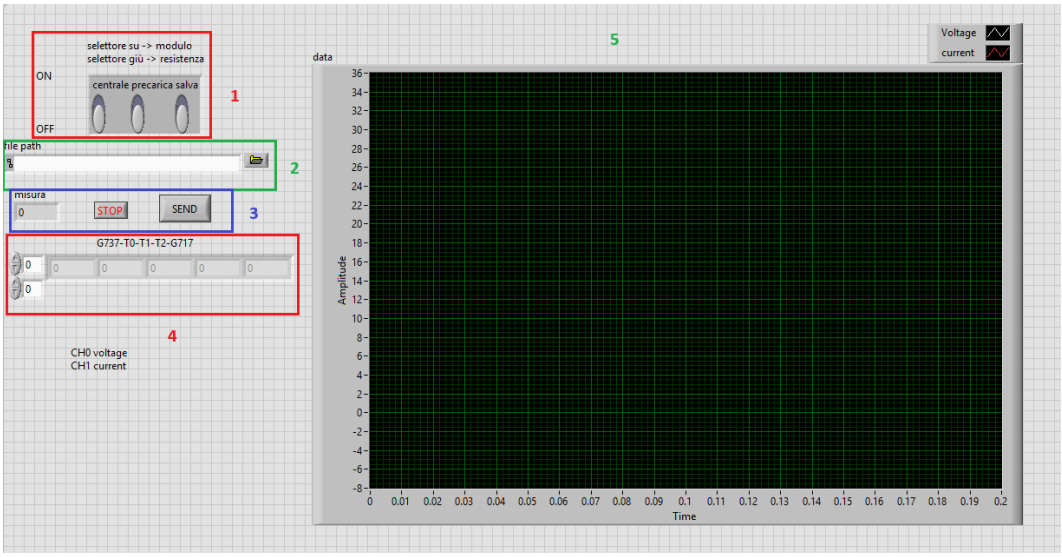

Fig. 5.2 Front panel of the LabVIEW application, with numbered elements corresponding to the functional description in Section 5.1.1.

Streaming) is a binary file format developed by National Instruments for the efficient storage and streaming of large volumes of structured measurement data together with associated metadata. During routine measurements, data saving is typically enabled; however, during debugging or hardware tests, the operator can disable logging to reduce disk usage and simplify the workflow.

Element 2: File Path Input Field

Element 2 is a text box where the user specifies the path of the TDMS output file. This path is read by the consumer loop whenever a measurement is executed. All electrical and environmental quantities corresponding to each acquisition are appended to this file.

Element 3: Measurement Counter and Command Buttons

Element 3 comprises three controls/indicators:

- **Measurement counter.** A numeric indicator displaying the number of measurement cycles completed since the program was started.

- **Stop button.** A button that, when pressed, generates an event processed by the producer loop, leading to a safe shutdown of the system (Section 5.1.4).
- **Send button.** A button that instructs the producer loop to enqueue a "send" command in the local queue. This command is then interpreted by the consumer loop as a request to perform one complete measurement cycle, including relay actuation, data acquisition and optional logging.

Element 4: Environmental Probe Array

Element 4 is an array indicator summarizing the outputs of the environmental sensors. For each measurement, it displays:

- the module temperature,
- the ambient air temperature,
- the irradiance on the plane of the module.

These quantities are acquired synchronously with the electrical waveforms and are stored together with the electrical data in the TDMS output file.

Element 5: Electrical Waveform Display

Element 5 is a waveform chart that displays, at the end of each acquisition, the measured current and voltage time series. The chart provides immediate visual feedback to the operator regarding the shape and quality of the measured transient responsible for the I–V curve.

5.1.2 Data Acquisition Hardware and Experimental Framework

The system employs two National Instruments (NI) data acquisition subsystems:

- **Electrical measurements.** Electrical quantities are measured using an NI USB-6251 multifunction data acquisition (DAQ) device, connected to the host PC via a USB interface. The current signal is wired to analogue input

channel `AI0`, while the voltage signal is wired to analogue input channel `AI1`. These channels are simultaneously sampled during each acquisition in order to preserve time coherence between voltage and current measurements.

- **Environmental measurements and relay control.** Environmental quantities and relay actuation are handled by an NI cDAQ-9174 CompactDAQ chassis, also connected to the PC via USB, hosting three modules:
  - an NI 9216 module for temperature measurements, supporting up to eight Pt100 RTDs; both the rear-side module temperature sensor and the ambient temperature sensor are connected to this module;
  - an NI 9219 module with four universal analogue input channels, used to acquire the signal from the irradiance sensor;
  - an NI 9482 digital output module, used to drive the relays in the measurement circuit, including the switching elements R_1 and R_2.

  All devices are configured and accessed through a LabVIEW application using the NI-DAQmx driver.

An analogue trigger is implemented on the voltage channel of the NI USB-6251. The acquisition is initiated when the capacitor voltage crosses 0 V from negative values. For each acquisition, a total of 5 kSa per channel are recorded at a sampling frequency of 20 kHz. These parameters can be modified via NI Measurement & Automation Explorer (NI MAX) or, if required, directly from the LabVIEW application.

The characterisation of the commercial PV modules is based on the charging transient of a capacitive load. During each measurement, a single PV module supplies an initially discharged capacitor. As the capacitor charges, the operating point of the module naturally evolves from short-circuit conditions, corresponding to an approximately zero capacitor voltage, to open-circuit conditions, as the capacitor voltage approaches the module open-circuit voltage. The capacitance value C is selected such that the duration of the charging transient remains below one second, in accordance with [42] and taking into account the expected short-circuit current I_{sc} and open-circuit voltage V_{oc} of the modules under test.

The measurement circuit incorporates relay actuators to automate the operating sequence. Upon completion of the charging phase, the relays disconnect the PV

branch and connect the capacitor to a resistive path in order to discharge the load and prepare the system for the subsequent measurement. The overall schematic of the experimental setup is shown in Fig. 5.3.

The main technical characteristics of the setup are summarised as follows:

- A multifunction data acquisition board featuring a successive-approximation A/D converter with 16-bit resolution, a maximum sampling rate of 1.25 MSa/s, a ± 10 V input range with programmable gains for lower ranges, and an input multiplexer. The device operates as a voltage probe with a stated uncertainty of $\pm 0.1\%$ of reading. A $\frac{1}{10}$ voltage divider extends the measurable voltage range up to ± 100 V.
- A Hall-effect current probe with a sensitivity of 100 mV/A for currents up to ± 30 A, providing current measurements with an uncertainty of $\pm 0.5\%$ of reading.
- A secondary standard pyranometer for measuring the plane-of-array irradiance G, with an uncertainty of $\pm 1.42\%$.
- A RTD sensor for measuring the rear-side module temperature T_m, with an uncertainty of $\pm 0.26\%$.
- One NI 9216 module, with 24-bit resolution and a sampling rate of 50 Sa/s, for RTD signal acquisition, and one NI 9219 module, with 24-bit resolution and a sampling rate of 100 Sa/s, for pyranometer signal acquisition. These modules are installed in a four-slot NI CompactDAQ chassis with USB interface.
- A personal computer running LabVIEW to supervise the acquisition process and to log both electrical and environmental quantities.
- A capacitive load with a nominal capacitance of 10 mF.
- A discharge resistor with a nominal resistance of 5 Ω.

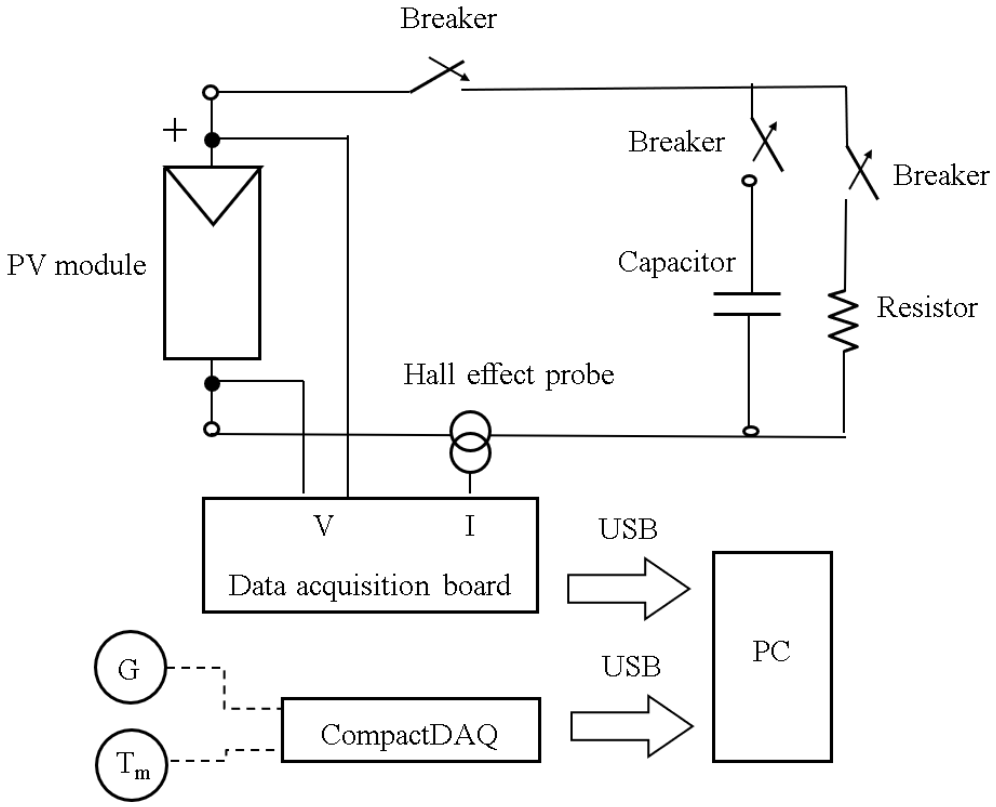

Fig. 5.3 Schematic of the experimental setup for commercial PV modules.

5.1.3 Block Diagram and Control Logic

Producer–Consumer, Event-Driven Architecture

The block diagram is organized around a producer–consumer architecture with event-driven producer logic. This design decouples user interaction from data acquisition, ensuring that the user interface remains responsive while the measurement logic is executed deterministically in the consumer loop.

Producer loop. The producer loop is implemented as a `for`-loop containing an event structure whose timeout is set to `-1`. This configuration causes the loop to remain idle until an event is generated by the front panel. The main events of interest are the activation of the *Stop* button and the *Send* button (Element 3). When such an event is detected, the producer loop encapsulates the corresponding command as a message and writes it to a local queue. No direct hardware interaction occurs in

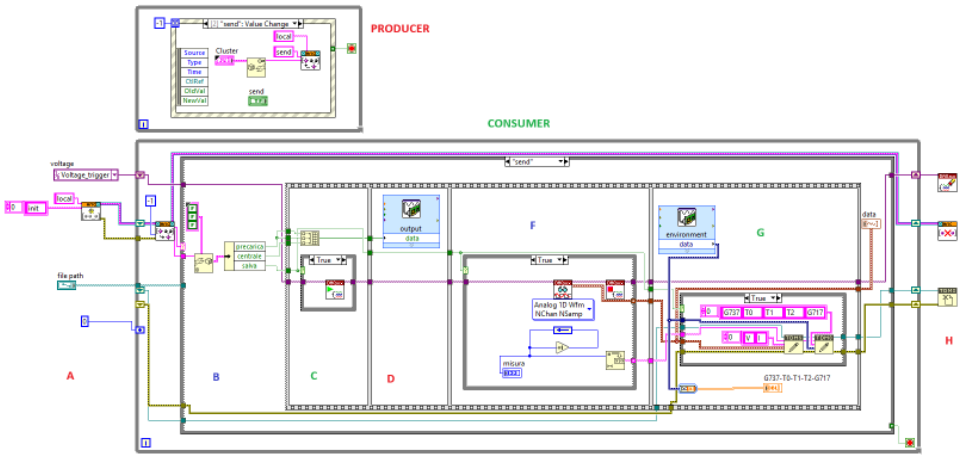

Fig. 5.4 Block diagram of the LabVIEW implementation, annotated with reference letters (A–H) corresponding to the measurement sequence.

the producer loop; its sole role is to capture user actions and forward them to the consumer loop in a thread-safe manner.

Initialization block (Point A). Before entering the consumer loop, an initialization section (Point A in the block diagram) is executed. This section:

- initializes the virtual instruments (VIs) that interface with the NI USB-6251 and the NI cDAQ-9174,
- creates and initializes the local command queue,
- resets the internal measurement counter.

Consumer loop. The consumer loop is also implemented as a `for`-loop, where each iteration is triggered by the arrival of a new message in the queue. The queue reader primitive is configured with a timeout of `-1`, so the loop remains blocked until a command is available. Once a message is dequeued, a case structure dispatches control to one of three logical cases:

- `init` (not shown in the simplified diagrams): performs possible re-initialization steps during operation, if needed;

- `send`: executes a complete measurement cycle;
- `stop` (not shown): performs an orderly system shutdown.

Measurement Sequence in the `send` Case

The `send` case is the core of the application and is structured into several logical points, labelled B–H in the block diagram.

1. **Acquisition of slider states (Point B).** The boolean states of the three sliders in Element 1 (main switch, pre-charge, and data-saving) are read from the front panel and stored in local variables or shift registers. This guarantees that the configuration used throughout the cycle is internally consistent, even if the operator changes a slider while a measurement is ongoing.
2. **DAQ activation according to configuration (Point C).** Based on the state of the main switch slider, the DAQ VIs are either armed for acquisition or bypassed. When acquisition is enabled, NI DAQmx tasks for the NI USB-6251 channels `AI0` (current) and `AI1` (voltage) are configured with the appropriate sampling parameters and analogue trigger on the voltage channel.
3. **Relay actuation (Point D).** Commands are sent to the NI 9482 digital output module to set the states of relays R_1 and R_2:
   - the main switch R_1 is set according to the corresponding slider (connection/disconnection of the DUT),
   - the pre-charge relay R_2 is set according to the pre-charge slider to apply or remove the negative pre-charge on the capacitor.

   This step defines the electrical configuration of the measurement circuit for the duration of the acquisition.
4. **Electrical acquisition (Point F).** Once the DAQ tasks are armed and the relays are in the desired state, the system waits for the analogue trigger on the voltage channel. When the capacitor voltage reaches 0 V, the NI USB-6251 simultaneously samples the current and voltage signals. For each measurement, 5 kSa per channel are recorded at 20 kSa/s. The acquired arrays represent the

full transient waveform from which the I–V curve of the PV module is later reconstructed.

5. **Environmental acquisition and logging (Point G).** In parallel with the electrical acquisition, the environmental quantities are sampled through the NI 9216 (module and ambient temperatures) and the NI 9219 (irradiance). For each measurement, these channels produce scalar values. All electrical and environmental data are then written to the TDMS output file specified in Element 2, provided that the data-saving slider is enabled. The electrical waveforms are simultaneously plotted in the waveform chart of Element 5, allowing immediate inspection by the operator.

The flowchart in Fig. 5.5 summarises the control logic implemented in the `send` case, explicitly highlighting the decoupling between user interaction, relay actuation and data acquisition. The diagram shows that the consumer loop always operates on well-defined configurations, since the slider states are latched at the beginning of each cycle and subsequently used to configure both the DAQ tasks and the relay states. The central role of the analogue trigger on the DUT voltage is emphasised, as it ensures that all electrical waveforms are synchronised with the zero-crossing of the capacitor voltage, thus providing consistent starting conditions for the reconstruction of the I–V curves. Finally, the flowchart makes explicit that environmental quantities are acquired and logged together with the electrical waveforms, enforcing a strict temporal coupling between operating conditions and the corresponding electrical response of the PV module.

Each TDMS output file contains multiple measurements. For every measurement, the environmental channels store scalar values (one sample per measurement), whereas the electrical channels store arrays containing the full current and voltage waveforms corresponding to the triggered acquisition. This structure facilitates subsequent post-processing and correlation between electrical and environmental data.

5.1.4 Shutdown Procedure

When the *Stop* button is pressed, the producer loop generates a `stop` message that is enqueued and subsequently processed by the consumer loop (Point H). The shutdown sequence includes:

- stopping and closing all NI DAQmx tasks associated with the NI USB-6251 and the NI cDAQ-9174 modules;
- flushing and closing the TDMS output file, ensuring that all buffered data are written to disk;
- releasing and destroying the local command queue.

This procedure guarantees that all hardware resources are left in a consistent state and that no file corruption occurs.

5.1.5 Post-Processing and *I–V* Curve Reconstruction

The LabVIEW application is strictly responsible for generating and acquiring the measurement data; no numerical processing or curve reconstruction is performed online. After the experimental campaign, all TDMS output files are imported into Python, where post-processing, *I–V* curve reconstruction, parameter extraction and further simulations are carried out. This separation of concerns allows the measurement software to remain relatively simple and robust, while delegating advanced analysis to a flexible, script-based environment.

5.2 Description of an Electronic Load-Based PV Test Circuit

In addition to the capacitor-charging circuit described in the previous section, a second measurement setup was developed in order to characterize PV modules under controlled operating conditions by means of a programmable electronic load. In this configuration, the module under test is driven along a prescribed sequence of current setpoints, and the corresponding voltage response is recorded, thus enabling the reconstruction of the *I–V* curve without relying on a dedicated capacitor branch. In practice, the admissible operating points are constrained by the DUT, so that the current and voltage can only be explored within the physical ranges $0\,\mathrm{A} \leq I \leq I_{\mathrm{sc}}$ and $0\,\mathrm{V} \leq V \leq V_{\mathrm{oc}}$; however, within these bounds the electronic load allows one to define an arbitrary, not necessarily uniformly spaced, array of measurement points. As a

consequence, the sampling pattern along the I–V curve (in current or in voltage) can be explicitly tailored to the identification problem at hand rather than being dictated by the dynamics of the measurement circuit, a feature that is exploited extensively in the Cramér–Rao lower bound analysis discussed in Chapter 7.

The measurement setup is schematically shown in Fig. 5.6. The PV module is connected directly to a programmable electronic load (HH PLA812), which operates primarily in constant-current mode and is controlled via SCPI commands from a Python application running on the host PC. Electrical and environmental quantities are acquired and synchronized by means of NI data acquisition hardware and the NI-DAQmx driver, as detailed below.

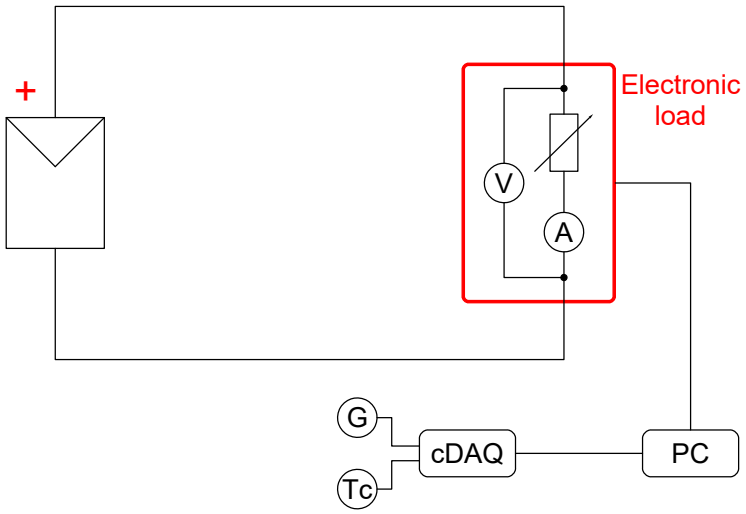

Fig. 5.6 Schematic of the measurement circuit adopted for PV module characterization using a programmable electronic load.

5.2.1 Measurement Hardware and Experimental Setup

The electronic-load-based setup relies on the following hardware components:

- **Programmable electronic load.** A HH PLA812 electronic load is connected to the PV module terminals and operated as a programmable load. The instrument is controlled from a Python application via a serial VISA interface. Communication is performed using SCPI (*Standard Commands for Programmable Instruments*), a standardised ASCII-based command set used

to configure instruments and query measurement data. During a programmed sweep, the load internally measures the instantaneous voltage V at the PV terminals and the current I flowing through the DUT. These quantities are queried through SCPI commands, either during the execution of the sweep or after its completion. According to the manufacturer specifications, the voltage measurement accuracy is given by $(\pm 0.1\% \times \text{measured value} + \pm 0.05\% \times \text{range})$ over a maximum measurable voltage of 120 V, while the current measurement accuracy is $(\pm 0.2\% \times \text{measured value} + \pm 0.05\% \times \text{range})$, with the current range customised to a maximum value of 18 A.

- **Environmental measurements.** Environmental quantities are acquired using an NI cDAQ-9174 CompactDAQ chassis hosting:
  - an NI 9216 module for module temperature measurements via a Pt100 resistance temperature detector (RTD);
  - an NI 9219 module for the acquisition of the voltage output of a reference cell proportional to the plane-of-array irradiance.

  The reference cell voltage is converted into irradiance G using a calibration factor obtained from prior laboratory calibration, while the Pt100 measurement is converted into the cell temperature T_c through the RTD linearization routines provided by the NI-DAQmx driver. All environmental quantities are acquired from within the Python application via the NI-DAQmx Python API.

- **Host PC and software environment.** The host personal computer runs a Python-based application that coordinates the measurement sequence, communicates with the electronic load via the `pyvisa` library, and accesses the NI cDAQ channels through the NI-DAQmx Python interface. The same software environment is used for data storage, preliminary visualization of the measured I–V curves, and, subsequently, for detailed post-processing within a fully script-based workflow.

In contrast to the capacitor-charging circuit, relay actuation and analogue triggering are entirely delegated to the internal control logic of the electronic load. The operating point of the PV module is directly defined by the current or voltage setpoint imposed by the load, and the resulting voltage and current are measured internally by the instrument. The NI cDAQ system is solely responsible for the acquisition of

environmental conditions, namely plane-of-array irradiance and module temperature, and does not intervene in the electrical operating point of the DUT.

5.2.2 Control Software and Measurement Sequence

The electronic load is driven by a Python script that implements a deterministic measurement sequence, encapsulating all the operations required to acquire a complete *I–V* curve and the corresponding environmental conditions. The script is organized into three main components:

- a `PLA_ElectronicLoad` class, which wraps the SCPI communication with the HH PLA812 (initialisation, configuration of operating modes, LIST sweep execution, and data retrieval);
- a set of helper functions (`measure_average_temperature`, `measure_average_irradiance` and `process_list`) that implement environmental acquisition and parsing of the LIST data;
- a `main()` function that orchestrates the overall measurement sequence and handles data storage and plotting.

The sequence executed by `main()` can be summarised as follows.

1. **Environmental acquisition.** At the beginning of each measurement, the script calls the functions `measure_average_temperature` and `measure_average_irradiance`. Each function creates a dedicated NI-DAQmx task on the corresponding NI cDAQ module (NI 9216 for the Pt100, NI 9219 for the reference cell), reads `NUM_ENV_SAMPLES` successive samples (five in the current implementation) with a delay `ENV_SAMPLE_INTERVAL` (0.2 s) between them, and returns the arithmetic mean. The results are stored as two scalar quantities: the average module temperature T_{avg} and the average irradiance G_{avg}.
2. **Preliminary electrical measurements.** The electronic load is first configured in constant-voltage mode via the method `set_voltage(0.0)` of the `PLA_ElectronicLoad` class. With the input enabled (`start_load()`), and after a

short settling time (0.5 s), the internal measurements `read_voltage()` and `read_current()` are queried to obtain an approximate short-circuit operating point (V_{sc}, I_{max}). The load is then disabled (`stop_load()`), and, after another settling interval, the open-circuit voltage V_{oc} is obtained by querying `read_voltage()` with the input open. These values are printed to the console for monitoring and diagnostic purposes.

3. **Definition of the current sweep.** The number of points in the LIST sweep, `n_meas`, and the dwell time per point, `dwell_time`, are defined in the `main()` function. In the present configuration, `n_meas` is set to 100 and `dwell_time` to 0.01 s. A one-dimensional NumPy array `curr_set` is constructed by linearly spacing the current from 0 A to I_{max} using `np.linspace(0.0, curr_max, n_meas)`. This array defines the discrete current levels to be applied sequentially by the electronic load in LIST mode.

4. **Execution of the LIST sweep.** The method `list_function(curr_set, dwell_time)` of the `PLA_ElectronicLoad` class configures and executes the LIST sweep on the instrument. Internally, this method sends the sequence of current setpoints to the load (`LIST:CURRENT`), sets a zero ramp time (`LIST:RTIM`) and a constant dwell time equal to `dwell_time` for all steps (`LIST:DWEL`), enables acquisition (`LIST:ACQ ON`), and starts the LIST execution (`LIST:STAT ON`). The script then waits for a duration equal to the total sweep time plus a safety margin, after which the LIST mode and acquisition are stopped and the input is turned off. The instrument is queried for the number of acquired points (`DATA:POINTS?`) and the corresponding data are retrieved via `DATA:REMOVE?`, which returns a comma-separated string of interleaved triplets (t_i, V_i, I_i).

5. **Data parsing, storage and visualisation.** The raw string returned by `list_function` is passed to the helper function `process_list`, which converts it into a `pandas.DataFrame` with three columns: `timestamp_s`, `voltage_V` and `current_A`. The rows are sorted by `timestamp_s` to ensure chronological ordering. Two additional columns, `irradiance_Wm2` and `module_temperature_degC`, are then appended and filled with the scalar values G_{avg} and T_{avg} obtained at the beginning of the measurement. The resulting DataFrame is written to disk as a CSV file (currently named `irradiated_measurement.csv`)

and the corresponding *I–V* curve is plotted using `matplotlib`, by displaying `current_A` as a function of `voltage_V`.

5.2.3 Python Implementation

The implementation follows a modular structure: the class `PLA_ElectronicLoad` encapsulates all low-level SCPI communication with the HH PLA812, the functions `measure_average_temperature`, `measure_average_irradiance` and `process_list` implement environmental acquisition and data parsing, while the `main()` function orchestrates the complete measurement cycle (environmental acquisition, preliminary electrical check, LIST sweep, data storage and plotting).

The flowchart in Fig. 5.7 details the implementation of the Python code. The block labelled "Set measurement parameters" corresponds to the initial configuration of the user-defined constants (`n_meas`, `dwell_time`, `NUM_ENV_SAMPLES`, `ENV_SAMPLE_INTERVAL`) and to the construction of the `PLA_ElectronicLoad` object. The subsequent block "Acquire environmental conditions" represents the calls to `measure_average_temperature` and `measure_average_irradiance`, which return the averaged values T_{avg} and G_{avg}.

The block "Preliminary electrical measurement with load" summarizes the part of `main()` where the electronic load is configured in constant-voltage mode, the quasi short-circuit condition is imposed (`set_voltage(0.0)` and `start_load()`), and the approximate short-circuit current I_{max} and open-circuit voltage V_{oc} are measured. The block "Define current sweep" corresponds to the construction of the NumPy array `curr_set` via `np.linspace(0.0, curr_max, n_meas)`.

The central block "Run LIST *I–V* sweep on electronic load" encapsulates the call to `list_function(curr_set, dwell_time)`, which internally configures the LIST mode of the PLA812, executes the sweep and retrieves the time-stamped (t_i, V_i, I_i) samples. The following blocks "Process raw data" and "Attach environmental metadata" represent the invocation of `process_list`, the construction of the `pandas.DataFrame` and the addition of the columns `irradiance_Wm2` and `module_temperature_degC`. Finally, the block "Save results and visualize" corresponds to saving the DataFrame to CSV and plotting the *I–V* curve using the pair `(voltage_V, current_A)`.

Overall, the flowchart provides an intuitive high-level view of the measurement pipeline, while the Python listing exposes the full implementation details in a form that can be directly executed and adapted to different experimental conditions.

5.3 Comparison of Measurement Systems and Post-Processing Integration

5.3.1 Complementary Features of the Two Measurement Platforms

The two measurement platforms described in this chapter provide complementary capabilities for the experimental characterization of PV modules. A qualitative comparison is summarised in Table 5.1.

The capacitor-charging system is particularly suited to the investigation of dynamic effects and to the rapid acquisition of I–V curves from transient waveforms. Its reliance on an analogue trigger tightly couples the timing of the acquisition to the physical evolution of the capacitor voltage. Moreover, the sweep direction is inherently constrained: the voltage increases monotonically from the pre-charge condition to the natural open-circuit value, and the operating points are determined by the RC transient and by the behaviour of the DUT rather than by explicit operator choice. This also means that only voltage-driven sweeps are possible, and the density of sampled points cannot be tuned independently of the circuit dynamics.

Conversely, the electronic-load-based system provides fine control of the operating point in quasi steady-state conditions. By imposing a prescribed current profile and reading the corresponding voltage, it allows the direct comparison between measured I–V points and model-based predictions under well-characterised irradiance and temperature. Within the admissible physical range ($0 \leq I \leq I_{\mathrm{sc}}$ and $0 \leq V \leq V_{\mathrm{oc}}$), the user can define an arbitrary vector of operating points, enabling both forward and backward sweeps as well as non-uniform, optimised, or problem-specific sampling patterns. This flexibility is essential for the estimation-theoretic analysis discussed in Section 7, where the measurement points must be deliberately placed in regions of high Fisher information.

In addition, the electronic load supports operating modes unavailable in the capacitor-based system, such as MPPT tracking when the module is not being measured, and voltage- or current-regulated operation for stability tests. Finally, certain classes of electronic loads can return energy to the grid instead of dissipating it internally, which makes them suitable for in-field measurements without requiring module disconnection or external heat sinks. By contrast, the capacitor-based approach excels when the module is isolated from its installation, producing dense waveforms with very high temporal resolution.

5.3.2 Unified Data Format and Post-Processing Pipeline

Despite their different operating principles, both platforms are designed to produce measurement data that can be ingested by a common post-processing pipeline implemented in Python.

In the capacitor-charging system, each TDMS output file contains multiple acquisitions. For every measurement, the environmental channels store scalar values (one sample per measurement), whereas the electrical channels store arrays containing the full current and voltage waveforms corresponding to the triggered transient. These TDMS output files are imported into Python, where the transient waveforms are processed in order to reconstruct the corresponding I–V curves, extract model parameters and perform further numerical analyses.

In the electronic-load system, each execution of the Python script produces a CSV file containing one complete I–V sweep. Each row of the file corresponds to a sample (t_i, V_i, I_i) acquired by the electronic load in LIST mode, while the environmental columns contain constant values equal to T_{avg} and G_{avg} for that sweep. This structure is consistent with the data organisation adopted for the capacitor-charging circuit, in the sense that both systems associate each I–V dataset with a unique pair of environmental descriptors (irradiance and module temperature) and a well-defined acquisition time window.

The unified post-processing pipeline operates on both data sources in a homogeneous way. For the capacitor-charging measurements, transient waveforms are first converted into discrete I–V pairs; for the electronic-load measurements, the I–V pairs are directly available from the CSV files. Subsequent steps—including I–V curve fitting, parameter extraction for equivalent-circuit models, computation of perfor-

mance indicators and numerical simulations under varying operating conditions—are applied using the same set of scripts and analysis routines.

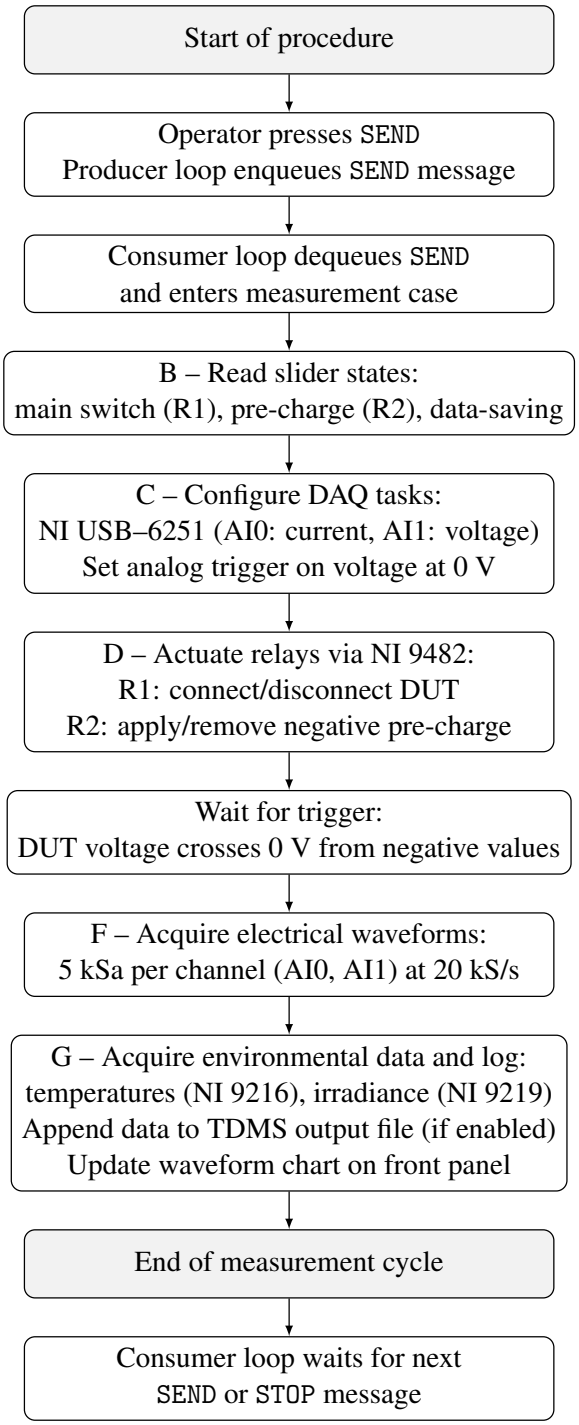

Fig. 5.5 Flowchart of the measurement procedure executed in the `send` case of the consumer loop.

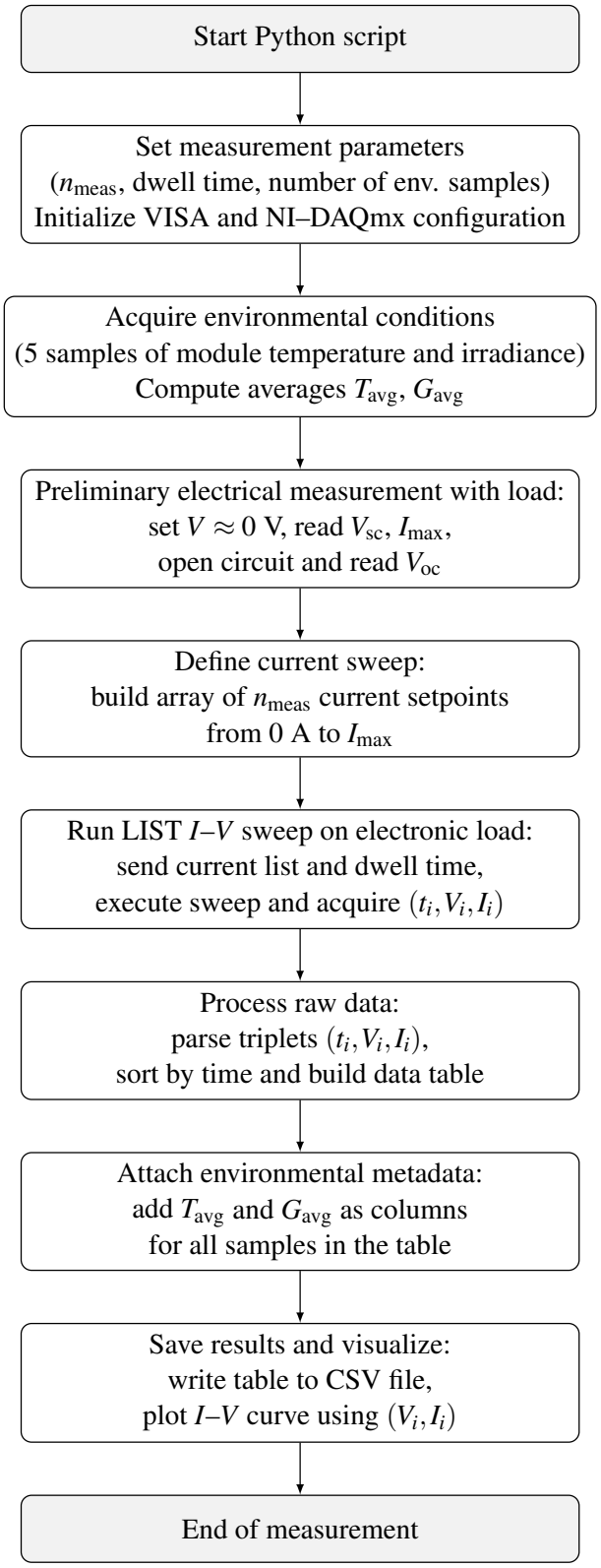

Fig. 5.7 High-level flowchart of the Python-based measurement procedure using the HH PLA812 electronic load and NI cDAQ

Table 5.1 Comparison between the capacitor-charging and electronic-load measurement systems.

	Capacitor-charging system	Electronic-load system
Type of control	Transient, passive response to capacitor connection	Steady-state or quasi–steady-state, active current/voltage control
Triggering mechanism	Analogue trigger on capacitor voltage zero-crossing	Time-based sequence (LIST mode) or direct setpoint control
Sweep direction	Monotonic, from the lowest voltage to the open-circuit voltage	Forward or backward sweep; arbitrary ordering of samples
Domain of control	Voltage-driven sweep only (capacitor charge)	Fully programmable: current sweep, voltage sweep, or mixed operating points
Sampling pattern	Uniform in time (determined by RC transient and DUT)	Arbitrary, not necessarily equispaced sampling pattern within $0 \leq I \leq I_{sc}$ and $0 \leq V \leq V_{oc}$
Environmental acquisition	Synchronous with electrical transient	Averaged before the I–V sweep (scalar metadata)
Suitability	Dynamic/transient behaviour, fast phenomena	Accurate steady-state I–V sampling, model validation, CRLB-oriented sampling design
Additional operating capabilities	None (transient only)	MPPT mode available when not measuring; stand-alone regulation
Field applicability	Good for isolated modules disconnected from plant	Some loads can dissipate or return power to the grid, enabling in-field testing during normal operation
Primary limitations	Sensitive to trigger noise and wiring parasitics; fixed monotonic sweep	Requires reliable SCPI communication and timing

Chapter 6

Two-Test Parameter Identification of PV Modules under Partial Shading

6.1 Proposed Method

Positioning with respect to the state of the art

A substantial body of literature has investigated the effects of partial shading on the module-level I–V characteristic, focusing on the appearance of multiple local maxima in the power–voltage curve [43], the activation of bypass diodes, and the associated mismatch losses [44]. Equivalent-circuit models for shaded PV modules have been proposed to reproduce the overall module response under non-uniform irradiance [17], and several works have adjusted model parameters empirically to account for reduced illumination levels. However, none of the existing approaches provides a procedure to recover the I–V characteristic of an *individual shaded cell* from measurements taken exclusively at the module terminals.

This gap has a practical origin: commercial PV modules do not expose the terminals of individual cells, so only the module's positive and negative output terminals are accessible to external instrumentation. Under uniform irradiance, the I–V curve of a single cell can be approximated by dividing the module characteristic

by the number of series-connected cells, since all cells are nominally identical. This assumption breaks down as soon as one cell is shaded, because the shaded cell operates in a fundamentally different regime — lower photogenerated current, higher recombination, reduced shunt resistance — that cannot be inferred from the remaining cells.

The method proposed in this chapter addresses this open problem directly. By exploiting the algebraic difference between two module-level I–V curves acquired within a short time interval — one under uniform irradiance and one with a single cell intentionally shaded — the contribution of the shaded cell is isolated without requiring any physical access to individual cell terminals. This differential approach, referred to as the "One Module, Two Tests" procedure, is novel in the photovoltaic context and has no direct precedent in the literature.

The method is further extended to commercial half-cell modules, whose internal architecture — three subunits each comprising two parallel strings of 18 half-cells protected by a bypass diode — makes the extraction substantially more involved than for conventional full-cell designs, for which simpler series-only circuit models suffice. The iterative parameter adjustment procedure described in Section 6.1.4 explicitly reconstructs the module I–V curve from cell-level parameters, accounting for bypass diode activation, string-level parallelisation, and the series connection of subunits.

The indirect method is validated against a direct "Two Modules, One Test" bridge-circuit measurement, which provides an independent quantitative reference for the shaded-cell I–V characteristic under controlled and repeatable conditions. This combined validation strategy has not been reported in previous research on partial-shading characterisation of commercial PV modules.

The aim of this study is to introduce a procedure that enables the determination of the equivalent circuit parameters not only for irradiated PV cells but also for cells subject to shading in recent commercial modules with rated power of approximately 400 W that incorporate half-cell technology. The first objective is to estimate the parameters of the PV cells forming a single-string mini-module with rated power of a few watts under conditions of uniform irradiance and partial shading. Subsequently, the parameter estimates obtained for the mini-modules are employed to reconstruct the I–V curve of a single shaded cell within the commercial modules under investigation.

The proposed approach relies on two measured *I–V* curves, namely one acquired on the PV module under natural sunlight without shading and a second acquired on the same module with one cell intentionally shaded. The two measurements are recommended to be performed within a very short interval of time, with a maximum suggested separation of a couple of minutes, in order to minimise fluctuations in the ambient temperature and the solar irradiance. This procedure, referred to as the "One Module (or One String), Two Tests" method, requires both *I–V* curves to be collected under high irradiance level, namely above 800 $\mathrm{W/m^2}$. In the first acquisition, the module or the string is uniformly irradiated under natural sunlight, which yields the yellow curve labelled "N_s irradiated cells" in Figure 6.1. In the second acquisition, the *I–V* characteristic is measured for the module or the string with $N_\mathrm{s} - 1$ irradiated cells and one shaded cell, which yields the blue curve labelled "1 shaded cell and $N_\mathrm{s} - 1$ irradiated cells" in Figure 6.1. Although the two *I–V* curves can be obtained within a short time window, the environmental conditions will not generally be identical. International Standards provide procedures to correct voltage and current measurements to compensate for differing weather conditions. Therefore, in order to reduce errors due to such differences, the procedure recommends correcting the curve measured under uniform irradiance to the environmental conditions prevailing during the partially shaded measurement.

The remainder of this section details the extraction of the differential curve for both the single-string mini-modules and the commercial modules.

6.1.1 Performance Metrics for Parameter Validation

The accuracy of the parameter identification used for *I–V* curve reconstruction in PV generators was assessed by means of four indicators, namely the Normalised Root Mean Square Error (*NRMSE*), the deviation at the Maximum Power Point (MPP), the Normalised Mean Absolute Error (*NMAE*), and the Normalised Mean Bias Error (*NMBE*). With the exception of the MPP deviation, each indicator associated with a simulated *I–V* curve was normalised with respect to the average current of that curve, thereby allowing direct comparison of results obtained under different environmental conditions. The four indicators were evaluated for both the mini-modules and the commercial modules. For the mini-modules, the indicators were computed for each *I–V* dataset comprising n points in order to quantify the deviation between the measured set $\{(V_{\mathrm{meas},j}, I_{\mathrm{meas},j})\}_{j=1}^{n}$ and the model-estimated set $\{(V_{\mathrm{meas},j}, I_{\mathrm{cal},j})\}_{j=1}^{n}$.

In this case, the latter set was constructed by evaluating the model current at each measured voltage $V_{\mathrm{meas},j}$. For the commercial modules, an interpolation step was introduced to align the experimental voltages and the model voltages. Specifically, the measured currents were linearly interpolated onto the voltage grid used by the model. This alignment enabled a pointwise comparison between the two datasets, and the indicators were then computed as follows.

- The *NRMSE* provides a normalised measure of the global deviation between the model and the measurements, with increased penalisation of large discrepancies.

$$NRMSE = \frac{\sqrt{\frac{1}{n}\sum_{j=1}^{n}\left(I_{\mathrm{cal},j} - I_{\mathrm{meas},j}\right)^2}}{\frac{1}{n}\sum_{j=1}^{n} I_{\mathrm{meas},j}}. \tag{6.1}$$

  In the iterative parameter adjustment for the commercial module described in Section 6.1.4, a threshold on *NRMSE* was used as a stopping criterion.

- The MPP deviation quantifies the fidelity of the model in estimating the maximum deliverable PV power.

$$\Delta P_{\mathrm{MPP}} = 100 \times \frac{\left|P_{\mathrm{cal,MPP}} - P_{\mathrm{meas,MPP}}\right|}{P_{\mathrm{meas,MPP}}}, \tag{6.2}$$

  where $P_{\mathrm{meas,MPP}}$ is the maximum power extracted from the experimental *I–V* curve and $P_{\mathrm{cal,MPP}}$ is the maximum power predicted by the model.

- The *NMAE* quantifies the average absolute deviation between the measurements and the model and is typically less sensitive to outliers than *NRMSE*.

$$NMAE = \frac{\frac{1}{n}\sum_{j=1}^{n}\left|I_{\mathrm{cal},j} - I_{\mathrm{meas},j}\right|}{\frac{1}{n}\sum_{j=1}^{n} I_{\mathrm{meas},j}}. \tag{6.3}$$

- The *NMBE* reveals the presence of a systematic bias in the model, with positive values indicating overestimation and negative values indicating underestimation.

$$NMBE = \frac{\frac{1}{n}\sum_{j=1}^{n}\left(I_{\mathrm{cal},j} - I_{\mathrm{meas},j}\right)}{\frac{1}{n}\sum_{j=1}^{n} I_{\mathrm{meas},j}}. \tag{6.4}$$

6.1.2 Differential Curve Extraction for Single-String Mini-Module

To isolate the *I–V* curve of the shaded cell in a single-string mini-module comprising N_s series-connected cells, the following two-step procedure is proposed.

- **Evaluation of the curve for the module with $N_\mathrm{s}-1$ irradiated cells in series.** The *I–V* curve of an individual cell can be approximated by dividing the *I–V* characteristic of a mismatch-free string or module by the number of series-connected cells. Accordingly, the *I–V* curve of the module with $N_\mathrm{s}-1$ irradiated cells is derived by the proportional relation

$$V_{\mathrm{Ns\text{-}1}} = V_{\mathrm{Ns}} \cdot \frac{N_\mathrm{s}-1}{N_\mathrm{s}}\,, \tag{6.5}$$

  where V_{Ns} and $V_{\mathrm{Ns\text{-}1}}$ denote the voltages of the module with N_s and $N_\mathrm{s}-1$ irradiated cells in series, respectively.

- **Evaluation of the *I–V* curve for the shaded cell.** The curve of a single shaded cell is obtained by subtracting, at equal current, the voltage of the module with $N_\mathrm{s}-1$ irradiated cells from the voltage measured on the configuration with one shaded cell and $N_\mathrm{s}-1$ irradiated cells, denoted by the subscript "1sh". Prior to subtraction, the currents of the $N_\mathrm{s}-1$ curve are linearly interpolated to match the current samples of the 1sh curve. Hence, for each k^{th} current value I_k, the shaded-cell voltage $V_{\mathrm{sh,k}}$ is computed as

$$V_{\mathrm{sh,k}} = V_{\mathrm{1s,k}} - V_{(\mathrm{Ns\text{-}1}),k}\,. \tag{6.6}$$

The indirect method extracts the *I–V* curve of a single solar cell under partial shading by exploiting the difference between two measurements of the module *I–V* characteristic taken under the same irradiance and ambient temperature. In addition to the "one PV module, two tests" approach, an experimental verification was performed using a "two PV modules, one test" arrangement designed to measure directly the contribution of the shaded cell under controlled and repeatable conditions. The direct approach employs a simple unbalanced bridge circuit, shown in Figure 6.2, in which one branch contains two identical PV modules in series and the other branch contains two high-value precision resistors, namely $R_1 = 1\,\mathrm{M\Omega}$ and $R_2 = 750\,\mathrm{k\Omega}$, with negligible current draw. The voltage across the bridge output terminals CD

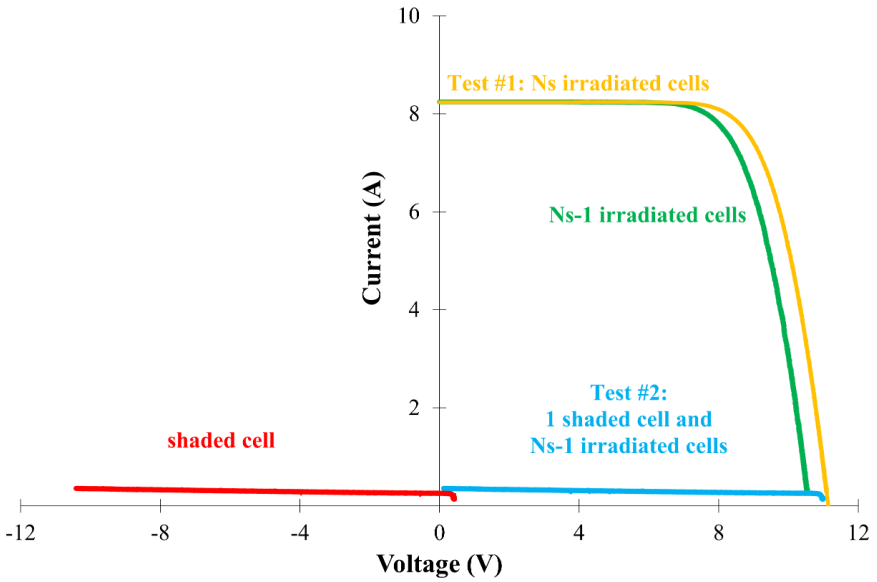

Fig. 6.1 I–V curves used by the method to recover the characteristic of the shaded cell.

is proportional to the voltage across the partially shaded cell and is observed over the common current stimulus of the two modules in series, which decays from the short-circuit current to zero during the charging transient of a suitably chosen capacitor powered by the series-connected modules. A resistor R_3 is connected across the output terminals CD of the bridge and has a value of 1 GΩ, which is much larger than the other resistors. Consequently, the current through R_3 is negligible, the resistors R_1 and R_2 behave approximately as a series combination, and the module voltages scale proportionally with the resistor values.

The shaded-cell voltage can be derived analytically from the voltages measured at the bridge terminals AD and BD by applying Kirchhoff's current law at node C as follows.

$$\frac{V_{\mathrm{AC}}}{R_1} = \frac{V_{\mathrm{CD}}}{R_3} - \frac{V_{\mathrm{BC}}}{R_2}\,. \tag{6.7}$$

The above relation can be rearranged to obtain the voltage across the terminals of the single shaded cell $V_{\mathrm{cell,sh}}$.

$$V_{\mathrm{cell,sh}} = V_{\mathrm{mod,sh}} - \frac{3}{4}V_{\mathrm{mod,irr}} = -\left(\frac{7}{4} + \frac{R_2}{R_3}\right)V_{\mathrm{CD}}\,, \tag{6.8}$$

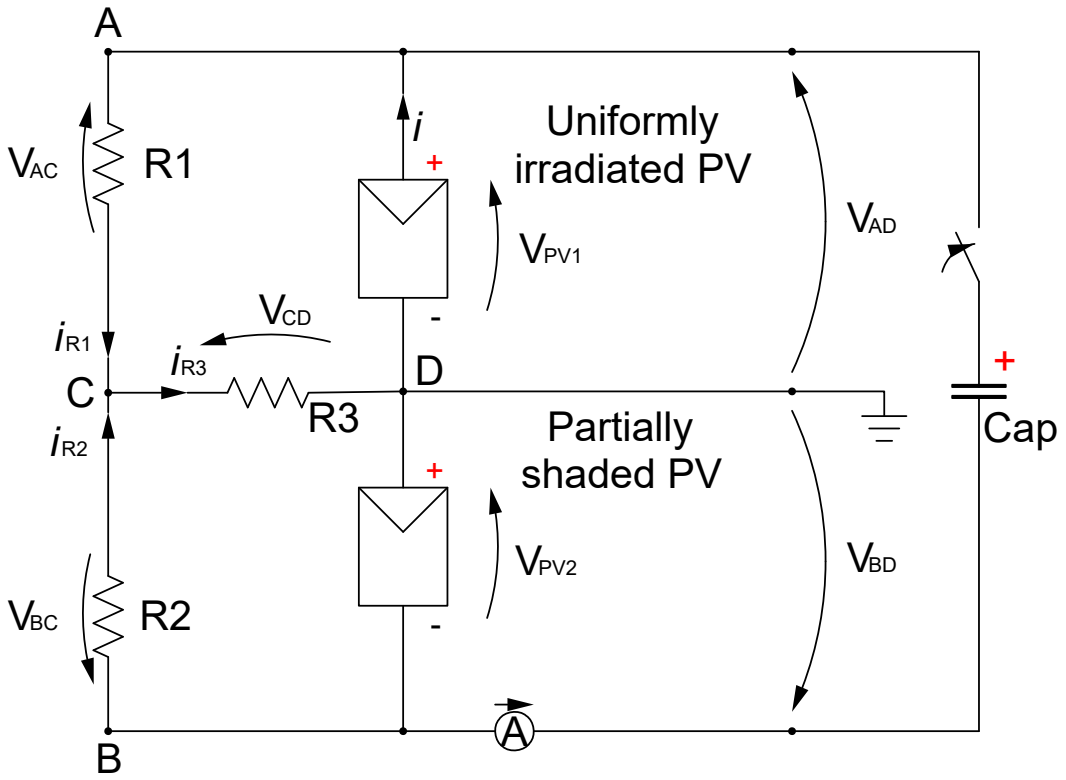

Fig. 6.2 Schematic of the measurement system.

where $V_{\mathrm{mod,sh}}$ and $V_{\mathrm{mod,irr}}$ are the voltages at the terminals of the two identical PV modules under partial shading and full irradiance, respectively, and the ratio R_2/R_3 is negligible.

This direct measurement provides a quantitative reference for comparison with the indirect difference method, thereby furnishing independent and functional feedback for validating the reconstruction approach used in the “One Module, Two Tests” procedure.

6.1.3 Uncertainty Evaluation and Error Propagation

This subsection defines the uncertainty components and the propagation formulae associated with the indirect method introduced above. The uncertainty contributions for the measured *I–V* curves are as follows.

- The uncertainties for measurements obtained under partial shading are $u_{\mathrm{V,sh}} = \pm 0.1\%$ for voltage and $u_{\mathrm{I,sh}} = \pm 0.5\%$ for current.
- For measurements obtained under uniform irradiance, the associated uncertainties account for the interpolation performed to align the currents to those of the partially shaded dataset. Specifically, for a generic current value I, the voltage uncertainty due to linear interpolation is

$$u_{\mathrm{V,irr}}(I) = \sqrt{\left(\frac{I_b - I}{I_b - I_a}\right)^2 u_{V_a}^2 + \left(\frac{I - I_a}{I_b - I_a}\right)^2 u_{V_b}^2}\,, \tag{6.9}$$

  where I_a and I_b denote the two adjacent current samples from the partially shaded curve that bracket I, and u_{V_a} and u_{V_b} are the associated voltage uncertainties weighted by the relative distances of I from I_a and I_b.
- The uncertainty associated with the shaded-cell voltage is obtained via standard error propagation as

$$u_{\mathrm{V,cell,sh}}(I) = \sqrt{u_{V,sh}^2 + u_{V,irr}^2}\,. \tag{6.10}$$

  This expression accounts for the interpolation of the generic current I from the uniformly irradiated curve between the points with currents I_a and I_b on the partially shaded curve. The total relative uncertainty on the shaded-cell voltage is $\pm 0.756\%$, whereas the total relative uncertainty on current is $\pm 0.5\%$.

6.1.4 Differential Curve Extraction for the Commercial PV Module

Commercial PV modules comprise multiple strings in parallel, each string being formed by series-connected cells equipped with bypass diodes. Consequently, the

extraction of the shaded-cell I–V curve requires a more articulated procedure, which is described in the following steps.

- **Initialisation of parameters.** Two initial parameter sets are defined, one for an irradiated cell and one for a shaded cell. Each set corresponds to the five-parameter single-diode model and includes the photogenerated current I_{ph}, the reverse saturation current I_0, the diode ideality factor n, the series resistance R_{s}, and the shunt resistance R_{sh}. The parameters of the irradiated cell can be estimated numerically from the uniformly irradiated I–V curve. By contrast, the shaded-cell parameters require additional assumptions, and some of them can be inferred from the portion of the partially shaded curve where the bypass diodes are inactive. To this end, the relevant segment of the measured curve is selected and translated towards the origin of the voltage axis by subtracting the minimum voltage from all sampled voltages. The photogenerated current is approximated by the short-circuit current of the shifted curve, whereas the ideality factor n is estimated numerically. The resistances are obtained experimentally from the slopes of the partially shaded I–V curve, namely $R_{\mathrm{sh}} \approx -1/m$ at short circuit and $R_{\mathrm{s}} \approx -1/m$ at open circuit, where m denotes the local slope of the I–V characteristic.

- **String-level I–V curve calculation.** The shaded-cell I–V curve is first computed by solving the single-diode equation with the shaded-cell parameters. This curve is then combined with the I–V curve of the remaining $N_{\mathrm{s,str}} - 1$ irradiated cells in the string. For each current sample I_k, the string voltage is obtained as the sum of the shaded-cell voltage and the voltage of the $N_{\mathrm{s,str}} - 1$ irradiated cells,

$$V_{\mathrm{str},k} = V_{\mathrm{shd},k} + V_{(N_{\mathrm{s,str}}-1),k}\,, \tag{6.11}$$

  where $V_{\mathrm{str},k}$ denotes the voltage of the string containing the shaded cell at current I_k.

- **Parallel connection including the shaded string.** The I–V curve of the parallel association between the shaded string and one fully irradiated string of $N_{\mathrm{s,str}}$ cells is constructed by summing the string currents at each common voltage V_j, namely

$$I_{\mathrm{par},j} = I_{\mathrm{str,shd},j} + I_{\mathrm{str,irr},j}\,, \tag{6.12}$$

where $I_{\mathrm{par},j}$ is the current of the partially shaded parallel group at voltage V_j and $I_{\mathrm{str,shd},j}$ and $I_{\mathrm{str,irr},j}$ are the currents of the shaded and irradiated strings, respectively.

- **Parallel connections of the irradiated strings.** The I–V curve of the remaining fully irradiated strings, which are paired in parallel, is obtained by current summation at each voltage as

$$I_{\mathrm{par},j} = I_{\mathrm{str,shd},j} + I_{\mathrm{str,irr},j}\,, \tag{6.13}$$

with the understanding that in this step both contributing strings are fully irradiated.

- **Complete circuit construction.** The module I–V curve is assembled by combining the partially shaded parallel group with the parallel groups of fully irradiated strings. Each parallel group of two strings is connected to a bypass diode. The resulting parallel groups are then connected in series to yield the overall module characteristic. In the voltage region where a bypass diode conducts due to shading, the diode forward drop is subtracted. The estimated module voltage at sample index m can be written compactly as

$$V_{\mathrm{mod},m} = \begin{cases} \sum_{i=1}^{N_{\mathrm{irr}}} V_{\mathrm{irr},i} + V_{\mathrm{par},j}, & V_{\mathrm{bd}} < V_f \\ \sum_{i=1}^{N_{\mathrm{irr}}} V_{\mathrm{irr},i} - V_{\mathrm{bd}}, & V_{\mathrm{bd}} \geq V_f \end{cases} \tag{6.14}$$

where V_{bd} is the bypass-diode voltage, N_{irr} is the number of fully irradiated strings, and V_f is the diode forward, or activation, voltage.

- **Iterative parameter adjustment.** The calculated module I–V curve under partial shading is compared with the corresponding measurement. Parameter estimation proceeds by minimising the *RMSE* between the model prediction and the measurement, and the *RMSE* threshold is used as a convergence criterion. Formal definitions of *RMSE*, MPP deviation, *NMAE*, and *NMBE* are provided in Section 6.1.1. In this work, the iterative adjustment explores I_0 in the range from 1 nA to 1 µA for uniformly irradiated cells and from 1 µA to 100 µA for shaded cells until convergence is achieved. The following steps summarise the adopted update policy.

- Update of I_{ph}. The photogenerated current is scaled proportionally to the irradiance level for both mini-modules and commercial modules.
- Update of n. The ideality factor is treated as invariant between the mini-modules and the commercial modules.
- Update of R_{s}. The series resistance is inferred from the open-circuit region of the commercial-module I–V curve and approximated as $R_{\mathrm{s}} \approx -1/m_{\mathrm{oc}}$, where m_{oc} is the local slope near open circuit.
- Update of R_{sh}. The shunt resistance is inferred from the short-circuit region and approximated as $R_{\mathrm{sh}} \approx -1/m_{\mathrm{sc}}$, where m_{sc} is the local slope near short circuit.
- Update of I_0. The reverse saturation current is reduced iteratively in decrements of $\Delta I_0 = 1\,\mathrm{nA}$ until the *RMSE* falls below one percent.

Figure 6.3 reports the flowchart that summarises the iterative parameter adjustment.

6.2 Description of the Acquisition Systems

The analysis reported in this work draws on measurements gathered using two distinct acquisition systems at Politecnico di Torino, Turin, Italy. In particular, the electrical performance of the PV mini-modules was measured with an electronic-load-based setup, whereas the commercial PV modules under test were characterised using an experimental setup that exploits a capacitive load. Both measurement systems are described in detail in Chapter 5.

6.2.1 PV Modules Under Test

The datasets considered in this study comprise measurements on PV mini-modules and on commercial modules, all employing monocrystalline silicon half-cell technology. The two acquisition systems used to gather these datasets are described in the preceding subsections. The commercial devices are Hanwha Qcells modules, model Q.PEAK DUO M-G11 400. Each commercial module is organised into three series-connected subunits. Each subunit consists of the parallel association of one

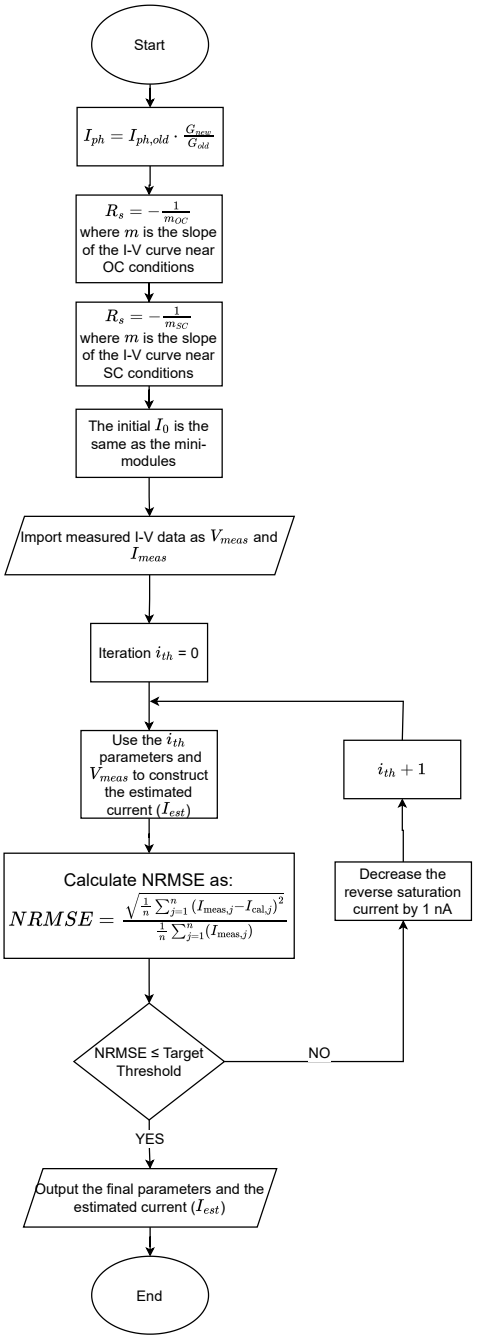

Fig. 6.3 Flowchart of the iterative adjustment of the parameters.

bypass diode and two strings. Each string contains 18 half-cells connected in series. In contrast, each mini-module comprises a single string of four series-connected half-cells without bypass diodes. Figure 6.4 illustrates the electrical interconnections for the mini-modules and the commercial modules under test, and also shows representative photographs of both device types. The rated electrical specifications of the tested devices at standard test conditions, STC, are listed in Table 6.1.

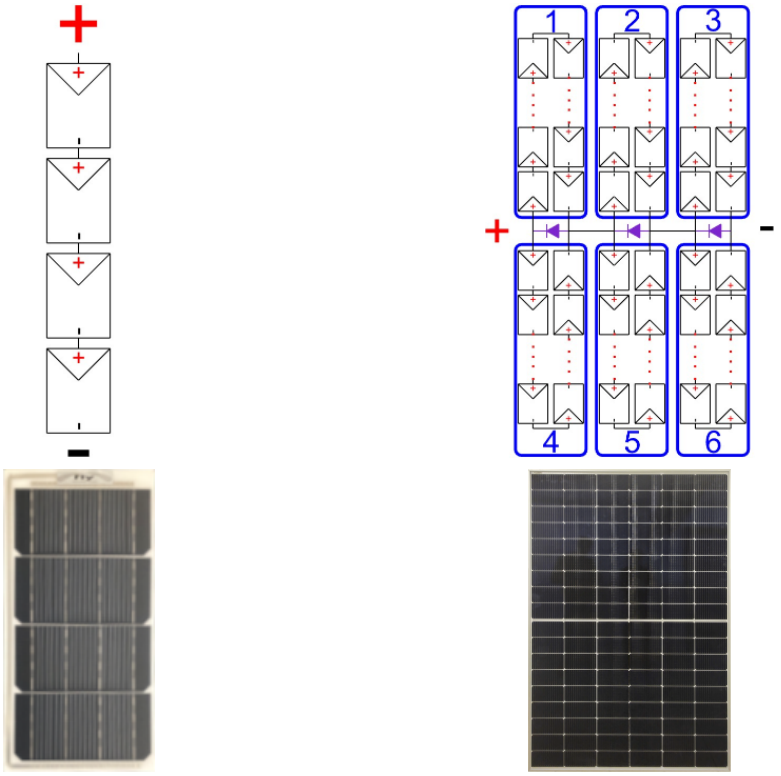

(a) (b)

Fig. 6.4 Electrical connections of PV cells for the mini-modules 6.4a and for the commercial modules 6.4b under test.

6.3 Results

6.3.1 Results for the Mini-Module

A first outcome of this study is the experimental validation of the indirect "One Module, Two Tests" procedure. Figure 6.5 compares the I–V characteristic of a single

Table 6.1 Electrical Specifications of the PV Modules Under Test at STC

Electrical quantity	Mini-modules	Q.PEAK DUO M-G11 400
Open-circuit voltage	2.40	37.16 V
Short-circuit current	3.51	13.54 A
Voltage at MPP	1.72	31.00 V
Current at MPP	3.23	12.90 A
Maximum power	5.56	400 W
Efficiency	–	$\geq 20.8\%$

shaded cell in a mini-module obtained via the indirect method, yellow markers, with that obtained via the direct "Two Modules, One Test" approach, blue markers. The comparison confirms the effectiveness of the indirect method. Although the indirect reconstruction shows a slightly larger spread in current than the direct measurement, the absolute discrepancies remain very small and never exceed 2.48 mA.

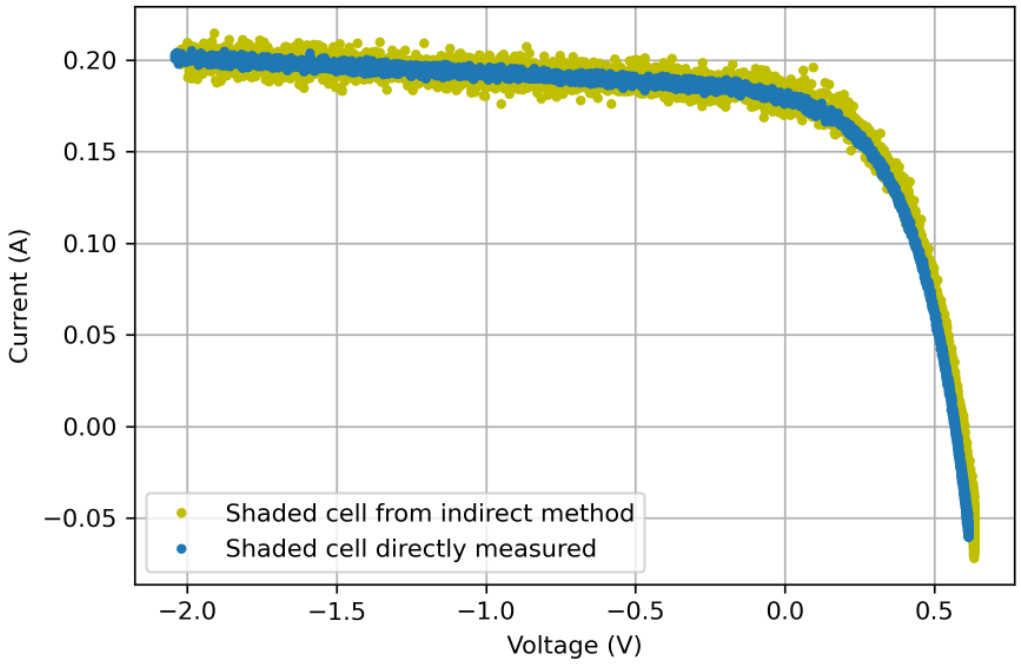

Fig. 6.5 Comparison between I–V curves of a single shaded cell obtained with the direct and indirect methods.

Subsequently, the parameters of the equivalent circuits were estimated for ten flexible photovoltaic mini-modules comprising four half-cells, both under natural sunlight and under partial shading. In particular, parameters were numerically identi-

fied for four models. The 3P, I_{ph}, I_0, n. The 4P, I_{ph}, I_0, n, R_s. The 5P, $I_{ph}, I_0, n, R_s, R_{sh}$. Finally, the 7P, $I_{ph}, I_{0,1}, n_1, I_{0,2}, n_2, R_s, R_{sh}$. The resulting I–V reconstructions were compared to identify the model offering the best compromise between accuracy and computational cost for both illumination conditions. For each circuit, Table 6.2 reports, over the ten mini-modules, the median Normalised Root Mean Square Error, *NRMSE*, the median Normalised Mean Absolute Error, *NMAE*, the median Normalised Mean Bias Error, *NMBE*, the deviation at the Maximum Power Point, MPP, and the execution time.

Across both conditions, the 3P model was the least accurate, with median *RMSE* values of 8.88% and 6.53% and median MPP deviations of 5.54% and 15.8% under uniform irradiance and partial shading, respectively. Figure 6.6 corroborates these findings by showing, for a representative cell from module #2 at high irradiance, the measured I–V curve alongside modelled curves. The 3P curve exhibits the largest departures from the measurements. Conversely, its parameter estimation time was the lowest, below one second in both scenarios.

Although the 7P model entailed the highest computational burden, well above 15 s per fit, it did not deliver the best accuracy in either scenario. As expected, under uniform irradiance it achieved the lowest medians for *RMSE* and MPP deviation, 1.00% and 1.81% respectively, but these were essentially comparable to those of 4P and 5P. Under partial shading, 7P did not outperform 5P. Both yielded a median *RMSE* of 1.41%, while 5P achieved a lower median MPP deviation of 0.79%. These results do not support the routine use of 7P in fault-detection contexts, because its substantially higher computation time is not balanced by a clear accuracy gain. Under uniform irradiance its performance is comparable to simpler models, and under shading it is not superior.

Under uniform irradiance, 4P and 5P delivered similar medians for *RMSE* and MPP deviation, both around one and two percent, respectively, while 5P required roughly twice the execution time of 4P, about 8 s versus 4 s. Accordingly, in uniform conditions, 4P constitutes the most favourable compromise, combining near-best accuracy with modest runtime. Under partial shading, however, 4P's behaviour approaches that of 3P rather than 5P. For the same representative cell considered in Figure 6.6, Figure 6.7 shows the measured I–V curve under mismatch together with the model fits. Here, the 4P approximation is as poor as that of 3P, reflecting the importance of R_{sh} under shading. Although the median MPP deviation of 4P

is comparable to, and even slightly lower than, that of 5P, 0.75% versus 0.79%, its *RMSE* is approximately five times larger. Therefore, under shading, 5P offers a superior trade-off by markedly improving the full-curve accuracy at an acceptable computational cost.

The *NMAE* and *NMBE* medians in Table 6.2 support the same conclusions. Under uniform irradiance, 4P, 5P, and 7P are nearly equivalent with *NMAE* values of 1.16%, 1.11%, and 1.08% and *NMBE* values of 0.50%, 0.49%, and 0.48%, respectively. Under partial shading, 4P is substantially less accurate with $NMAE = 7.65\%$ and $NMBE = 0.25\%$, whereas 5P and 7P achieve $NMAE = 1.19\%$ and $NMBE \approx -0.15\%$.

Figures 6.8 and 6.9 display, for uniform irradiance and partial shading respectively, the distributions of MPP deviation and *RMSE* together with their relationships to computation time. Each figure comprises a matrix of plots. Diagonal panels show kernel density estimates for *RMSE*, MPP deviation, and runtime, and off-diagonal panels show pairwise correlations. For the panels relating error to time, the optimal region is the bottom left, combining low error with low runtime. By this criterion, the 3P and 7P models lie far from optimal due to poor accuracy, 3P, or excessive cost, 7P, across both conditions. Under uniform irradiance, 4P lies closest to the optimal region.

Under partial shading, the picture changes as indicated by Figure 6.9. The *RMSE* distribution for 4P is broad with a median above that of 3P. Even though 4P's MPP deviation distribution resembles that of 5P, its overall *I*–*V* fit is much worse. Thus, in shading scenarios, 5P is the preferred model, offering the best balance of accuracy and computational effort.

6.3.2 Results for the Commercial PV Module

The results in this subsection refer to the five-parameter single-diode model. This choice is motivated by the mini-module study, where 5P offered the most favourable balance of accuracy and computational time under partial shading. Furthermore, parameter estimation under shading was performed for one cell per substring in each of the two commercial modules. Table 6.3 summarises the median, minimum, and maximum values of the 5P parameters identified for a shaded half-cell. The series and shunt resistances were taken from the shaded-cell characterisation of the

Table 6.2 Median results for the mini-modules under uniform irradiance and partial shading.

Mini-modules under uniform irradiance

Parameter	3P	4P	5P	7P
RMSE(%)	8.88	1.20	1.05	1.00
NMAE (%)	8.38	1.16	1.11	1.08
NMBE (%)	-3.19	0.50	0.49	0.48
Deviation at MPP (%)	5.54	2.04	2.14	1.81
Execution time (s)	1.1	4.1	7.8	36.2

Mini-modules under partial shading

Parameter	3P	4P	5P	7P
RMSE(%)	6.52	8.73	1.41	1.41
NMAE (%)	5.79	7.65	1.19	1.19
NMBE (%)	0.82	0.25	-0.15	-0.13
Deviation at MPP (%)	16.1	0.72	0.79	1.08
Execution time (s)	0.8	1.4	4.44	15.9

Table 6.3 Equivalent-circuit parameters for the shaded half-cell of commercial modules.

Parameter	Median	Min	Max
I_{ph} (A)	0.56	0.46	0.86
I_0 (μA)	1.84	0.88	4.26
n (-)	1.48	1.48	1.48
R_s (Ω)	0.042	0.042	0.042
R_{sh} (Ω)	50.8	50.8	50.8

mini-modules, yielding $R_{\text{s}} \approx 42$ mΩ and $R_{\text{sh}} \approx 50$ Ω. The Schottky bypass diodes that protect shaded strings exhibit a typical forward drop between 0.55 and 0.60 V, and a value of $V_f = 0.60$ V was adopted.

For comparison, Table 6.4 reports the corresponding 5P parameters for an irradiated half-cell. The influence of shading on the parameters is as follows. The reverse saturation current increases by roughly two orders of magnitude, from tens of nA to µA, and the series resistance increases by about one order of magnitude, from mΩ to tens of mΩ. By contrast, the ideality factor shows a modest rise from 1.36 to 1.48, and the shunt resistance drops markedly from the order of kΩ to the order of tens of Ω. These trends are consistent with the literature [45], as reduced

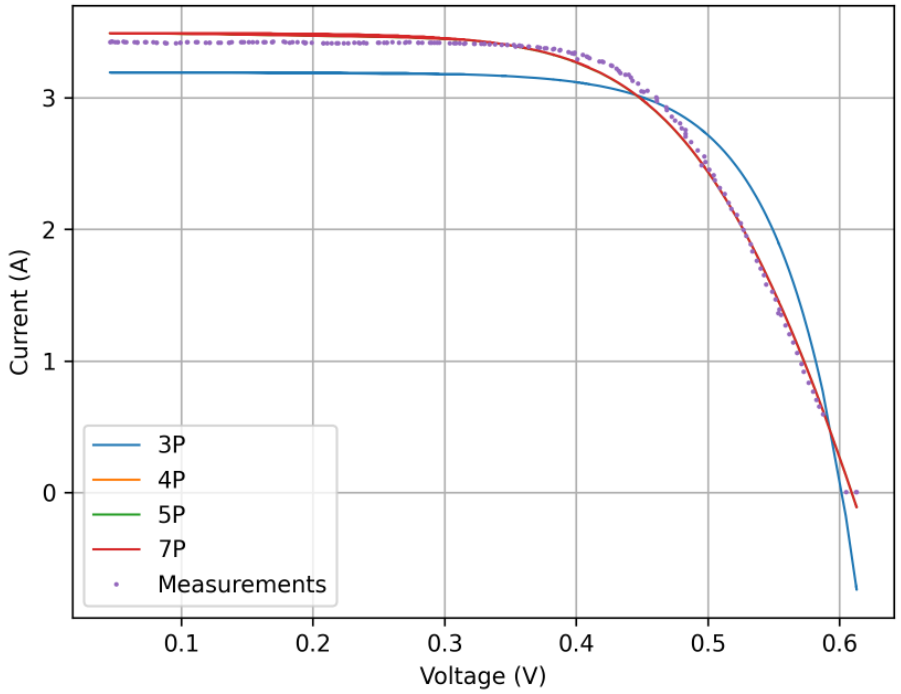

Fig. 6.6 Measured I–V curve and model reconstructions under sunlight for one cell of module #2.

irradiance enhances recombination and resistive effects. It is worth noting that the I–V measurements under uniform irradiance and partial shading were performed within less than one minute. Therefore, although a shaded cell would generally warm relative to an irradiated one, the short interval supports the assumption of approximately constant cell temperature.

Figure 6.10 illustrates simulated I–V curves under several operating conditions. The blue trace corresponds to a string with one shaded cell among eighteen cells, that is, seventeen irradiated and one shaded. The red trace represents the entire string under partial shading. The orange and green traces correspond to a single cell and a full string, respectively, under uniform irradiance. Finally, the purple trace shows the parallel combination of one irradiated string with one partially shaded string.

Figure 6.11 compares the simulated I–V curve of the complete commercial module, obtained using the parameters identified by the procedure in Section 6.1,

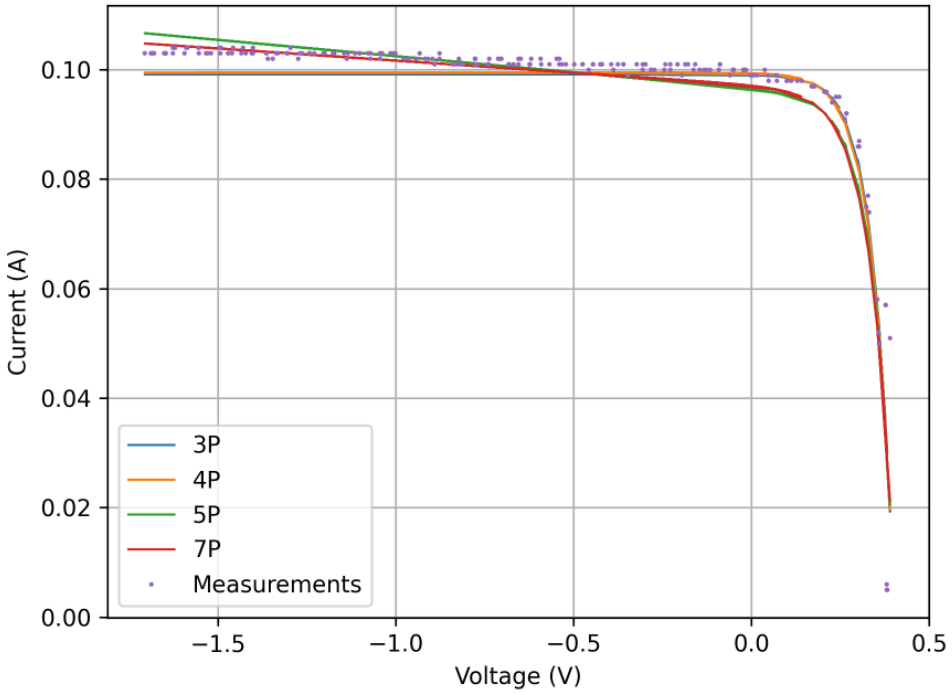

Fig. 6.7 Measured I–V curve and model reconstructions under partial shading for one cell of module #2.

red line, with the experimental data, green markers. The agreement is good over the full operating range.

Table 6.5 summarises the median, minimum, and maximum values of the indicators defined in Section 6.1.1. All median values are below 0.5%, and the observed ranges are narrow, spanning approximately from -0.55% to $+1.5\%$. These findings support the robustness of the 5P model and indicate the absence of material systematic bias in parameter identification under partial shading.

Finally, the parameter estimation based on the 5P model required less than ten seconds per shaded cell on a standard laptop. This computational demand is compatible with real-time applications for partial-shading detection in PV systems. The intended application is an algorithm that discriminates between healthy and faulty modules on the basis of the inferred equivalent-circuit parameters. The algorithm will periodically update parameters with a target cadence between one and five minutes without disrupting plant operation. Accordingly, the computational load

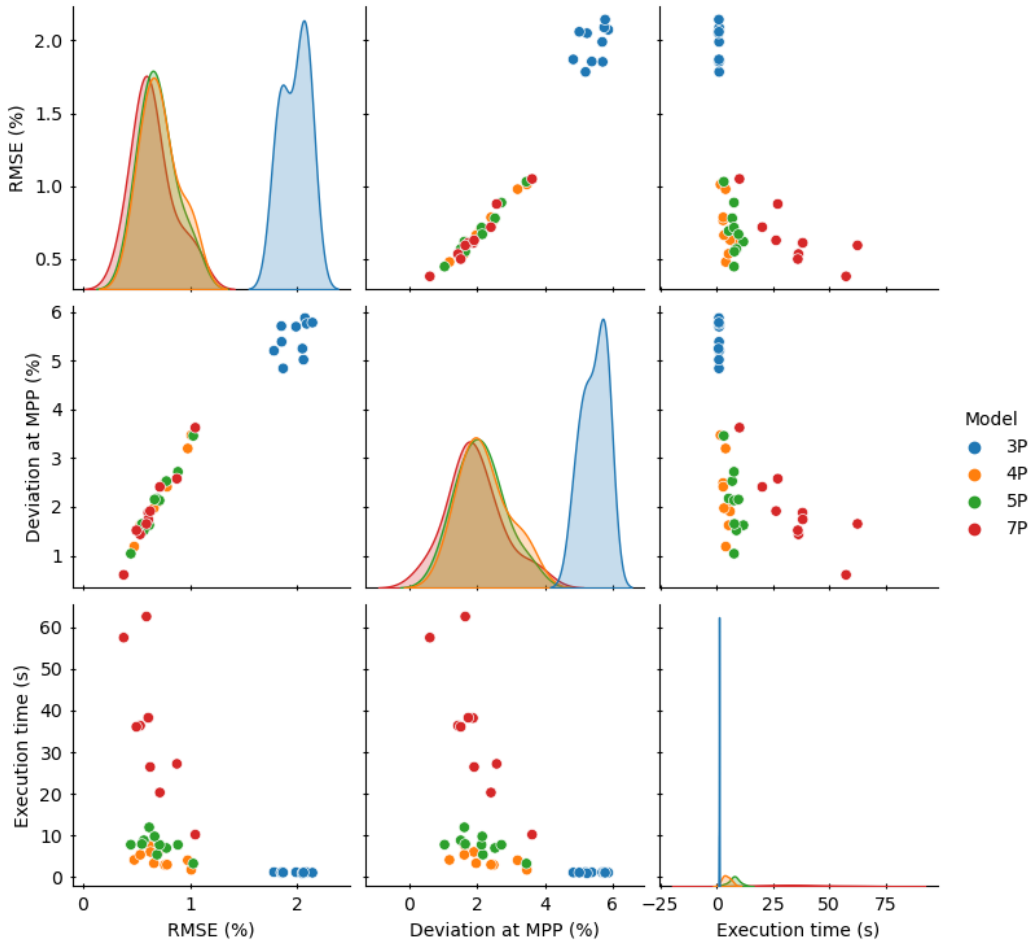

Fig. 6.8 Error and runtime distributions for modules under uniform irradiance.

of the estimation procedure is suitable for deployment within embedded monitoring platforms.

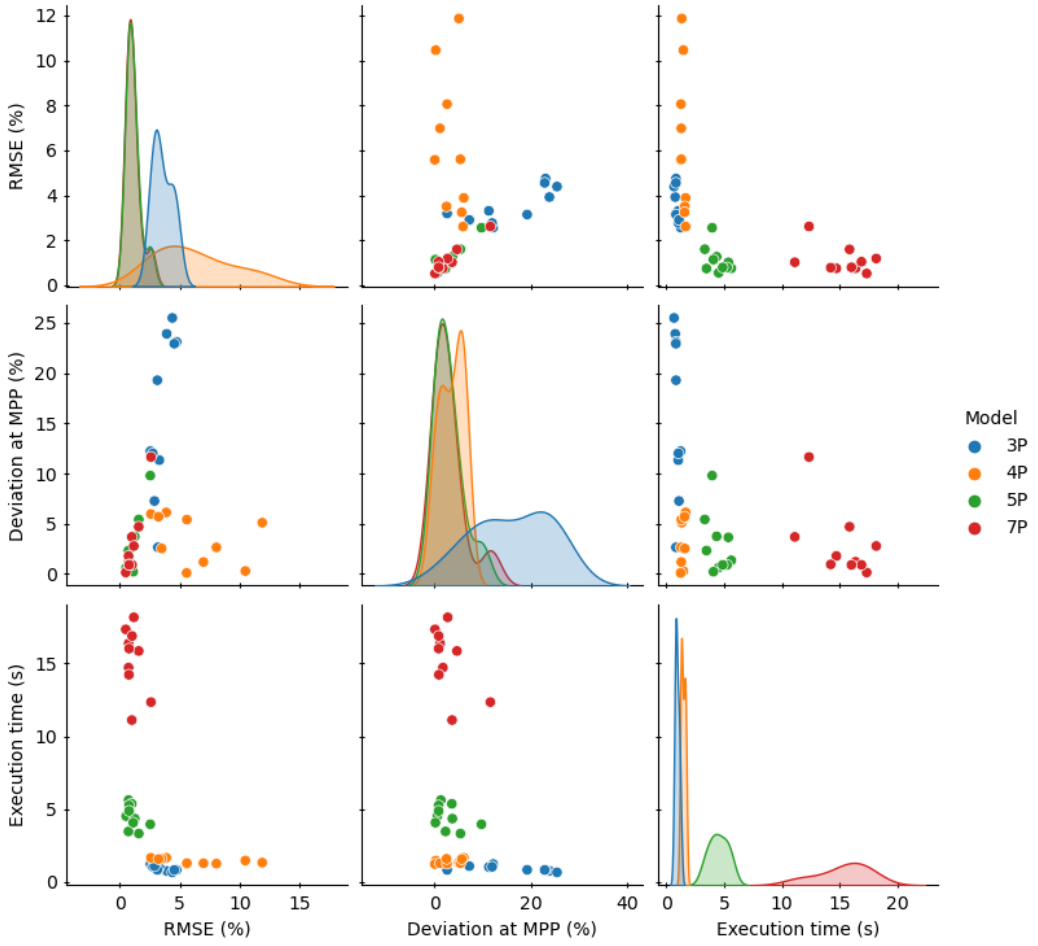

Fig. 6.9 Error and runtime distributions for modules under partial shading.

Table 6.4 Equivalent-circuit parameters for the irradiated half-cell of commercial modules.

Parameter	Median	Min	Max
I_{ph} (A)	6.19	6.09	6.69
I_0 (μA)	0.057	0.033	0.058
n (-)	1.36	1.36	1.36
R_s (Ω)	0.0035	0.0035	0.0035
R_{sh} (Ω)	9511	9511	9511

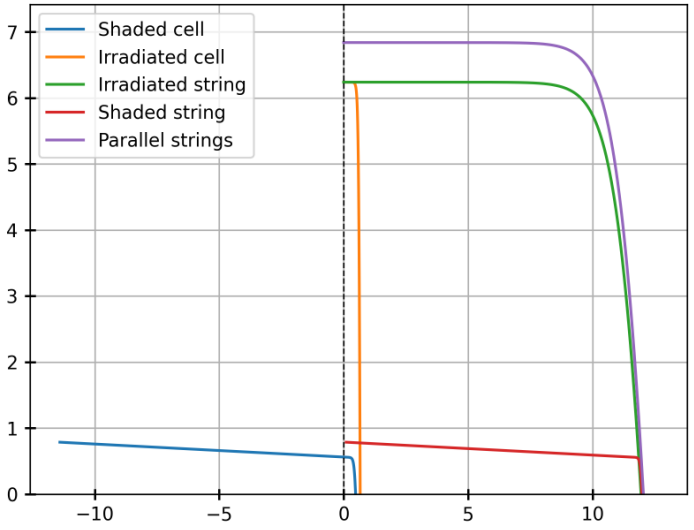

Fig. 6.10 Extraction of the shaded-cell I–V curve from measured string characteristics.

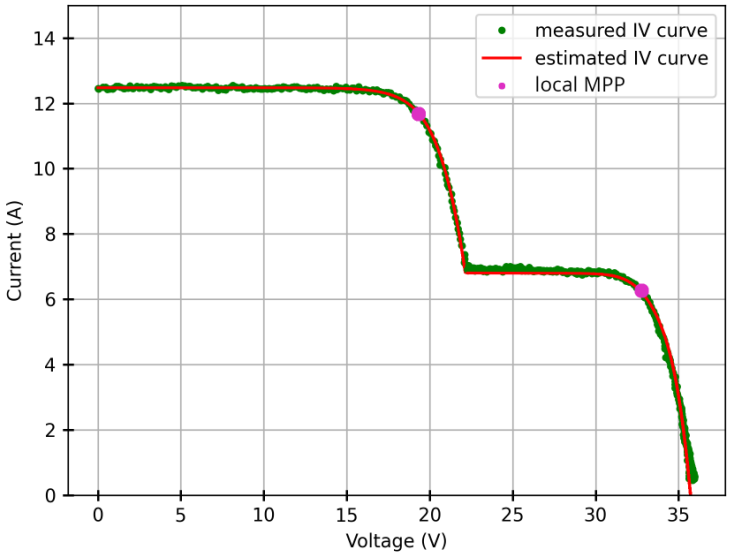

Fig. 6.11 Measured and reconstructed I–V curve of the full commercial module under partial shading using the 5P model.

Table 6.5 *NRMSE*, *NMBE*, *NMAE*, and MPP deviation for the commercial module, 5P model.

Metric	Median	Min	Max
RMSE(%)	0.39	0.15	0.63
NMBE (%)	-0.34	-0.55	-0.12
NMAE (%)	0.34	0.13	0.55
Deviation at MPP (%)	0.074	0.0076	1.22

Chapter 7

D-Optimal FIM-Based Parameter Estimation of Photovoltaic Modules

Positioning with respect to the state of the art

Parameter estimation for photovoltaic equivalent-circuit models has been the subject of extensive research over the past two decades. The proposed methods can be broadly grouped into three families: analytical approaches based on characteristic-point extraction [3–6], numerical iterative methods such as the Levenberg–Marquardt and trust-region algorithms [9, 10], and metaheuristic techniques including genetic algorithms, particle swarm optimisation, differential evolution, and their hybrids [1, 10, 13, 46]. Comprehensive surveys of these approaches are available in [47, 48, 46], which together benchmark over a hundred algorithms on standard cell datasets.

Despite the breadth of this literature, a fundamental limitation is shared by virtually all existing methods: the choice of how to sample the I–V curve is either left to the practitioner or implicitly assumed to be uniform in voltage or current. No existing work rigorously addresses the question of *which operating points along the I–V curve are most informative for parameter estimation*, and how the sampling distribution should be adapted to maximise the precision of the identified parameters. This is a consequential omission, because the amount of information contributed

by each measurement point is not uniform along the I–V characteristic: it varies with the operating regime and depends on the sensitivity of the model output to each parameter at that point. Uniform sampling therefore leads to a systematic and avoidable waste of measurement resources.

In other fields involving nonlinear parameter estimation from electrical measurements — most notably lithium-ion cell modelling — this problem has been addressed through estimation-theoretic tools: the Fisher Information Matrix (FIM) and the Cramér–Rao Lower Bound (CRLB) [18, 19]. The FIM quantifies the information content of a set of measurements with respect to the model parameters, and the CRLB provides the theoretical minimum variance achievable by any unbiased estimator. D-optimal experimental design, which selects the measurement locations that maximise the determinant of the FIM, has proven particularly effective in reducing the volume of the parameter confidence ellipsoid in these contexts [49].

However, the application of these estimation-theoretic tools to photovoltaic equivalent-circuit models has not been explored prior to the present work. In particular, the formulation of a D-optimal sampling strategy in the current domain — rather than the voltage domain, which is more natural for electronic load measurements — and its extension to the non-smooth, piecewise I–V characteristics arising under partial shading due to bypass diode activation, are entirely novel contributions. Two aspects distinguish the proposed approach from a straightforward transfer of the D-optimal methodology from other domains. First, the FIM is derived simultaneously for both the current-imposed and the voltage-imposed measurement modes, yielding a compact expression for the incremental information contributed by each sample point that accounts for noise in both observables. Second, the framework is applied under partial shading conditions, where the I–V curve exhibits multiple plateaux and non-smooth transitions that concentrate the information content in specific, non-obvious regions of the operating range; in this regime, the benefit of optimal sampling over uniform sampling is shown to be substantially larger than under uniform irradiance.

The present chapter introduces this framework, derives the theoretical foundations, and validates the method through Monte Carlo simulations on synthetic data and experimental campaigns on five commercial PV modules of different technologies under both uniform and partially shaded conditions.

This chapter presents a methodology for the optimal estimation of photovoltaic module parameters based on the Fisher Information Matrix, with particular emphasis on D-optimal experimental design for I–V curve sampling and on the theoretical limits imposed by the Cramér–Rao Lower Bound.

7.1 Model and I–V Curve Sampling Optimization Method

7.1.1 General Assumptions of the Procedure

The following assumptions are imposed.

1. The voltage and current measurement noise models are known and are Independent and Identically Distributed (IID).
2. A specific parametric equivalent-circuit model is selected a priori by the modeller.
3. The sampling is sufficiently fast that T_{c} and the irradiance G can be treated as known, unbiased, and noise-free constants.
4. The methodology is applicable in laboratory and field conditions, provided irradiance is adequate to represent both uniform and partially shaded operation [16].

In realistic settings, temperature and irradiance may be uncertain, but here they are treated as exogenous inputs rather than decision variables. Because the proposed method optimizes the sampling of electrical variables only, uncertainties in T_c and G fall outside the optimization scope and are not mitigated by the algorithm. Moreover, complete I–V acquisition typically requires less than 100 ms. Over such a short interval, T_{c} and G can be regarded as constant, which justifies the assumption of unbiased, noiseless inputs for the present analysis.

Let the sampling points (I,V) be ordered by increasing current, from open circuit to short circuit. Define the column vector $\mathbf{m}$ as the stack of the model-predicted

currents and voltages at the noiseless operating points, i.e.,

$$\begin{aligned}\mathbf{m} = [&I_1(\theta, \boldsymbol{v}), V_1(\theta, \boldsymbol{i}), \ldots, \\ &I_i(\theta, \boldsymbol{v}), V_i(\theta, \boldsymbol{i}), \ldots, \\ &I_N(\theta, \boldsymbol{v}), V_N(\theta, \boldsymbol{i})]^\top.\end{aligned} \tag{7.1}$$

Analogously, the vector of measurements is $\tilde{\mathbf{m}} = [\tilde{I}_1, \tilde{V}_1, \ldots, \tilde{I}_i, \tilde{V}_i, \ldots, \tilde{I}_N, \tilde{V}_N]^\top$. The circuit parameters are estimated as $\hat{\theta} = [\hat{I_{\mathrm{ph}}}, \hat{I}_0, \hat{n}, \hat{R}_{\mathrm{s}}, \hat{R}_{\mathrm{sh}}]^\top$ via a constrained least-squares problem [10], with parameter bounds $\theta_{\min}$ and $\theta_{\max}$ taken from the literature. Under the IID noise assumption, the residuals are weighted by the inverse measurement covariance $\tilde{\mathbf{Q}}$, arranged block-diagonally as $\tilde{\mathbf{Q}} = \mathrm{diag}(\tilde{\mathbf{Q}}_1, \ldots, \tilde{\mathbf{Q}}_{\mathrm{N}})$, with $\tilde{\mathbf{Q}}_i = \mathrm{diag}(\sigma_{\mathrm{V}}^2, \sigma_{\mathrm{I}}^2)$, as detailed in Section 7.1.2.

The estimator is thus

$$\begin{aligned}\hat{\theta} = \arg\min_{\theta} &(\tilde{\mathbf{m}} - \mathbf{m})^\top \tilde{\mathbf{Q}}^{-1} (\tilde{\mathbf{m}} - \mathbf{m}), \\ &\text{s.t.} \quad \theta_{\min} \le \theta \le \theta_{\max}.\end{aligned} \tag{7.2}$$

7.1.2 Probabilistic Metrology Aspects

Following [18], we derive the Fisher Information by assuming Gaussian measurement noise. For commercial instruments, datasheets often specify voltage and current uncertainties, Δ_V and Δ_I, as percentages of the Full Scale Range (FSR). Under the three-sigma rule, an unbiased error lies within the 99.73% interval, and the corresponding standard deviations are approximated by $\sigma_{\mathrm{V}} = \Delta_V/3$ and $\sigma_{\mathrm{I}} = \Delta_I/3$. Hence $\tilde{\mathbf{Q}}_i = \mathrm{diag}(\sigma_{\mathrm{V}}^2, \sigma_{\mathrm{I}}^2)$ for all $i = 1, \ldots, \mathrm{N}$.

The cost for N measurements becomes

$$\hat{\theta} = \arg\min_{\theta} \sum_{i=1}^{\mathrm{N}} \left(\begin{bmatrix} \tilde{I}_i \\ \tilde{V}_i \end{bmatrix} - \begin{bmatrix} I_i(\theta, V) \\ V_i(\theta, I) \end{bmatrix} \right)^\top \tilde{\mathbf{Q}}_i^{-1} \left(\begin{bmatrix} \tilde{I}_i \\ \tilde{V}_i \end{bmatrix} - \begin{bmatrix} I_i(\theta, V) \\ V_i(\theta, I) \end{bmatrix} \right). \tag{7.3}$$

7.1.3 Cramér–Rao Lower Bound for PV Circuit Parameters

To quantify the best achievable accuracy in parameter recovery, we compute the Cramér–Rao Lower Bound (CRLB). Let $\mathbf{d}_{\theta,\mathbf{v}} = \tilde{\mathbf{i}} - \mathbf{i}(\theta, \mathbf{v})$ and $\mathbf{d}_{\theta,\mathbf{i}} = \tilde{\mathbf{v}} - \mathbf{v}(\theta, \mathbf{i})$ be residual vectors at the sampled operating points. Denote by $\mathscr{I}$ and $\mathscr{V}$ the random

vectors of measured currents and voltages, respectively. With Gaussian noise, the conditional densities read

$$\mathrm{PDF}(\mathscr{V}|\theta,\boldsymbol{i}) = \frac{1}{\sqrt{(2\pi)^{\mathrm{N}}\det\tilde{\mathbf{Q}}}}\exp\!\Big(-\tfrac{1}{2}\mathbf{d}_{\theta,\mathbf{i}}^{\top}\tilde{\mathbf{Q}}^{-1}\mathbf{d}_{\theta,\mathbf{i}}\Big), \tag{7.4}$$

$$\mathrm{PDF}(\mathscr{I}|\theta,\boldsymbol{v}) = \frac{1}{\sqrt{(2\pi)^{\mathrm{N}}\det\tilde{\mathbf{Q}}}}\exp\!\Big(-\tfrac{1}{2}\mathbf{d}_{\theta,\mathbf{v}}^{\top}\tilde{\mathbf{Q}}^{-1}\mathbf{d}_{\theta,\mathbf{v}}\Big). \tag{7.5}$$

The log-likelihoods are

$$\begin{aligned} L(\theta,\boldsymbol{i}|\mathscr{V}) &= -\tfrac{\mathrm{N}}{2}\ln 2\pi - \tfrac{1}{2}\ln\det\tilde{\mathbf{Q}} - \tfrac{1}{2}\boldsymbol{d}_{\theta,\boldsymbol{i}}^{\top}\tilde{\mathbf{Q}}^{-1}\boldsymbol{d}_{\theta,\boldsymbol{i}},\\ L(\theta,\boldsymbol{v}|\mathscr{I}) &= -\tfrac{\mathrm{N}}{2}\ln 2\pi - \tfrac{1}{2}\ln\det\tilde{\mathbf{Q}} - \tfrac{1}{2}\boldsymbol{d}_{\theta,\boldsymbol{v}}^{\top}\tilde{\mathbf{Q}}^{-1}\boldsymbol{d}_{\theta,\boldsymbol{v}}. \end{aligned} \tag{7.6}$$

For the first derivatives with respect to θ_j, $j = 1,\ldots,M$, we note that $\tilde{\mathbf{Q}}$ is constant, which annuls the trace terms. Thus,

$$\frac{\partial L(\theta,\boldsymbol{i}|\mathscr{V})}{\partial\theta_j} = \frac{\partial\boldsymbol{\varepsilon}^{\top}(\theta,\boldsymbol{i})}{\partial\theta_j}\,\tilde{\mathbf{Q}}^{-1}\,\boldsymbol{d}_{\theta,i}, \qquad \frac{\partial L(\theta,\boldsymbol{v}|\mathscr{I})}{\partial\theta_j} = \frac{\partial\boldsymbol{\varepsilon}^{\top}(\theta,\boldsymbol{v})}{\partial\theta_j}\,\tilde{\mathbf{Q}}^{-1}\,\boldsymbol{d}_{\theta,v}. \tag{7.7}$$

Let $\mathscr{F}\in\mathbb{R}^{M\times M}$ denote the Fisher Information Matrix, with (k,ℓ) entry

$$\mathscr{F}(\theta)_{k,\ell} = \mathbb{E}\left[\frac{\partial L(\theta,\boldsymbol{i}|\mathscr{V})}{\partial\theta_k}\,\frac{\partial L(\theta,\boldsymbol{i}|\mathscr{V})}{\partial\theta_\ell} + \frac{\partial L(\theta,\boldsymbol{v}|\mathscr{I})}{\partial\theta_k}\,\frac{\partial L(\theta,\boldsymbol{v}|\mathscr{I})}{\partial\theta_\ell}\right]. \tag{7.8}$$

A compact expression is [19]

$$\mathscr{F}(\theta)_{k,\ell} = \frac{1}{\sigma_{\mathrm{I}}^2}\sum_{i=1}^{\mathrm{N}}\frac{\partial I(\theta,V_i)}{\partial\theta_k}\frac{\partial I(\theta,V_i)}{\partial\theta_\ell} + \frac{1}{\sigma_{\mathrm{V}}^2}\sum_{i=1}^{\mathrm{N}}\frac{\partial V(\theta,I_i)}{\partial\theta_k}\frac{\partial V(\theta,I_i)}{\partial\theta_\ell}. \tag{7.9}$$

Ordering the N samples by increasing V_i, the total information accumulates as

$$\mathscr{F}(\theta)_{k,\ell} = \sum_{i=1}^{\mathrm{N}}\Delta\mathscr{F}_i(\theta)_{k,\ell}. \tag{7.10}$$

Each sample contributes differently to each parameter [19]. For a generic point (I,V), the incremental contribution is

$$\Delta\mathscr{F}(\theta)_{k,\ell} = \frac{1}{\sigma_{\mathrm{I}}^2}\frac{\partial I(\theta,V)}{\partial\theta_k}\frac{\partial I(\theta,V)}{\partial\theta_\ell} + \frac{1}{\sigma_{\mathrm{V}}^2}\frac{\partial V(\theta,I)}{\partial\theta_k}\frac{\partial V(\theta,I)}{\partial\theta_\ell}. \tag{7.11}$$

The CRLB is obtained by evaluating $\mathscr{F}$ at the true parameters θ^* (unknown in practice[1]). Denote $\mathscr{F}^* = \mathscr{F}(\theta)\big|_{\theta=\theta^*}$, and set CRLB $:= \mathscr{F}^{*-1}$. The minimum achievable variance for each parameter obeys

$$\sigma_{\theta_i}^2 := \mathrm{Var}(\theta_i) \geq \mathscr{F}_{i,i}^{*-1}, \quad i = 1,\ldots,M. \tag{7.12}$$

7.1.4 Least-Variance Identification via D-Optimal Design

We aim to select measurement points that maximize global parameter informativeness by maximizing $\det(\mathscr{F})$, the D-optimality criterion. The matrix $\mathscr{F}$ is symmetric, real, positive semidefinite, and (under identifiability) invertible, so its eigenvalues are nonnegative and $\det(\mathscr{F}) \geq 0$. Maximizing $\det(\mathscr{F})$ is equivalent to minimizing $\det(\mathscr{F}^{-1})$. This also minimizes the volume of the M-dimensional confidence ellipsoid,

$$\boldsymbol{\omega}_M = \frac{2}{M}\frac{\pi^{M/2}}{\Gamma\left(\frac{M}{2}\right)}\frac{1}{\sqrt{\det(\mathscr{F})}}, \tag{7.13}$$

with $\Gamma(\cdot)$ the Gamma function. A smaller $\boldsymbol{\omega}_M$ indicates overall improved precision in $\hat{\theta}$, even if individual standard deviations may trade off.

7.1.5 Algorithm for Current-Space Sampling via D-Optimality

Algorithm 1 modifies the current-sampling locations so that, for a fixed number of samples N, the resulting set yields more informative data than a uniform current partition. The initial and optimized selections, $\mathbf{i}_{\mathrm{init}} \in \mathbb{R}^{\mathrm{N}}$ and $\mathbf{i}_{\mathrm{opt}} \in \mathbb{R}^{\mathrm{N}}$, span the same range $[0, \mathrm{I_{sc}}]$.

- `GenerateIVCurve` produces a simulated I–V characteristic with additive noise to better emulate realistic conditions for parameter inference and op-

[1] Section 7.2.2 discusses practical handling.

Algorithm 1 Current sampling distribution optimization using D-optimal design

Input: Number of parameters N, Noisy voltage and current data $\mathbf{v}_{\text{noise}}, \mathbf{i}_{\text{noise}}$, Voltage and current variances σ_{V}^2, σ_{I}^2, Initial guess θ_{init}
Output: Estimated parameters $\hat{\theta}$, Optimized current sampling vector $\mathbf{i}_{\text{opt}}$

Procedure: MAIN(N, $\mathbf{v}_{\text{noise}}, \mathbf{i}_{\text{noise}}, \sigma_{\text{V}}^2, \sigma_{\text{I}}^2, \theta_{\text{init}}$)
/* These are inputs only when the optimization is performed on real measurements. When the measurements are synthetic, the procedure `GenerateIVCurve` is used. */
$\theta_{\text{est}}, \sigma_{\text{est}}^2 \leftarrow$ `EstimateParameters`$(\mathbf{v}_{\text{noise}}, \mathbf{i}_{\text{noise}})$
$\mathbf{v}_{\text{opt}}, \mathbf{i}_{\text{opt}} \leftarrow$ `OptCurrentDist`$(\mathbf{i}_{\text{init}}, \theta_{\text{est}}, \sigma_{\text{V}}^2, \sigma_{\text{I}}^2)$
$\hat{\theta}, \sigma_{\text{opt}}^2 \leftarrow$ `EstimateParameters`$(\mathbf{v}_{\text{noise\_opt}}, \mathbf{i}_{\text{noise\_opt}})$
return $\hat{\theta}, \mathbf{i}_{\text{opt}}$

Procedure: GENERATEIVCURVE(θ^*, V_{oc}, N, σ_{V}^2, σ_{I}^2, T_{c})
/* Generate current sample selection */
$\mathbf{i} \leftarrow \text{sampling}(0, I_{\text{sc}}, \text{N})$
/* Compute noiseless voltage values */
$\mathbf{v} \leftarrow$ `IVModel`$(\mathbf{i}, \theta^*, T_{\text{c}})$
/* Corrupt voltage with Gaussian independent noise */
$\mathbf{v}_{\text{noise}} \leftarrow \mathbf{v} + \text{normal}(0, \sigma_{\text{V}}^2)$
/* Corrupt current with Gaussian independent noise */
$\mathbf{i}_{\text{noise}} \leftarrow \mathbf{i} + \text{normal}(0, \sigma_{\text{I}}^2)$
return $\mathbf{v}_{\text{noise}}, \mathbf{i}_{\text{noise}}$

Procedure: ESTIMATEPARAMETERS($\mathbf{v}_{\text{noise}}, \mathbf{i}_{\text{noise}}$)
/* θ_{est} is the tuple of estimated parameters, and Σ_{est} is the estimated approximate covariance matrix of θ_{est}. The diagonal elements of Σ_{est} provide the variance of the parameter estimates σ_{est}^2. */
$\theta_{\text{est}}, \Sigma_{est} \leftarrow \text{curve\_fit}(\text{IVModel}, \mathbf{v}_{\text{noise}}, \mathbf{i}_{\text{noise}}, \theta_{\text{init}})$
$\sigma_{\text{est}}^2 \leftarrow \text{diag}(\Sigma_{est})$
return $\theta_{\text{est}}, \sigma_{\text{est}}^2$

Procedure: COMPUTEFIM($\mathbf{v}_{\text{noise}}, \mathbf{i}_{\text{noise}}, \theta_{\text{est}}$)
$FIM \leftarrow \text{FisherInformationMatrix}(\mathbf{v}_{\text{noise}}, \mathbf{i}_{\text{noise}}, \theta_{\text{est}})$
$CRLB \leftarrow \text{diag}(\text{inv}(FIM))$
return $FIM, CRLB$

Procedure: OBJECTIVEFUNCTION($\mathbf{v}_{\text{noise}}, \theta_{\text{est}}$)
$FIM \leftarrow$ `ComputeFIM`$(\mathbf{v}_{\text{noise}}, \mathbf{i}_{\text{noise}}, \theta_{\text{est}})$
/* Objective function: $-\log(\det(FIM))$ */
return $-\log(\det(FIM))$

Procedure: OPTCURRENTDIST($\mathbf{i}_{\text{init}}, \theta_{\text{est}}, \sigma_{\text{V}}^2, \sigma_{\text{I}}^2$)
/* Initialize an empty array to store variances */
variances $\leftarrow [\,]$
while not converged **do**
/* Estimate parameters for the iteration */
$\theta_{\text{iter}} \leftarrow$ `EstimateParameters`(θ_{est})
/* Estimate the variance of the estimated parameters */
$\sigma_{\text{iter}}^2 \leftarrow \text{estimateVariance}(\theta_{\text{iter}}, \sigma_{\text{V}}^2, \sigma_{\text{I}}^2)$
/* Store the variance in the array */
$\text{add}(\sigma_{\text{iter}}^2, \text{variances})$
/* Optimize for the current iteration */
$\mathbf{i}_{\text{opt}} \leftarrow \text{MinimizeIteration}(\texttt{ObjectiveFunction}, \mathbf{i}_{\text{init}}, \theta_{\text{iter}}, \sigma_{\text{V}}^2, \sigma_{\text{I}}^2)$
end while
/* Return the optimized current selection and the array of variances */
return $\mathbf{i}_{\text{opt}}$, variances

timization. It accepts as inputs the ground-truth parameter vector θ^* (as specified in Section 7.2.2), the short-circuit current I_{sc}, the desired number of samples N over the current axis, and the voltage and current variances, σ_V^2 and σ_I^2, respectively. The routine constructs a uniformly spaced array of current values spanning $[0, I_{sc}]$ to serve as the sampling grid for *I–V* curve synthesis. Invoking the five-parameter *I–V* model `IVModel`, it evaluates the corresponding noiseless voltage samples $\mathbf{v}$ at those currents given θ^*. Zero-mean Gaussian perturbations are then added to both current and voltage to obtain the noisy arrays $\mathbf{i}_{noise}$ and $\mathbf{v}_{noise}$, which represent the measured observations. The procedure returns $\mathbf{i}_{noise}$ and $\mathbf{v}_{noise}$ for use in subsequent stages. If the *I–V* curve is generated by sampling uniformly in voltage, the roles of $\mathbf{i}$ and $\mathbf{v}$ are interchanged throughout.

- `EstimateParameters` initializes the parameter-identification stage using voltage–current data together with σ_V^2, σ_I^2, and an initial parameter guess. Its outputs are the estimated parameters and the optimized current sampling distribution. Based on (7.2), it solves for the equivalent-circuit parameters from the noisy *I–V* measurements and computes the associated parameter variances [50]. In this work, the nonlinear least-squares problem is solved using the Levenberg–Marquardt algorithm.

- `ComputeFIM` evaluates the Fisher Information Matrix (FIM) using the current parameter estimates and the noisy voltage–current observations, as prescribed by Equation (7.9). The diagonal of the inverse FIM yields the Cramér–Rao lower bounds (CRLB), which provide lower bounds on the variances of unbiased parameter estimates [51].

- `ObjectiveFunction` specifies the optimization criterion derived from the FIM computed by `ComputeFIM`. The objective is defined as the negative log-determinant of the FIM, following Equation (7.9), thereby steering the optimization toward reduced parameter uncertainty.

- `OptCurrentDist` carries out the iterative optimization of the current sampling distribution via a numerical minimization routine. At each iteration, it re-estimates the parameters, evaluates their variances, and records these values in an array. It returns the optimized current sampling distribution together with the variance history, thereby providing insight into convergence behavior.

- `Main` orchestrates the complete workflow as follows:
  - It first invokes `EstimateParameters` to obtain an initial estimate from the unoptimized current sampling distribution.
  - It then calls `OptCurrentDist` to refine the current sampling distribution.
  - Subsequently, it calls `EstimateParameters` again on the optimized distribution to improve the parameter estimates.
  - The function outputs the final optimized parameter set and the optimized current sampling distribution.

7.2 Application of the method to PV modules

This section applies the procedure introduced in Section 7.1. The discussion is structured in three parts:

1. A concise overview of common topologies used in commercial PV modules.
2. Numerical experiments in which I–V data are generated synthetically.
3. Experimental tests conducted on an operating PV module.

7.2.1 Algorithm for Generation of Synthetic Data

The routine `GenerateIVCurve` (Algorithm 2) serves to synthesize noisy I–V datasets resembling measured curves. As discussed in Section 7.1, σ_I^2 and σ_V^2 reflect the metrological performance of the current and voltage sensors. A Gaussian perturbation model is used to represent this measurement noise on both observables, enabling rigorous testing of the current-adaptation procedure for parameter estimation prior to field deployment. By reproducing typical measurement uncertainties, the algorithm supports robust parameter inference and current-sampling optimization.

Beyond noise modelling, the routine explicitly reproduces partial-shading conditions at the module level. For each of the three strings, the current is imposed and the corresponding voltage is computed using the five-parameter model, with a distinct parameter set per string. For a given current, the three string voltages are summed

up and the bypass-diode forward drop is subtracted from the total if applicable. This mechanism reproduces bypass activation and treats each string as an independent unit contributing to the aggregate module response.

The same approach naturally extends to modules with an arbitrary number of strings by augmenting the loop and assigning per-string parameters. When all strings share identical parameters, the model reduces to uniform-irradiance behaviour. Parameter heterogeneity yields controlled mismatch representative of partial shading, soiling, or other non-uniformities.

Algorithm 2 Synthesis of noisy I–V curves under partial shading

1: **Procedure:** `GENERATEIVCURVE`()
2: **Input:** $\theta = \{\theta_0, \theta_1, \theta_2\}$, $\mathrm{I_{sc}}$, T, n_{meas}, σ_{V}, σ_{I}
3: $\mathbf{i} \leftarrow \mathrm{linspace}(0, \mathrm{I_{sc}}, n_{\mathrm{points}})$
4: **for** $j \in \{0,1,2\}$ **do**
5: $\mathbf{v}_j \leftarrow \mathtt{IVModel}(\mathbf{i}, \theta_j) \cdot N_s - V_{f,j}$
6: Set $\mathbf{v}_j \leftarrow$ NaN wherever $\mathbf{v}_j < 0$
7: **end for**
8: $\mathbf{v} \leftarrow \mathbf{v}_0 + \mathrm{fillna}(\mathbf{v}_1, 0) + \mathrm{fillna}(\mathbf{v}_2, 0)$
9: /* Add voltage noise */
10: $\mathbf{v} \leftarrow \mathbf{v} + \mathrm{normal}(0, \sigma_{\mathrm{V}})$
11: /* Add current noise */
12: $\mathbf{i} \leftarrow \mathbf{i} + \mathrm{normal}(0, \sigma_{\mathrm{I}})$
13: **return** $\mathbf{v}, \mathbf{i}$

The operations in Algorithm 2 are clarified below for a three-string module consistent with Figure 3.3.

- Line 2: `GenerateIVCurve` takes as inputs three parameter sets $\theta_0, \theta_1, \theta_2$ defining the five-parameter model per string; $\mathrm{I_{sc}}$ to set the simulation range; T (cell temperature) for thermal-voltage terms; n_{meas} samples; and the noise standard deviations σ_{V} and σ_{I}.
- Line 3: A uniformly spaced current array $\mathbf{i} \in [0, \mathrm{I_{sc}}]$ with n_{meas} points is created; voltages are evaluated at these currents.
- Lines 4–7: For $j \in \{0,1,2\}$, the per-string voltage $\mathbf{v}_j$ is obtained from `IVModel` using θ_j and scaled by N_s; a forward drop $V_{f,j}$ is subtracted if the bypass diode conducts. Negative (non-physical) voltages are masked as NaN.

- Line 8: The module voltage $\mathbf{v}$ is computed by summing the string contributions while replacing NaNs with zero (inactive or bypassed strings). This operation mimics strings in parallel within the half-cell substructure.
- Line 10: Gaussian noise with standard deviation σ_{V} is added to $\mathbf{v}$ (e.g., via SciPy [52]).
- Line 12: Gaussian noise with standard deviation σ_{I} is added to $\mathbf{i}$ to emulate current-measurement uncertainty.
- Line 13: The routine returns $(\mathbf{v},\mathbf{i})$, i.e., synthetic I–V data incorporating noise and partial shading effects.

7.2.2 Numerical Simulation

For the five-parameter equivalent-circuit model, the ground-truth vector is $\theta^* = [I_{\mathrm{ph}}^*, \log(I_0)^*, n^*, R_{\mathrm{s}}^*, R_{\mathrm{sh}}^*]$, with per-string values given in Table 7.1. The inputs include the known, unbiased, noise-free cell temperature T_{c} (K) and a uniformly spaced noiseless current sampling over $[0, \mathrm{I_{sc}}]$.

The noiseless I–V characteristics are computed using the explicit five-parameter formulas. Two closed-form expressions are employed depending on the choice of independent variable. If current is the input, the terminal voltage follows the Lambert W expression [4]:

$$\begin{aligned} V = {} & -I \cdot R_s - I \cdot R_{sh} + \exp(\log(I_0)) \cdot R_{sh} + \\ & I_{ph} \cdot R_{sh} - \left(\frac{n \cdot k_B \cdot T_c}{q} \right) \\ & \cdot \mathrm{W} \left(\frac{\exp(\log(I_0)) \cdot R_{sh} \cdot \exp\left(\frac{R_{sh} \cdot (-I + \exp(\log(I_0)) + I_{ph})}{\left(\frac{n \cdot k_B \cdot T_c}{q} \right)} \right)}{\left(\frac{n \cdot k_B \cdot T_c}{q} \right)} \right). \end{aligned} \tag{7.14}$$

If voltage is the input, the current is given by:

$$I = \frac{I_{ph} + \exp(\log(I_0)) - \frac{V}{R_{sh}}}{1 + \frac{R_s}{R_{sh}}} - \frac{\frac{n \cdot k_B \cdot T_c}{q}}{R_s} \\ \mathrm{W}\left(\frac{R_s \exp(\log(I_0))}{\frac{n \cdot k_B \cdot T_c}{q}\left(1 + \frac{R_s}{R_{sh}}\right)} \exp\left(\frac{R_s(I_{ph} + \exp(\log(I_0))) + V}{\frac{n \cdot k_B \cdot T_c}{q}\left(1 + \frac{R_s}{R_{sh}}\right)} \right) \right). \tag{7.15}$$

Table 7.1 Ground-truth parameters

Case	String	I_{ph} (A)	$\log(I_0)$ (-)	n (-)	R_{s} (mΩ)	R_{sh} (Ω)
Partial shading	0	10	-18	1.35	1	2
	1	7	-13	1.6	5	2
	2	5	-12	1.6	5	2
Uniform irradiation	0	10	-18	1.35	1	2
	1	10	-18	1.35	1	2
	2	10	-18	1.35	1	2

The routine `GenerateIVCurve` produces the synthetic observations $\tilde{\mathbf{v}}_{\mathrm{init}}$ and $\tilde{\mathbf{i}}_{\mathrm{init}}$. To evaluate the FIM and CRLB, σ_{V}^2 and σ_{I}^2 must be specified. Representative values for a typical instrument chain are listed in Table 7.2.

Table 7.2 Numerical inputs used in the simulation

$\mathrm{I_{sc}}$ (A)	T_{c} (°C)	σ_{V}^2 (V^2)	σ_{I}^2 (A^2)
10.0	40.0	1e-4	2.56e-2

As discussed in Section 7.1.3, the information content per measurement depends on the parameter and the operating point.

Figure 7.1 reports the normalized contributions to the diagonal entries of the FIM, computed as $[\Delta\mathscr{F}]_{kk}$ via Equation (7.11) over the full range of $(\tilde{\mathbf{v}}, \tilde{\mathbf{i}})$. The example corresponds to one string under partial shading.

In this analysis, voltage and current noise variances are treated as known and mutually uncorrelated, consistent with an IID Gaussian model. Although real noise may deviate from this idealization, the method extends to any noise model with an analytically tractable PDF. In particular, the FIM and CRLB can be generalized to non-Gaussian or correlated noise if the distribution is known or can be reliably estimated. In the considered setup, voltage and current are acquired by independent

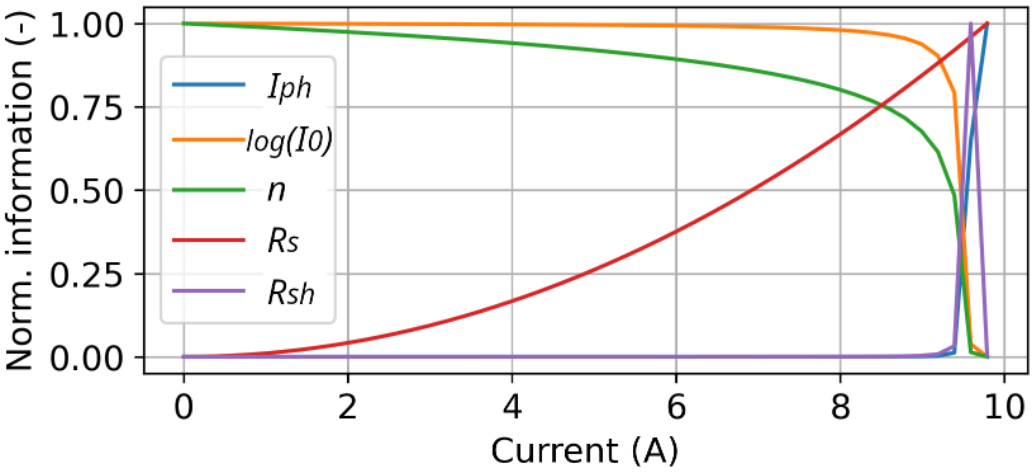

Fig. 7.1 Normalized FIM contribution of each parameter as a function of current.

sensors, which reduces the likelihood of cross-correlated noise. Low-frequency drifts, however, introduce biases that lie outside the unbiased-estimation framework assumed here; such effects can be mitigated via proper calibration and drift compensation.

To validate the approach, we compare estimation quality before and after optimizing the current sampling:

- The CRLB.
- The parameter estimates $\hat{\theta}$.
- The variances of the estimates.

Simulation under Partial Shading Conditions

Synthetic I–V datasets are generated with `GenerateIVCurve` (Algorithm 2). Parameter estimation is repeated 1000 times, yielding a statistically meaningful sample. The sample mean of the estimates is denoted $\hat{\theta}_u$, and the mean of the estimated variances across runs is denoted σ_u^2.

From these data, the FIM and CRLB are computed. The CRLB associated with uniform sampling is denoted CRLB_u and is obtained using $(\tilde{\mathbf{v}}_u, \tilde{\mathbf{i}}_u)$ with ground-truth θ^*. Table 7.3 summarizes the unoptimized results.

Table 7.3 Estimation results with uniform sampling for a partially shaded simulated module.

String	Parameter	$\mathrm{CRLB_u}$	$\hat{\theta}_\mathrm{u}$	σ_u^2
String 0	I_{ph} (A)	5.17e-06	9.9992e+00	5.81e-06
	$\log(I_0)$ (-)	3.68e-01	-1.7854e+01	3.80e-01
	n (-)	1.57e-03	1.3604e+00	1.69e-03
	R_s (mΩ)	1.14e-04	8.9959e-01	1.52e-04
	R_{sh} (Ω)	4.47e-04	2.0079e+00	5.03e-04
String 1	I_{ph} (A)	5.52e-05	7.0032e+00	6.45e-05
	$\log(I_0)$ (-)	7.49e-01	-1.3647e+01	8.37e-01
	n (-)	7.81e-03	1.5410e+00	8.11e-03
	R_s (mΩ)	6.99e-04	5.4944e+00	7.00e-04
	R_{sh} (Ω)	2.53e-02	1.9719e+00	2.78e-02
String 2	I_{ph} (A)	1.04e-03	5.0040e+00	1.07e-03
	$\log(I_0)$ (-)	1.47e+00	-1.2117e+01	2.04e+00
	n (-)	2.62e-02	1.6014e+00	2.97e-02
	R_s (mΩ)	3.02e-03	4.8331e+00	3.14e-03
	R_{sh} (Ω)	3.56e-01	2.0425e+00	8.58e-01

Figure 7.2 depicts intermediate stages of the optimization, showing the CRLB trajectories versus iteration count for each parameter (log scale on the vertical axis to emphasize variance changes). The stopping rule is triggered when the change in $\log\det(\mathscr{F})$ falls below 10^{-9} and remains under this threshold for at least 15 consecutive iterations.

A box constraint ensures that the optimized sampling $\tilde{\mathbf{i}}_{\mathrm{opt}}$ lies within the initial range of $\tilde{\mathbf{i}}_{\mathrm{init}}$.

Figure 7.3 shows, for each string, the optimized current selection that maximizes $\det(\mathscr{F})$, compared to the initial uniform sampling. As the strings have different $\mathrm{I_{sc}}$, the number of valid current points may differ across strings. Figure 7.4 reports the combined optimized distribution over all strings.

After optimization, parameters are re-estimated using $\tilde{\mathbf{i}}_{\mathrm{opt}}$, yielding $\hat{\boldsymbol{\theta}}_\mathrm{o}$ with empirical variances σ_o^2. These variances closely approach the optimized CRLB, denoted $\mathrm{CRLB_o}$.

Table 7.4 reports the post-optimization results. Relatively to Table 7.3, a systematic reduction in parameter variances is observed.

For the partially shaded case, the relative reductions in variance are:

Table 7.4 Estimation results with optimized sampling for a partially shaded simulated module.

String	Parameter	$\mathrm{CRLB_o}$	$\hat{\theta}_o$	σ_o^2
String 0	I_{ph} (A)	1.77e-06	1.0000e+01	4.29e-06
	$\log(I_0)$ (-)	1.31e-01	-1.7917e+01	3.10e-01
	n (-)	5.73e-04	1.3559e+00	1.40e-03
	R_s (mΩ)	6.26e-05	9.6015e-01	1.08e-04
	R_{sh} (Ω)	8.32e-05	1.9955e+00	2.24e-04
String 1	I_{ph} (A)	6.08e-06	7.0004e+00	1.23e-05
	$\log(I_0)$ (-)	1.26e-01	-1.3173e+01	2.65e-01
	n (-)	1.44e-03	1.5862e+00	2.90e-03
	R_s (mΩ)	2.32e-04	5.2005e+00	4.69e-04
	R_{sh} (Ω)	7.67e-04	2.0048e+00	1.59e-03
String 2	I_{ph} (A)	3.63e-05	5.0030e+00	1.00e-04
	$\log(I_0)$ (-)	2.67e-01	-1.2202e+01	7.71e-01
	n (-)	3.66e-03	1.5798e+00	9.70e-03
	R_s (mΩ)	8.44e-04	5.0631e+00	2.28e-03
	R_{sh} (Ω)	6.91e-03	1.9591e+00	1.64e-02

- String 0: 26.2% (I_{ph}), 18.4% ($\log(I_0)$), 17.2% (n), 28.9% (R_s), 55.5% (R_{sh}).
- String 1: 80.9% (I_{ph}), 68.3% ($\log(I_0)$), 64.2% (n), 33.0% (R_s), 42.8% (R_{sh}).
- String 2: 90.6% (I_{ph}), 65.1% ($\log(I_0)$), 67.3% (n), 27.4% (R_s), 98.1% (R_{sh}).

The empirical variances remain close to their CRLB counterparts, indicating efficient estimation under partial shading. These observations confirm that D-optimal sampling enhances parameter precision, particularly under challenging irradiance patterns.

Simulation under Uniform Irradiance Conditions

A second simulation campaign assesses performance under uniform irradiance. All three strings operate under identical environmental and electrical conditions, suppressing shading-induced mismatch. Small inter-string variability may still occur in practice, but the ground-truth parameters θ^* are set equal for all strings, matching string 0 of the partially shaded case in Table 7.1. This design enables a direct comparison with the previous scenario and quantifies the benefit of current-sampling optimization even without irradiance disparities.

As before, synthetic I–V curves are generated with `GenerateIVCurve`, and estimation is repeated 1000 times for both uniform and optimized sampling. Performance is compared via the CRLB, $\hat{\theta}$, and the empirical variances per string.

Tables 7.5 and 7.6 provide the numerical results before and after optimization, respectively.

Table 7.5 Estimation results with uniform sampling for a uniformly irradiated simulated module.

String	Parameter	CRLB_u	$\hat{\theta}_\mathrm{u}$	σ_u^2
String 0	I_ph (A)	3.29e-06	9.9997e+00	3.30e-06
	$\log(I_0)$ (-)	2.34e-01	-1.7965e+01	2.35e-01
	n (-)	1.00e-03	1.3534e+00	1.01e-03
	R_s (mΩ)	7.31e-05	1.0139e+00	7.83e-05
	R_sh (Ω)	2.56e-04	2.0031e+00	2.87e-04
String 1	I_ph (A)	3.31e-06	1.0000e+01	3.41e-06
	$\log(I_0)$ (-)	2.35e-01	-1.7946e+01	2.41e-01
	n (-)	1.00e-03	1.3543e+00	1.04e-03
	R_s (mΩ)	7.31e-05	9.8116e-01	8.09e-05
	R_sh (Ω)	2.86e-04	2.0045e+00	2.99e-04
String 2	I_ph (A)	3.31e-06	9.9996e+00	3.03e-06
	$\log(I_0)$ (-)	2.35e-01	-1.7908e+01	2.14e-01
	n (-)	9.25e-04	1.3567e+00	9.39e-04
	R_s (mΩ)	7.31e-05	9.5525e-01	8.54e-05
	R_sh (Ω)	2.46e-04	2.0007e+00	2.65e-04

For the uniformly irradiated case, the relative variance reductions are:

- String 0: 19.1% (I_ph), 14.0% ($\log(I_0)$), 15.1% (n), 6.4% (R_s), 53.7% (R_sh).
- String 1: 18.8% (I_ph), 14.5% ($\log(I_0)$), 14.6% (n), 6.6% (R_s), 54.5% (R_sh).
- String 2: 4.3% (I_ph), 0.9% ($\log(I_0)$), 2.2% (n), 21.5% (R_s), 44.9% (R_sh).

As in the shaded case, empirical variances track the CRLB closely, indicating statistical efficiency of the estimator throughout the optimization process.

Sensitivity Analysis to the Initial Parameter Error

In the simulations above, the FIM and CRLB were computed at the ground-truth parameters. In practice, these are unknown, and the FIM/CRLB are evaluated at

Table 7.6 Estimation results with optimized sampling for a uniformly irradiated simulated module.

String	Parameter	$\mathrm{CRLB_o}$	$\hat{\theta}_o$	σ_o^2
String 0	I_{ph} (A)	1.05e-06	1.0000e+01	2.67e-06
	$\log(I_0)$ (-)	7.73e-02	-1.8111e+01	2.02e-01
	n (-)	3.38e-04	1.3432e+00	8.57e-04
	R_s (mΩ)	3.08e-05	1.0934e+00	7.33e-05
	R_{sh} (Ω)	5.24e-05	2.0001e+00	1.33e-04
String 1	I_{ph} (A)	1.05e-06	1.0001e+01	2.77e-06
	$\log(I_0)$ (-)	7.73e-02	-1.8095e+01	2.06e-01
	n (-)	3.38e-04	1.3435e+00	8.88e-04
	R_s (mΩ)	3.08e-05	1.0103e+00	7.56e-05
	R_{sh} (Ω)	5.24e-05	1.9893e+00	1.36e-04
String 2	I_{ph} (A)	1.05e-06	1.0000e+01	2.90e-06
	$\log(I_0)$ (-)	7.73e-02	-1.7985e+01	2.12e-01
	n (-)	3.38e-04	1.3512e+00	9.18e-04
	R_s (mΩ)	3.08e-05	9.8322e-01	6.70e-05
	R_{sh} (Ω)	5.24e-05	1.9997e+00	1.46e-04

estimated parameters that carry uncertainty. To quantify the impact, a sensitivity study was carried out by perturbing the true parameter set with relative offsets from 0% to 10%. For each level $X \in \{1\%, 2\%, \ldots, 10\%\}$, 1000 random parameter vectors were generated by applying independent uniform multiplicative perturbations within $\pm X\%$ to each component, and the corresponding FIM and CRLB were recomputed. Figure 7.5 summarizes the CRLB distributions as boxplots versus offset level. The results indicate that deviations become appreciable only when the initial error reaches approximately 4–5%, which is comparatively large in relation to the parameter accuracies reported in Section 7.2.3. An illustrative example is provided in Section 7.2.3.

Computational Performance Analysis

The computational burden of the optimization framework was assessed by executing 1000 independent runs on a workstation with an AMD Ryzen 7 5800X CPU and 16 GB DDR4 RAM. For each run, the execution time, its variance, peak memory usage, and the convergence rate were recorded. Table 7.7 reports the aggregated metrics.

Execution time was stable with low variance, and convergence was consistently achieved.

Table 7.7 Computational performance metrics of the optimization algorithm

Metric	**Value**
Execution time (mean)	13.997 s
Execution time (variance)	0.018 s
Memory usage	132.8 MiB
Convergence rate	100%

Sensitivity Analysis to Measurement Noise Levels

The estimation framework assumes known measurement-noise levels on voltage and current, derived from typical full-scale specifications. To evaluate robustness, the noise variances were varied independently across 90 levels. At each level, the complete estimation pipeline was executed and the empirical parameter-variance was recorded, quantifying the propagation of measurement uncertainty through the optimization.

Figure 7.6 shows the dependence of parameter-variance on current-noise variance. Figure 7.7 presents the analogous results for voltage-noise variance. The red marker identifies the nominal variances used elsewhere in the simulations.

Across the explored ranges, the estimator exhibits stable behaviour, with parameter variances increasing smoothly as measurement noise grows.

Statistical Reliability of Parameter Estimates

To characterize estimation variability under repeated acquisitions, the empirical distributions of parameter estimates are visualized via boxplots for each string under both uniform and partial irradiance. Figure 7.8 summarizes results for uniform irradiance, where tight clustering and consistent medians are observed across strings, consistent with homogeneous operating conditions. Figure 7.9 reports the partially shaded case, showing larger dispersion, especially for I_{ph} due to irradiance non-uniformity; similar, albeit milder, trends are visible for n and R_{s}, reflecting their sensitivity to the shifted operating points.

7.2.3 Experimental Validation

Under on-site operating conditions, the I–V curve of a PV module can be acquired using either an electronic load or a capacitive load, each suited to different measurement objectives. In the capacitive approach, a capacitor is charged by the PV module and the resulting transient is used to rapidly trace the I–V characteristic. This technique is advantageous for preliminary diagnostics because it enables the collection of many samples over a short interval and can be applied under both uniform irradiance and partial shading. In this study, the capacitive method was first employed to verify correct module operation across a range of irradiance scenarios.

For the parameter-estimation methodology introduced in this work, however, an electronic load is required. Unlike the capacitive method, an electronic load provides precise control of the operating point by directly imposing the current, which is essential for the current sampling optimization described in Algorithm 1.

The proposed framework was validated experimentally on five commercial PV modules:

- Qcells Q.PEAK DUO M-G11 410 (monocrystalline Si),
- LG370Q1C-V5 with manufacturing defects (back contact),
- SANYO HIP 230HDE1 (heterojunction with intrinsic thin layer),
- JA Solar JAP60S01-280/SC (polycrystalline Si),
- HT-SAAE HT54-18XN-435 (TOPCon).

The principal STC electrical specifications for the tested modules are reported in Table 7.8.

The overall measurement architecture is shown in Figure 7.10.

The following instrumentation was used:

- HH PLA 812 electronic load, serving as both programmable DC load and voltage/current meter. Table 7.9 lists the uncertainty figures. As is typical for high-grade laboratory instruments, the datasheet provides a reading uncertainty (Δ_{read}) and a full-scale range uncertainty (Δ_{FSR}). As most commercial

Table 7.8 Specifications at STC for the tested PV modules

Model	P_{mpp} (W)	V_{oc} (V)	V_{mpp} (V)	I_{sc} (A)	I_{mpp} (A)	Tech.	Cells
Q.PEAK DUO	410	37.18	31.22	13.57	12.97	m-Si	108 (half)
LG370Q1C-V5	370	39.9	34.5	11.5	10.73	Back Con.	60
HIP 230HDE1	230	44.6	35.9	5.45	5.1	HIT	72
JAP60S01-280/SC	280	38.65	31.61	9.37	8.86	p-Si	60
HT54-18XN-435	435	38.4	32.0	14.31	13.60	TOPCon	108 (half)

Table 7.9 Electrical characteristics of the measurement system

	V	I
$\Delta_{read}(3\sigma)$	$\pm$ 0.1%	$\pm$ 0.2%
$\Delta_{FSR}(3\sigma)$	$\pm$ 0.05%	$\pm$ 0.05%
FSR	100 (V)	18 (A)
σ^2	2.5 $\left(\mathrm{mV}^2\right)$	0.225 $\left(\mathrm{mA}^2\right)$

datasheets report only FSR values, a constant variance equal to the FSR-based uncertainty is assumed for all readings in this work.

- Pt100 surface probe for cell-temperature measurement.
- Reference solar cell for irradiance monitoring.
- NI-9219 universal analogue input module for temperature and irradiance logging.
- NI-cDAQ-9174 chassis for data acquisition.
- A laptop running LabVIEW for instrument control and data logging.

The proposed method was further validated on a PV module operating outdoors under natural sunlight. The workflow mirrors Algorithm 1, with the distinction that the noisy *I–V* samples are now obtained from real measurements. Since the true parameters of the physical device are unknown, estimates are used to compute the FIM and CRLB. A total of 50 points is considered, as motivated in Section 7.3.

Qcells Q.PEAK DUO M-G11 410 Module

Environmental conditions:

- Partial shading: $T_c = 40.22\,^{\circ}\mathrm{C}$, $G = 986.3\ \mathrm{W/m^2}$
- Uniform irradiance: $T_c = 41.37\,^{\circ}\mathrm{C}$, $G = 1001.6\ \mathrm{W/m^2}$

The shading arrangement adopted for the Q.PEAK DUO M-G11 410 is shown in Figure 7.11. Two vertical regions were masked to reproduce realistic substring-level shading. This physical configuration was used to apply the intended irradiance pattern during testing.

Figure 7.12 presents the *I–V* characteristics acquired under partial shading. Blue markers correspond to the preliminary capacitive-load sweep; orange markers show uniformly spaced current samples taken with the electronic load; green markers denote the D-optimal current samples. Table 7.10 lists the selected current and voltage points as percentages of I_{sc} and V_{oc}, respectively, and highlights the MPP to assist manufacturers and plant operators with MPP tracking under mismatch.

Table 7.10 Optimized current and voltage points under partial shading (percentages of I_{sc} and V_{oc}). MPP highlighted.

Index	Current (% I_{sc})	Voltage (% V_{oc})	Power (% P_{mpp})	
1–25	0.00	100.00	0.00	
26–27	34.70–34.72	92.76–92.75	45.11–45.82	
28–30	47.16–48.98	84.60–74.13	100.00	MPP
31–33	51.80–51.83	64.02–64.01	85.01–84.73	
34–38	67.20–69.39	55.84–40.01	58.62–55.93	
39	72.22	34.63	36.55	
40–44	76.84–80.05	34.22–33.88	23.81–23.06	
45–50	100.00	0.00	0.00	

Tables 7.11 and 7.12 report the estimated parameters using, respectively, uniform and D-optimal current sampling. The optimization improves identifiability under non-uniform irradiance, where parameter inference is intrinsically more demanding.

The pronounced reduction in empirical variances and their proximity to the CRLB support the effectiveness of D-optimal sampling when irradiance is spatially non-uniform and identifiability is more challenging.

Figure 7.13 shows the *I–V* characteristics under uniform irradiance: blue markers indicate the capacitive-load pre-sweep; orange markers indicate uniformly spaced current samples; green markers are the D-optimal samples. Table 7.13 reports the

Table 7.11 Estimation results with uniform sampling for the partially shaded module.

String	Parameter	$\mathrm{CRLB_u}$	$\hat{\theta}_\mathrm{u}$	σ_u^2
String 0	I_{ph} (A)	5.23e-06	1.3643e+01	5.30e-06
	$\log(I_0)$ (-)	1.83e-01	-2.5894e+01	1.98e-01
	n (-)	3.85e-04	1.2690e+00	3.87e-04
	R_{s} (mΩ)	1.22e-05	1.4907e+01	1.24e-05
	R_{sh} (Ω)	1.53e-04	1.5178e+00	1.58e-04
String 1	I_{ph} (A)	4.48e-05	9.9307e+00	8.97e-04
	$\log(I_0)$ (-)	3.61e-01	-1.6598e+01	1.46e+00
	n (-)	9.64e-04	1.9487e+00	1.52e-02
	R_{s} (mΩ)	4.41e-05	1.7435e+01	4.72e-05
	R_{sh} (Ω)	2.78e-03	3.7637e+00	1.19e+00
String 2	I_{ph} (A)	1.82e-05	6.8540e+00	1.52e-04
	$\log(I_0)$ (-)	6.99e-01	-1.3668e+01	2.13e+00
	n (-)	2.27e-03	1.8199e+00	2.80e-02
	R_{s} (mΩ)	1.78e-05	1.2372e+00	1.51e-03
	R_{sh} (Ω)	1.58e-02	5.0944e+00	5.29e+00

selected points as percentages of $\mathrm{I_{sc}}$ and $\mathrm{V_{oc}}$, and marks the MPP.

Tables 7.14 and 7.15 summarize uniform versus optimized sampling outcomes for the uniformly irradiated module. For string 0 under optimized sampling (Table 7.15), the CRLBs are 6.23e-07 A^2 for I_{ph}, 4.02e-02 for $\log(I_0)$, 1.23e-04 for n, 7.00e-12 Ω^2 for R_{s}, and 1.30e-05 Ω^2 for R_{sh}. Compared against the maxima observed in the noise-sensitivity sweep of Section 7.2.2 (Figure 7.5)—approximately 6×10^{-4} A^2, 10^2, 4×10^{-1}, 10^{-6} Ω^2, and 8 Ω^2—these are lower by roughly three to five orders of magnitude.

The consistency obtained under uniform irradiance corroborates the robustness of the D-optimal strategy. The tight correspondence between observed variances and CRLB across the optimization confirms statistical efficiency on real modules under uniform conditions.

LG370Q1C-V5 Module (Defective)

Environmental conditions:

- Partial shading: $T_c = 47.16\,^{\circ}\mathrm{C}$, $G = 782.9\ \mathrm{W/m^2}$

Table 7.12 Estimation results with optimized sampling for the partially shaded module.

String	Parameter	$\mathrm{CRLB_o}$	$\hat{\theta}_o$	σ_o^2
String 0	I_{ph} (A)	6.28e-07	1.3643e+01	1.50e-06
	$\log(I_0)$ (-)	3.43e-02	-2.5967e+01	8.23e-02
	n (-)	6.67e-05	1.2655e+00	1.59e-04
	R_s (mΩ)	4.23e-06	1.4933e+01	1.01e-05
	R_{sh} (Ω)	5.63e-06	1.5192e+00	1.35e-05
String 1	I_{ph} (A)	1.11e-06	1.0043e+01	2.98e-06
	$\log(I_0)$ (-)	4.53e-02	-2.4385e+01	1.23e-01
	n (-)	1.23e-04	1.3858e+00	3.31e-04
	R_s (mΩ)	1.18e-05	2.0915e+01	3.18e-05
	R_{sh} (Ω)	3.22e-05	1.9252e+00	8.71e-05
String 2	I_{ph} (A)	4.50e-07	6.8922e+00	1.69e-06
	$\log(I_0)$ (-)	4.87e-02	-2.0301e+01	1.83e-01
	n (-)	1.60e-04	1.2831e+00	6.04e-04
	R_s (mΩ)	3.72e-05	5.7674e+00	1.41e-04
	R_{sh} (Ω)	4.18e-05	2.4586e+00	1.59e-04

- Uniform irradiance: $T_c = 46.76°\mathrm{C}$, $G = 786.9\ \mathrm{W/m^2}$

The LG370Q1C-V5 exhibits manufacturing defects evidenced by electroluminescence (EL) imaging. Figure 7.14 highlights regions with inactive or degraded cells.

During testing, two of the three strings were deliberately shaded: one fully and one approximately half its length, as shown in Figure 7.15. The "COVER" annotations indicate the masked areas applied to the physical module.

Figure 7.16 shows the measured *I–V* curves under partial shading: blue (capacitive), orange (uniform current samples), and green (D-optimal samples).

Table 7.16 lists the optimized current/voltage points as percentages of $\mathrm{I_{sc}}$ and $\mathrm{V_{oc}}$, with the MPP indicated.

Parameter estimates for uniform and optimized sampling are reported in Tables 7.17 and 7.18, respectively.

Uniform-irradiance tests were also conducted to isolate the effect of defects without irradiance mismatch. Figure 7.17 shows the *I–V* curve with uniform and optimized sampling. Table 7.19 lists the selected points and the MPP.

Table 7.13 Optimized current and voltage points under uniform irradiance (percentages of I_{sc} and V_{oc}). MPP highlighted.

Index	Current (% I_{sc})	Voltage (% V_{oc})	Power (% P_{mpp})	
1–15	0.00	100.00	0.00	
16	68.62	92.97	85.40	
17	70.98	92.51	89.20	
18–20	73.85–74.20	91.81–91.89	94.50–95.10	
21	76.20	91.33	97.80	
22	80.44	90.14	99.20	
23	82.67	89.39	99.80	
24	84.26	88.78	100.00	MPP
25–31	96.64–96.99	74.19–71.72	92.50–91.40	
32–35	98.08–98.10	53.07–52.49	64.20–63.80	
36–50	100.00	0.00	0.00	

Estimation results for uniform versus optimized sampling under uniform irradiance are provided in Tables 7.20 and 7.21.

SANYO HIP 230HDE1 Module (HIT Technology)

Environmental conditions:

- Partial shading: $T_c = 62.02\,^{\circ}\mathrm{C}$, $G = 967.8\ \mathrm{W/m^2}$
- Uniform irradiance: $T_c = 57.52\,^{\circ}\mathrm{C}$, $G = 974.1\ \mathrm{W/m^2}$

The HIT-based SANYO HIP 230HDE1 was tested under both uniform and partially shaded conditions. In the shaded scenario, one of the three series strings contains fewer cells than the others, producing a distinct electrical response that is evident in the measured *I–V* curve.

Figure 7.18 shows the measured *I–V* curves (capacitive, uniform current, and optimized current sampling).

Optimized sampling points (percentages of I_{sc} and V_{oc}) and the MPP are listed in Table 7.22.

Figure 7.19 documents the applied shading geometry.

Table 7.14 Estimation results with uniform sampling under uniform irradiation (QCells module).

String	Parameter	$\mathrm{CRLB_u}$	$\hat{\theta}_u$	σ_u^2
String 0	I_{ph} (A)	1.28e-05	1.3819e+01	2.04e-03
	$\log(I_0)$ (-)	3.11e-01	-9.6950e+00	4.55e+00
	n (-)	9.41e-04	1.6625e+00	3.87e-03
	R_s (mΩ)	2.56e-05	1.7141e+00	5.63e-03
	R_{sh} (Ω)	1.19e-03	2.0815e+00	2.87e-03
String 1	I_{ph} (A)	1.28e-05	1.3818e+01	2.03e-03
	$\log(I_0)$ (-)	3.11e-01	-9.7150e+00	4.52e+00
	n (-)	9.41e-04	1.6582e+00	3.82e-03
	R_s (mΩ)	2.56e-05	1.8172e+00	5.57e-03
	R_{sh} (Ω)	1.19e-03	2.0756e+00	2.83e-03
String 2	I_{ph} (A)	1.28e-05	1.3819e+01	2.18e-03
	$\log(I_0)$ (-)	3.11e-01	-9.5514e+00	4.70e+00
	n (-)	9.41e-04	1.7047e+00	4.19e-03
	R_s (mΩ)	2.56e-05	1.5420e+00	6.03e-03
	R_{sh} (Ω)	1.19e-03	2.1406e+00	3.28e-03

Uniform and optimized sampling results for partial shading are listed in Tables 7.23 and 7.24; the variance reductions confirm the benefits of D-optimal design despite architectural asymmetries.

Uniform-irradiance results for the same module are depicted in Figure 7.20, with sampling details and MPP in Table 7.25. Corresponding estimation results are collected in Tables 7.26 and 7.27.

JA Solar Module (Polycrystalline – Voltage Sampling)

Environmental conditions:

- Uniform irradiance: $T_c = 44.85\,^{\circ}\mathrm{C}$, $G = 991.0\ \mathrm{W/m^2}$

To assess voltage-domain sampling, a JA Solar polycrystalline module was tested under uniform irradiance using an electronic load to impose voltage while recording current. The D-optimal design was reformulated in the voltage domain within the same information-theoretic framework.

Figure 7.21 shows the measured I–V curve (blue), the initial uniform voltage samples (orange), and the optimized voltage samples (red).

Table 7.15 Estimation results with optimized sampling under uniform irradiation (QCells module).

String	Parameter	$\mathrm{CRLB_o}$	$\hat{\theta}_o$	σ_o^2
String 0	I_{ph} (A)	6.23e-07	1.3938e+01	2.25e-04
	$\log(I_0)$ (-)	4.02e-02	-2.6205e+01	1.46e-01
	n (-)	1.23e-04	1.5913e+00	4.42e-04
	R_s (mΩ)	7.00e-06	1.2218e+01	2.51e-04
	R_{sh} (Ω)	1.30e-05	2.0954e+00	4.64e-05
String 1	I_{ph} (A)	6.23e-07	1.3938e+01	2.34e-06
	$\log(I_0)$ (-)	4.02e-02	-2.6156e+01	1.52e-01
	n (-)	1.23e-04	1.5943e+00	4.60e-04
	R_s (mΩ)	7.00e-06	1.2210e+01	2.61e-04
	R_{sh} (Ω)	1.30e-05	2.0945e+00	4.80e-05
String 2	I_{ph} (A)	6.23e-07	1.3938e+01	2.16e-06
	$\log(I_0)$ (-)	4.02e-02	-2.6147e+01	1.40e-01
	n (-)	1.23e-04	1.5945e+00	4.27e-04
	R_s (mΩ)	7.00e-06	1.2189e+01	2.42e-04
	R_{sh} (Ω)	1.30e-05	2.0969e+00	4.48e-05

The optimized locations cluster in regions of high sensitivity—near short-circuit and the knee—consistent with the behaviour observed for current-based sampling under uniform irradiance.

Table 7.28 lists the selected voltage and corresponding current points as percentages of $\mathrm{V_{oc}}$ and $\mathrm{I_{sc}}$, with the MPP region highlighted.

These results confirm that the D-optimal framework extends naturally to voltage-imposed measurements under uniform conditions, providing a practical alternative when voltage control is preferred by the test setup.

Table 7.29 summarizes the estimation performance for uniform and optimized voltage-domain sampling.

HT54-18XN-435 Module (Monocrystalline Half-Cut Cells)

Environmental conditions:

- Partial shading: $T_c = 48.23\,^{\circ}\mathrm{C}$, $G = 919.6\ \mathrm{W/m^2}$
- Uniform irradiance: $T_c = 47.63\,^{\circ}\mathrm{C}$, $G = 924.7\ \mathrm{W/m^2}$

Table 7.16 Optimized sampling under partial shading (LG370Q1C-V5): points as % of I_{sc} and V_{oc}; MPP highlighted.

Index	Current (% I_{sc})	Voltage (% V_{oc})	Power (% P_{mpp})	
1	0.00	100.00	0.00	
2	33.66	97.42	73.69	
3	43.39	96.27	93.87	
4	43.56	96.22	94.19	
5	52.78	84.31	100.00	MPP
6	53.83	81.13	98.13	
7	54.27	79.67	97.16	
8	54.82	77.80	95.83	
9	54.99	77.18	95.38	
10	62.68	44.10	62.11	
11	66.13	42.85	63.68	
12	66.13	42.85	63.68	
13	68.76	41.55	64.20	
14	72.82	38.24	62.58	
15	80.27	24.43	44.07	
16	93.35	2.04	4.28	
17-50	100.00	0.00	0.00	

Figures 7.22 and 7.23 show the measured *I–V* curves under partial shading and uniform irradiance, respectively, for the HT54-18XN-435 half-cut module. In both regimes, D-optimal sampling concentrates measurements at the most informative operating points, enabling accurate estimation with a limited number of samples. The shading arrangement corresponds to that of Figure 3.4.

7.3 Selecting the Number of Points for the *I–V* Sweep

All results so far assume a fixed number of current samples. To fully exploit the proposed selection scheme, one must choose a total count of voltage–current measurements that strikes a balance between computational cost and estimation accuracy.

Crucially, the algorithm itself is agnostic to how many points are acquired. Its role is not to set the sample count, but to optimally redistribute any user—specified number of samples along the *I–V* curve so as to minimize the determinant of the

Table 7.17 Uniform-sampling estimation results (partial shading, LG370Q1C-V5).

String	Parameter	$\mathrm{CRLB_u}$	$\hat{\theta}_u$	σ_u^2
String 0	I_{ph} (A)	2.97e-07	8.2007	2.77e-05
	$\log(I_0)$ (-)	4.20e-02	-30.1785	1.55e-01
	n (-)	1.10e-04	1.6550	4.02e-04
	R_s (mΩ)	1.35e-05	41.048	2.91e-05
	R_{sh} (Ω)	4.91e-05	3.2094	3.84e-03
String 1	I_{ph} (A)	2.97e-07	3.8067	6.72e-04
	$\log(I_0)$ (-)	4.20e-02	-10.2872	4.44e-01
	n (-)	1.10e-04	1.1955	4.71e-03
	R_s (mΩ)	1.35e-05	30.875	9.44e-04
	R_{sh} (Ω)	4.91e-05	0.5246	1.33e-03
String 2	I_{ph} (A)	2.97e-07	0.2012	1.90e-04
	$\log(I_0)$ (-)	4.20e-02	-9.7692	2.27e+01
	n (-)	1.10e-04	1.0357	2.31e-01
	R_s (mΩ)	1.35e-05	6.8135	2.80e-01
	R_{sh} (Ω)	4.91e-05	2.5665	5.60e+00

CRLB. In practice, the procedure concentrates measurements where the expected information gain is largest, thereby enhancing parameter accuracy.

The information content of a design is measured via the volume of the confidence ellipsoid implied by the FIM, which serves as the optimization target. As illustrated in Figure 7.24, we apply an elbow (knee) analysis to this volume to show how information grows with the number of samples, both pre— and post—optimization.

From this analysis, we select a total of 50 samples: beyond this threshold, additional points deliver only marginal improvements in estimation quality.

With 50 points, the optimization finishes in about 14 s on a typical desktop (AMD Ryzen 7 5800X, 16 GB DDR4). Thus, the method is well suited to offline characterization and analysis, but is not yet compatible with applications that impose tight real–time budgets, such as high–rate MPP tracking.

Table 7.18 Optimized-sampling estimation results (partial shading, LG370Q1C-V5).

String	Parameter	$\mathrm{CRLB_o}$	$\hat{\theta}_\mathrm{o}$	σ_o^2
String 0	I_ph (A)	7.04e-08	8.1055	2.65e-03
	$\log(I_0)$ (-)	1.49e-02	-25.5249	2.74e+00
	n (-)	3.99e-05	1.9331	1.34e-02
	R_s (mΩ)	7.12e-06	38.915	5.75e-04
	R_sh (Ω)	4.55e-06	4.5669	1.15e+00
String 1	I_ph (A)	2.08e-07	3.8055	4.36e-04
	$\log(I_0)$ (-)	2.78e-02	-10.3690	2.96e-01
	n (-)	6.99e-05	1.1941	2.73e-03
	R_s (mΩ)	8.12e-06	29.115	5.95e-04
	R_sh (Ω)	2.91e-05	0.6363	8.88e-04
String 2	I_ph (A)	2.38e-07	0.9861	1.51e-04
	$\log(I_0)$ (-)	2.63e-02	-8.5220	1.37e+01
	n (-)	7.24e-05	1.0912	1.67e-01
	R_s (mΩ)	1.01e-05	6.2951	1.95e-01
	R_sh (Ω)	3.29e-05	2.6083	4.04e+00

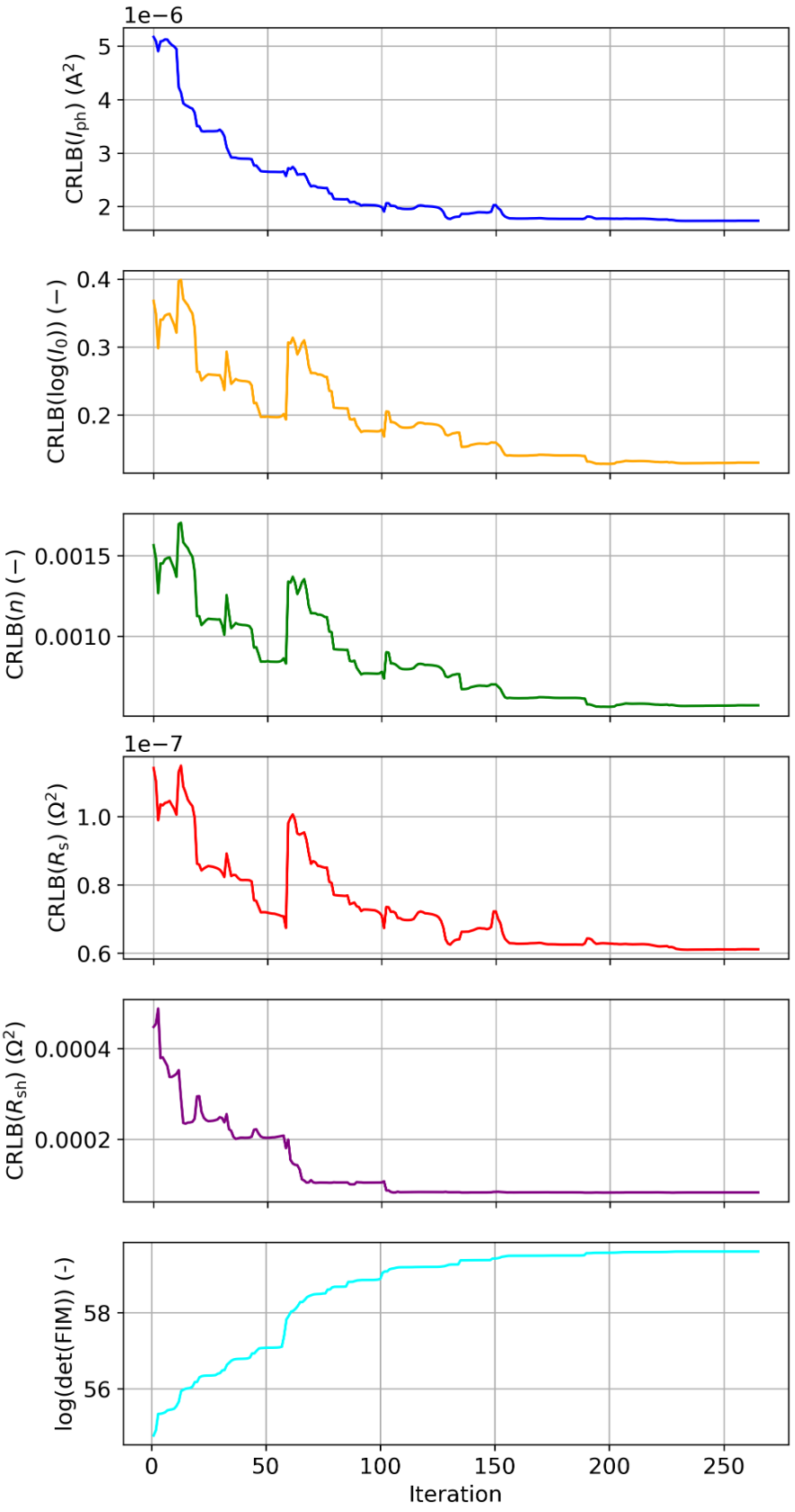

Fig. 7.2 Synthetic experiment for string 0: CRLB of each parameter across optimization iterations (log scale).

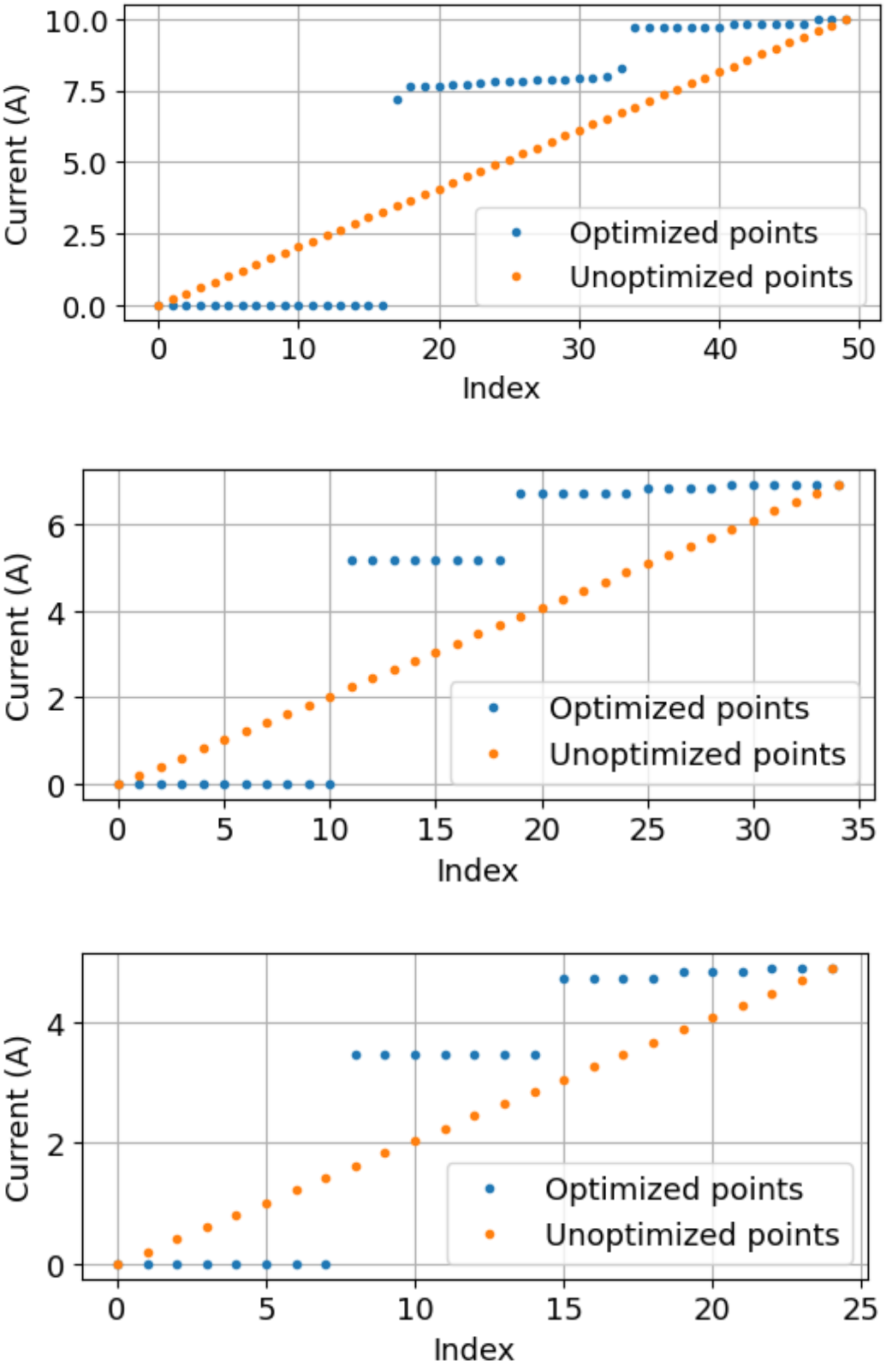

Fig. 7.3 Optimized current sample selection compared with uniform sampling for the three strings.

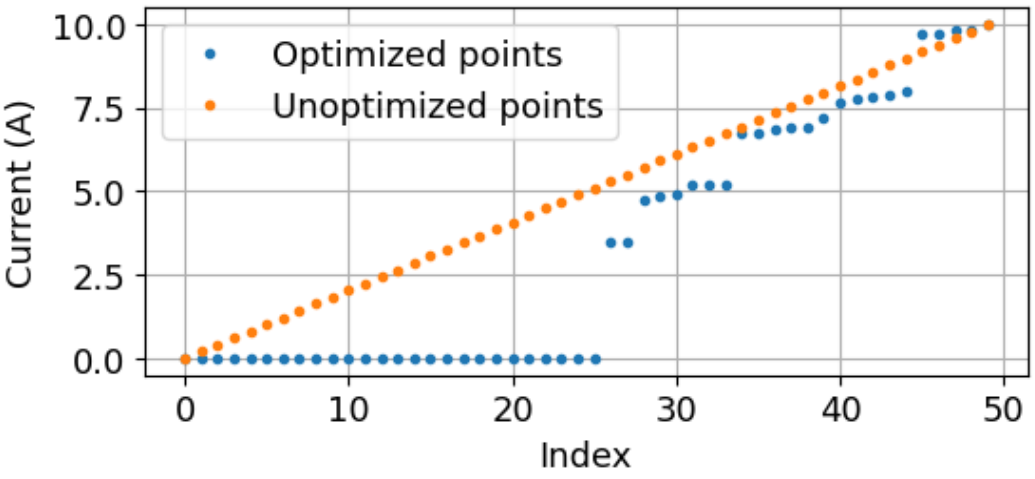

Fig. 7.4 Overall optimized current selection versus uniform sampling for $N = 50$.

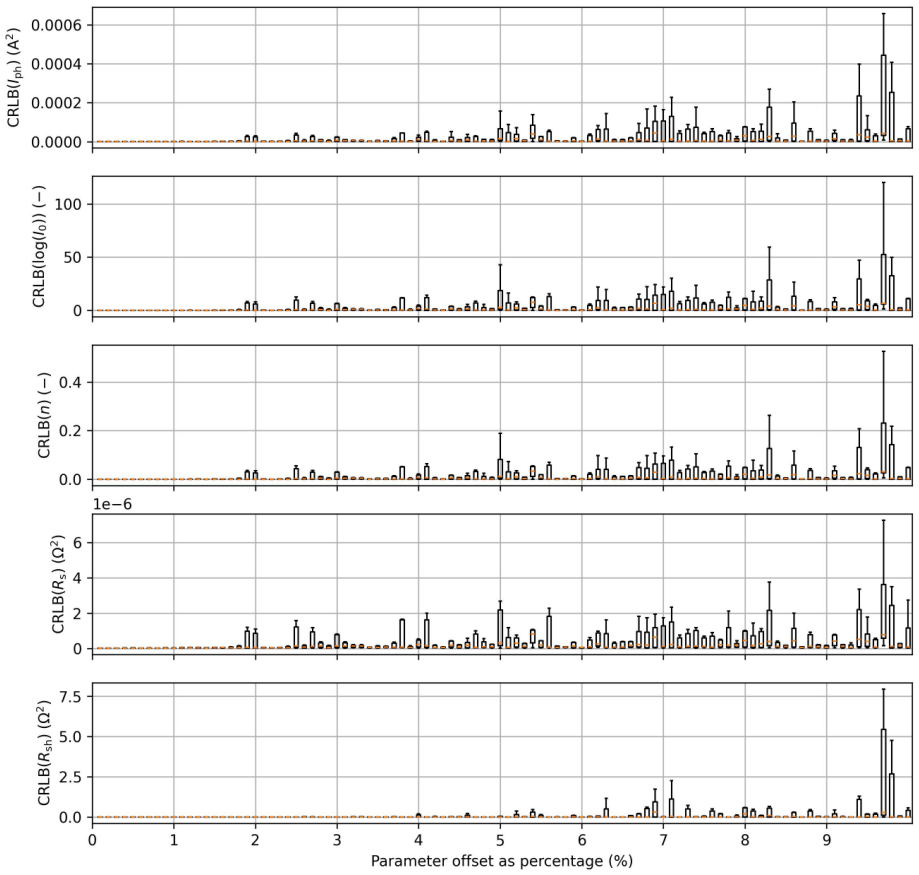

Fig. 7.5 CRLB sensitivity to parameter perturbations. Each box corresponds to 1000 random perturbations at a given offset level (0–10%).

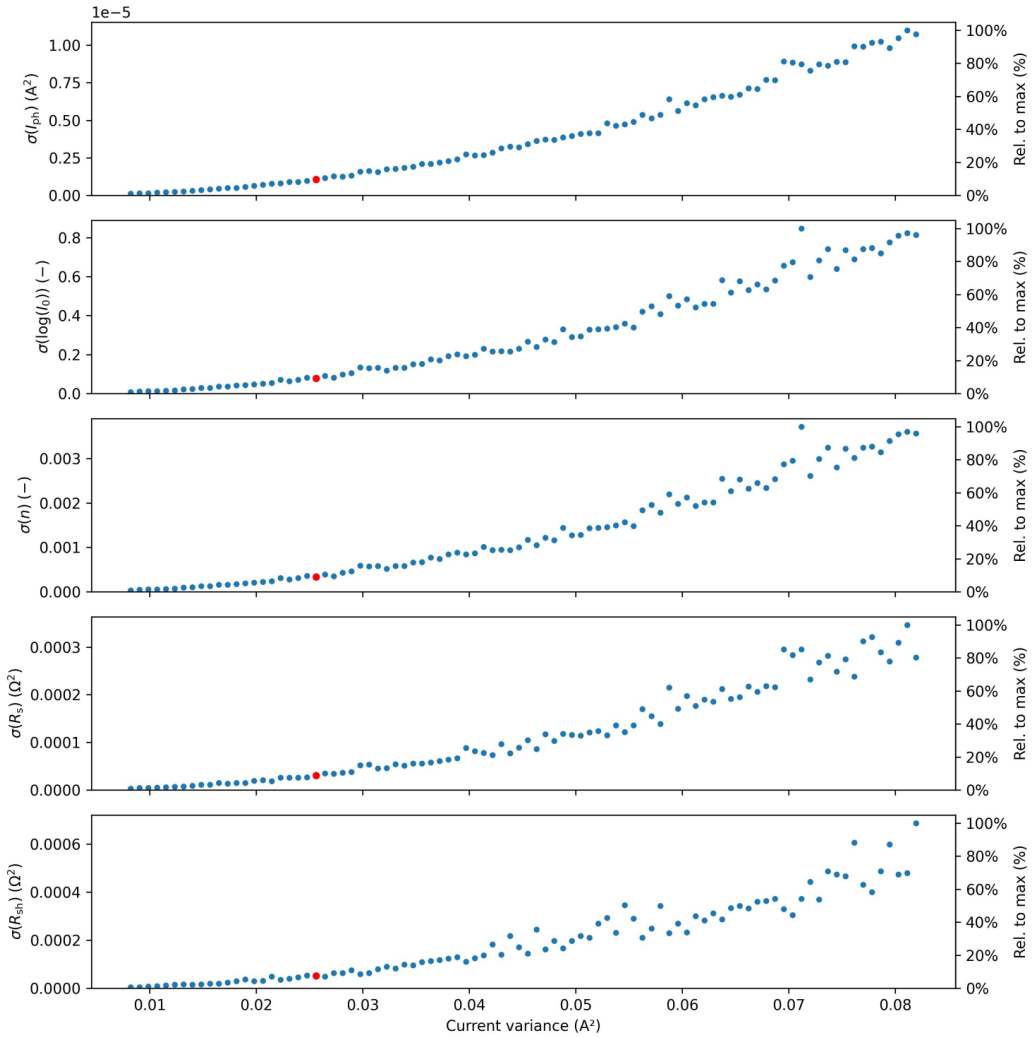

Fig. 7.6 Empirical variance of each parameter versus current-measurement variance. Red markers: nominal values used in other simulations.

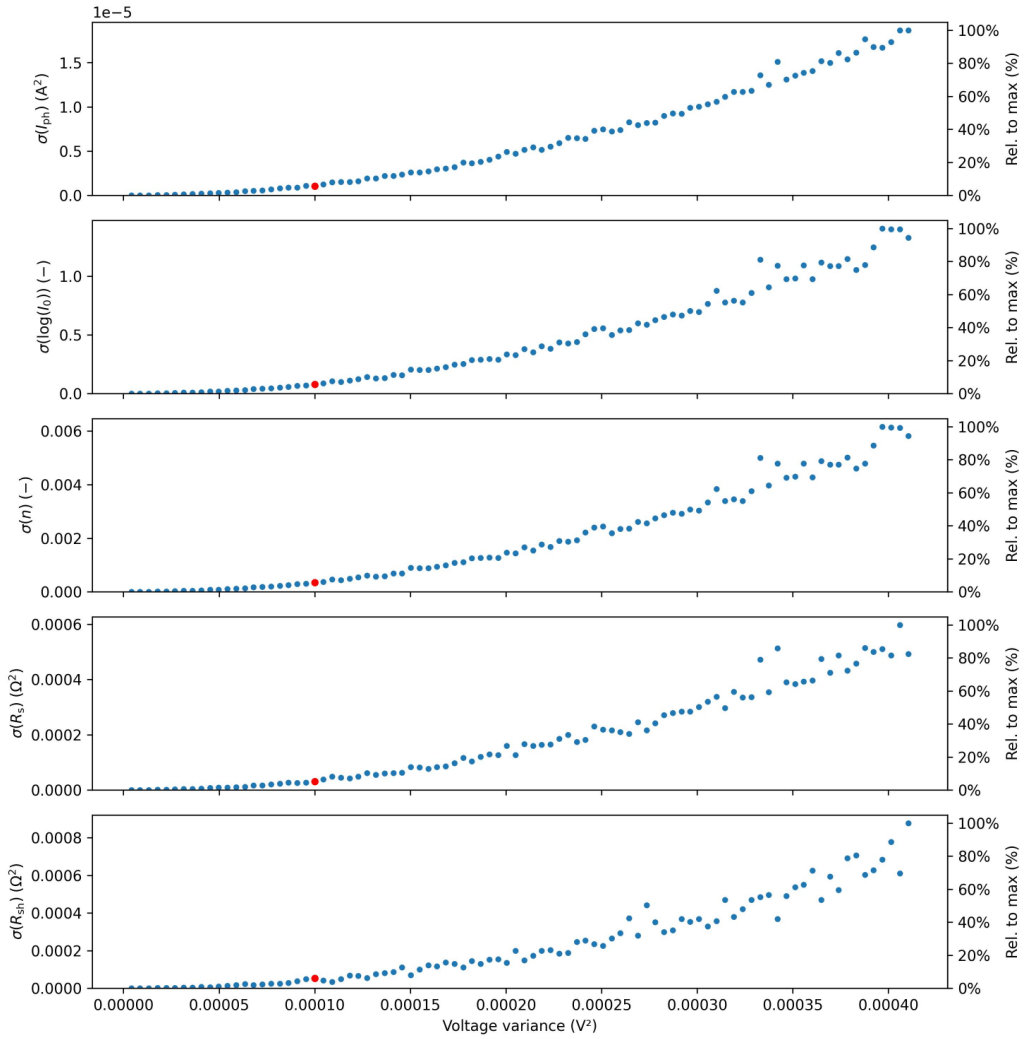

Fig. 7.7 Empirical variance of each parameter versus voltage-measurement variance. Red markers: nominal values used in other simulations.

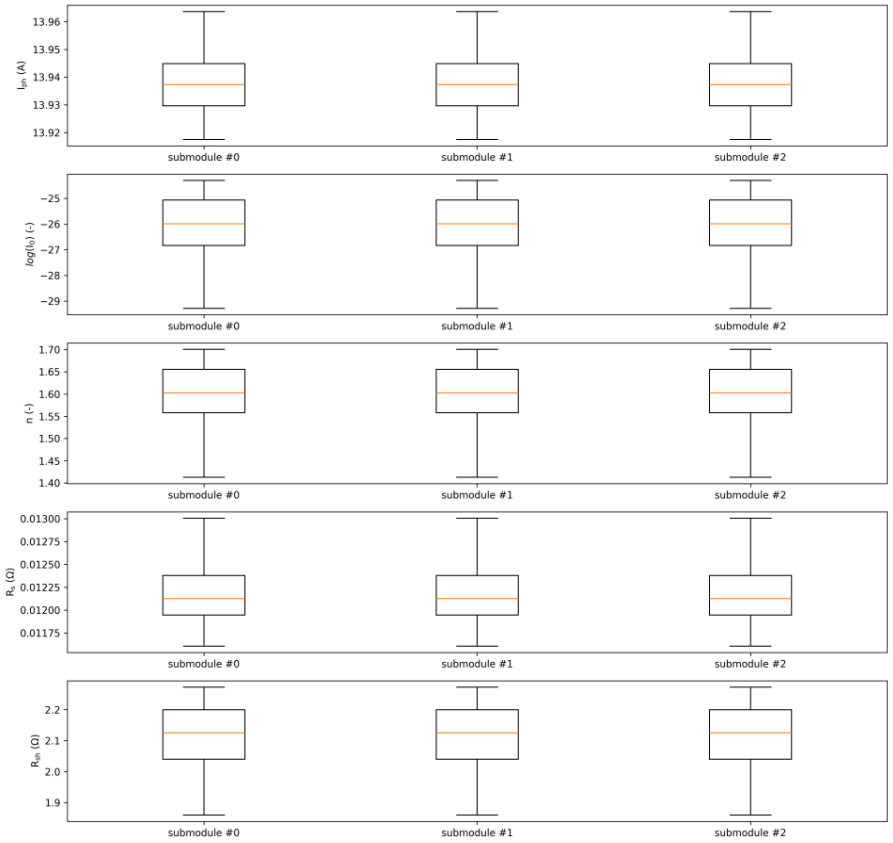

Fig. 7.8 Boxplots of estimated parameters for each string of the uniformly irradiated QCells module.

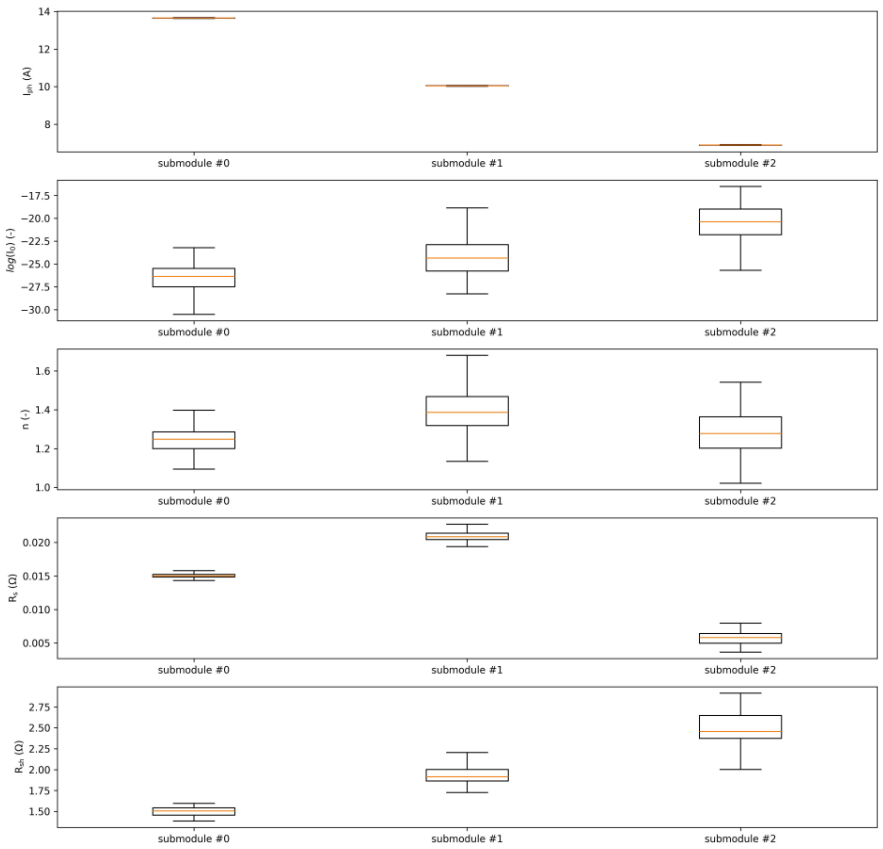

Fig. 7.9 Boxplots of estimated parameters for each string of the partially shaded QCells module.

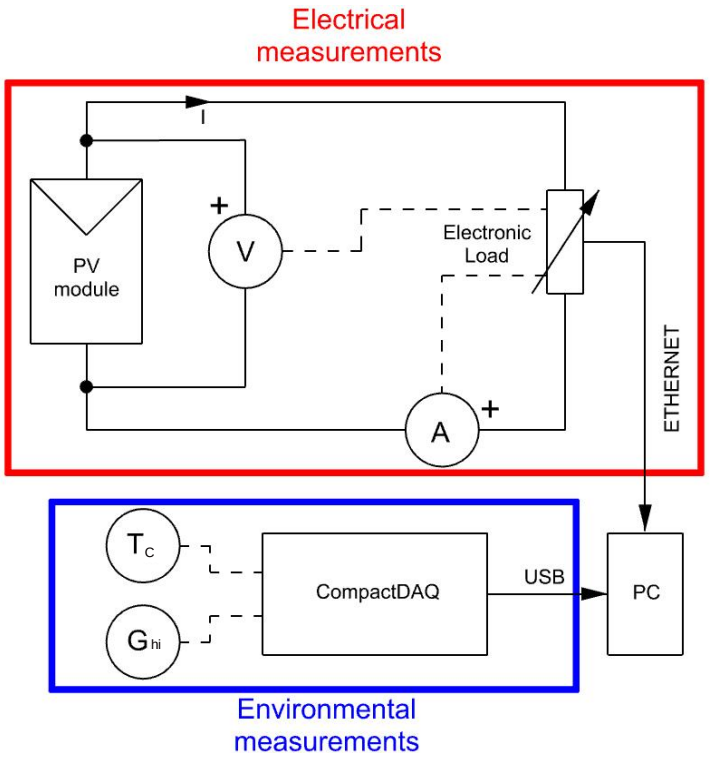

Fig. 7.10 Schematic of the measurement system.

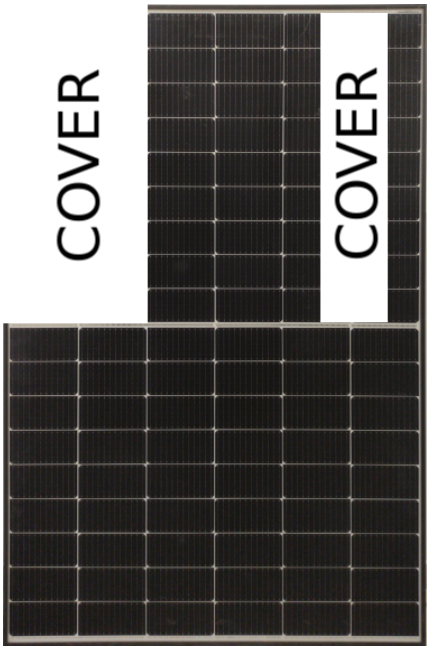

Fig. 7.11 Partial-shading mask applied to the Q.PEAK DUO M-G11 410 during testing.

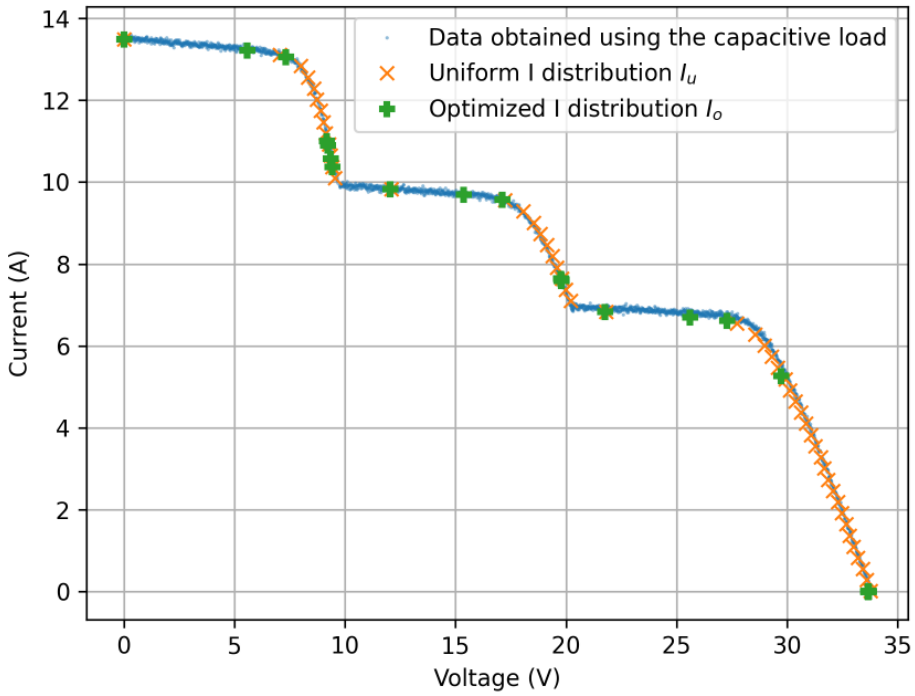

Fig. 7.12 Measured I–V curves under partial shading (Q.PEAK DUO M-G11 410).

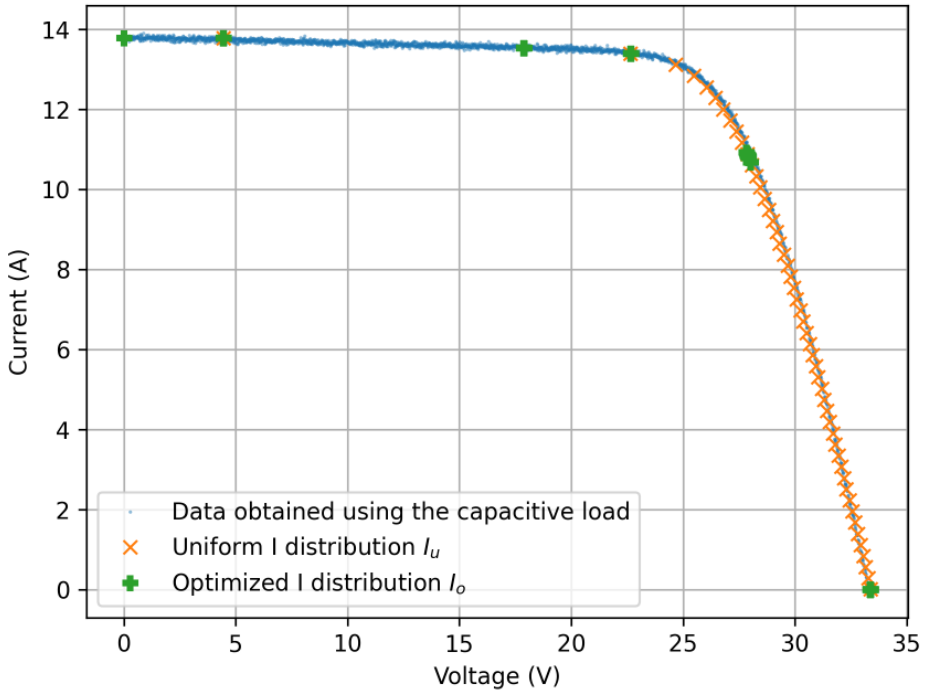

Fig. 7.13 Measured I–V curves under full irradiance (Q.PEAK DUO M-G11 410).

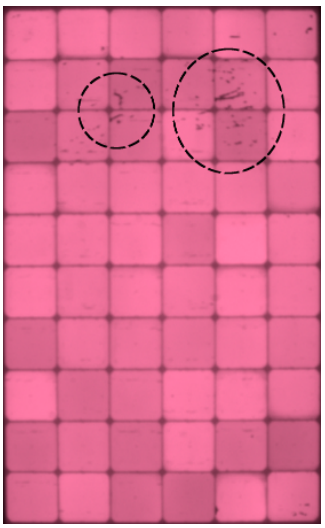

Fig. 7.14 Electroluminescence image of the LG370Q1C-V5 showing cell-level defects.

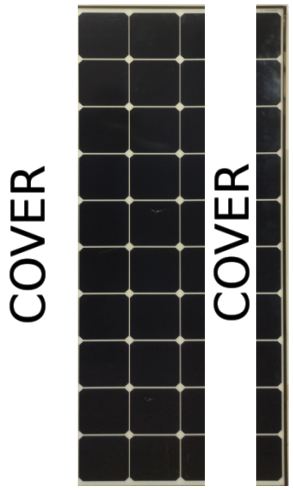

Fig. 7.15 Photograph of the LG370Q1C-V5 with the applied shading used in partial-shading tests.

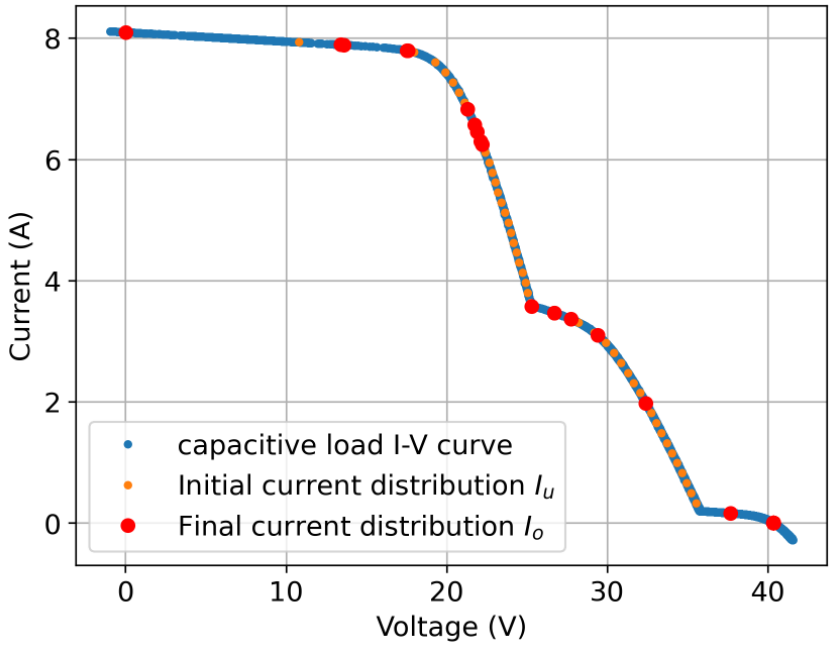

Fig. 7.16 Measured I–V curves under partial shading (LG370Q1C-V5).

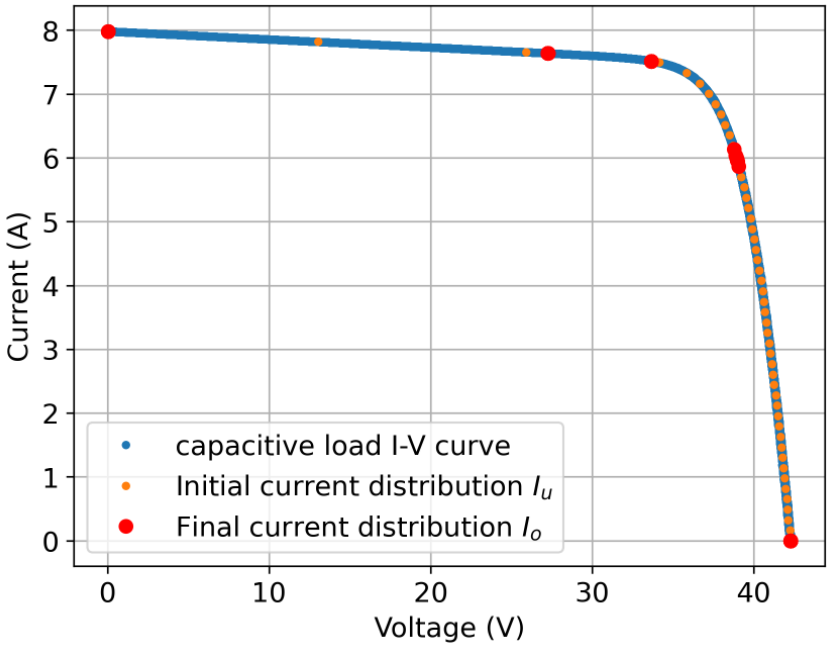

Fig. 7.17 Measured I–V curves under uniform irradiance (LG370Q1C-V5).

Table 7.19 Optimized sampling under uniform irradiance (LG370Q1C-V5): points as % of I_{sc} and V_{oc}; MPP highlighted.

Index	Current (% I_{sc})	Voltage (% V_{oc})	Power (% P_{mpp})	
1-5	0.00	100.00	0.00	
6	64.44	95.70	82.25	
7	64.46	95.70	82.26	
8	64.46	95.69	82.27	
9	64.47	95.69	82.28	
10	64.47	95.69	82.28	
11	64.48	95.69	82.30	
12	64.52	95.69	82.35	
13	79.62	94.15	99.98	
14	79.63	94.15	99.98	
15	79.63	94.15	99.99	
16	79.63	94.15	99.99	
17	79.63	94.15	99.99	
18	79.63	94.15	99.99	
19	79.63	94.15	99.99	
20	79.64	94.15	99.99	
21	79.64	94.15	100.00	MPP
22	91.71	76.87	94.02	
23	91.98	75.66	92.81	
24	92.05	75.34	92.48	
25	92.08	75.18	92.33	
26	92.15	74.82	91.96	
27	92.16	74.80	91.93	
28	92.16	74.80	91.93	
29	92.16	74.77	91.90	
30	92.17	74.75	91.88	
31	92.19	74.66	91.79	
32	92.19	74.63	91.76	
33	92.23	74.44	91.57	
34	92.43	73.44	90.53	
35-50	100.00	0.00	0.00	

Table 7.20 Uniform-sampling estimation results (uniform irradiance, LG370Q1C-V5).

String	Parameter	CRLBo	$\hat{\theta}$u	σ_u^2
String 0	I_{ph} (A)	1.03e-06	7.9999	1.15e-06
	$\log(I_0)$ (-)	1.49e-01	-28.2961	1.72e-01
	n (-)	3.38e-04	1.4357	3.76e-04
	R_s (mΩ)	4.37e-05	5.0661	4.87e-05
	R_{sh} (Ω)	3.70e-05	2.1972	4.12e-05
String 1	I_{ph} (A)	1.03e-06	8.0003	1.01e-06
	$\log(I_0)$ (-)	1.49e-01	-27.8825	1.46e-01
	n (-)	3.38e-04	1.4556	3.36e-04
	R_s (mΩ)	4.37e-05	4.9692	4.33e-05
	R_{sh} (Ω)	3.70e-05	2.2025	3.67e-05
String 2	I_{ph} (A)	1.03e-06	7.9997	1.19e-06
	$\log(I_0)$ (-)	1.49e-01	-28.2035	1.78e-01
	n (-)	3.38e-04	1.4405	3.92e-04
	R_s (mΩ)	4.37e-05	5.0955	5.07e-05
	R_{sh} (Ω)	3.70e-05	2.2025	4.30e-05

Table 7.21 Optimized-sampling estimation results (uniform irradiance, LG370Q1C-V5).

String	Parameter	CRLBo	$\hat{\theta}$o	σ_o^2
String 0	I_{ph} (A)	6.89e-07	8.0013	8.36e-07
	$\log(I_0)$ (-)	1.08e-01	-27.9514	1.10e-01
	n (-)	2.58e-04	1.4527	2.79e-04
	R_s (mΩ)	3.13e-05	5.0182	3.62e-05
	R_{sh} (Ω)	2.82e-05	2.2051	3.04e-05
String 1	I_{ph} (A)	7.68e-07	8.0022	8.44e-07
	$\log(I_0)$ (-)	1.23e-01	-27.9872	1.05e-01
	n (-)	2.71e-04	1.4562	2.15e-04
	R_s (mΩ)	2.96e-05	4.9423	3.10e-05
	R_{sh} (Ω)	2.56e-05	2.1984	3.43e-05
String 2	I_{ph} (A)	9.92e-07	7.9990	9.73e-07
	$\log(I_0)$ (-)	1.44e-01	-28.1005	1.07e-01
	n (-)	2.45e-04	1.4483	2.23e-04
	R_s (mΩ)	3.50e-05	5.0736	4.00e-05
	R_{sh} (Ω)	3.15e-05	2.2044	3.38e-05

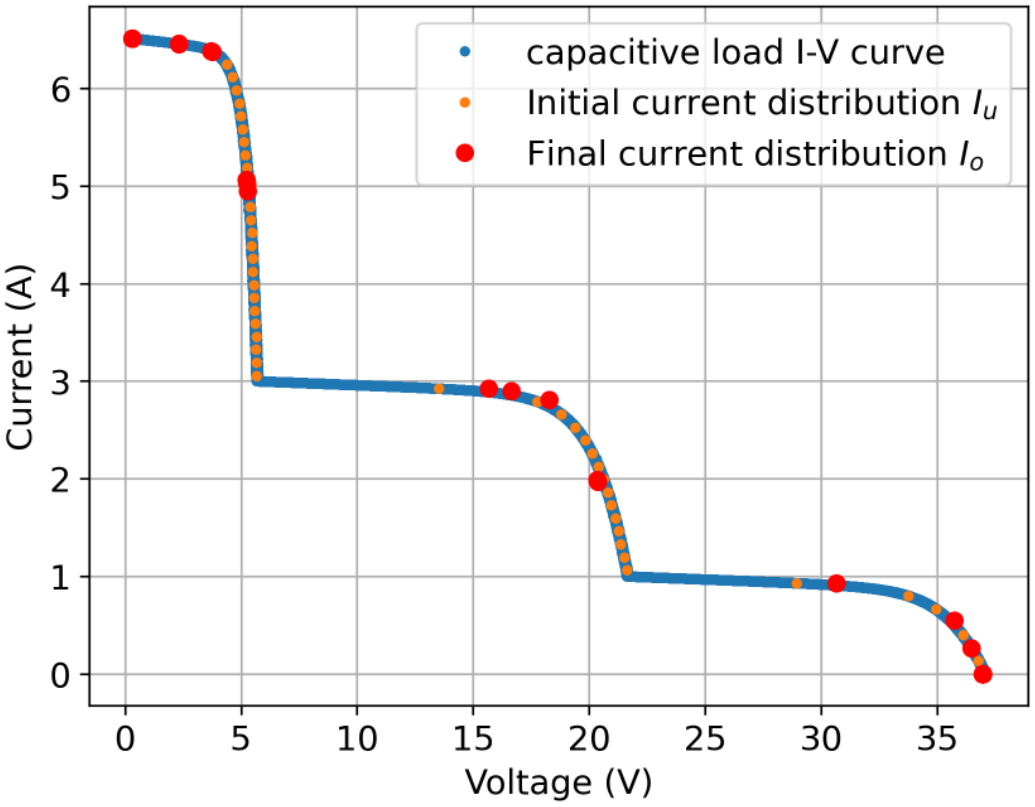

Fig. 7.18 Measured I–V curves under partial shading (SANYO HIP 230HDE1).

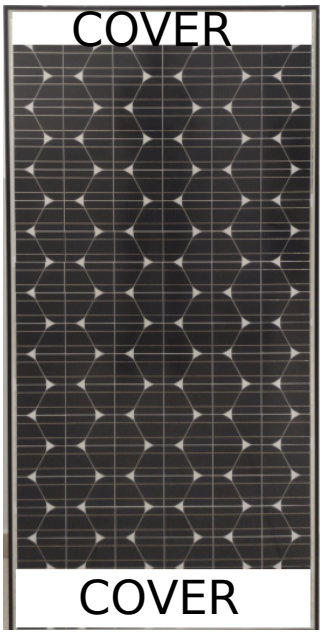

Fig. 7.19 Shading layout used for the SANYO HIP 230HDE1 during partial-shading tests.

Table 7.22 Optimized sampling under partial shading (SANYO HIP 230HDE1): points as % of I_{sc} and V_{oc}; MPP highlighted.

Index	Current (% I_{sc})	Voltage (% V_{oc})	Power (% P_{mpp})	
1-4	0.00	100.00	0.00	
5	6.26	99.13	29.10	
6	6.30	99.13	29.31	
7	10.05	97.99	46.19	
8	10.18	97.90	46.74	
9	14.17	77.71	51.66	
10	14.20	77.17	51.41	
11	14.27	75.97	50.84	
12	42.40	44.89	89.27	
13	45.05	44.56	94.12	
14	49.47	43.11	100.00	MPP
15	55.09	30.50	78.80	
16	55.14	30.24	78.19	
17	82.95	14.28	55.56	
18	96.67	8.42	38.17	
19	98.69	4.08	18.88	
20-50	100.00	0.00	0.00	

Table 7.23 Uniform-sampling estimation results (partial shading, SANYO HIP 230HDE1).

String	Parameter	CRLBu	$\hat{\theta}$u	σ_u^2
String 0	I_{ph} (A)	8.40e-07	6.5171	8.54e-05
	$\log(I_0)$ (-)	7.82e-02	-8.5231	3.73e+00
	n (-)	6.27e-04	1.7170	9.68e-02
	R_s (mΩ)	6.51e-05	0.1543	7.23e-03
	R_{sh} (Ω)	1.10e-02	5.0465	2.72e+01
String 1	I_{ph} (A)	8.40e-07	2.9510	3.39e-03
	$\log(I_0)$ (-)	7.82e-02	-10.8982	2.60e+00
	n (-)	6.27e-04	1.3813	3.31e-02
	R_s (mΩ)	6.51e-05	0.6512	6.09e-03
	R_{sh} (Ω)	1.10e-02	8.9671	5.31e+02
String 2	I_{ph} (A)	8.40e-07	1.0209	6.00e-03
	$\log(I_0)$ (-)	7.82e-02	-13.5422	2.94e+01
	n (-)	6.27e-04	1.1346	1.86e-01
	R_s (mΩ)	6.51e-05	1.3684	2.54e-01
	R_{sh} (Ω)	1.10e-02	3.2658	3.84e+02

Table 7.24 Optimized-sampling estimation results (partial shading, SANYO HIP 230HDE1).

String	Parameter	CRLBo	$\hat{\theta}$o	σ_o^2
String 0	I_{ph} (A)	2.87e-07	6.5231	2.21e-05
	$\log(I_0)$ (-)	2.51e-02	-11.7665	8.48e-01
	n (-)	2.14e-04	1.2789	2.66e-02
	R_s (mΩ)	2.26e-02	0.140	2.75
	R_{sh} (Ω)	4.84e-03	2.9194	5.68e+00
String 1	I_{ph} (A)	1.84e-07	3.0291	1.02e-03
	$\log(I_0)$ (-)	3.34e-02	-11.5922	9.34e-01
	n (-)	2.32e-04	1.2673	1.76e-02
	R_s (mΩ)	1.91e-02	0.120	2.19
	R_{sh} (Ω)	3.73e-03	2.9231	8.23e+00
String 2	I_{ph} (A)	4.42e-07	1.0386	1.94e-03
	$\log(I_0)$ (-)	1.75e-02	-12.2965	1.02e+00
	n (-)	1.63e-04	1.2738	3.74e-02
	R_s (mΩ)	2.79e-02	0.100	58.1
	R_{sh} (Ω)	5.47e-03	2.9202	1.44e+01

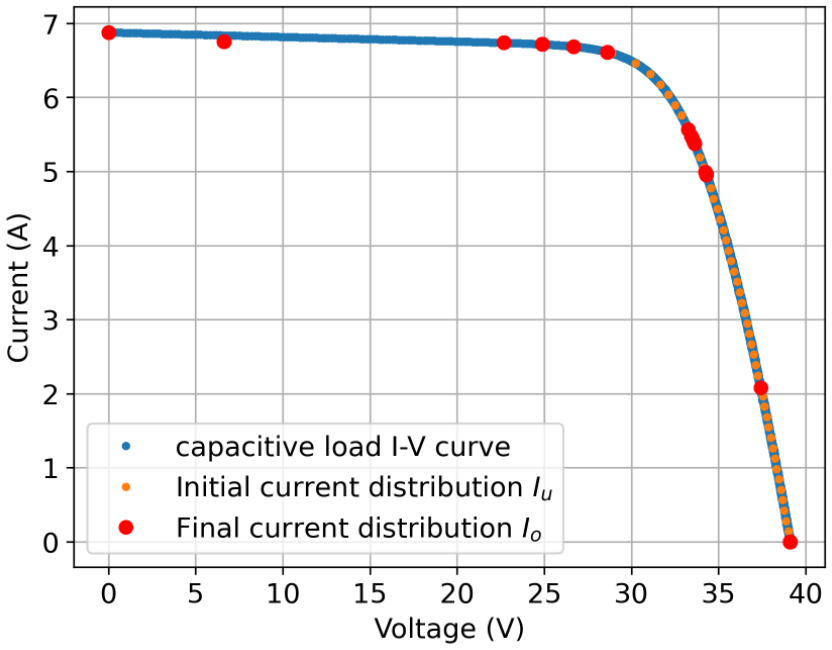

Fig. 7.20 Measured I–V curves under uniform irradiance (SANYO HIP 230HDE1).

Table 7.25 Optimized sampling under uniform irradiance (SANYO HIP 230HDE1): points as % of I_{sc} and V_{oc}; MPP highlighted.

Index	Current (% I_{sc})	Voltage (% V_{oc})	Power (% P_{mpp})	
1	0.00	100.00	0.00	
2	16.92	98.23	23.63	
3	16.94	98.23	23.66	
4	57.98	97.95	80.73	
5	57.98	97.95	80.73	
6	57.98	97.95	80.73	
7	63.59	97.66	88.29	
8	63.59	97.66	88.29	
9	63.60	97.66	88.29	
10	63.60	97.66	88.29	
11	63.60	97.66	88.29	
12	63.60	97.66	88.30	
13	68.17	97.23	94.22	
14	68.18	97.22	94.23	
15	73.16	96.14	99.99	
16	73.16	96.14	99.99	
17	73.16	96.14	99.99	
18	73.16	96.14	99.99	
19	73.16	96.14	99.99	
20	73.17	96.14	100.00	MPP
21	85.04	80.90	97.80	
22	85.47	79.63	96.75	
23	85.60	79.24	96.42	
24	85.82	78.56	95.84	
25	85.94	78.16	95.50	
26	87.54	72.57	90.31	
27	87.64	72.16	89.91	
28	87.65	72.15	89.90	
29	87.65	72.12	89.86	
30	87.66	72.10	89.85	
31	87.67	72.07	89.81	
32	87.68	72.03	89.78	
33	95.65	30.19	41.05	
34-50	100.00	0.00	0.00	

Table 7.26 Uniform-sampling estimation results (uniform irradiance, SANYO HIP 230HDE1).

String	Parameter	CRLBu	$\hat{\theta}$u	σ_u^2
String 0	I_{ph} (A)	2.98e-07	6.8582	3.86e-02
	$\log(I_0)$ (-)	8.84e-02	-20.6462	4.98e+00
	n (-)	2.40e-04	1.3115	4.60e-02
	R_s (mΩ)	3.54e-05	8.259	2.19e-03
	R_{sh} (Ω)	1.79e-04	4.7805	7.92e+01
String 1	I_{ph} (A)	2.98e-07	6.8573	3.78e-02
	$\log(I_0)$ (-)	8.84e-02	-20.6808	5.04e+00
	n (-)	2.40e-04	1.3071	4.61e-02
	R_s (mΩ)	3.54e-05	8.196	2.22e-03
	R_{sh} (Ω)	1.79e-04	4.7683	7.69e+01
String 2	I_{ph} (A)	2.98e-07	6.8582	3.83e-02
	$\log(I_0)$ (-)	8.84e-02	-20.6372	4.90e+00
	n (-)	2.40e-04	1.3121	4.53e-02
	R_s (mΩ)	3.54e-05	8.232	2.16e-03
	R_{sh} (Ω)	1.79e-04	4.7822	7.86e+01

Table 7.27 Optimized-sampling estimation results (uniform irradiance, SANYO HIP 230HDE1).

String	Parameter	CRLBo	$\hat{\theta}$o	σ_o^2
String 0	I_{ph} (A)	1.19e-07	6.8912	1.27e-02
	$\log(I_0)$ (-)	3.54e-02	-21.9451	1.59e+00
	n (-)	9.61e-05	1.2664	1.55e-02
	R_s (mΩ)	1.15e-05	10.951	0.85e-03
	R_{sh} (Ω)	5.42e-05	3.4262	2.87e+01
String 1	I_{ph} (A)	1.29e-07	6.9023	1.38e-02
	$\log(I_0)$ (-)	3.70e-02	-21.9763	1.63e+00
	n (-)	1.01e-04	1.2637	1.66e-02
	R_s (mΩ)	1.21e-05	10.895	0.91e-03
	R_{sh} (Ω)	5.76e-05	3.4131	2.94e+01
String 2	I_{ph} (A)	1.24e-07	6.8956	1.35e-02
	$\log(I_0)$ (-)	3.62e-02	-21.9824	1.61e+00
	n (-)	9.98e-05	1.2641	1.58e-02
	R_s (mΩ)	1.18e-05	10.912	0.88e-03
	R_{sh} (Ω)	5.60e-05	3.4227	2.91e+01

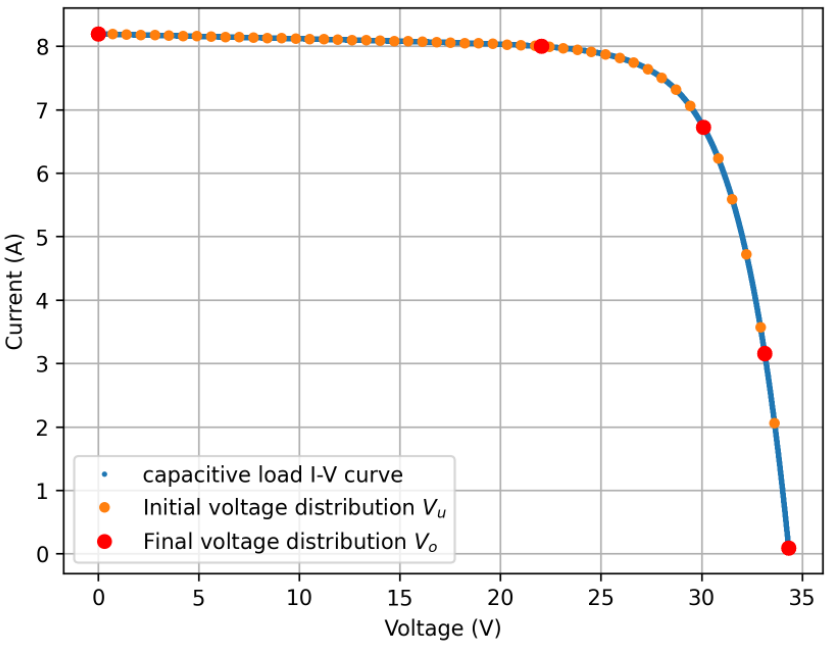

Fig. 7.21 Measured I–V curve and optimized voltage samples under uniform irradiance (JA Solar).

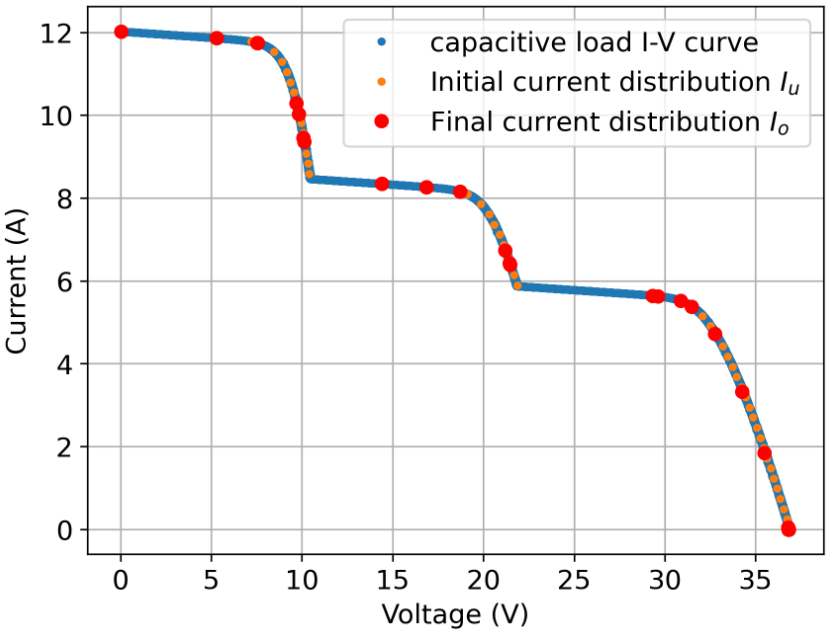

Fig. 7.22 Measured I–V curves under partial shading (HT54-18XN-435 module).

Table 7.28 Optimized voltage-domain sampling under uniform irradiance (JA Solar): points as % of V_{oc} and I_{sc}; MPP highlighted.

Index	Current (% I_{sc})	Voltage (% V_{oc})	Power (% P_{mpp})	
1-15	0.00	100.00	0.00	
16	64.15	97.60	87.04	
17	64.16	97.60	87.05	
18	64.19	97.60	87.08	
19	64.20	97.60	87.10	
20	64.21	97.60	87.11	
21	64.21	97.60	87.11	
22	64.22	97.60	87.12	
23	87.67	82.06	100.00	MPP
24	87.67	82.05	99.99	
25	87.68	82.04	99.98	
26	87.68	82.04	99.98	
27	87.68	82.03	99.97	
28	87.68	82.03	99.97	
29	87.69	82.01	99.96	
30	87.69	82.00	99.95	
31	87.70	81.99	99.94	
32	96.53	38.53	51.70	
33	96.53	38.53	51.69	
34	96.53	38.52	51.68	
35	96.53	38.52	51.68	
36	96.53	38.52	51.68	
37	96.53	38.51	51.68	
38	96.53	38.51	51.68	
39-50	100.00	1.13	1.57	

Table 7.29 Estimation results for the JA Solar module under uniform irradiance with voltage-based sampling.

Sampling	Parameter	CRLB	$\hat{\theta}$	σ^2
Uniform	I_{ph} (A)	3.12e-05	8.2162e+00	3.11e-05
	$\log(I_0)$ (-)	4.30e-02	-1.3984e+01	4.26e-02
	n (-)	5.31e-04	1.8102e+00	5.30e-04
	R_s (mΩ)	1.70e-05	9.8237e-01	1.70e-05
	R_{sh} (Ω)	2.49e-02	3.0633e+00	2.71e-02
Optimized	I_{ph} (A)	2.56e-05	8.2016e+00	2.55e-05
	$\log(I_0)$ (-)	3.81e-02	-1.4034e+01	3.77e-02
	n (-)	4.47e-04	1.8050e+00	4.46e-04
	R_s (mΩ)	1.39e-05	9.9641e-01	1.39e-05
	R_{sh} (Ω)	1.91e-02	3.0312e+00	2.08e-02

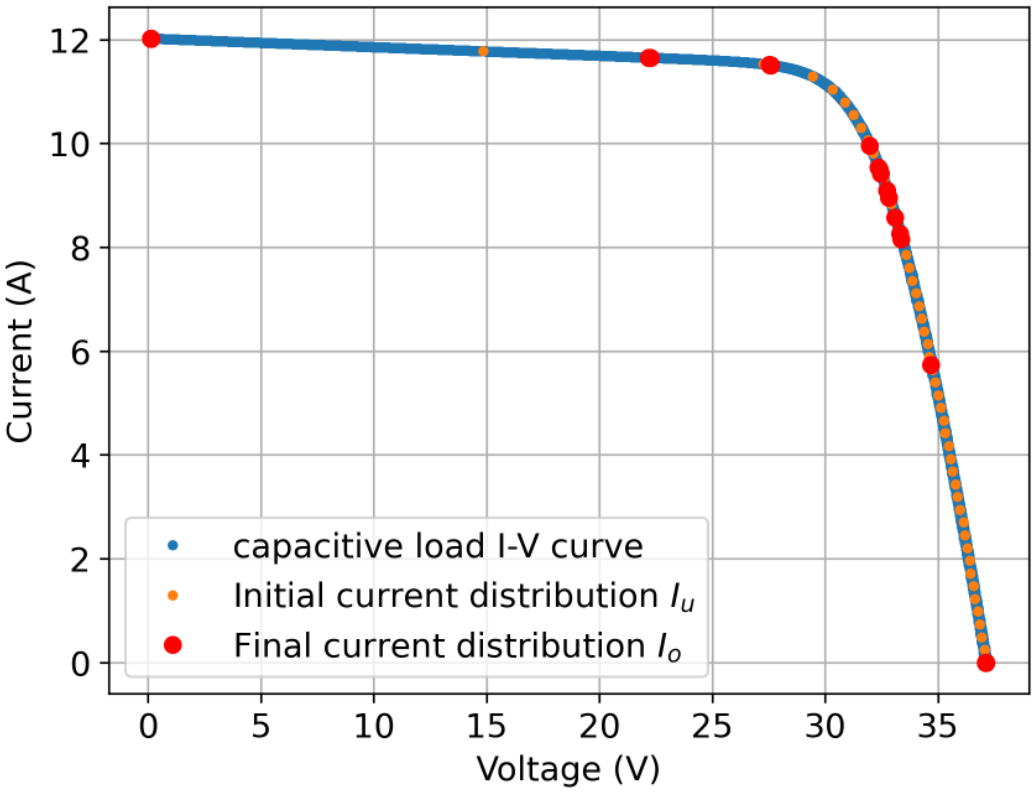

Fig. 7.23 Measured I–V curves under uniform irradiance (HT54-18XN-435 module).

Table 7.30 Optimized sampling under partial shading (HT54-18XN-435): points as % of I_{sc} and V_{oc}; MPP highlighted.

Index	Current (% I_{sc})	Voltage (% V_{oc})	Power (% P_{mpp})	
1	0.00	100.00	0.00	
2	14.38	98.66	36.89	
3	14.38	98.66	36.90	
4	20.43	97.69	51.89	
5	20.45	97.69	51.95	
6	20.51	97.67	52.09	
7	26.32	85.61	58.59	
8	26.68	83.44	57.90	
9	27.38	78.63	55.99	
10	27.49	77.81	55.62	
11	39.09	69.38	70.53	
12	39.09	69.38	70.53	
13	45.78	68.75	81.83	
14	45.78	68.75	81.84	
15	50.82	67.82	89.63	
16	57.54	56.00	83.79	
17	58.19	53.47	80.90	
18	58.27	53.16	80.55	
19	79.58	46.93	97.12	
20	80.39	46.82	97.88	
21	83.85	45.86	100.00	MPP
22	85.48	44.72	99.39	
23	88.93	39.29	90.87	
24	93.04	27.65	66.91	
25	96.37	15.34	38.46	
26	99.92	0.32	0.85	
27	99.99	0.01	0.02	
28-50	100.00	0.00	0.00	

Table 7.31 Uniform-sampling estimation results (partial shading, HT54-18XN-435).

String	Parameter	CRLBu	$\hat{\theta}$u	σ_u^2
String 0	I_{ph} (A)	1.15e-06	12.0781	1.15e-06
	$\log(I_0)$ (-)	6.12e-02	-18.9970	6.02e-02
	n (-)	3.66e-04	1.7057	3.69e-04
	R_s (mΩ)	1.441	12.13	1.443
	R_{sh} (Ω)	4.89e-04	2.6170	5.20e-04
String 1	I_{ph} (A)	1.01e-04	8.4980	1.05e-04
	$\log(I_0)$ (-)	2.63e-01	-18.9792	2.60e-01
	n (-)	1.64e-03	1.7071	1.68e-03
	R_s (mΩ)	8.095	12.08	8.194
	R_{sh} (Ω)	2.32e-02	2.6346	2.69e-02
String 2	I_{ph} (A)	1.25e-02	5.9141	1.24e-02
	$\log(I_0)$ (-)	1.68e+00	-19.1600	1.66e+00
	n (-)	1.09e-02	1.6964	1.11e-02
	R_s (mΩ)	6.2155	12.12	6.3072
	R_{sh} (Ω)	1.37e+00	2.9135	1.01e+01

Table 7.32 Optimized-sampling estimation results (partial shading, HT54-18XN-435).

String	Parameter	CRLBo	$\hat{\theta}$o	σ_o^2
String 0	I_{ph} (A)	1.82e-07	12.0789	4.26e-07
	$\log(I_0)$ (-)	1.04e-02	-19.0498	2.42e-02
	n (-)	6.31e-05	1.7012	1.49e-04
	R_s (mΩ)	4.4858	12.16	1.0547
	R_{sh} (Ω)	1.84e-05	2.6031	4.36e-05
String 1	I_{ph} (A)	1.16e-06	8.4993	3.60e-06
	$\log(I_0)$ (-)	2.61e-02	-19.0102	8.02e-02
	n (-)	1.66e-04	1.7045	5.15e-04
	R_s (mΩ)	2.211	12.06	6.857
	R_{sh} (Ω)	1.41e-04	2.6055	4.38e-04
String 2	I_{ph} (A)	3.32e-04	5.9144	6.13e-04
	$\log(I_0)$ (-)	1.64e-01	-19.3788	3.17e-01
	n (-)	1.07e-03	1.6761	1.96e-03
	R_s (mΩ)	1.4652	12.40	2.7342
	R_{sh} (Ω)	3.54e-02	2.4736	5.62e-02

Table 7.33 Optimized sampling under uniform irradiance (HT54-18XN-435): points as % of I_{sc} and V_{oc}; MPP highlighted.

Index	Current (% I_{sc})	Voltage (% V_{oc})	Power (% P_{mpp})	
1-7	0.00	100.00	0.00	
8	59.75	96.93	81.22	
9	59.78	96.93	81.26	
10	59.79	96.93	81.27	
11	59.82	96.93	81.31	
12	59.83	96.93	81.33	
13	59.87	96.93	81.37	
14	59.91	96.93	81.43	
15	60.02	96.92	81.58	
16	74.22	95.76	99.67	
17	74.27	95.75	99.73	
18	74.30	95.75	99.77	
19	74.31	95.74	99.78	
20	74.31	95.74	99.78	
21	74.32	95.74	99.79	
22	74.33	95.75	99.80	
23	86.14	82.78	100.00	MPP
24	87.19	79.36	97.04	
25	87.29	79.01	96.72	
26	87.46	78.38	96.14	
27	88.18	75.64	93.53	
28	88.45	74.52	92.44	
29	89.19	71.31	89.19	
30	89.74	68.75	86.51	
31	89.92	67.86	85.57	
32	93.48	47.70	62.53	
33-50	100.00	0.00	0.00	

Table 7.34 Uniform-sampling estimation results (uniform irradiance, HT54-18XN-435).

String	Parameter	CRLBu	$\hat{\theta}$u	σ_u^2
String 0	I_{ph} (A)	2.33e-06	12.0809	2.74e-06
	$\log(I_0)$ (-)	2.20e-01	-29.4074	2.68e-01
	n (-)	7.73e-04	1.8794	9.04e-04
	R_s (mΩ)	4.237e-01	1.229	4.940e-01
	R_{sh} (Ω)	1.42e-04	2.5860	1.62e-04
String 1	I_{ph} (A)	2.33e-06	12.0779	2.38e-06
	$\log(I_0)$ (-)	2.20e-01	-28.8261	2.18e-01
	n (-)	7.73e-04	1.9140	7.96e-04
	R_s (mΩ)	4.237e-01	1.207	4.371e-01
	R_{sh} (Ω)	1.42e-04	2.6058	1.48e-04
String 2	I_{ph} (A)	2.33e-06	12.0803	2.45e-06
	$\log(I_0)$ (-)	2.20e-01	-29.2212	2.34e-01
	n (-)	7.73e-04	1.8906	8.11e-04
	R_s (mΩ)	4.237e-01	1.222	4.447e-01
	R_{sh} (Ω)	1.42e-04	2.5948	1.49e-04

Table 7.35 Optimized-sampling estimation results (uniform irradiance, HT54-18XN-435).

String	Parameter	CRLBo	$\hat{\theta}$o	σ_o^2
String 0	I_{ph} (A)	9.68e-07	12.0795	1.43e-06
	$\log(I_0)$ (-)	8.93e-02	-29.1062	1.72e-01
	n (-)	3.36e-04	1.8976	5.04e-04
	R_s (mΩ)	2.1284	12.18	3.2058
	R_{sh} (Ω)	5.32e-05	2.5979	7.63e-05
String 1	I_{ph} (A)	7.55e-07	12.0793	1.65e-06
	$\log(I_0)$ (-)	7.41e-02	-29.0755	1.68e-01
	n (-)	2.76e-04	1.8964	4.85e-04
	R_s (mΩ)	2.0865	12.13	3.1074
	R_{sh} (Ω)	5.15e-05	2.5974	6.73e-05
String 2	I_{ph} (A)	1.01e-06	12.0791	1.81e-06
	$\log(I_0)$ (-)	6.64e-02	-29.1608	1.65e-01
	n (-)	2.94e-04	1.8962	4.77e-04
	R_s (mΩ)	1.8494	12.17	2.9360
	R_{sh} (Ω)	4.87e-05	2.5975	6.34e-05

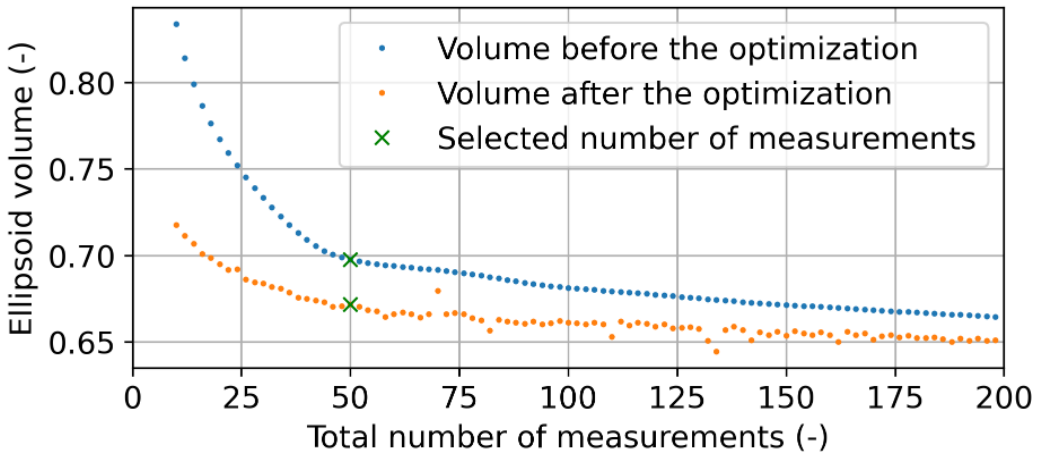

Fig. 7.24 Confidence–ellipsoid volume from the FIM, before and after optimization, versus the number of samples.

Chapter 8

Energy Yield Assessment of Different PV Technologies across Multiple Climates

Positioning with respect to the state of the art

The estimation of photovoltaic energy production over extended periods is a well-established research topic, and a broad range of models has been proposed in the literature. The simplest approaches relate output power linearly to incident irradiance, as in the irradiance-proportionality (I–P) model [21] and the PESRC formulation [20]. Temperature-corrected variants augment this baseline with a power temperature coefficient [22]. More elaborate semi-empirical models introduce additional meteorological predictors such as wind speed and air mass [23, 24], or adopt piecewise irradiance-based representations [53]. While these approaches are computationally inexpensive and require only a small number of module-level parameters, their coefficients are typically calibrated on a specific device and installation, limiting their transferability to different technologies or climates.

A more physically grounded alternative consists of expressing the five parameters of the single-diode equivalent circuit as functions of irradiance and temperature, and

propagating these functions to predict power output at arbitrary operating conditions. The foundational framework for this approach was established by De Soto et al. [14], whose five-parameter model introduced semi-empirical regression equations for each circuit parameter. Subsequent contributions by Tossa et al. [26] and Malik and Chandel [27] proposed refinements to the temperature and irradiance dependences of individual parameters. However, several limitations persist in this body of work. First, the regression coefficients are rarely provided for commercial modules, and when available they are often derived from older PV technologies — predominantly first-generation monocrystalline and polycrystalline silicon — whose electrical characteristics differ significantly from those of contemporary high-efficiency architectures such as Heterojunction (HJT), Tunnel Oxide Passivated Contact (TOPCon), and Interdigitated Back Contact (IBC). Second, no existing study systematically validates the approach across multiple climatic sites using independent acquisition systems, making it difficult to assess the geographic and seasonal robustness of the identified parameter equations. Third, the integration of a robust data-filtering pipeline — capable of automatically excluding measurements affected by partial shading, transient irradiance, or instrumental noise — has not been addressed as a formal component of the methodology.

The present chapter addresses these limitations by introducing a four-step workflow that combines multi-criteria data preprocessing, per-curve parameter extraction via a cascaded Simulated Annealing and Nelder–Mead optimisation, nonlinear regression of the five SDM parameters as functions of irradiance and temperature, and power and energy reconstruction. The methodology is validated on ten crystalline-silicon PV modules spanning a wide range of technologies and rated powers (up to 450 W), tested at two outdoor sites with different latitudes and climates: Politecnico di Torino (Italy) and Universidad de Jaén (Spain). Up to approximately 15 000 I–V curves were acquired per module over monitoring periods of up to eleven months, enabling a statistically robust assessment of the parameter regression and energy prediction accuracy.

The proposed approach is benchmarked against five representative models from the literature: the Jones–Underwood formulation [23], the Al-Bashir empirical regression [24], the Park piecewise model [53], the SAM semi-empirical formulation [22], and the PESRC irradiance-proportional baseline [20]. None of these benchmarks exploits device-level equivalent-circuit parameters identified from experimental I–V curves; the comparison therefore directly quantifies the benefit of

physically-grounded modelling over empirical or simplified approaches, particularly for the most recent cell technologies that are increasingly dominant in the current market.

8.1 Methodology

This study introduces an innovative methodological framework aimed at estimating the energy production of photovoltaic (PV) modules with improved accuracy compared to the models currently available in the literature. The complete workflow of the proposed approach, which is articulated in four main steps, is schematically illustrated in Figure 8.1.

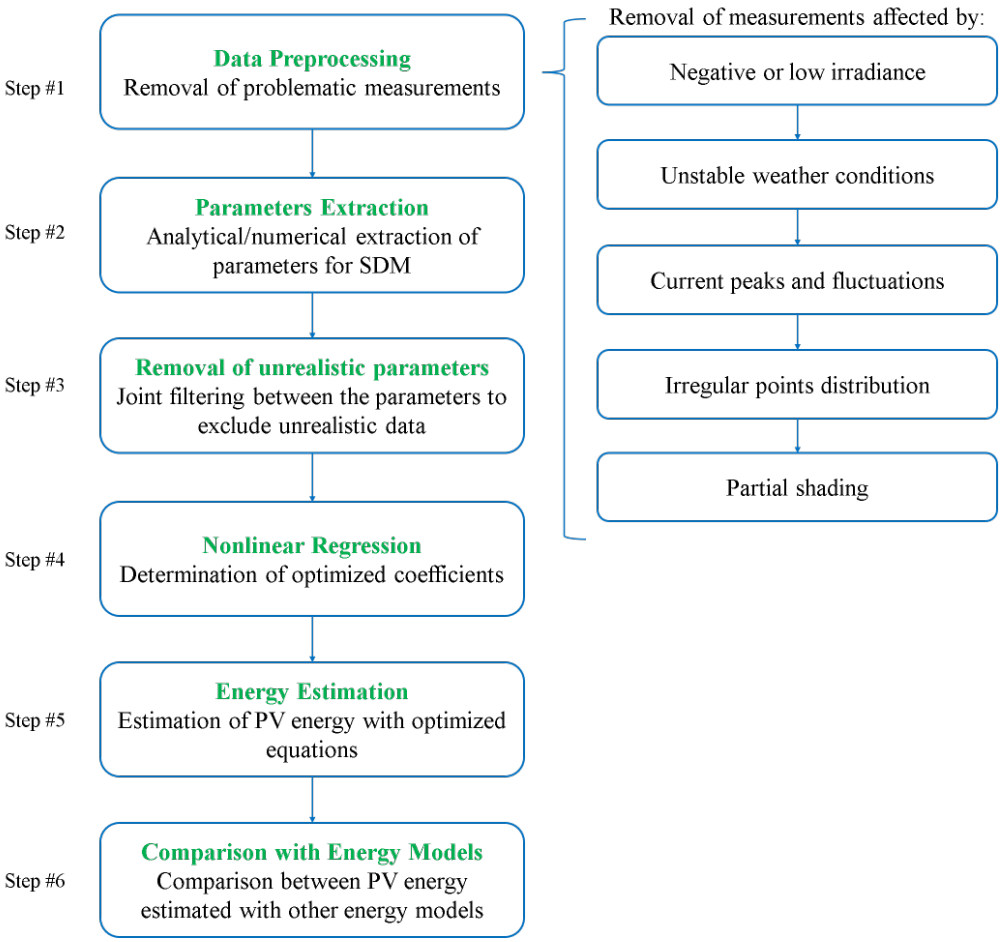

Fig. 8.1 Flowchart of the proposed procedure.

8.1.1 Step #1 — Data Preprocessing

The first stage involves the preprocessing of the experimental *I–V* data through a series of filtering operations designed to eliminate measurements affected by unstable meteorological conditions, electrical mismatches, instrumental inaccuracies, or other anomalies. The following criteria are sequentially applied:

- **Low or negative irradiance.** Measurements characterized by plane-of-array irradiance lower than 100 W/m^2 are discarded. The proposed methodology is intended to operate in the irradiance range commonly observed in multi-megawatt PV installations, i.e., between 100 and 1000 W/m^2.

- **Unstable environmental conditions.** For each electrical measurement, the normalized root mean square error (NRMSE) of the M irradiance and temperature samples is computed as:

$$\begin{aligned} NRMSE_{\mathrm{G}} &= \frac{\sqrt{\frac{\sum_{j=1}^{M}(G_{\mathrm{j}}-G_{\mathrm{ave}})^2}{M}}}{G_{\mathrm{ave}}} \\ NRMSE_{\mathrm{T}} &= \frac{\sqrt{\frac{\sum_{j=1}^{M}(T_{\mathrm{PV,j}}-T_{\mathrm{PV,ave}})^2}{M}}}{T_{\mathrm{PV,ave}}} \end{aligned} \tag{8.1}$$

  where G_{j} and $T_{\mathrm{PV,j}}$ denote the j^{th} irradiance and module temperature samples, while G_{ave} and $T_{\mathrm{PV,ave}}$ represent their corresponding mean values. Measurements are excluded when $NRMSE_{\mathrm{G}} \geq 2\%$, $NRMSE_{\mathrm{T}} \geq 3\%$, or when the average wind speed exceeds 1 m/s, indicating significant meteorological variability.

- **Current peaks and fluctuations.** When the module performance is assessed using a capacitive load, spurious current oscillations may arise due to parasitic capacitances or inductances associated with the series interconnection of solar cells [54]. These disturbances are typically mitigated by applying a negative precharge to the capacitor, thus confining the irregularities to the negative voltage region and preserving the first-quadrant *I–V* characteristics.

- **Irregular point distribution.** To enhance the stability of the numerical parameter extraction, the algorithm operates more efficiently on *I–V* curves exhibiting a uniform distribution of sampling points between the short-circuit

and open-circuit regions. If the number of samples beyond the MPP voltage exceeds five times the number of samples before it, a weighted reduction is applied, ensuring a balanced point distribution.

- **Partial shading.** Measurements affected by partial shading are detected and removed through an analysis of the power-voltage (P-V) characteristics. The exclusion criteria are as follows:
  - Presence of more than one local maximum with prominence $\geq 1\%$ of the maximum power.
  - Occurrence of steep declines where dP/dV decreases by more than 10% of the maximum power.
  - Existence of discontinuities exceeding 10% of the maximum power.

8.1.2 Step #2 — Parameters Extraction

Equivalent circuit models with different parameterizations can reproduce the experimental I–V behavior of PV devices [55]. In this work, the Single Diode Model (SDM) [7] is employed, where the five governing parameters—photogenerated current (I_{ph}), reverse saturation current (I_0), diode ideality factor (n), series resistance (R_s), and shunt resistance (R_sh)—are determined through numerical optimization techniques.

Appropriate physical constraints and parameter bounds, as defined in [54], are imposed to prevent non-physical results and to ensure numerical convergence. A hybrid optimization scheme combining Simulated Annealing (SA) and Nelder–Mead (NM) algorithms is implemented. The SA algorithm first explores the global solution space to avoid local minima, while the NM algorithm refines the optimum in the neighbourhood of the global minimum.

The initial parameter estimates are derived analytically following the method described in Section 8.2 of [6], which allows the computation of four parameters, excluding R_sh. The shunt resistance is often neglected in the literature because its influence on the I–V characteristics is minimal under uniform illumination [56]. However, in the presence of shading, the slope m of the I–V curve near the short-circuit condition—related to R_sh through $R_\mathrm{sh} \approx -1/m$—may vary significantly. Accordingly, in this study, the initial value of R_sh for each I–V curve is set to $-1/m$.

The numerical optimization is performed on the SDM equation:

$$I = I_{ph} - I_0 \cdot \left(\exp\left(\frac{q \cdot V_j}{n \cdot k_B \cdot T} \right) - 1 \right) - \frac{(V + R_\mathrm{s} \cdot I)}{R_\mathrm{sh}} \tag{8.2}$$

where q denotes the electron charge (1.6×10^{-19} C), k_B is the Boltzmann constant (1.38×10^{-23} J/K), V_j is the junction voltage, and the other symbols have their usual meaning. The resistances R_s and R_sh are scaled by the number of cells N_s in the module. Hence, the optimization is performed at cell level, and the module-level resistances are obtained by multiplying the cell values by N_s. Unless otherwise specified, all subsequent parameters refer to the module level.

The reconstructed I–V curve is then obtained from the optimized parameters, and the deviation in maximum power ΔP between the simulated and experimental data is computed. Curves with $\Delta P > 1\%$ are excluded. The main substeps of this phase are schematically illustrated in Figure 8.2 [54].

8.1.3 Step #3 — Nonlinear Regression

The dependence of the SDM parameters on environmental variables is expressed through the following empirical relations, where the coefficients highlighted in bold are optimized by nonlinear regression techniques [26, 27, 57, 58]:

$$I_{ph} = \boldsymbol{I}_{ph,\mathrm{STC}} \cdot \left[1 + \alpha \cdot (T_\mathrm{c} - T_{c,\mathrm{STC}}) \right] \cdot \frac{G}{G_\mathrm{STC}} \tag{8.3}$$

where α represents the temperature coefficient of the short-circuit current, T_c and $T_{c,\mathrm{STC}}$ are the actual and standard cell temperatures, and G and G_STC denote the irradiance and its standard reference value, respectively.

$$I_0 = \boldsymbol{I}_{0,\mathrm{STC}} \cdot \left(\frac{T_\mathrm{c}}{T_{c,\mathrm{STC}}} \right)^3 \cdot \exp\left[\left(\frac{E_{g,\mathrm{STC}}}{T_\mathrm{STC}} - \frac{E_g(T_\mathrm{c})}{T_\mathrm{c}} \right) \cdot \frac{1}{k_b} \right] \tag{8.4}$$

where $E_g(T_\mathrm{c})$ and $E_{g,\mathrm{STC}}$ denote the semiconductor bandgap energy at the actual and standard temperatures, respectively.

$$n = \boldsymbol{n_0} + \boldsymbol{n_G} \cdot G + \boldsymbol{n_T} \cdot T_\mathrm{c} \tag{8.5}$$

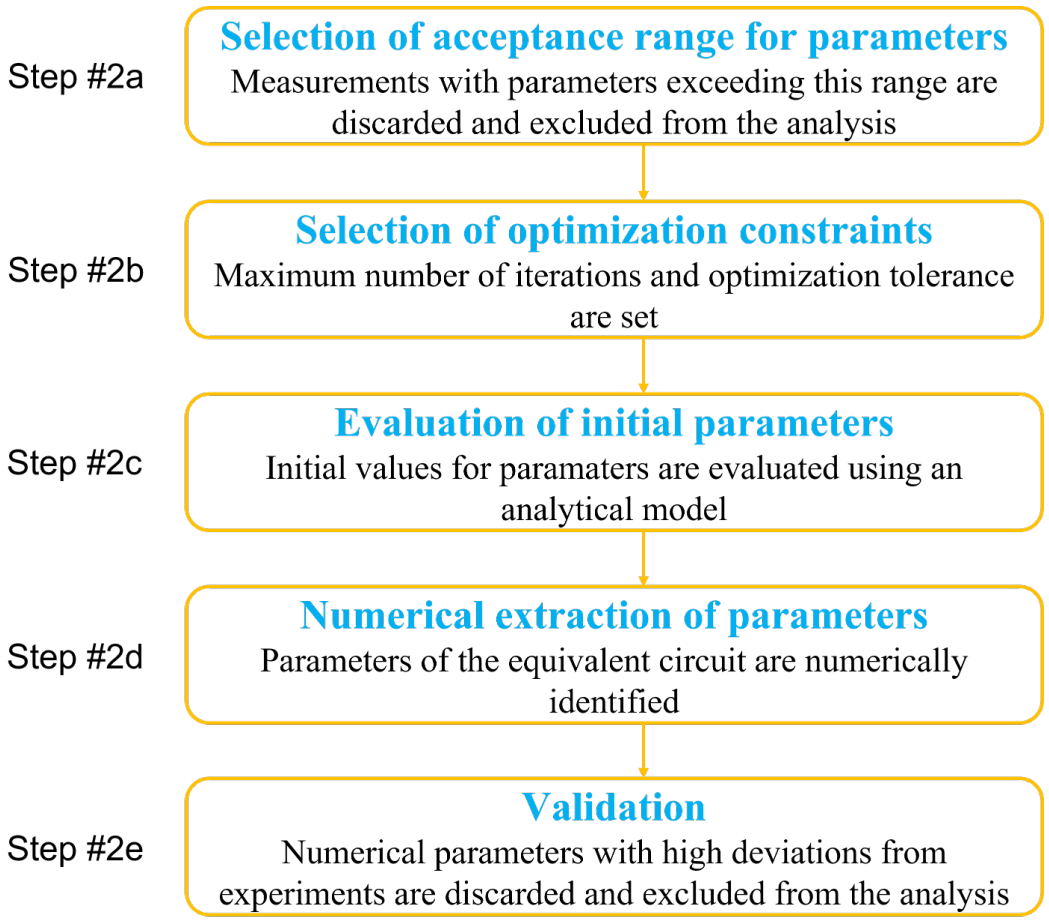

Fig. 8.2 Flowchart of step #2.

The dependence of the diode ideality factor on irradiance and temperature varies across the literature. In this study, a polynomial dependence on both variables is assumed, and this hypothesis is validated by the regression results.

$$R_{\mathrm{s}} = \boldsymbol{R}_{s,\mathrm{STC}} \cdot \frac{T_{\mathrm{c}}}{T_{c,\mathrm{STC}}} \cdot \left(1 - \boldsymbol{k}_{\mathrm{Rs}} \cdot \ln\left(\frac{G}{G_{\mathrm{STC}}}\right)\right) \tag{8.6}$$

where $R_{s,\mathrm{STC}}$ is the series resistance at STC, and k_{Rs} quantifies the irradiance dependence of R_{s}.

$$R_{\mathrm{sh}} = \boldsymbol{R}_{sh,\mathrm{STC}} \cdot \frac{G_{\mathrm{STC}}}{G} \tag{8.7}$$

where $R_{sh,\mathrm{STC}}$ denotes the shunt resistance at STC. The coefficients in bold, not explicitly provided in [26], are determined in this work through nonlinear least-squares regression, by minimizing the following objective function:

$$\min \sum_{i=1}^{N} \left(y_{\mathrm{i,exp}} - y_{\mathrm{i,mod}} \right)^2 \tag{8.8}$$

where $y_{\mathrm{i,exp}}$ and $y_{\mathrm{i,mod}}$ represent, respectively, the experimentally extracted and modelled values of the generic parameter y.

8.1.4 Step #4 — Power and Energy Estimation

In the final stage, the optimized parameter equations (from 8.3 to 8.7) are used to compute, for each measured pair of irradiance and temperature, the corresponding SDM parameters. The I–V curve is then reconstructed by solving Equation (8.2), from which the maximum power at each time step is obtained. Assuming constant power within each 1-minute interval, the total generated energy is calculated and compared with the experimental energy as well as with the prediction of the Irradiance-Proportionality (I–P) model [21]:

$$P = P_{\mathrm{STC}} \cdot \frac{G}{G_{\mathrm{STC}}} \cdot (1 + \gamma \cdot \Delta T) \tag{8.9}$$

where P_{STC} is the rated power at STC, γ is the power temperature coefficient, and $\Delta T = T_{\mathrm{c}} - 25\ ^{\circ}\mathrm{C}$. The deviations between the modelled and experimental energies are expressed as:

$$\Delta E_{\mathrm{opt}} = \frac{E_{\mathrm{opt}} - E_{\mathrm{exp}}}{E_{\mathrm{exp}}} \tag{8.10}$$

$$\Delta E_{\mathrm{I\text{-}P}} = \frac{E_{\mathrm{I\text{-}P}} - E_{\mathrm{exp}}}{E_{\mathrm{exp}}} \tag{8.11}$$

where E_{opt} and $E_{\mathrm{I\text{-}P}}$ are the energies estimated using the proposed optimized equations and the conventional I–P model, respectively, while E_{exp} denotes the experimental reference energy.

8.1.5 Comparison of energy predicted by other models

To validate the proposed methodology, the energy estimated by the optimized equations is benchmarked against predictions obtained from representative models widely cited in the literature. The following subsections concisely summarize each reference model.

Jones and Underwood

The approach by Jones and Underwood [23] is a compact analytical formulation for PV power, expressed as:

$$P = C_{FF} \cdot N_m \cdot \eta_{conv} \cdot \frac{G \cdot \ln(10^6 \cdot G)}{T} \tag{8.12}$$

where N_m is the number of modules, η_{conv} denotes the MPPT efficiency, T is the module temperature, G is the in-plane global irradiance, and C_{FF} is computed as:

$$C_{FF} = \frac{FF \cdot T_{ref}}{G_{ref}} \cdot \frac{[I_{sc} + k_1(T - T_{ref})]\,[V_{oc} + k_v(T - T_{ref})]}{\ln(10^6 \cdot G_{ref})} \tag{8.13}$$

Here, T_{ref} and G_{ref} are the STC temperature and irradiance, respectively, and FF is the fill factor, i.e., the ratio between the maximum power and the product of short-circuit current and open-circuit voltage.

Al-Bashir et al.

Al-Bashir et al. [24] introduce an empirical linear model that relates PV power to the hourly global solar irradiance (I_H), the average hourly module temperature (T_H), and the average hourly wind speed (V_H):

$$P_H = -509.5 + 2.1849\, I_H - 2.007\, T_H + 24.07\, V_H \tag{8.14}$$

The numerical coefficients in this equation were obtained by multivariate linear regression on 625 hourly measurements collected from a specific off-grid installation at the Hashemite University, Zarqa, Jordan, consisting of five series-connected polycrystalline modules with a total rated power of 1425 W_p. As a consequence, the

equation is not directly transferable to PV systems of different size or technology: its coefficients are device- and site-specific, and would need to be re-identified from experimental data for any other installation. In the present work, the model is applied as originally reported by the authors and serves as a representative benchmark for empirical linear regression approaches, rather than as a general-purpose predictive tool. The comparison is therefore intended to illustrate the limitations of site-calibrated empirical models relative to the physically grounded equivalent-circuit approach proposed in this chapter.

Park

The analytical method in [53] adopts a piecewise representation based on irradiance levels:

$$P_{array} = \begin{cases} N_m \cdot P_{\mathrm{STC}} \cdot \left(\dfrac{G_i^2}{G_{\mathrm{STC}} \cdot R_c} \right), & 0 \leq G_i \leq R_c \\ N_m \cdot P_{\mathrm{STC}} \cdot \dfrac{G_i}{G_{\mathrm{STC}}}, & R_c < G_i \leq G_{\mathrm{STC}} \\ N_m \cdot P_{\mathrm{STC}}, & G_i > G_{\mathrm{STC}} \end{cases} \tag{8.15}$$

where N_m is the number of modules, P_{STC} is the module rated power at STC, G_i is the incident irradiance, and R_c is a threshold irradiance typically set to 150 $\mathrm{W\,m^{-2}}$.

SAM

This model incorporates site- and installation-dependent coefficients determined empirically [22]. PV power is evaluated as:

$$P_{PV} = G \cdot S \cdot \eta_{pv} \tag{8.16}$$

$$\eta_{pv} = \eta_{nom} \cdot \left[1 + \gamma \cdot (T_{\mathrm{c}} - T_{c,\mathrm{STC}}) \right] \tag{8.17}$$

$$T_{\mathrm{c}} = T_{amb} + G_i \exp\left(A + BV_f\right) + G_i \cdot \frac{\Delta T}{G_{\mathrm{STC}}} \tag{8.18}$$

with:

- S: module area ($\mathrm{m^2}$);
- η_{pv}: instantaneous PV efficiency;

- η_{nom}: nominal module efficiency;
- A, B: empirical coefficients (tabulated in [22]);
- ΔT: temperature offset between irradiated cells and the dark back surface;
- V_f: wind speed.

For the modules analyzed in this study, the following coefficients are adopted: $A = -3.56$, $B = -0.0750$, and $\Delta T = 3$.

PESRC

The simplest irradiance-proportional formulation in the literature relates PV power linearly to incident irradiance [20]:

$$P_{PV} = \frac{G_i}{G_{\text{STC}}} \cdot P_{\text{STC}} \tag{8.19}$$

All the above models are applied to the available dataset to obtain energy predictions; subsequently, the deviations between the energy estimated by each model and the measured energy are computed.

8.2 Measurement System

This study employs datasets acquired with distinct electronic measurement platforms that are periodically calibrated to ensure traceability and accuracy.

8.2.1 Experimental setup in Italy

Module performance at the Politecnico di Torino (Italy) campus was monitored with two independent systems. The modules described in [59] were characterized in a short-term campaign using a capacitor-based arrangement described in Chapter 5.

In addition, three modules based on more recent technologies were monitored in a long-term outdoor campaign at Torino (Italy) with a dedicated station, hereafter "System #2 — Italy", consisting of:

- Three programmable electronic loads (800 W each, 16-bit resolution) with uncertainties $\leq \pm 0.25\%$ (current) and $\pm 0.15\%$ (voltage). The loads periodically scan the *I–V* curves and maintain operation at the maximum power point (MPP) via a perturb-and-observe algorithm derived from the *P–V* curve. Each electronic load is dedicated to one PV module.

- Three Pt100 sensors (0.1°C resolution, uncertainty $\leq \pm 0.3$°C) measuring the rear-side temperature of the three modules under test.

- One spectrally flat class A pyranometer (uncertainty $\leq \pm 3\%$) acquiring plane-of-array irradiance *G*.

- One weather station including: an anemometer for wind speed (0.01 m/s resolution, uncertainty $\leq \pm 1\%$) and direction (0.1° resolution, uncertainty $\leq \pm 1\%$); a piezoresistive barometer (0.1 mbar resolution, uncertainty $\leq \pm 0.4$ mbar); a Pt100 for ambient temperature (0.1°C resolution, uncertainty $\leq \pm 0.3$°C); and a capacitive hygrometer for relative humidity (0.1% resolution, uncertainty $\leq \pm 2.5\%$).

- A personal computer running control software in the LabVIEW environment to store all measurements in a database.

8.2.2 Experimental setup in Spain

A capacitor-based method is employed to determine the *I–V* characteristics: a power breaker controls a generator that charges a capacitor initially at zero voltage.

Two systems using the developed ADAS are installed on the roof of the solar energy laboratory at Universidad de Jaén (Spain). The key distinction is that one system includes a two-axis solar tracker (“Tracking System”, TS), whereas the other remains fixed (“Fixed System”, FS). Both platforms perform periodic acquisition of meteorological variables and *I–V* characteristics for four PV modules. Figure 8.3 shows the layout: equipment within purple and orange boxes correspond to TS and FS, respectively; devices in blue boxes are shared. Most instrumentation is housed inside the laboratory; however, the primary sensors (voltage, current, irradiance, air temperature, and module temperature), together with the PV modules and their metallic mounting structures, are located on the roof.

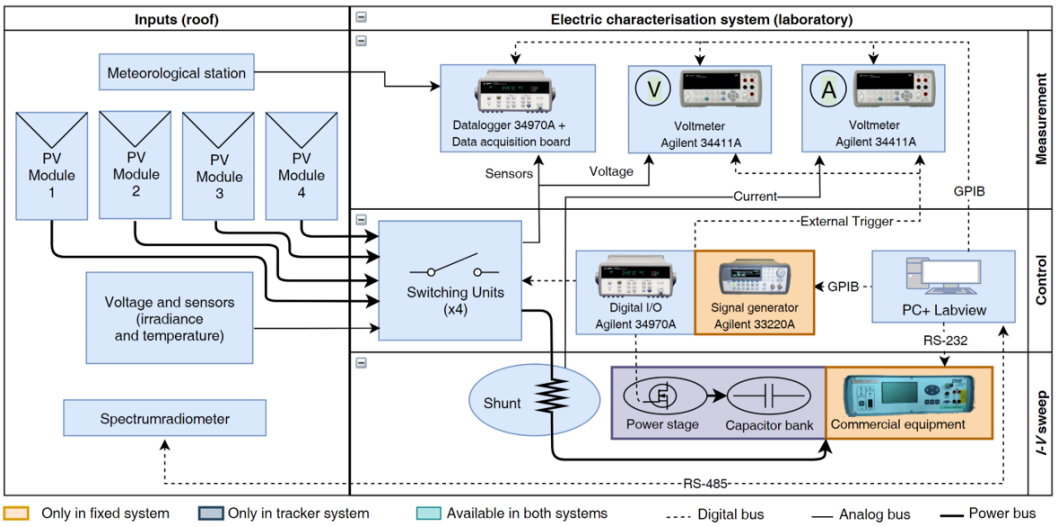

Fig. 8.3 Schematic of the measurement circuit in Spain.

The ADAS of the Spanish tracking platform ("System #3 — Spain") comprises:

- A custom circuit board—designed by the IDEA research group at Universidad de Jaén—integrated into the junction box of each PV module.
- One Pt100 sensor mounted on the rear of each module to measure cell/module temperature.
- Two high-accuracy multimeters measuring the terminal voltage and the voltage drop across a class 0.5 shunt resistor to infer current; the meters provide $6\frac{1}{2}$-digit resolution and < 1 mV uncertainty under operating conditions.
- A capacitive load with capacitance of 10 mF.
- A secondary standard pyranometer for irradiance with inaccuracy $< 2\%$.
- A datalogger ($6\frac{1}{2}$-digit resolution, annual uncertainty $\pm 0.04\%$) rated up to 300 V and 1 A, used to trigger and synchronize the multimeters.

The overall energy yield of any module tested with the Jaén systems can be determined with a total error below $\pm 1.3\%$.

Table 8.2 summarizes the principal uncertainty budgets for the three acquisition systems. Voltage, current, and power uncertainties are reported for the operating point of the module with the highest rated power under irradiance near STC (approximately 1000 $\mathrm{W\,m^{-2}}$).

8.3 Modules under Test

Tables 8.3, 8.4, and 8.5 summarize, based on manufacturers' datasheets, the key electrical specifications of the photovoltaic (PV) modules analyzed in this work (see Fig. 8.4). Before commencing the measurement campaigns, all modules underwent a verification procedure in which their I–V characteristics were measured under outdoor conditions and subsequently corrected to Standard Test Conditions (STC).

Additionally, modules #4 through #7 were subjected to Electroluminescence (EL) inspection [60] to detect potential defects such as microcracks or inactive cell regions. The comparison between the experimentally determined maximum power and the manufacturer's rated values confirmed that the deviations were within the uncertainty limits of the measurement systems. No anomalies or structural issues were revealed by the EL analysis.

8.4 Results

Two independent test campaigns were carried out at the Universidad de Jaén (Spain) and at Politecnico di Torino (Italy) during 2021 and 2024/2025. Modules #1–#7 were evaluated in spring 2021—devices #1–#3 in Spain and #4–#7 in Italy—whereas modules #8–#10 underwent a long-term outdoor campaign in Italy from April 2024 to February 2025. The latter set comprises state-of-the-art technologies: Tunnel Oxide Passivated Contact (TOPCon, #8), Interdigitated Back Contact (IBC, #9), and Heterojunction (HJT, #10). Across the entire dataset, a broad range of environmental conditions was explored (irradiance and module temperature), with up to approximately 15,000 I–V curves acquired for the modules with the most extensive monitoring.

Irradiance spanned from 150 $\mathrm{W/m^2}$ to 1200 $\mathrm{W/m^2}$, while module temperature varied between 25 °C and 70 °C. The filters described in Section 8.1 were applied to retain only measurements obtained under stable conditions of irradiance, temperature, and wind speed, and to remove records affected by partial shading or measurement artifacts. Subsequently, the equivalent-circuit parameters were identified by numerical fitting of the experimental I–V curves using a cascaded optimization scheme (Simulated Annealing followed by Nelder–Mead) to solve Equation (8.2).

#4
m-Si

#5
m-Si (all-back contact)

#6
p-Si

#7
p-Si (half cells)

#8
m-Si (half cells)

#9
m-Si (half cells)

#10
m-Si/a-Si (half cells)

Fig. 8.4 Photographs of the photovoltaic modules under analysis.

Figure 8.5 reports the distributions of the Normalized Root Mean Square Error (*NRMSE*) over the *I–V* curves and the deviation at the maximum power point (*MPP*) [61]. The *NRMSE* quantifies the discrepancy between measured and modelled currents:

$$NRMSE = \frac{\sqrt{\frac{\sum_{i=1}^{N}(I_{i,mod}-I_{i,exp})^2}{N}}}{\frac{\sum_{i=1}^{N} I_{i,exp}}{N}} \tag{8.20}$$

where, for each sampled voltage of the experimental *I–V* curve, $I_{i,mod}$ is the current reconstructed from the fitted parameters and $I_{i,exp}$ is the measured current. The second indicator represents the difference between the measured and modelled maximum power. The best agreement is observed for the Italian long-term campaign (modules #8–#10), for which the error at the *MPP* is always below 1 W and the corresponding *NRMSE* values remain below 0.8%. Modules tested in Spain (#1–#3) also show excellent results, with among the lowest *NRMSE* values and *MPP* errors below 1%. Although modules #4–#7 present comparatively higher discrepancies, their fitting accuracy remains within acceptable limits and the overall model agreement is satisfactory.

Overall, Fig. 8.5 corroborates the robustness of the parameter-extraction procedure, with the majority of *NRMSE* values below 0.5% and most *MPP* errors confined within $\pm$2.5 W.

In the second stage of the methodology, the boldface coefficients in (8.3)–(8.7) were optimized.

Figure 8.6 summarizes the dependence of the equivalent-circuit parameters on irradiance and temperature for each device under test. Each subfigure juxtaposes the optimized relations (continuous curves) with the parameters extracted from the experimental curves (markers), reported at module level. The results are consistent with the expected trends reported in the literature. Among the parameters, the reverse saturation current I_0 and the series resistance R_s are the most challenging to identify due to potential non-uniqueness (i.e., different parameter sets can yield nearly identical *I–V* characteristics), which may lead to overfitting. Nevertheless, clear and physically plausible trends are observed for all modules: saturation currents up to 10^{-5} A and series resistances below 1 Ω. The highest-performing devices—modules #8–#10—exhibit the lowest values of I_0 and R_s, consistent with the performance improvements introduced by recent cell technologies. Conversely, the ideality factor n displays comparable magnitudes across most modules.

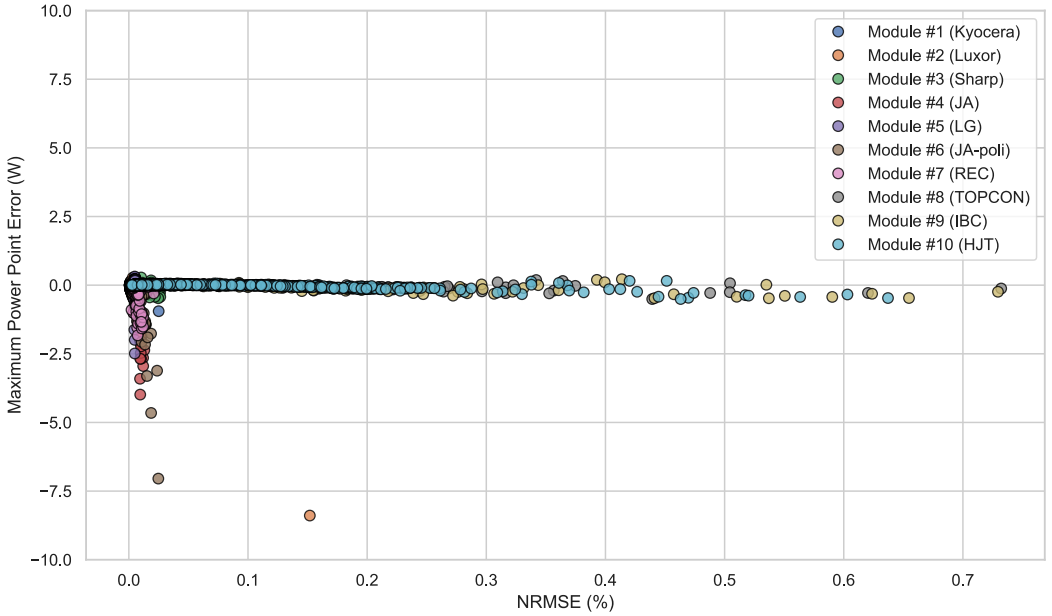

Fig. 8.5 Distributions of *NRMSE* for the *I*–*V* curves and of the error at the *MPP*.

The optimized coefficients are listed in Table 8.6. For the reverse saturation current, the fitted $I_{0,\mathrm{STC}}$ lies in the range $\approx 10^{-11}$–10^{-8} A for modules tested in 2021 (#1–#7), whereas the most recent devices (#8–#10) show the lowest values, in line with their higher efficiencies and improved cell designs. Similarly, the extracted R_s values are smallest for the newest modules, with the notable exception of module #5, whose reduced series resistance is attributable to its back-contact architecture. The identified ideality factors n generally fall between 1 and 2, except for module #7, for which n is approximately constant at 0.58. Moreover, n is nearly invariant with irradiance and temperature for most modules, with the exceptions of #2 and #5, where n increases with both variables; in contrast, the HJT module (#10) shows a decreasing n with temperature.

The plot of shunt resistance R_sh versus irradiance is omitted. As frequently discussed in the literature, R_sh can be weakly identifiable and sometimes assume non-physical values; consequently, many studies adopt four-parameter models that exclude R_sh, given its negligible influence on the *I*–*V* expression under uniform conditions [56]. However, R_sh becomes relevant under partial shading, since the slope of the *I*–*V* curve near short circuit—directly related to R_sh—can change. In the presence of scattered estimates, R_sh is treated as constant (entries marked with * in Table 8.6) and set equal to its average value.

The optimized coefficients were then substituted into (8.3)–(8.7) to compute the energy yield over the respective monitoring periods.

For the earlier-generation modules #1–#3 (Spain), the proposed approach (light blue bars) provides the most accurate energy estimates, with deviations of approximately 3–5%, outperforming the alternative models. In this subset, the Osterwald model ranks second overall, although it performs poorly for module #1. For the most recent technologies (#8–#10), the proposed method achieves excellent accuracy with deviations of roughly 1–6%. The advantage over competing models is evident: the best-performing alternative yields deviations of about 8% for module #9, while the others exhibit errors typically in the 15–20% range. For modules #4–#7 (Italy), the proposed method is not the top performer for #4 and #5; however, these technologies are no longer prevalent in the current market. Given that future deployments will be dominated by TOPCon, IBC, and HJT, the proposed methodology offers the most reliable option for PV energy assessment moving forward.

The superior accuracy on modern technologies is not merely a consequence of the larger dataset or the more recent measurement campaign. It reflects a fundamental advantage of the equivalent-circuit approach: by identifying the five SDM parameters directly from experimental I–V curves and regressing them individually as functions of irradiance and temperature, the method captures technology-specific behaviours that fixed-coefficient empirical models cannot represent.

In particular, the identified parameter equations reveal behaviours that are characteristic of advanced cell architectures and that deviate from the assumptions underlying the benchmark models. For the HJT module (#10), the fitted ideality factor n exhibits a negative temperature dependence, it decreases as T_c increases, which is opposite to the trend observed in conventional p-type crystalline silicon and reflects the temperature sensitivity of the amorphous silicon passivation layers inherent to HJT technology. For the IBC module (#9), the identified I_0 and R_s values are among the lowest in the dataset, consistent with the absence of front-contact shading losses and the high-quality passivation of both cell surfaces; under these conditions, the fill factor and MPP location vary with operating conditions in a non-linear manner that is not captured by irradiance-proportional or fixed-γ formulations. For the TOPCon module (#8), the irradiance dependence of R_s, quantified by the fitted coefficient k_{R_s}, is among the strongest in the dataset, a consequence of

the tunnel-oxide passivation contact whose resistive behaviour is more sensitive to injection level than conventional Al-BSF or PERC contacts.

In contrast, the benchmark models relate output power to irradiance and temperature through fixed empirical coefficients that were either derived from older cell technologies or calibrated on a specific installation. They are structurally unable to reproduce the technology-specific dependences of n, I_0, and R_s on operating conditions. The data-filtering pipeline in Step #1 further contributes to the accuracy on modern modules by ensuring that only stable, spectrally representative measurements are used for regression — a particularly important requirement for HJT devices, whose short-circuit current is known to be sensitive to spectral conditions and to low-irradiance operation.

The results for modules #4 and #5 are consistent with this interpretation. These are first-generation crystalline silicon devices whose electrical behaviour under varying irradiance and temperature is relatively well approximated by the simpler empirical formulations on which the benchmark models were originally calibrated. For these technologies, the non-linear parameter dependences that the proposed method is specifically designed to capture are less pronounced, and the additional complexity of the equivalent-circuit regression does not yield a systematic accuracy advantage over simpler models. This observation does not undermine the proposed approach; rather, it confirms that its primary value lies in modelling technologies whose parameter dependences deviate significantly from the assumptions of conventional empirical models, precisely the modern high-efficiency architectures that now dominate the market and for which no well-calibrated benchmark currently exists.

Table 8.1 Summary of selected PV energy-estimation models and their required inputs.

Model	Synopsis	Required Inputs
Jones and Underwood [23]	Compact analytical model using irradiance, temperature, and fill factor to estimate PV power.	• Global irradiance (G) • Module temperature (T) • Number of modules (N_m) • MPPT efficiency (η_{conv}) • Fill factor (FF) • STC references (G_{ref}, T_{ref})
Al-Bashir et al. [24]	Empirical linear regression with meteorological predictors.	• Hourly global irradiance (I_H) • Hourly average module temperature (T_H) • Hourly average wind speed (V_H)
Park [53]	Piecewise analytical law conditioned on irradiance regime.	• Incident irradiance (G_i) • Rated power at STC (P_{STC}) • Number of modules (N_m) • Threshold irradiance ($R_c \approx 150$ W/m^2)
SAM (System Advisor Model) [22]	Semi-empirical formulation with installation-dependent coefficients.	• Irradiance (G) • Module area (S) • Nominal efficiency (η_{nom}) • Cell temperature (T_{c}) • Empirical coefficients ($A, B, \Delta T$) • Wind speed (V_f)
PESRC [20]	Irradiance-proportional baseline model.	• Incident irradiance (G_i) • Rated power at STC (P_{STC})

Table 8.2 Uncertainties for the sensors of the three acquisition systems

Quantity	System #1 Italy	System #2 Italy	System #3 Spain
		Uncertainty	
Voltage	±0.1%	±0.1%	±9 mV
Current	±1%	±0.25%	±80 mA
Power	±1%	±0.27%	±3.2 W
Irradiance	$< \pm 30$ W/m^2	$< \pm 30$ W/m^2	±20 W/m^2
Temperature	$< \pm 0.3$°C	$< \pm 0.3$°C	±0.3°C

Table 8.3 Manufacturer parameters of PV module tested at University of Jaén.

ID	#1	#2	#3
P_{nom}	135 W	100 W	245 W
$\eta_{\mathbf{STC}}$	13.5%	15.5%	14.9%
V_{oc}	22.1 V	21.6 V	37.5 V
I_{sc}	8.37 A	5.87 A	8.73 A
α	0.06%/°C	0.05%/°C	0.05%/°C
β	-0.36%/°C	-0.35%/°C	-0.347%/°C
Power tolerance	(-5%, +5%)	(0, +5%)	(-5%, +10%)

Table 8.4 Electrical parameters (manufacturer data) of PV modules tested at Politecnico di Torino – short-term campaign.

ID	#4	#5	#6	#7
P_{nom}	310 W	370 W	280 W	285 W
$\eta_{\mathbf{STC}}$	19%	21.4%	17.1%	17.1%
V_{oc}	40.3 V	42.8 V	38.65 V	38.6 V
I_{sc}	9.91 A	10.82 A	9.37 A	9.66 A
α	0.06%/°C	0.04%/°C	0.058%/°C	0.066%/°C
β	-0.3%/°C	-0.24%/°C	-0.33%/°C	-0.3%/°C
Power tolerance	(0, +5W)	(0, +3%)	(0, +5W)	(0, +5W)

Table 8.5 Electrical parameters (manufacturer data) of PV modules tested at Politecnico di Torino – long-term campaign.

ID	#8	#9	#10
P_{nom}	450 W	440 W	440 W
$\eta_{\mathbf{STC}}$	22.5%	22.5%	22.5%
V_{oc}	52.9 V	39.53 V	40.83 V
I_{sc}	10.74 A	14.3 A	13.4 A
α	0.04%/°C	0.05%/°C	0.04%/°C
β	-0.24%/°C	-0.23%/°C	-0.24%/°C
Power tolerance	(-3%, +5W)	(-3%, +3%)	(-3%, +3%)

Table 8.6 Main optimized parameters for the PV generators ($^{*}R_{\mathrm{sh}} = \mathrm{const}$).

Module ID	#1	#2	#3	#4	#5	#6	#7	#8	#9	#10
$I_{\mathrm{sc,STC}}$ (A)	8.64	5.74	8.55	10.08	10.47	9.11	9.42	10.72	14.01	13.57
$I_{0,\mathrm{STC}}$ (A) (10^{-9})	8.90	1.52	20.8	1.10	41.7	1.97	4.08	0.48	0.32	0.029
n_0	0.80	0.58	1.14	1.30	2.48	1.49	0.58	1.06	1.43	3.09
n_{G} (m^2/W) (10^{-5})	-25.7	18.2	5.42	4.23	73.7	11.3	-	6.46	11.7	9.35
n_{T} (1/°C) (10^{-4})	20.3	12.2	3.74	-6.10	-46.2	-13.9	-	3.60	-1.10	-63.7
$R_{\mathrm{s,STC}}$ (Ω)	0.19	0.36	0.30	0.30	0.0037	0.22	0.16	0.079	0.086	0.090
k_{Rs}	-0.15	0.12	0.04	-0.49	17.19	0.07	0.29	0.53	0.21	0.15
$R_{\mathrm{sh,STC}}$ (Ω)	179.3	5090*	1000*	1000*	112.1	1032*	348*	1000*	1000*	1000*

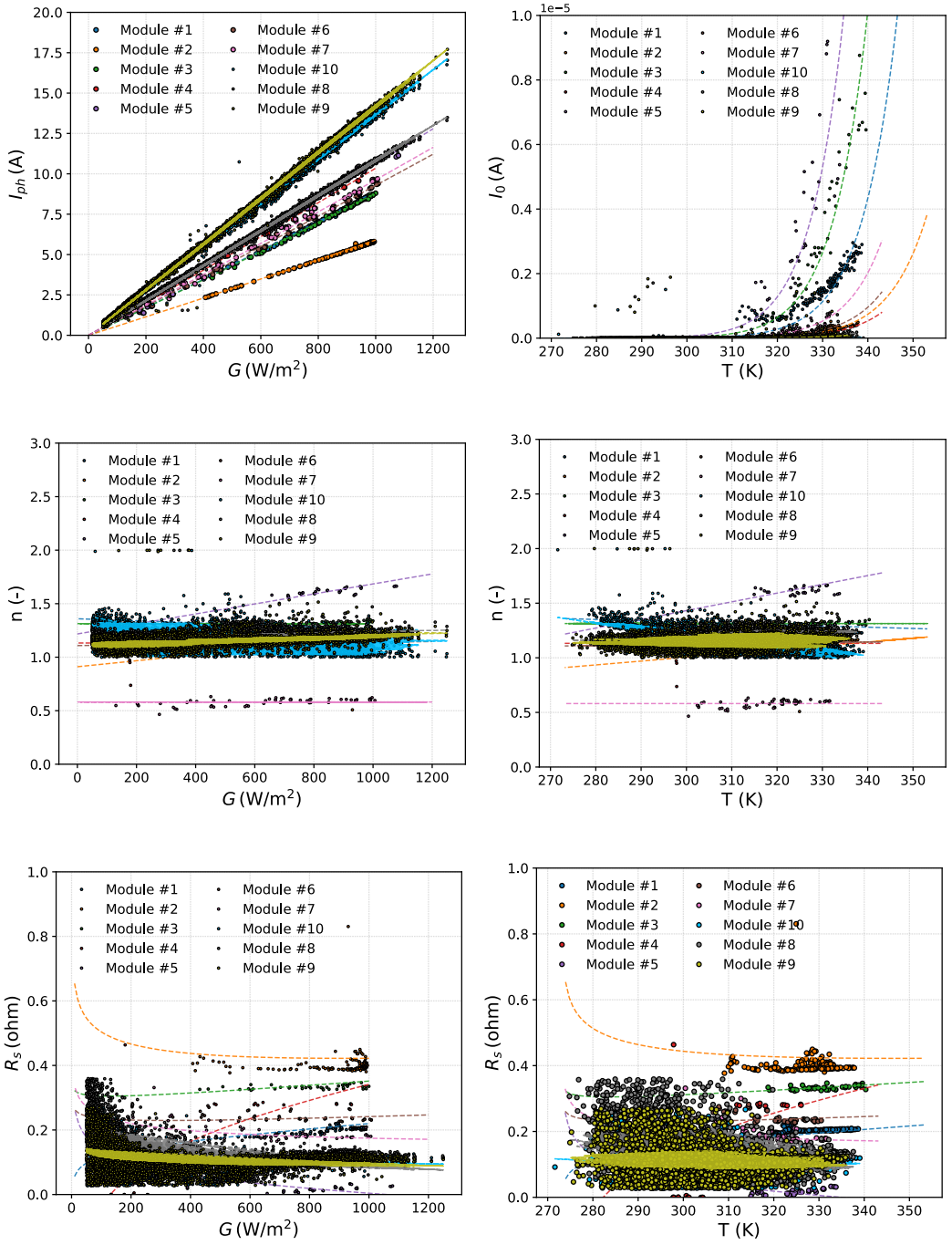

Fig. 8.6 Equivalent-circuit parameters as functions of G and T_c.

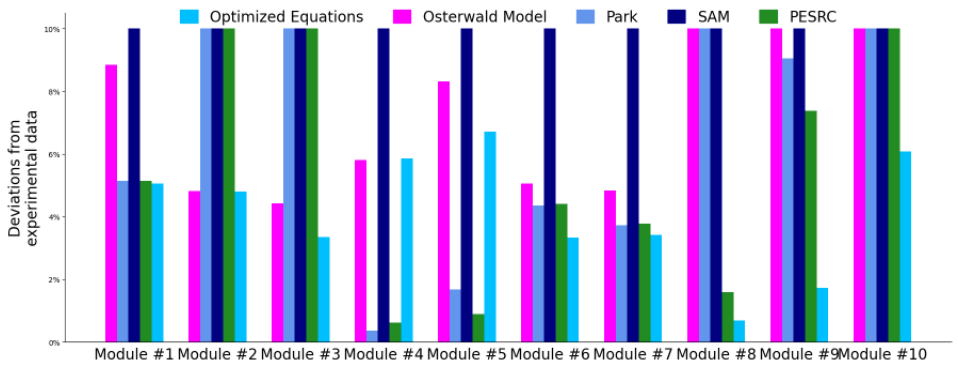

Fig. 8.7 Model deviations with respect to measurements for energy estimation.

Chapter 9

Conclusions

This Ph.D. thesis has developed and validated a unified methodological framework for the modelling, experimental characterisation, and parameter identification of photovoltaic cells and modules under realistic operating conditions. The work is structured around a recurring and coherent workflow, consisting of the formulation of a theoretical model, the design of an experimental setup aimed at validating such a model, and the subsequent recalibration of its parameters in order to achieve accurate and physically consistent representations of photovoltaic behaviour.

The scientific contributions of this thesis, which advance the state of the art in photovoltaic modelling and characterisation, can be summarised as follows.

1. **A "One Module, Two Tests" identification procedure for shaded PV cells in commercial half-cell modules.** Existing parameter identification methods for PV modules typically assume uniform irradiance and smooth single-diode I–V characteristics, or require dedicated test benches that isolate individual cells. The proposed procedure recovers the equivalent-circuit parameters of a single shaded cell within a commercial half-cell module by exploiting the algebraic difference of two module-level I–V curves, one acquired under uniform irradiance and one with a single cell intentionally shaded, both collected within a time window of less than two minutes under natural sunlight. The method was validated on flexible mini-modules against a direct "Two Modules, One Test" bridge-circuit measurement, with absolute current mismatches never exceeding 2.48 mA, and then extended to commercial 400 W half-cell modules. A systematic comparison of 3P, 4P, 5P, and 7P equivalent-circuit

models showed that the five-parameter single-diode model offers the most favourable trade-off between accuracy and computational cost under partial shading, achieving median NRMSE values below 0.5% and median MPP deviations below 0.08% on commercial modules, with execution times below ten seconds per shaded cell. This result is directly relevant to fault-detection algorithms embedded in PV monitoring platforms.

2. **A D-optimal, Fisher-Information-Matrix-based framework for *I–V* curve sampling optimisation in PV parameter estimation, extended to partial shading conditions.** While D-optimal experimental design has been applied in other estimation contexts, its systematic derivation and application to the five-parameter equivalent-circuit model of PV modules, including under partial shading conditions that introduce piecewise, non-smooth *I–V* characteristics due to bypass diode activation, constitutes a novel contribution. By deriving the Fisher Information Matrix associated with the single-diode model and maximising its determinant, the proposed algorithm redistributes any user-specified number of sampling points along the *I–V* curve so as to minimise the volume of the parameter confidence ellipsoid. Applied to five commercial modules of different technologies (monocrystalline Si, back-contact, HIT, polycrystalline Si, and TOPCon half-cut cells), D-optimal sampling achieved systematic reductions in parameter variance with respect to uniform sampling: up to 90.6% for I_{ph}, 98.1% for R_{sh}, and 80.9% for I_0 under partial shading, with the empirical variances remaining close to the theoretical Cramér–Rao Lower Bound, confirming statistical efficiency. A sensitivity analysis demonstrated that the CRLB computation is robust to parameter errors up to approximately 4–5%, which is well within the accuracy of the identified parameters. A complementary elbow analysis on the confidence-ellipsoid volume established that 50 samples provide a near-optimal operating point beyond which additional measurements yield only marginal information gains. To the best of the author's knowledge, this is the first systematic application of D-optimal design to *I–V* curve sampling optimisation for shaded PV modules, providing a theoretically grounded strategy for informative measurement acquisition.

3. **An integrated outdoor experimental infrastructure combining transient and steady-state *I–V* acquisition for PV characterisation under uniform and non-uniform irradiance.** Both a capacitive-load-based system and an

electronic-load-based system were developed, automated via LabVIEW, and deployed for outdoor measurements on five commercial PV modules. The synchronised acquisition of electrical quantities (voltage, current), cell temperature, and irradiance enabled a direct and repeatable comparison between measured I–V characteristics and model predictions. Unlike setups reported in prior literature that typically rely on a single acquisition modality, the combined infrastructure allowed cross-validation between the two methods and supported both the parameter identification workflow and the D-optimal sampling optimisation.

4. **A four-step energy yield estimation methodology based on identified equivalent-circuit parameters, validated across multiple PV technologies and climates.** Existing energy estimation models in the literature, including the irradiance-proportional model, the Jones–Underwood formulation, the Al-Bashir empirical regression, the Park piecewise model, and the SAM semi-empirical approach, do not exploit device-level equivalent-circuit parameters identified from experimental I–V curves. The proposed methodology introduces a four-step workflow: data preprocessing under stability constraints, per-curve parameter estimation via a cascaded Simulated Annealing and Nelder–Mead optimisation, nonlinear regression of the five SDM parameters as functions of irradiance and temperature, and power and energy reconstruction. Validated on ten PV modules of different technologies (including TOPCon, IBC, and HJT) tested at two sites, Politecnico di Torino (Italy) and Universidad de Jaén (Spain), the proposed approach achieved energy prediction deviations of approximately 1–6% for the most recent technologies (#8–#10), outperforming all benchmark models, for which deviations of 8–20% were observed on the same devices. This result demonstrates that accurate device-level characterisation directly translates into improved system-level energy estimation, particularly for advanced cell technologies that are increasingly dominant in the current market.

The analysis of photovoltaic module architectures provided the structural and electrical basis for understanding the behaviour of PV generators under uniform and non-uniform operating conditions. Particular attention was devoted to the impact of partial shading on the I–V characteristic, highlighting the role of bypass diodes, substring interconnections, and internal parallelisation. These aspects were shown

to be critical for both modelling accuracy and parameter identifiability, as shaded conditions introduce multiple local minima and non-smooth features that challenge conventional identification techniques. This chapter established the architectural constraints that must be explicitly considered when developing parameter estimation strategies for shaded cells and modules.

The experimental characterisation of a first-order RC filtering stage served as a controlled validation of the proposed modelling and identification methodology. By applying the full workflow to a simple and analytically tractable system, the consistency between theoretical predictions, experimental measurements, and recalibrated model parameters was quantitatively assessed. This preparatory exercise validated the adopted measurement techniques and curve-fitting procedures, providing confidence in their applicability to photovoltaic devices, where additional nonlinearities and sources of uncertainty are present.

Dedicated experimental setups were then developed to enable the controlled acquisition of I–V characteristics of photovoltaic modules under outdoor conditions. Both transient, capacitor-based methods and steady-state electronic-load-based techniques were implemented and automated through dedicated software architectures. These systems were designed to ensure synchronised acquisition of electrical and environmental quantities, thereby enabling a direct comparison between measured data and model predictions. This experimental infrastructure constitutes a key element of the thesis, as it provides the empirical basis required for rigorous parameter estimation and subsequent energy-yield analysis.

Building on the validated measurement framework, the thesis addressed the estimation of equivalent-circuit parameters for photovoltaic cells and modules operating under partial shading. The identification process explicitly accounted for the non-ideal and piecewise behaviour of the I–V curve induced by bypass diode activation. By recalibrating the model parameters on the basis of experimental data, the resulting equivalent-circuit representations were shown to accurately reproduce the electrical response of shaded devices. This chapter demonstrated how physically meaningful parameters can still be estimated under adverse operating conditions, provided that the modelling assumptions and sampling strategies are carefully aligned with the underlying device architecture.

A central contribution of the thesis is the introduction of a Cramér–Rao Lower Bound (CRLB)-based framework for analysing parameter uncertainty and optimising

I–V curve sampling. By deriving the Fisher Information Matrix associated with the equivalent-circuit model, theoretical lower bounds on the variance of the estimated parameters were obtained. This analysis enabled the identification of operating regions that are most informative for parameter estimation and guided the design of optimal sampling strategies. The CRLB study reinforces the methodological loop of the thesis, as it formally links the theoretical model to the experimental design, ensuring that measurements are not only accurate but also maximally informative. To the best of the author's knowledge, this is the first systematic application of D-optimal design to *I–V* sampling optimisation for PV equivalent-circuit models under both uniform and partial shading conditions, extending classical estimation-theoretic tools to the non-smooth regime introduced by bypass diode activation. This feature is especially relevant in operating contexts where the number of accessible sampling points is intrinsically limited, such as in maximum power point tracking algorithms implemented in photovoltaic inverters, where measurement actions must be minimised to preserve energy extraction and ensure real-time operation.

The final stage of the workflow addressed the estimation of photovoltaic energy production using the identified and recalibrated equivalent-circuit models. By propagating the experimentally identified parameters across varying irradiance and temperature conditions, the models were employed to predict power output and energy yield over extended periods. This approach demonstrates how accurate parameter identification directly translates into improved energy estimation, bridging the gap between device-level characterisation and system-level performance assessment. The results highlight the importance of robust modelling under non-ideal conditions, such as partial shading, for reliable energy-yield prediction.

Overall, the thesis demonstrates that accurate photovoltaic modelling requires a tight integration of theory, experimentation, and parameter recalibration. The proposed methodology provides a scalable foundation for future developments, including the statistical analysis of large datasets of photovoltaic module parameters grouped by technology. In this perspective, embedding the proposed identification, CRLB-based optimisation, and energy estimation procedures within inverters directly connected to photovoltaic plants represents a promising direction for real-time monitoring, adaptive modelling, and long-term performance evaluation of photovoltaic systems.

References

[1] A. Rezaee Jordehi. Parameter estimation of solar photovoltaic (PV) cells: A review. *Renewable and Sustainable Energy Reviews*, 61:354–371, 2016.

[2] Rabeh Abbassi, Abdelkader Abbassi, Mohamed Jemli, and Souad Chebbi. Identification of unknown parameters of solar cell models: A comprehensive overview of available approaches. *Renewable and Sustainable Energy Reviews*, 90:453–474, 2018.

[3] I. Nassar-Eddine, A. Obbadi, Y. Errami, A. El Fajri, and M. Agunaou. Parameter estimation of photovoltaic modules using iterative method and the Lambert W function: A comparative study. In *Energy Conversion and Management*, volume 119, 2016.

[4] Efstratios I Batzelis, Georgios Anagnostou, Chandan Chakraborty, and Bikash C Pal. Computation of the Lambert W function in photovoltaic modeling. In *ELECTRIMACS 2019:elected Papers; Springer: Berlin/Heidelberg, Germany; Volume 1;*, pages 583–595. Springer, 2020.

[5] Mohamed B H Rhouma, Adel Gastli, Lazhar Ben Brahim, Farid Touati, and Mohieddine Benammar. A simple method for extracting the parameters of the PV cell single-diode model. *Renewable energy*, 113:885–894, 2017.

[6] Radouane Majdoul, Elhassane Abdelmounim, Med Aboulfatah, Abd Wahed Touati, Ahmed Moutabir, and Abdelmjid Abouloifa. Combined analytical and numerical approach to determine the four parameters of the photovoltaic cells models. In *Proceedings of 2015 International Conference on Electrical and Information Technologies, ICEIT 2015*, pages 263–268, 2015.

[7] Ali M. Humada, Mojgan Hojabri, Saad Mekhilef, and Hussein M. Hamada. Solar cell parameters extraction based on single and double-diode models: A review, 2016.

[8] Vun Jack Chin, Zainal Salam, and Kashif Ishaque. Cell modelling and model parameters estimation techniques for photovoltaic simulator application: A review. *Applied Energy*, 154:500–519, 2015.

[9] Marcelo Gradella Villalva, Jonas Rafael Gazoli, and Ernesto Ruppert Filho. Comprehensive approach to modeling and simulation of photovoltaic arrays. *IEEE Transactions on power electronics*, 24(5):1198–1208, 2009.

[10] Samuel R Fahim, Hany M Hasanien, Rania A Turky, Shady HE Abdel Aleem, and Martin Ćalasan. A comprehensive review of photovoltaic modules models and algorithms used in parameter extraction. *Energies*, 15, 2022. Art. 8941.

[11] K Ishaque, Z Salam, H Taheri, and A Shamsudin. Parameter extraction of photovoltaic cell using differential evolution method. In *2011 IEEE Applied Power Electronics Colloquium (IAPEC)*, pages 10–15. IEEE, 2011.

[12] Dhiaa Halboot Muhsen, Abu Bakar Ghazali, Tamer Khatib, and Issa Ahmed Abed. A comparative study of evolutionary algorithms and adapting control parameters for estimating the parameters of a single-diode photovoltaic module's model. *Renewable Energy*, 96, 2016.

[13] Shuijia Li, Wenyin Gong, and Qiong Gu. A comprehensive survey on meta-heuristic algorithms for parameter extraction of photovoltaic models. *Renewable and Sustainable Energy Reviews*, 141:110828, 2021.

[14] W. De Soto, S. A. Klein, and W. A. Beckman. Improvement and validation of a model for photovoltaic array performance. *Solar Energy*, 80(1):78–88, 2006.

[15] K. J. Sauer, T. Roessler, and C. W. Hansen. Modeling the irradiance and temperature dependence of photovoltaic modules in PVsyst. *IEEE Journal of Photovoltaics*, 5(1):152–158, 2015.

[16] Cristiano Saboia Ruschel, Fabiano Perin Gasparin, and Arno Krenzinger. Experimental analysis of the single diode model parameters dependence on irradiance and temperature. *Solar Energy*, 217:134–144, 2021.

[17] A Ciocia, P Di Leo, S Fichera, F Giordano, G Malgaroli, and F Spertino. A novel procedure to adjust the equivalent circuit parameters of photovoltaic modules under shading. Institute of Electrical and Electronics Engineers Inc., 2020.

[18] Vladimir Sovljanski and Mario Paolone. On the use of Cramér-Rao lower bound for least-variance circuit parameters identification of Li-ion cells. *Journal of Energy Storage*, 94, 2024. Art. 112223.

[19] Steven M Kay. *Fundamentals of statistical signal processing: Practical algorithm development*, volume 3. Pearson Education, 2013.

[20] M. Fuentes, G. Nofuentes, J. Aguilera, D.L. Talavera, and M. Castro. Application and validation of algebraic methods to predict the behaviour of crystalline silicon pv modules in mediterranean climates. *Solar Energy*, 81(11):1396–1408, 2007.

[21] Mark B. Campanelli and Carl R. Osterwald. Effective irradiance ratios to improve I-V curve measurements and diode modeling over a range of temperature and spectral and total irradiance. *IEEE Journal of Photovoltaics*, 6(1), 2016.

[22] D L King, W E Boyson, and J A Kratochvil. Photovoltaic array performance model. Technical report, Sandia National Laboratory, 2003.

[23] S. G. Obukhov, I. A. Plotnikov, O. A. Surzhikova, and K. D. Savkin. Method for prediction of the power output from photovoltaic power plant under actual operating conditions. *IOP Conference Series: Materials Science and Engineering*, 189(1), 4 2017.

[24] Adnan ; Al-Bashir, Mohammad ; Al-Dweri, and Ahmed Alghandoor. Analysis of effects of solar irradiance, cell temperature and wind speed on photovoltaic systems performance. *International Journal of Energy Economics and Policy*, 10(1):353–359.

[25] Ricardo Oliveira and Carmen L. T. Borges. A comparison of photovoltaic models for estimating power generation: a case study of Brazilian data. *Clean Technologies and Environmental Policy*, 23(2):517–530, 2021.

[26] Alain K. Tossa, Y. M. Soro, Y. Azoumah, and D. Yamegueu. A new approach to estimate the performance and energy productivity of photovoltaic modules in real operating conditions. *Solar Energy*, 110, 2014.

[27] Prashant Malik and Shyam Singh Chandel. A new integrated single-diode solar cell model for photovoltaic power prediction with experimental validation under real outdoor conditions. *International Journal of Energy Research*, 45(1):759–771, 2021.

[28] Gabriele Malgaroli, Stefano Schubert, Alessandro Ciocia, Filippo Spertino, and Ali Faisal Murtaza. Two-tests procedure to determine the equivalent circuit's parameters of half-cells in commercial pv modules under sunlight and partial shading. *IEEE Transactions on Industry Applications*, 2025.

[29] Stefano Schubert, Vladimir Sovljanski, Filippo Spertino, Gianfranco Chicco, and Mario Paolone. Accurate parameter estimation on photovoltaic modules using fisher information matrix and d-optimal design. *IEEE Access*, 13:212378–212406, 2025.

[30] Gabriele Malgaroli, Alessandro Ciocia, Slawomir Gulkowski, José Vicente Muñoz Díez, Stefano Schubert, and Filippo Spertino. Innovative model for energy assessment of new crystalline silicon technologies tested under different climates. *IEEE Transactions on Industry Applications*, 2026.

[31] William Shockley. The theory of p-n junctions in semiconductors and p-n junction transistors. *Bell System Technical Journal*, 28(3):435–489, 1949.

[32] Antonio Luque and Steven Hegedus, editors. *Handbook of Photovoltaic Science and Engineering*. John Wiley & Sons, Chichester, UK, 2003.

[33] M. B.H. Rhouma and A. Gastli. An extraction method for the parameters of the solar cell single-diode-model. In *Proceedings - 2018 2nd European Conference on Electrical Engineering and Computer Science, EECS 2018*, 2018.

[34] Priyanka Singh and N. M. Ravindra. Temperature dependence of solar cell performance—an analysis. *Solar Energy Materials and Solar Cells*, 101:36–45, 2012.

[35] Olivier Dupré, Rodolphe Vaillon, and Martin A. Green. Physics of the temperature coefficients of solar cells. *Solar Energy Materials and Solar Cells*, 140:92–101, 2015.

[36] Martin A. Green, Ewan D. Dunlop, Masahiro Yoshita, et al. Solar cell efficiency tables (version 64). *Progress in Photovoltaics: Research and Applications*, 32(7):425–441, 2024.

[37] Rabindra Satpathy and Venkateswarlu Pamuru. Chapter 5 - manufacturing of crystalline silicon solar pv modules. In Rabindra Satpathy and Venkateswarlu Pamuru, editors, *Solar PV Power*, pages 135–241. Academic Press, 2021.

[38] John W. Bishop. Computer simulation of the effects of electrical mismatches in photovoltaic cell interconnection circuits. *Solar Cells*, 25(1):73–89, 1988.

[39] Paul Horowitz. Hill w. the art of electronics. *Cambridge: Cambridge University Press2 Edition*, 3, 2015.

[40] Gene F Franklin, J David Powell, Abbas Emami-Naeini, and J David Powell. *Feedback control of dynamic systems*, volume 7. Prentice hall Upper Saddle River, 2015.

[41] William H Press. *The art of scientific computing 3rd edition*. Cambridge university press, 2007.

[42] Filippo Spertino, Jawad Ahmad, Alessandro Ciocia, Paolo Di Leo, Ali F. Murtaza, and Marcello Chiaberge. Capacitor charging method for i–v curve tracer and mppt in photovoltaic systems. *Solar Energy*, 119:461–473, 2015.

[43] Mohammad Aminul Islam, Md. Akhtaruzzaman, Nowshad Amin, and Kamaruzzaman Sopian. Chapter 5 - commercial viability of different photovoltaic technologies. In Md. Akhtaruzzaman and Vidhya Selvanathan, editors, *Comprehensive Guide on Organic and Inorganic Solar Cells*, Solar Cell Engineering, pages 347–393. Academic Press, 2022.

[44] Franz Baumgartner, Cyril Allenspach, Ebrar Özkalay, Matthew Berwind, Anna Heimsath, Christof Bucher, David Joss, Sara Mirbagheri Golroodbari, Wilfried van Sark, Alexander Granlund, et al. Performance of partially shaded pv generators operated by optimized power electronics. 2024.

[45] Alessandro Ciocia, Paolo Di Leo, Stefania Fichera, Francesco Giordano, Gabriele Malgaroli, and Filippo Spertino. A novel procedure to adjust the equivalent circuit parameters of photovoltaic modules under shading. In *2020 International Symposium on Power Electronics, Electrical Drives, Automation and Motion (SPEEDAM)*, pages 711–715, 2020.

[46] Zaiyu Gu, Guojiang Xiong, and Xiaofan Fu. Parameter extraction of solar photovoltaic cell and module models with metaheuristic algorithms: A review. *Sustainability*, 15(4):3312, 2023.

[47] Jobayer, Md and Shaikat, Md Al Hasan and Rashid, Md Naimur and Hasan, Md Rakibul. A systematic review on predicting PV system parameters using machine learning. *Heliyon*, 9(6):e16815, 2023.

[48] Papul Changmai, Sunil Deka, Shashank Kumar, Thanikanti Sudhakar Babu, Belqasem Aljafari, and Benedetto Nastasi. A critical review on the estimation techniques of the solar PV cell's unknown parameters. *Energies*, 15(19):7212, 2022.

[49] Weinan Xu, Weng Kee Wong, Kay Chen Tan, and Jian-Xin Xu. Finding high-dimensional d-optimal designs for logistic models via differential evolution. *IEEE Access*, 7:7133–7146, 2019.

[50] Kay White Vugrin, Laura Painton Swiler, Randall M Roberts, Nicholas J Stucky-Mack, and Sean P Sullivan. Confidence region estimation techniques for nonlinear regression in groundwater flow: Three case studies. *Water Resources Research*, 43.3, 2007. Art. W03423.

[51] Charles R. Harris, K. Jarrod Millman, Stéfan J. van der Walt, Ralf Gommers, Pauli Virtanen, David Cournapeau, Eric Wieser, Julian Taylor, Sebastian Berg, Nathaniel J. Smith, Robert Kern, Matti Picus, Stephan Hoyer, Marten H. van Kerkwijk, Matthew Brett, Allan Haldane, Jaime Fernández del Río, Mark Wiebe, Pearu Peterson, Pierre Gérard-Marchant, Kevin Sheppard, Tyler Reddy, Warren Weckesser, Hameer Abbasi, Christoph Gohlke, and Travis E. Oliphant. Array programming with NumPy. *Nature*, 585(7825):357–362, September 2020.

[52] Pauli Virtanen, Ralf Gommers, Travis E. Oliphant, Matt Haberland, Tyler Reddy, David Cournapeau, Evgeni Burovski, Pearu Peterson, Warren Weckesser, Jonathan Bright, Stéfan J. van der Walt, Matthew Brett, Joshua Wilson, K. Jarrod Millman, Nikolay Mayorov, Andrew R. J. Nelson, Eric Jones, Robert Kern, Eric Larson, C J Carey, İlhan Polat, Yu Feng, Eric W. Moore, Jake VanderPlas, Denis Laxalde, Josef Perktold, Robert Cimrman, Ian Henriksen, E. A. Quintero, Charles R. Harris, Anne M. Archibald, Antônio H. Ribeiro, Fabian Pedregosa, Paul van Mulbregt, and SciPy 1.0 Contributors. SciPy 1.0: Fundamental Algorithms for Scientific Computing in Python. *Nature Methods*, 17:261–272, 2020.

[53] Ricardo Oliveira and Carmen L.T. Borges. A comparison of photovoltaic models for estimating power generation: a case study of Brazilian data. *Clean Technologies and Environmental Policy*, 23(2):517–530, 3 2021.

[54] Filippo Spertino, Gabriele Malgaroli, Angela Amato, Muhammad Qureshi, Alessandro Ciocia, and Hafsa Siddiqi. An innovative technique for energy assessment of a highly efficient photovoltaic module. *Solar*, 2, 2022.

[55] Alessandro Ciocia, Paolo Di Leo, Stefania Fichera, Francesco Giordano, Gabriele Malgaroli, and Filippo Spertino. A novel procedure to adjust the equivalent circuit parameters of photovoltaic modules under shading. *2020 International Symposium on Power Electronics, Electrical Drives, Automation and Motion, SPEEDAM 2020*, pages 711–715, 6 2020.

[56] Dhiaa Halboot Muhsen, Abu Bakar Ghazali, Tamer Khatib, and Issa Ahmed Abed. A comparative study of evolutionary algorithms and adapting control parameters for estimating the parameters of a single-diode photovoltaic module's model. *Renewable Energy*, 96:377–389, 2016.

[57] Tamer Khatib, Rezeq Direya, and Asmaa Said. An improved method for extracting photovoltaic module I–V characteristic curve using hybrid learning machine system. *Journal of Solar Energy Engineering*, 143(5):051006, 2021.

[58] Fatima Ezzahra Ait Salah, Noureddine Maouhoub, Kawtar Tifidat, Yunyoung Nam, and Mohamed Abouhawwash. An efficient analytical approach for forecasting the peak power of PV panels working in outdoor conditions based on explicit model. *Energy Conversion and Management: X*, 20:100423, 2023.

[59] Gabriele Malgaroli, Alessandro Ciocia, Slawomir Gulkowski, José Vicente Muñoz Díez, Stefano Schubert, and Filippo Spertino. Comparative study of power prediction for photovoltaic modules with different technologies tested in Italy and in Spain. In *2024 IEEE International Conference on Environment and Electrical Engineering and 2024 IEEE Industrial and Commercial Power Systems Europe (EEEIC/I&CPS Europe)*, pages 1–6. IEEE, 2024.

[60] Alessandro Ciocia, Alessio Carullo, Paolo Di Leo, Gabriele Malgaroli, and Filippo Spertino. Realization and use of an IR camera for laboratory and on-field electroluminescence inspections of silicon photovoltaic modules. In *2019 IEEE 46th Photovoltaic Specialists Conference (PVSC)*, pages 2734–2739, 2019.

[61] Yazhong Sun, Yanchao Wu, Jia Liu, Sunan Zhang, Guoliang Li, Guibin Zou, and Kaikai Zhang. Ultra-short-term photovoltaic power prediction based on improved kmeans algorithm and VMD-SVR-LSTM model. In *2022 6th International Conference on Power and Energy Engineering (ICPEE)*, pages 47–51, 2022.